Fractured reservoir characterisation using shear-wave splitting in microseismic data: A case study from Oman

by

Othman Harith Al-Harrasi

A dissertation submitted to the University of Bristol in accordance with the requirements for award of degree of PhD in the Faculty of Science.

Department of Earth Sciences

University of Bristol

October 2010

Advisor

Prof. J.-Michael Kendall

Author's Declaration

I declare that the work in this dissertation was carried out in accordance with the requirements of the University's Regulations and Code of Practice for Research Degree Programmes and that it has not been submitted for any other academic award. Except where indicated by specific reference in the text, the work is the result of the candidate's own independent research performed at the University of Bristol, Department of Earth Sciences, between October 2007 and October 2010. Work done in collaboration with, or with the assistance of others, is indicated as such. Any views expressed in the dissertation are those of the author and not necessarily those of the University.

Othman Harith Al-Harrasi

Signed: ..... Date: ...../...../.....

Abstract

Traditionally, hydrocarbon reservoir characterisation relies on active seismic surveying. This thesis explores the potential of using passive microseismic monitoring as an imaging technique for reservoir characterisation, specifically delineating fracture networks. The study is based on estimating seismic anisotropy from observations of shear-wave splitting (SWS). The case study is a petroleum field in Oman. The microseismic experiment involved five monitoring wells, each instrumented with 8-level seismic arrays. The dataset consists of nearly 3400 microseismic events distributed over a period of 457 days.

Generally, SWS analysis is performed manually. However, manual analysis introduces inconsistency and it becomes too time consuming when processing large microseismic datasets. In this study I develop a (semi-) automated approach to SWS analysis. The approach combines the use of familiar cross-correlation and eigenvalue minimisation methods, both optimised using a statistical cluster analysis technique. Based on the misfit between the results from both methods, an automated quality measure is given to each estimate of SWS. Using this approach I am able to minimise the visual inspection of the diagnostic plots to only measurements with high quality ($\sim$20% of the total number of observations). The analysis yields 8500 SWS measurements. However, stringent quality control reduces the number of reliable measurements to 325.

The obtained splitting measurements are then used to describe the nature of anisotropy in the field. The difference between the fast and slow shear-wave velocities along the raypath (δV_s) ranges between 0% and 18%, and it is controlled by lithology and proximity to the NE-SW trending graben fault system that cuts the field formations. The anisotropy is interpreted in terms of aligned fractures or cracks superimposed on an intrinsic vertical transversely isotropic (VTI) rock fabric. The highest magnitudes of anisotropy are within the highly fractured Natih A reservoir (4.5%). Anisotropy decreases with depth, with the lowest magnitudes are found in the deep part of the non-producing Natih B-G formation (1.2%). The Fiqa shale cap rocks exhibit moderate amounts of anisotropy (3.9%). Anisotropy also varies laterally with the highest anisotropy occurring either side of the south-eastern graben fault. The predominant fracture strikes are consistent with the trends of the main faults (NE-SW and NW-SE). The majority of splitting observations indicate subvertical fracture dip ($>70°$).

In the next step the SWS observations are inverted using rock physics modelling to understand the mechanisms behind the observed anisotropy in a more quantitative way. The inversion esti-

mates fracture strike and density, and also the strength of the VTI anisotropy. Two inversions are performed assuming orthorhombic and monoclinic anisotropic symmetry classes. Due to the spatial variation in anisotropy and the limited ray coverage the inversion yields poorly constrained parameters in most cases. Nevertheless, the results generally agree with those obtained using ordinary SWS analysis. The inverted fracture strikes are consistent with the fault patterns (NE-SW and NW-SE). The estimates of fracture density show uniform distribution of fractures which contradicts with the observed spatial variation in anisotropy. However, these estimates are poorly constrained. The strength of the VTI anisotropy is weak (γ=0.02), as expected for carbonate rocks. Weak VTI anisotropy is observed in the NW block and within the Fiqa shale and the Natih B-G formation. In contrast, the highly fractured parts of the field (i.e., SE and Graben blocks, and the Natih A reservoir) appear to lack any significant VTI anisotropy.

Evidence of frequency-dependent anisotropy has been observed in the dataset. The observations are modelled to estimate fracture size and density. The model is based on squirt fluid flow mechanisms in porous fractured media. The results show that fracture size varies from the microscale within the Fiqa shale cap rocks, to the metre-scale within the Natih A gas reservoir, to the centimetre-scale within the non-producing part of the carbonate formation (Natih B-G). Fracture density decreases with depth from 0.18 in the Fiqa, to 0.11 in the Natih A, to 0.09 in the Natih B-G. There is also a lateral variation in fracture density from 0.13 in the SE block to 0.075 in the NW block. These estimates agree with the depth and lateral variations in δV_s magnitudes.

Finally, I perform a feasibility study of using SWS tomography with microseismic data. The field is divided into domains separated by the planes of the graben faults and by the formation boundaries. Each domain is represented by an elastic tensor parameterised by rotation angles and strength parameter. The inversion fails when investigating the lateral variation in anisotropy but works well when assuming a layered model. This most likely indicates that the lateral variation in anisotropy is more complicated compared to the variation with depth. The best-fit models indicate NW-SE fracture strike with a transition in fracture dip from subvertical in the Fiqa and Natih A to subhorizontal in the Natih B-G formation.

Cumulatively, these observations show how studies of SWS using microseismic data can be used to characterise fractures, important information for the exploitation of many reservoirs. This thesis serves as a cookbook for studies of SWS in microseismic data.

Acknowledgments

My sincere praise and ultimate thank must go to my God almighty for all his blessing and bounties which with I was able to undertake and complete this research.

The success in carrying out various aspects of this work would not have been possible without the generous contributions and volunteer support provided by many people. My heartfelt appreciation is given to all the persons involved. The list of names is long and I offer my sincere apologies if I fail to mention any particular name or organisation.

I am heartily thankful to my supervisor, Mike Kendall, who has supported me throughout my thesis with his patience and knowledge whilst allowing me the room to work in my own way. The fruitful discussions with Mike have greatly improved my understanding of the subject.

A special thank must go to Petroleum Development Oman (PDO) who funded me to do this research. PDO also provided me with the microseismic data for this study and gave me the permission to publish the results. I am grateful to many staff in PDO. Not to forget, Fahad Al-Kindy who facilitated the delivery of the data and Abdullah Al-Anboori who helped me with his advice and consultancies, and gave me the permission to use his codes. Part of the data was kindly delivered by Steve Oates (Shell). Thank you Steve.

I would like to acknowledge Andy Wuestefeld and James Wookey for their guidance and contributions to this piece of work. Andy helped me with the automation of shear-wave splitting analysis, whereas James allowed me to use his tomography code. I also appreciate the help of James Verdon on the shear-wave splitting inversion. Mark Chapman is thanked for using his frequency-dependent anisotropy code. I am grateful to Ian Bastow for his help with GMT and LaTeX. I would also like to thank Heidy Mader and James Wookey for being in my PhD committee. I benefited a lot from their guidance and advices.

In my daily work I have been blessed with a friendly and cheerful group of colleagues (Dave, Glenn, JV, Richardo, Nowacki, Jenny, Wuestefeld, Ian, Kit, Hammond, Wookey and George Helffrich). With the atmosphere of joy and fun they make, I was able to release the PhD stress and overcome the pain of being away from home. Not to forget their help in programming and improving my writing. Beyond science, I spent a wonderful time with my Omani friends here in Bristol. Thank you buddies.

Last but not least, I owe my everlasting gratefulness to my parents, wife, brothers and sisters. I thank them for their patience, encouragement and endless love. Finally, I can return to them with something worth all these years of waiting. It has been a fantastic six years of knowledge seeking that I spent in Leeds and Bristol. Finally, the time has come to rest my exhausted brain, at least for a while.

Dedication

This thesis is dedicated to those who covered me with their sincere and endless love: my mother, father and wife.

Table of Contents

List of Figures

List of Tables

Abbreviations, Symbols and Conventions

Abbreviations

Field M	A name given to the field studied in this thesis
PDO	Petroleum Development Oman
VSP	Vertical Seismic Profiling
FMI	Formation Micro Images
STWF	Simple Triggered Waveform interchange Format
RMS	Root Mean Square
ENZ	Geographic east, north and vertical coordinates
HTI	Transverse isotropy with a horizontal symmetry axis
VTI	Transverse isotropy with a vertical symmetry axis
TTI	Transverse isotropy with a tilted symmetry axis
SWS	Shear-wave splitting
FDA	Frequency-dependent anisotropy
XC	Cross-correlation method
EV	Eigenvalue minimisation method
NA	Neighbourhood Algorithm

Symbols (Latin)

a, b, c	Ray frame components
a_f	Fracture size
C,C_{ijkl}	Stiffness tensor
D	Raypath length
f	Frequency
$f_\circ$	Reference frequency
f_c	Corner frequency
f_d	Dominant frequency
K_f	Fluid bulk modulus
$M_\circ$	Seismic moment
M	Moment magnitude
M_c	Magnitude of completeness
N	Number of S-wave analysis windows
$P(f)$	Power spectrum
Q, q	Quality of shear-wave splitting
r	Source radius
R	Ratio of delay time
R_θ	Angle dependent radiation correction factor
s	Strength parameter (shear-wave splitting tomography)
S_h	Horizontal S-wave component
S_v	Vertical S-wave component
S_{fast}	Fast split S-wave velocity
S_{slow}	Slow split S-wave velocity
t_{env}	S-wave envelope duration
T_p	P-wave time pick
T_s	S-wave time pick
T_{start}	Start of S-wave analysis window
T_{stop}	End of S-wave analysis window
V_p	P-wave velocity
V_s	S-wave velocity
$V_{s_{(avg)}}$	Average S-wave velocity

Symbols (Greek)

α	Fracture strike
β_1,β_2,β_3	Rotation angles of elastic tensor
δt	Delay time
δV_s	Percentage difference between the fast and slow shear-wave velocities along the raypath
$\Delta\sigma$	Stress drop
ΔT	Separation between P- and S-wave time picks
ϵ_{kl}	Strain
ε,γ,δ	Thomson's parameter
ε_c	Crack density
η	Fluid viscosity
κ	Permeability
λ,μ	Lamé parameters
ξ	Fracture density
ρ	Rock density
ϱ	Fracture dip
σ_{ij}	Stress
σ_H	Maximum horizontal stress
σ_h	Minimum horizontal stress
ς	Grain size
τ_m	Relaxation time
τ_f	Relaxation time (associated with fractures)
Φ	Fast shear-wave polarisation orientation
Φ_p	Porosity
χ	Misfit function in shear-wave splitting tomography
$\Omega_\circ$	Low-frequency spectral level of the far-field displacement spectra
Ω	Normalised misfit in Φ

Conventions

- Azimuth is calculated from north clockwise.
- Inclination is calculated from vertical (except for shear-wave splitting tomography where it is calculated from horizontal). Up is positive.
- Fracture dip is calculated from horizontal. Up is positive.
- Fracture strike is calculate from north clockwise.
- Fracture density (ξ) is defined as $\xi = Na^3/V$, where N is the number of fractures with radius a within a rock volume V.

List of Publications

Journal articles

Al-Harrasi, O., Al-Anboori, A., Wüstefeld, A., and Kendall, J.-M., (2010). Seismic anisotropy in a hydrocarbon field estimated from microseismic data, *Geophysical Prospecting, DOI:10.1111/j.1365-2478.2010.00915.x*

Al-Harrasi, O., Kendall, J.-M. and Chapman, M., (2010). Fracture characterisation using frequency-dependent shear-wave anisotropy analysis of microseismic data, *Geophysical Journal International, in review.*

Expanded abstracts

Al-Harrasi, O., Wüstefeld, A., and Kendall, J.-M. (2009). Towards a fully automated shear-wave splitting analysis of microseismic data, *71st EAGE Conference & Exhibition, Amsterdam, The Netherlands, Expanded Abstracts, X013.*

Al-Harrasi, O. and Kendall, J.-M. (2010). Modelling frequency-dependent anisotropy observations made on microseismic data, *72nd EAGE Conference & Exhibition, Barcelona, Spain, Expanded Abstracts, F016.*

Al-Harrasi, O.; Kendall, J.-M., Wookey, J., Wüstefeld, A., and Verdon, J. (2011). A multi faceted study of reservoir anisotropy using microseismic data, *Third EAGE Passive Seismic Workshop, Athens, Greece.*

Co-authored publications

Wüstefeld, A., **Al-Harrasi, O.**, Verdon, J. P., Wookey, J. and Kendall, J.-M. (2010). A strategy for automated analysis of passive microseismic data to study seismic anisotropy and fracture characteristics, *Geophysical Prospecting, 58(5), 755–773.*

Kendall, J.-M., **Al-Harrasi, O.**, Verdon, J. P., Wüstefeld, A., and Al-Anboori, A., (2009). Fracture characterisation using estimates of shear-wave splitting from microseismic data, *EAGE Workshop on Passive Seismic, Limassol, Cyprus, Expanded Abstracts, A07.*

Wüstefeld, A., **Al-Harrasi, O.**, Verdon, J. P., Kendall, J.-M. (2009). Towards fully automated fracture characterisation in microseismic datasets using shear-wave splitting, *I-GET Final Conference, Potsdam, Germany.*

1 Introduction

"Producing reservoirs have been talking to us for long time. Now we can listen to them and understand how are they doing using microseismic technology. Shear-wave splitting analysis is a way of decoding their language."

O. Al-Harrasi

1.1 Microseismic monitoring

Microseismic monitoring, also known as passive seismic monitoring, involves measuring energy emitted by abundant small earthquakes using arrays of multi-component geophones. It has been used widely in mining (e.g., Young et al., 1992) and geothermal energy (e.g., Baria et al., 1999) industries. The interest on microseismic monitoring from the hydrocarbon industry has increased significantly since the 1990s. This relatively new technology is being driven by the high demand for real-time information on hydraulic and geomechanical processes occurring within and around reservoirs. Furthermore, it is considered a cost-effective imaging tool that can be used to support reservoir management and field development (Wilson et al., 2004).

Passive seismic monitoring can be performed using a surface network of sensors (e.g., Chambers et al., 2010) or wireline array of receivers deployed at shallow depths (few 100s of meters) or deeper at reservoir levels (e.g., Dyer et al., 1999; Jones et al., 2004) (Figure 1.1). A recent study in Saudi Arabia utilised the three types of networks: surface, shallow and deep (Jervis & Dasgupta, 2009). Downhole sensors have better recording sensitivity, whereas surface sensors provide improved spatial recording aperture. The combination of the two installation types gives a unique 4D image of subsurface activities. The installation is usually temporary but sometimes permanent, especially with the cases of surface networks (e.g., the Valhall Life-of-Field-Seismic (LoFS) project (Fischer, 2004)).

1.1.1 Origin of microseismicity

Microseismic events are small earthquakes, usually Richter magnitude (M_L) < 0 (Jupe et al., 2003), that are a consequence of stress changes. Microearthquakes occur naturally or are induced by some form of human activity and can be due to fault reactivation and fracture formation or

deformation associated with volumetric changes. Engineering activities (e.g., fluid production and injection) can alter the rock properties and induce perturbations to the *in situ* stress conditions. The rate of induced seismicity varies depending on the changing stress state, fracture distribution and reservoir geomechanics (Jupe et al., 2003). Most microseismic events are small in magnitude, however, they can cause significant social and economic problems due to their proximity to wells and surface infrastructures. For example, they may be precursory to borehole failure (Kristiansen et al., 2000; Maxwell & Urbancic, 2001), a problem that costs the oil industry fortune every year.

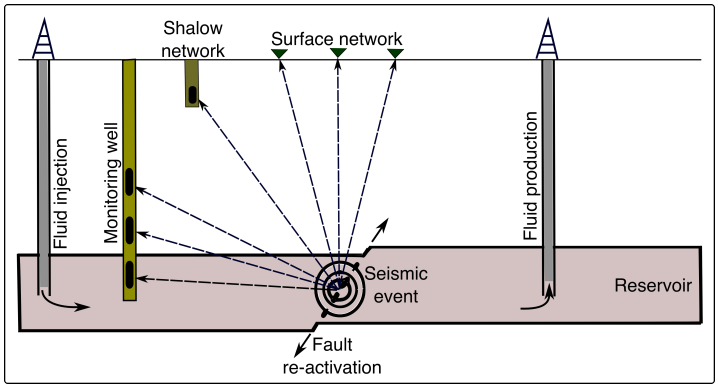

Figure 1.1: A cartoon showing the three types of microseismic monitoring installation used in hydrocarbon industry: surface, shallow and deep networks.

1.1.2 Applications of microseismic monitoring

Microseismic monitoring can deliver real-time information about subsurface behaviour. The technology is thought to be a crucial part of future instrumented hydrocarbon fields (Maxwell & Urbancic, 2001). Since microseismic activities result from changes in stress, mapping microseismic events identifies those geomechanically unstable volumes of the reservoir both in space and time (Wilson et al., 2004). In addition to mapping locations of events, passive seismic monitoring has a broad range of potential applications, such as: (1) delineating reservoir structures that can not be imaged using conventional seismic surveys (Maxwell et al., 1998; Rutledge et al., 1998), (2) mapping fluid movements inside reservoirs (Jupe et al., 2003; Jones et al., 2004), (3) mapping hydraulic fracturing (Li et al., 1998; Rutledge & Phillips, 2003), (4) estimating fault regime and stress (Rutledge et al., 1998; Zoback & Zinke, 2002), (5) identifying reservoir compartmentalisation (Jones et al., 2004), (6) characterising reservoir permeability properties (Audigane et al., 2002; Shapiro et al., 2002), (7) identifying seismically active zones and assessing the potential for well failure (Kristiansen et al., 2000), (8) mapping strain due to compaction (Grasso, 1992) and

(9) mapping fracture patterns using observations of anisotropy (Teanby et al., 2004a; Al-Anboori, 2006; Kendall et al., 2009).

Better understanding and mapping of reservoir dynamic processes can be gained by integrating passive seismic data with reflection and borehole seismology (Wilson et al., 2004). For instance, House et al. (2004) combined data from surface seismic, vertical seismic profiling (VSP) and microseismic monitoring to improve production from a tight gas reservoir. Shemeta et al. (2007) showed that better understanding of growth and geometry of hydraulic fractures in the Rulison field in Colorado can be achieved by integrating microseismic data with multicomponent 3D seismic data.

1.2 Fracture systems

1.2.1 Importance

The extraction of hydrocarbons from existing mature fields is becoming more challenging. The shift of frontiers in the hydrocarbon industry to deep and tight reservoirs and the use of enhanced recovery have increased the demand for better reservoir characterisation. Fracture systems have significant impact on reservoir performance and thus their identification and characterisation is crucial. Fractures play a role in controlling the mechanical strength and transport properties of reservoirs. They can improve reservoir porosity and facilitate fluid flow. However, fractures can act negatively. For example, if they are open, they can increase water cut rates in water flooded reservoirs and cause fluid leakage through cap rocks. In contrast, if they are cemented, they can form fluid barriers and reduce permeability. Also, fractures increase the softness of rocks and decrease their mechanical stability and thus increase seismic hazard (e.g., walls and roof stability in mines and, compaction and subsidence in hydrocarbon settings). Exploitation of fracture systems, therefore, can optimise recovery, guide drilling strategies, mitigate seismic hazard and consequently reduce economic risk.

1.2.2 Occurance

According to Ameen (2003), fractures are defined as "all discontinuities that occur in rocks due to brittle or semi-brittle deformation" and they are divided into two types: natural and induced. Natural fractures result from natural deformation of rock. Examples include faults, cracks, joints, veins and stylolites. In contrast, induced fractures are those induced by artificial mean like coring, drilling and fluid injection (Ameen, 2003). Fractures exist in different scales in nature. Their size

ranges from micro-scale cracks (visible under microscope) to large scale faults (imaged by standard seismic techniques) to continental scale failures. Surface and subsurface observations of fractures suggest that they occur as aligned sets, reflecting regional stress history (e.g., Filbrandt et al., 2006). Fractures tend to align along the direction of maximum horizontal stress. However, the switching of stress regimes over time can introduce new fracture sets with different orientations. Also, deformation processes such as folding and shearing can cause multiple fracture sets with different alignments. Such deformation processes can form structurally complex reservoirs. Figure 1.2 shows examples of single and multiple aligned fracture sets in outcrops. Present-day *in situ* stress can play a role in re-defining fracture alignment. Generally, fractures aligned parallel to the *in situ* stress will remain open whereas those perpendicular to it will be closed as long as the pore pressure is low (e.g., Zatsepin & Crampin, 1997; Boness & Zoback, 2004).

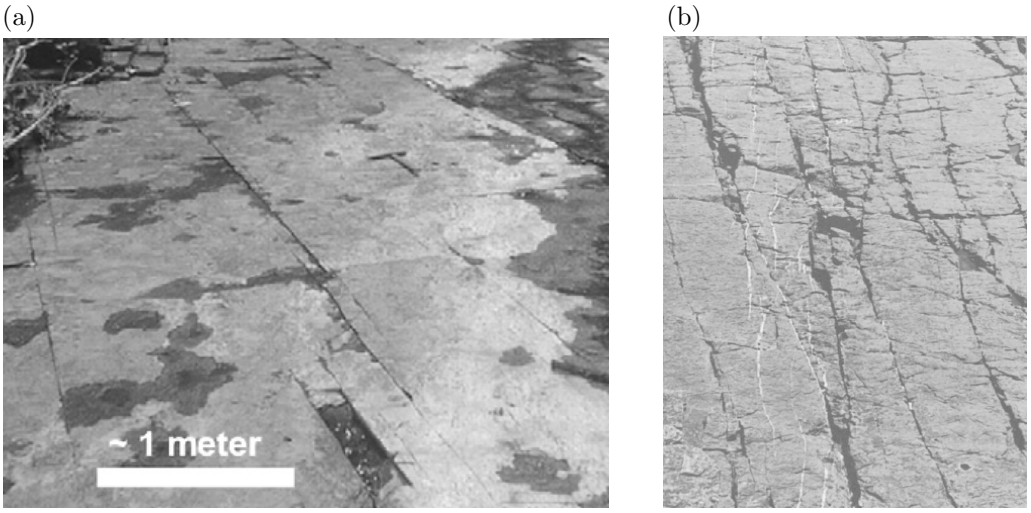

Figure 1.2: Examples of fracture alignments in outcrops. (a) Single aligned fracture set (after Herman, 2009). (b) Multiple fracture sets having different orientations (after Dunne & North, 1990).

1.2.3 Detection and characterisation

Fracture characterisation involves detecting, diagnosing and quantifying fractures (Ameen, 2003). Description of fracture patterns requires many parameters, but researchers limit their interest to those parameters controlling the elastic and hydraulic responses of the fractured medium (Liu et al., 2005). This includes describing fracture density, orientation, length, size, aperture, surface roughness and permeability. Fracture characterisation is performed by combining and integrating multi-scale observations, for example, from microscope, borehole images, cores and seismic data.

Core samples and well logs can provide little and doubtful information about fracture systems. This is because vertical borehole trajectories are nearly parallel to fracture sets and in many cases the diameter of borehole is much smaller than the spacing between large fractures (Laubach et al., 2000). In contrast, seismic techniques can provide field-scale information about subsurface fractures.

Fracture alignment can cause a medium to exhibit an effective elastic anisotropy (e.g., Hudson, 1980; Crampin, 1984). Hence, insights into fracture properties can be gained by observing the variations in seismic attributes like travel time, velocity and amplitude. Such observations are often made on reflection seismic data, VSPs and cross-hole surveys. Several techniques have been developed to account for the P-wave response to the presence of aligned fractures. For example, amplitude variation with offset (AVO) and more recently amplitude variation with offset and azimuth (AVOA) have been utilised to describe fracture properties (e.g., Sayers & Rickett, 1997; Mallick et al., 1998; Pérez et al., 1999a; Hall & Kendall, 2003). The analysis of normal-moveout (NMO) P-wave velocities is another way to study fractures (e.g., Tsvankin, 1997; Grechka & Tsvankin, 2000). The P-wave attributes will normally show elliptical azimuthal variation with the presence of single aligned fracture set. The long axis of the ellipse is assumed parallel to the fracture set orientation, whereas the ratio between the short and long axis is assumed proportional to fracture density.

The presence of aligned fractures can also influence the propagation of S-waves. The direct indicator of such impact is shear-wave splitting (SWS) when rays travel parallel or sub-parellel to fracture planes (covered in more details in the next section). Moreover, the S-wave AVOA analysis has potential use to determine fracture orientation, but only at near offset (Hall & Kendall, 2000). The analysis of S-wave amplitude anomalies can be used to characterise fracture density and orientation, and the nature of infill materials (Kendall & Kendall, 1996). There were also some attempts to analyse converted waves propagation in fractured media (also known as C-waves if the incident P-wave is converted to S-wave at reflector). The use of converted waves becomes practical with the advances in the processing of multi-component 3D data. Thomsen (1999) provided essential formulations needed to process such data. Practical examples of using converted waves include Ata & Michelena (1995), who used data from a fractured reservoir in Venezuela and Granger et al. (2000) who analysed data from the Valhall oil field in the North Sea. Combining results from analysing pure P- and S-phases (e.g., Lynn et al., 1995, 1999) and, pure and converted phases (e.g., Pérez et al., 1999b) can give better constrained fracture parameters.

Recently, Willis et al. (2006) characterised fractures using scattered coda waves. Scattered seismic energy can provide information about fracture orientation and density and more interestingly fracture spacing. Furthermore, Chichinina et al. (2006) assessed the use of azimuthal variation of attenuation with offset (QVOA) in P-wave reflection data to characterise fractures. The authors claim that QVAO can solve the ambiguity on fracture orientation that can arise when observing the elliptical azimuthal variation of AVO gradient. Factors which can lead to this orientation ambiguity include fracture infill material and crack aspect ratio (Hall & Kendall, 2000).

1.3 Seismic anisotropy and shear-wave splitting

Seismic anisotropy is defined as the change in seismic velocity with direction at a specific location. In contrast, inhomogeneity is defined as the dependence of physical properties upon location. The idea of directional dependence of velocity is about 175 years old (Helbig & Thomsen, 2005). However, the phenomena took its considerable importance when it was first introduced in hydrocarbon exploration. In exploration seismology, anisotropy was initially regarded as unwanted complication. In 1970s this view started to change and seismologists now use anisotropy as a source of information (Helbig & Thomsen, 2005; Kendall et al., 2007).

Shear-wave splitting (SWS) is the most commonly used indicator of seismic anisotropy. When a shear-wave enters an anisotropic medium, it is split into two orthogonally polarised components traveling at different speeds. Anisotropy can be characterised by the polarisation direction of the leading component (Φ) and the delay time between the two components (δt). Figure 1.3 shows a schematic illustration of SWS. The magnitude of δt is controlled by the anisotropy magnitude and the path length of the anisotropic medium. Usually, δt is normalised by the path length to yield the percentage difference between the fast and slow shear-wave velocities along the raypath (δV_s).

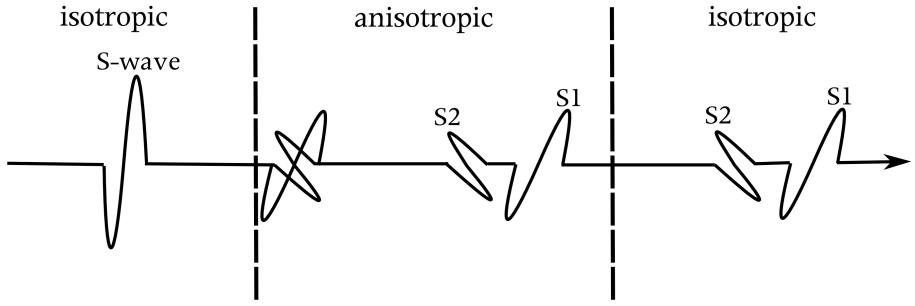

Figure 1.3: Shear-wave splitting. When a shear-wave enters an anisotropic medium it is split into orthogonally polarised fast (S1) and slow (S2) waves. The travel time difference between S1 and S2 is δt and the polarisation direction of S1 is Φ.

1.3.1 Causes of anisotropy

Anisotropy is an indicator of order within a medium. It can be influenced by past and present geological and geodynamical processes. It is subdivided into two types based on causes: intrinsic and extrinsic. The fundamental difference between the two types is that intrinsic anisotropy is independent of seismic wavelength, whereas extrinsic anisotropy is wavelength dependent (Kendall, 2000). Intrinsic anisotropy can result from the preferred orientation of crystals (so-called crystals preferred orientation (CPO) or lattice preferred orientation (LPO)). Another form of intrinsic anisotropy is lithologic anisotropy which occurs when individual grains are aligned at the time of deposition (Kendall, 2000). Examples of intrinsic anisotropy include the LPO of olivine in the oceanic upper mantle and shale in sedimentary basins. Extrinsic anisotropy results from the shape preferred orientation (SPO) of inclusions. It can result, for example, from periodic thin layering and preferred alignment of cracks and fractures.

Anisotropy in the upper crust

Most of our knowledge about the nature of anisotropy in the upper crust comes from studies of SWS in local earthquakes (up to few kilometres in depth). The mechanisms for seismic anisotropy in the upper crust can be sub-divided into two categories: stress-induced and structural anisotropy (Boness & Zoback, 2006). Figure 1.4 depicts a schematic illustration of the two types. The stress-induced anisotropy is generated by the alignment of open cracks parallel to the maximum *in situ* stress direction. In this type of anisotropy Φ is polarised parallel to the direction of the maximum *in situ* stress direction and δt (or δV_s) reflects intensity of fractures. In contrast, structural anisotropy is associated with the alignment of macroscopic features such as fault zone fabrics, aligned crystals or minerals, and sedimentary bedding planes. In this type of anisotropy Φ is oriented parallel to the strike of the feature.

The concept that open cracks is controlling SWS within the crust was first introduced by Crampin (1978) using the hypothesis of extensive dilatancy anisotropy (EDA). The EDA model assumes anisotropy is generated by the preferential alignment of vertical fluid-filled microcracks by the *in situ* stress field. Later, the EDA model has been modified to the anisotropic poroelasticity model (APE) (Zatsepin & Crampin, 1997; Crampin & Zatsepin, 1997). The new model suggests that at high pore pressure Φ changes by 90° relative to the direction at lower pressures. This is because high pore pressure allows low aspect ratio cracks perpendicular to the maximum *in situ* stress direction to open and consequently Φ becomes parallel to those newly opened cracks. The

assumption that anisotropy in the crust is controlled by fluid-filled aligned cracks is supported by numerous studies showing azimuthal variation in anisotropy (reviews of these studies can be found in Crampin & Chastin (2003) and Crampin & Peacock (2008)). It is also supported by the observations of temporal variation in anisotropy (discussed in section 1.3.2). However, studies of SWS in the vicinity of active fault zones have shown that anisotropy is controlled by both stress field and tectonic structures depending on the proximity to the fault planes. For example, Zinke & Zoback (2000), Boness & Zoback (2006) and Liu et al. (2008) analysed SWS observations around active faults in California and found that seismic stations above and close to major faults show fast strike parallel or sub-parellel to the fault trends, whereas those away from fault zones show fast strike parallel to the maximum compressive stress orientation. Numerous studies on the depth extent of crustal anisotropy showed that anisotropy is confined to the topmost few kilometers of the crust (e.g, Zhang & Schwartz, 1994; Munson et al., 1995; Liu et al., 2004). However, several studies have reported an increase in δt with depth (e.g., Shih & Meyer, 1990; Li et al., 1994). Also, petrophysical studies of the lower continental crust composition show that it is anisotropic (Tatham et al., 2008).

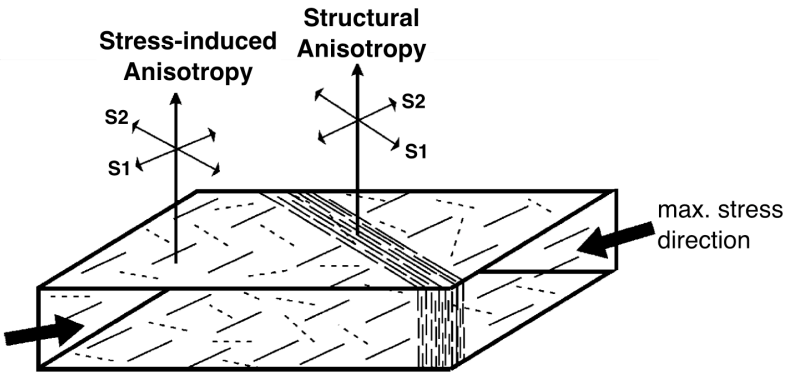

Figure 1.4: Two types of anisotropy in the upper crust: structural and stress-induced anisotropy. In structural anisotropy, the fast S-wave (S1) is polarised parallel to the strike of the feature (fault fabric in this case). In stress-induced anisotropy, S1 is polarised parallel to the fracture orientation which is controlled by the maximum stress direction (modified from Boness & Zoback (2006)).

Anisotropy in sedimentary rocks

Seismic anisotropy in sedimentary rocks can result from the alignment of cracks and fractures (e.g., Crampin et al., 1986; Sayers & van Munster, 1991), the alignment of minerals (e.g., Johnston & Christensen, 1995; Valcke et al., 2006; Kendall et al., 2007), fine layering (e.g., Backus, 1962) and non-hydrostatic stresses (e.g., Verdon et al., 2008). The nature of anisotropy within sedimentary basins depends on rock type. In siliciclastic rocks anisotropy is primarily controlled by the align-

ment of phylosilicate minerals (Hornby et al., 1994; Kendall et al., 2007) and, to a lesser extent the alignment of quartz and plagioclase (Kendall et al., 2007). In contrast, carbonate rocks are generally considered isotropic unless they are fractured or finely layered (Wang, 2002), whereas shales have a strong intrinsic anisotropy due to phylosilicate alignment (Kaarsberg, 1959).

Observations of SWS on VSP (e.g., Winterstein et al., 2001) and reflection seismic data (e.g., Lynn & Thomsen, 1990; Potters et al., 1999) have been increasingly used in exploration seismology to quantify shear-wave anisotropy within and around hydrocarbon reservoirs. Similar observations can be made on shear dipole sonic logs (e.g., Prioul et al., 2004) and cross-hole surveys (e.g., Liu et al., 2007). The use of SWS in characterising reservoirs is sometime favoured over the use of azimuthal variations of P-wave attributes. This is because SWS can be measured from a single raypath and, the estimate of Φ and δt are a direct representation of fracture orientation and density, respectively. In contrast, the successful use of P-wave data requires good ray coverage in the azimuth and offset domains. Yet, there has been a significant increase in acquiring 3D P-wave data, mainly because S-wave data cannot be recorded in offshore acquisition (except converted PS waves at the seafloor).

A recent study by Teanby et al. (2004a), using a microseismic dataset from the Valhall oil field in the North Sea, showed the potential of using microseismic data to estimate spatial and temporal variations in SWS. Microseismic data recorded using borehole sensors can provide a 3D image of anisotropy, which can not be obtained using subvertical rays recorded during active seismic surveys. The 3D coverage provided by microseismic data can be used to better characterise the anisotropy, estimating both the strike and dip of the anisotropic symmetry system (Al-Harrasi et al., 2010a).

1.3.2 Temporal variation in anisotropy

In addition to variation in space, the splitting parameters (Φ and δt) can vary over time if the SWS is controlled by stress magnitude and orientation. The phenomena of temporal variation in anisotropy is attributed to the change in pore pressure with respect to the confining stress in media with fluid-filled cracks. Cracks tend to open parallel to the maximum stress direction and hence any variation in the principle stress direction will change which crack set is opened and consequently alters Φ. In contrast, δt is affected by the magnitudes of stress and pore pressure which control crack density and dimension (aspect ratio). In some circumstances, the pore pressure magnitude can also change Φ. For instance, high pressure magnitudes can cause low aspect ratio cracks to open perpendicular to the maximum horizontal stress direction. This causes a 90°-flip in Φ, making

it perpendicular to the originally observed Φ at low pore pressure state. Such temporal variations in anisotropy are explained by the APE theory of Zatsepin & Crampin (1997) and Crampin & Zatsepin (1997).

Temporal variations in δt and Φ have been observed in splitting measurements from small events before and after large earthquakes, which are attributed to stress build-up and relaxation (see discussion and examples in Crampin & Peacock (2008)). Similar variations in the splitting parameters are observed before and after volcanic eruptions (e.g. Miller & Savage, 2001; Del Pezzo et al., 2004), during CO_2 injection (Angerer et al., 2002) and during borehole fluid injection (Bokelmann & Harjes, 2000). Teanby et al. (2004a) observed temporal variations in splitting parameter estimated using microseismic dataset from the Valhall oil field in the North Sea. They interpreted this in terms of changes in the tidal and/or oil field production processes over the period of acquisition (2 months).

1.3.3 Anisotropic symmetry classes

Seismic anisotropy can be described mathematically by the stiffness tensor (C_{ijkl}) which relates stress (σ_{ij}) to strain (ϵ_{kl}) by Hooke's Law (σ_{ij}=$C_{ijkl}\epsilon_{kl}$). The symmetry of the stress and strain tensor as well as energy constraints reduce the number of independent components describing C_{ijkl} from 81 to 21 for the most general anisotropic case (Aki & Richards, 2002).

The spatial patterns of velocities, polarisations and amplitudes of elastic waves are determined by the symmetry of the medium they are travelling through (Crampin, 1981). The spectrum of symmetry classes ranges from isotropic to triclinic media. Any isotropic medium can be described by two independent elastic constants. These are the Lamé parameters λ and μ. In contrast, the description of triclinic symmetry requires the definition of all 21 stiffness components. Between these two extreme symmetries, the three commonly recognised symmetries in seismology are hexagonal, orthorhombic and monoclinic. Other symmetry classes include tetragonal, trigonal and cubic.

Hexagonal symmetry has a single axis of rotational symmetry. The plane perpendicular to the symmetry axis is a plane of isotropy. Five independent stiffness constants are required when describing media with hexagonal symmetry. The term vertically transverse isotropy (VTI, Figure 1.5a) is commonly used to refer to the case where the symmetry axis is vertical. It is also known as polar or radial anisotropy. The term horizontally transverse isotropy (HTI, Figure 1.5b) is used to describe the case when the symmetry axis is horizontal and the velocities are azimuthally dependent (azimuthal anisotropy). If the symmetry axis is tilted then the anisotropy is referred

to as tilted transverse isotropy (TTI, Figure 1.5c). In exploration seismology, HTI, VTI and TTI are commonly used to describe the orientation of the symmetry axis.

An orthorhombic symmetry has different seismic velocities along three mutually perpendicular axes. In this case the stiffness tensor C_{ijkl} contains nine independent elastic constants. The superposition of HTI and VTI symmetries is a common form of orthorhombic symmetry (Figure 1.5d). Another example of orthorhombic symmetry is the case of two orthogonal sets of aligned fractures.

Monoclinic is another commonly used class of symmetry, the description of which requires 13 independent stiffness components. Monoclinic media contain one plane of mirror symmetry. An example of monoclinic symmetry is the case of two or more non-orthogonal aligned fracture sets (Figure 1.5e). Another example is a dipping fabric with vertical fractures or vice versa.

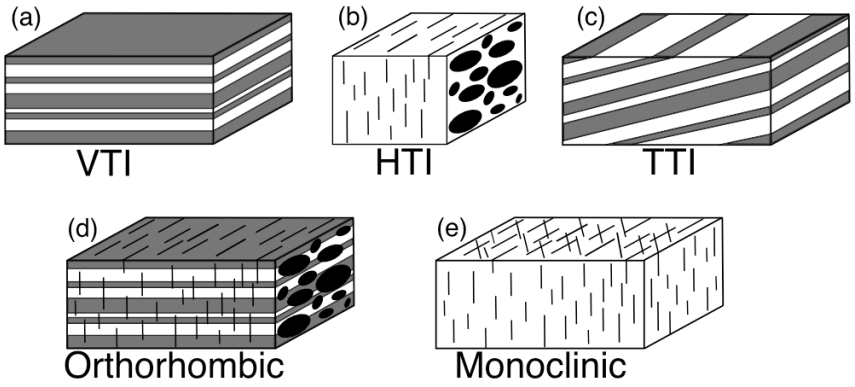

Figure 1.5: Commonly used symmetry systems to describe anisotropy in exploration seismology. (a) Vertical transverse isotropy (VTI) formed by the horizontal alignments of layers, (b) horizontal transverse isotropy (HTI) caused by the vertical alignment of fractures or cracks, (c) tilted transverse isotropy (TTI) formed by dipping layers, (d) orthorhombic medium made by fractures embedded in a horizontally layered medium and (e) monoclinic medium formed by two non-orthogonally oriented fracture sets.

1.4 Shear-wave splitting inversion

Inverting for the subsurface model of seismic anisotropy directly from SWS observations can be non-unique because of the different causes of anisotropy. The splitting parameters (Φ and δt) are highly dependent on the direction of ray propagation, for example, with respect to fracture orientation (e.g., Crampin & Peacock, 2008). In seismology, Φ and δt measurements are traditionally treated independently. It is common to directly assume that Φ corresponds to the strike of the fractures and/or the maximum horizontal stress orientation, and that δt (or δV_s) reflects fracture intensity.

However, these assumptions are limited to cases where the S-waves propagate subvertically. In the case of microseismic monitoring using downhole geophones, 3D ray coverage is often obtained and thus the interpretation of the splitting measurements becomes far less intuitive (Verdon et al., 2009). Furthermore, in sedimentary settings subsurface sedimentary fabrics can contribute to the overall estimated anisotropy making it even harder to interpret the results assuming aligned fractures as the only cause of anisotropy. In reality, both Φ and δt are controlled by the overall subsurface rock architecture and thus they must be used simultaneously to investigate the causes of anisotropy (Yang et al., 2005).

There have been several attempts in the past to invert SWS observations for anisotropy parameters from teleseismic, VSP and microseismic data. For instance, Sileny & Plomerova (1996) inverted global SWS observations recorded in southern Sweden to characterise the anisotropic upper mantle. Horne & MacBeth (1994) used a genetic algorithm to invert SWS observations for fracture parameters from VSP dataset.

Teanby et al. (2004a) used a two step modelling scheme to interpret observations of SWS made on microseismic data from the Valhall field. The first step was to calculate the elastic constants for a medium with multiple crack sets, following the approach of Schoenberg & Sayers (1995). The second step was to generate synthetic seismograms using a ray tracer (Guest & Kendall, 1993). The synthetic seismograms were processed in the same way as the real data to estimate Φ and δt and then compared with the data observations.

Yang et al. (2005) developed an inversion scheme to model SWS results recorded at the Geysers geothermal field in California. The scheme addresses the issue of non-linerity in the inversion of splitting measurements. It simplifies the inversion process by dividing the double-response regression problem into two connected single-response ones. Recently, Verdon et al. (2009) developed a SWS inversion approach that is able to account for the effect of fractures and sedimentary fabrics. The approach starts by building a rock physics model consisting of fractures embedded in rocks with sedimentary fabrics. The Christoffel equation is used to calculate Φ and δV_s, which are then compared with estimates from real data. The inversion is performed in an iterative way and the optimum model is chosen such that the root mean square (RMS) misfit between modelled and real data is minimum. All SWS inversion techniques share the same requirement of good ray coverage in the horizontal and vertical planes in order to accurately determine the dominant cause of seismic anisotropy.

1.5 Frequency-dependent anisotropy

Recent studies of anisotropy using teleseismic data (e.g., Marson-Pidgeon & Savage, 1997), VSP data (e.g., Chesnokov et al., 2001; Liu et al., 2003; Maultzsch et al., 2003) and microseismic data (Al-Anboori et al., 2006) have shown a dependence of anisotropy on frequency. The two most likely mechanisms that can cause velocity dispersion, and consequently frequency-dependent anisotropy, are scattering by inhomogenities and fluid flow in fractured porous rocks (Liu et al., 2003). Anisotropy induced by scattering occurs only when the seismic wavelength is longer than the size of the inhomogenities. A decrease in anisotropy and hence increase in scattering is observed with decrease in wavelength (i.e., the influence of hetrogenities decreases as frequency increases). A typical example of frequency-dependent scattering-induced anisotropy is wave propagation in finely layered media (e.g., Shapiro et al., 1994; Werner & Shapiro, 1999). The second proposed mechanism of frequency-dependent anisotropy accounts for fluid flow in fractured porous rocks, known as squirt-flow. Seismic wave propagating through fractured porous rocks can induce pressure gradients that causes fluid exchange between fractures and pore spaces to achieve pressure equalisation (e.g., Chapman, 2003).

Traditional equivalent medium theories for fractured media (e.g., Hudson, 1981; Thomsen, 1995) do not consider the frequency-dependence of elastic response. Such models lack the sensitivity to fracture size. For example, a medium with few large fractures will generate elastic constants equivalent to those produced by a medium containing many small cracks. In recent years, several frequency-dependent models have been proposed which incorporate the effect of wave-induced fluid motion (Hudson et al., 1996; van der Kolk et al., 2001). However, these models do not explain the frequency-dependece of seismic anisotropy appropriately, especially in the presence of fractures. Chapman et al. (2002) proposed a poroelastic theory which models the squirt flow at grain scale. Subsequently, Chapman (2003) developed this theory by considering the effect from adding aligned set of meso-scale fractures to the medium. The Chapman (2003) model considers two different scales: grain scale, where the pore space consists of microcracks and equant pores, and a scale larger that involves aligned fractures. Thus, the model has the ability to simulate the fluid flow at grain scale (traditional squirt-flow) and fluid flow in and out of fractures. The later is associated with a time scale constant that is dependent on fracture size and is larger than the relaxation time describing the grain scale squirt-flow. The model can explain attenuation and

velocity dispersion at seismic frequencies and thus can be used to invert for size of fractures and fluid type.

1.6 Shear-wave splitting tomography

As we discussed earlier, SWS is controlled by variety of mechanisms. Usually, the splitting we measure at recording stations represents the bulk effect of all the encountered anisotropic structures along the raypath which their strength and orientation can vary significantly. Existing SWS techniques are not able to deliver sufficient quantitative description of the distribution of anisotropy between source and receiver. The majority of researchers explain their SWS observations by comparing them with surface observations or existing models. Others attempt to explain their results using forward modelling (e.g., Hammond et al., 2010a,b). However, forward modelling of SWS observations suffers from the problem of non-uniqueness and it does not fully explore the true extent of the parameter space. To get a quantitative parameterisation of the spatial distribution of anisotropy, SWS observations should be interpreted in tomographic inversion fashion.

Thus far, there have been a few attempts of SWS tomography analysis. These include the studies by Zhang et al. (2007), Abt & Fischer (2008) and Wookey (2010). Zhang et al. (2007) developed a 3D SWS tomography which back projects SWS delay times (δt) along raypaths derived from a 3D shear velocity model. They applied the technique to image the 3D anisotropy structure of the Parkfield region in California. Their results are biased partly due to the simplification in the technique by not including the fast-shear wave polarisation (Φ) in the inversion. Abt & Fischer (2008) presented a SWS tomography method to resolve anisotropy associated with subduction zones. They parameterised the mantle as 3D block model of crystallographic orientations with elastic properties of olivine and orthopyroxene. The Christoffel equation is used to derive splitting operators (Φ and δt) in each block of the model. These splitting operators are applied to a synthetic wavelet which then processed using the eigenvalue minimization method of Silver & Chan (1991) (see Chapter 4 for more details) to estimate splitting parameters in each block. Finally, the splitting results are compared to those obtained from real data to choose the best-fit model. Wookey (2010) proposed an extension to the method of Abt & Fischer (2008) that incorporates the waveform data into the inversion, rather than using synthetic wavelets. The approach by Wookey (2010) treats the SWS inversion problem as generally non-linear. In this way the method is able to fully explore the complicated parameter space required to describe complicated and nonuniform anisotropic

models. Wookey (2010) applied the approach to SKS data from the North Canadian shield region to investigate the existence of two anisotropic layers within the lithosphere. His results show a good agreement with those previously determined by Snyder & Bruneton (2007) for the same data using a non-tomographic approach.

1.7 Aims and Objectives

This study aims to more fully utilise microseismic data as a reservoir monitoring tool. It explores the potential use of microseimic monitoring as an imaging technique to characterise reservoir physical properties. The microseismic dataset used in this study was acquired during an 18-months microseismic trial in a giant mature field located in Oman (hereafter referred to as Field M). The main focus of the research is on:

► Estimating Field M seismic anisotropy via the use of SWS analysis. The anisotropy provides insights into the field's fracture system by estimating fracture orientation and density.
► Using rock physics modelling to invert the SWS observations for subsurface architecture. Inversion will give quantitative estimates of fracture strike and density and, strength of sedimentary fabric.
► Performing frequency-dependent anisotropy analysis. This will help constrain fracture size and density.
► Performing SWS tomography imaging. This will provide a quantitative measure of the vertical and lateral distribution of anisotropy and the existence of nonuniform anisotropic models.
► Integrating the results from SWS observations with other field data (e.g., borehole data, production and injection rates) to characterise the field rocks and better understand its behaviour.

Previous studies of anisotropy using microseismic data (e.g., Teanby et al., 2004a; Al-Anboori, 2006) have dealt with small datasets. One of the goals of this thesis is to establish new techniques that can handle the ever increasing size of microseismic data volumes. Furthermore, traditionally, splitting parameters (Φ and δt) are treated independently or semi-independently when interpreting SWS results. Also, the interpretation is often based on comparing the results with existing geology models. In the case of reservoir seismology, the superposition of different anisotropic symmetries and the variability of raypath propagation directions make the treatment of Φ and δt independently

far less intuitive. Thus, this project attempts to explain SWS results in an inversion fashion using rock physics modelling where the splitting parameters are analysed simultaneously. This will provide more reliable interpretation of the splitting results. In studies of global and local seismology, the scale length of the anisotropy mechanism causing SWS is often ignored. However, when studying reservoir fracture-induced anisotropy, it is important to know the length scale of fractures as to understand their contribution in enhancing reservoir porosity and permeability. Determining fracture size by modelling observations of frequency-dependent anisotropy has been well established in studies of SWS in VSP data (Liu et al., 2003; Maultzsch et al., 2003). This thesis explores the potential of estimating fracture size using observations of frequency-dependent anisotropy in microseismic data. Finally, one of the limitations in the study of anisotropy is not understanding where along the raypath does the anisotropy exist. This issue has been recently addressed in studies of anisotropy in global seismology using SWS tomography techniques (Abt & Fischer, 2008; Wookey, 2010). This thesis marks the first attempt to test such techniques on reservoir microseismic data. Throughout the study, the success of using SWS to characterise the Field M rocks is assessed by comparing the results to those previously obtained from other seismic and non-seismic techniques, and to the field geology.

The outputs from this study will help constrain Field M reservoir models, mainly focusing on characterising the fracture network and estimating the stress direction. However, the outcomes are not limited to oil industry applications, but will contribute to other subject areas like volcanology, mining and geothermal energy. Furthermore, the study of reservoir seismic anisotropy provides insights into the nature of anisotropy in the shallowest parts of the upper crust and how it behaves in relation to lithology and tectonic setting.

1.8 Thesis outline

In this introductory chapter I have outlined some of the applications of passive seismic monitoring and presented a literature review on seismic anisotropy. Then, the aims and objectives of the study were presented.

In Chapter 2, I describe the geology of Field M and its tectonic setting. Furthermore, I outline the results from previous studies conducted to characterise the Field M fracture system and, the local and regional stress regimes. This chapter serves as a reference to help compare and contrast results presented in subsequent chapters.

In Chapter 3, I describe the Field M microseismic data acquisition and processing, and the event location methodology. Then, the spatial and temporal variation of seismicity is analysed by linking it to the field production and injection activities. Finally, I perform some statistical analysis on the event source parameters and estimate the b-value using the Gutenberg-Richter frequency-magnitude relation.

In Chapter 4, I present a complete workflow for SWS analysis of microseismic data. The SWS technique introduces a (semi-) automated quality control to determine the reliability of the measurements. This method is applied to the Field M dataset. The outcomes from this chapter have been presented at the 2009 EAGE Conference in Amsterdam (Al-Harrasi et al., 2009).

In Chapter 5, the SWS results from Chapter 4 are analysed to describe the nature of anisotropy in Field M. The SWS observations are interpreted in terms of fractures and cracks superimosed in rocks with intrinsic anisotropy. The interpretation is guided using SWS modelling in a range of rock models. This chapter is a more detailed expansion of the work presented in Al-Harrasi et al. (2010a).

In Chapter 6, rock physics modelling is used to invert for the optimum Field M properties using SWS measurements from Chapters 4 and 5. Prior to the interpretation, synthetic modelling is used to investigate the limitation of the inversion. The outputs from the inversion (sedimentary fabric strength and, fracture orientation and density) are compared to the previous findings in Chapter 5.

In Chapter 7, I perform frequency-dependent anisotropy analysis on Field M microseismic data. The SWS analysis technique described previously in Chapter 4, is applied to data filtered to different frequency bandwidths in order to observe any variations in anisotropy with frequency. The results are modelled using the Chapman (2003) model to estimate fracture parameters: size, density and orientation. The results from this chapter have been presented at the 2010 EAGE Conference in Barcelona (Al-Harrasi & Kendall, 2010) and have been recently submitted for publication (Al-Harrasi et al., 2010b).

In Chapter 8, I investigate the nature of anisotropy in Field M in a tomographic fashion. The SWS tomography approach of Wookey (2010) is used to explore the lateral and vertical distribution of anisotropy. The field is divided into domains separated by the planes of major faults and the boundaries between lithology units. Finally, the results are compared with those from Chapters 5 and 6.

In Chapter 9, I summarise the conclusions from each of the individual chapters and then synthesis them to build up an overall conclusion. Based on the obtained results, I give some recommendations to the Field M operator. Furthermore, I list what have been achieved and what can be done in future studies.

The programs, codes and scripts used in each chapter are listed in Appendix A. Detailed descriptions of each software package are provided therein.

2
Geology of Field M

2.1 Introduction

Field M is located within a large salt basin in North Oman. The field is in the form of a large, gently dipping dome, consisting of a series of relatively flat, stacked carbonate reservoirs. The flanks dip with angles between 4° and 5°. The dome-shape was created by a salt pillow at depth greater than 3.5 km (Litsey et al., 1986). Figure 2.1 shows a cross-section with the three main reservoirs indicated: the topmost Natih gas reservoir (858-1295 m depth), the Shuaiba oil reservoir (1410-1510 m depth) and, the Khuff oil and gas reservoir ($\sim$ 2800-3250 m depth). The Natih and Shuaiba reservoirs are overlain by the Fiqa and Nahr Umr shale cap rocks, respectively (Figure 2.1). Field M was discovered in 1962 and production from the Shuaiba reservoir commenced in 1969. Gas production from the Natih reservoir started in 1971.

In this study I am interested in the upper two reservoirs (Natih and Shuaiba), due to the limited coverage of the microseismic network (see Chapter 3 for detailed description of the microseismic network).

2.2 Tectonic setting

Field M has experienced three deformation phases. The first phase was the early salt movements, which created an extensional NE-SW graben system (Litsey et al., 1986). This was followed by late Cretaceous strike-slip movements caused by regional tectonics associated with the collision of the Eurasian and Arabian plates, forming the NW-SE oriented faults (Droste, 1998). The Field M tectonic setting map is shown in Figure 2.2. The NE-SW extensional faults have throws ranging from 10 to 50 m and were active from the Cambrian to the Permian (Droste, 1998). In contrast, the NW-SE faults were active during the Cretaceous, while the Shuaiba and Nahr Umr were deposited. Field M represents a tensional regime causing all faults to be high-angle normal faults (Litsey et al., 1986). The final deformation phase was the tilting and the reactivation of all the faults in the Tertiary (Droste, 1998). The tilting caused remigration of the initial hydrocarbon fill from the western to the eastern part of the field.

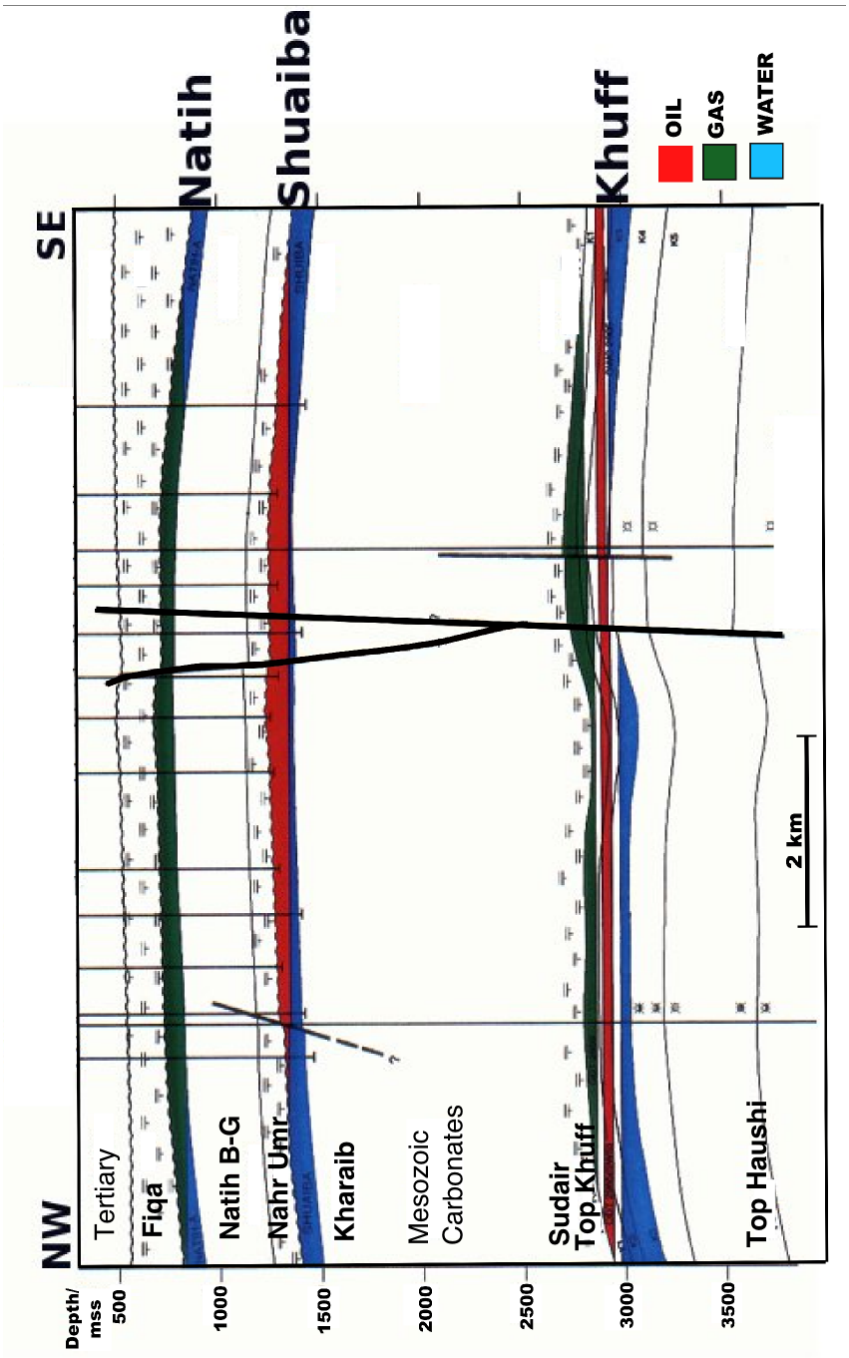

Figure 2.1: Cross-section across Field M showing the three main hydrocarbon reservoirs: the Natih, Shuaiba and Khuff. The high-angle normal faults forming the main graben are shown by thick black lines (Figure courtesy of PDO).

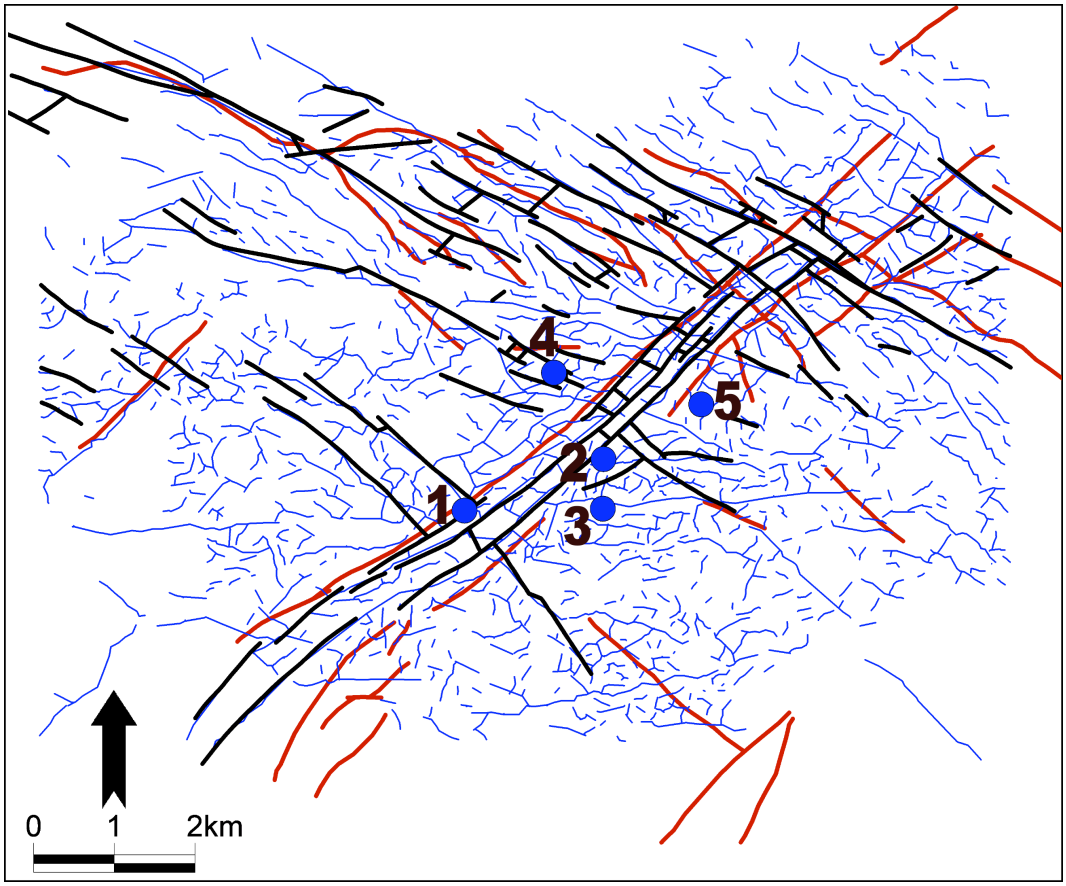

Figure 2.2: Tectonic map of Field M. The major faults cutting the base of Fiqa shale and mid-Shuaiba formation are shown by thick red and black lines, respectively. The minor faults inferred from the field 3D seismic data are shown by thin blue lines. The five microseismic monitoring wells are denoted by blue circles (see Chapter 3 for description of the microseismic network) (Figure courtesy of PDO).

2.3 Lithology and physical properties

The Natih and Shuaiba formations are chalky limestone reservoirs of Cretaceous age. Figure 2.3 shows the stratigraphic column of Oman, with details of the Cretaceous sequences. The contact between the Natih and Fiqa shale and between the Shuaiba and Nahr Umr shale are unconformities (Figures 2.1 and 2.3). Shale acts as seal for both the Natih and Shuaiba reservoirs.

2.3.1 Natih Formation

The Natih formation is a carbonate platform of middle Cretaceous age (Albine-Cenomanian, Figure 2.3). It was formed during a series of stacked regressive marine cycles alternating with more open marine deposits. It extends over an area of circa 16 x 18 km^3 and it comprises seven members: Natih A (top) to Natih G (bottom). The Natih B unit consists of fine-grained, chalky limestones. The Natih A unit is subdivided into 7 subunits (from bottom to top): A7 deep basinal mudstones, A6 and A5 outer to middle ramp wackstones and packstones, A4 inner ramp low energy wackstones and packstones, A3 high energy inner ramp grainstones, A2 low energy inner ramp packstones and A1 outer ramp wackstones and mudstones. In this study, I subdivide the Natih B-G formation into: upper part (Natih B-G1, 946-1120 m depth) and lower part (Natih B-G2, 1120-1295 m depth).

The Natih formation was subaerially exposed prior to deposition of the overlying Fiqa shales. During this period of exposure the formation underwent fresh-water leaching which formed connected solution channels, collapse breccias, solution enhanced fractures, isolated/connected vugs and fossil moulds, and resulted in significant permeability enhancement. Furthermore, the top of the Natih has been truncated and incised by a canyon system cutting up to 80 m into the formation. These channels merge towards the south-east, where most of the erosion has taken place by eroding the Natih A member.

Herz (2004) derived the mechanical properties of the Natih A and B formations using well logs and lithology information. The majority of the rocks of the Natih A submembers 1 to 6 have unconfined compressive strength (UCS) below 55 MPa. Rocks of the Natih A7 submember and the Natih B member are of higher strength and have UCS ranging between 55 and 220 MPa. Young's Modulus values vary between 5 and 25 GPa with a general increase with depth. The Natih A has the smallest value (average 7-8 GPa), whereas the average for the Natih B is about 11 GPa. Poisson's ratios change with depth from 0.17 to 0.46. The average values for the Natih A and Natih B formations are 0.24 and 0.3, respectively. The Natih A has an average Cohesive Strength of 10 MPa. The Cohesive Strength value increases with depth to reach 18 MPa in the Natih B unit.

Both porosity and permeability of the Natih reservoir were modified by diagenesis. The key diagenetic phases were early matrix replacive cementation, syndepositional karstification and precipitation of late blocky calcite cement (Coy, 2003). The late blocky calcite cementation reduced both porosity and permeability. Porosity within the Natih A reservoir generally ranges between 10% and 45% with an average of about 30% (Ozkaya et al., 2004). The average porosity decreases

to about 24% within the Natih B-G formation. The range of permeability within the Natih A is very broad. It varies from 0.1 mD to 1 D with an average of about 10 mD (Ozkaya et al., 2004). The average permeability within the Natih B-G formation is about 1 mD.

Gas in the Natih formation is believed to be derived from deep sources along the foreland bulge, where most of the gas in the Natih formation is expected to originate from thermal oil cracking in deep traps (Terken, 1999).

2.3.2 Shuaiba Formation

The oil bearing Shuaiba formation was deposited during the Cretaceous Berremian-Aptian time in a low energy shallow marine environment (Figure 2.3). The Shuaiba formation forms the uppermost part of the Lekhwair-Kharaib-Shuaiba super-sequence (Figure 2.3). It comprises a carbonate series of mudstone, wackstone and packstone. The reservoir can be subdivided into the Upper and Lower Shuaiba separated by the Upper Shuaiba mudstone. The Lower Shuaiba is characterised by relatively shallow water deposition, marking a widespread subtidal environment. Its thickness ranges from 30 to 35 m and it is a water bearing unit. The Upper Shuaiba sequence thickens from 15 m in the southeast to 30 m in the northwest. The main oil accumulation is found in the Upper Shuaiba.

Porosity in the Shuaiba reservoir generally increases vertically from the transition zone to the oil column and from south-east to the north-west. Porosity ranges from 30% to 35%, with an average field wide value of 32%. Matrix permeability varies from 1 mD at the base of the Shuaiba to 200 mD in the high permeability upper layer, with average matrix permeability of about 10 mD. However, permeabilities increase in fault and fracture zones.

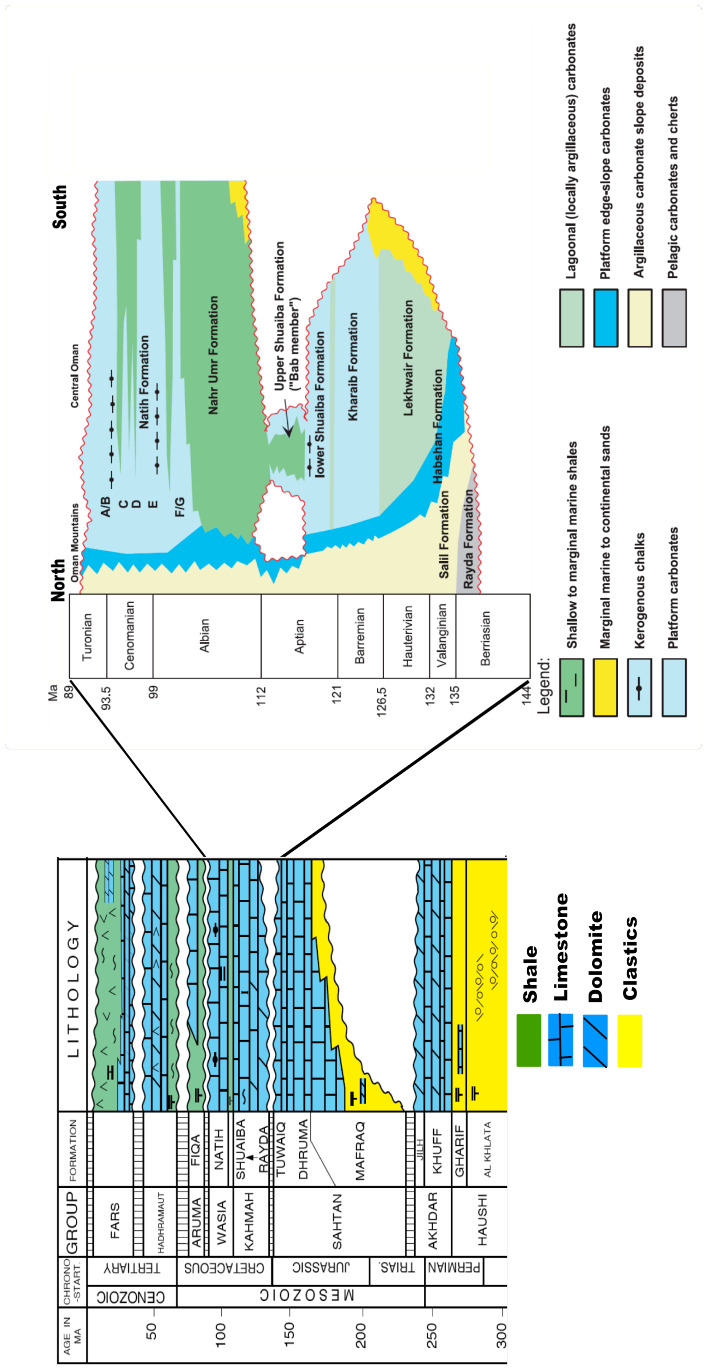

Figure 2.3: Stratigraphic column of Oman with a detailed N-S oriented cross-section of the Cretaceous sequences (modified from Droste & Steenwinkel (2004)).

2.4 Stress direction

An integrated study of borehole breakouts and induced fractures in North Oman by Filbrandt et al. (2006) has shown that the orientation of the present day first-order maximum compressive horizontal stress is NE-SW (Figure 2.4). This regional stress direction is probably induced by slab pull related to the subduction of the Makran oceanic zone, ridge push from the Red Sea and Gulf of Aden, and the relative convergence of the Arabian and Iranian Plates (McClusky et al., 2003; Filbrandt et al., 2006). Furthermore, Filbrandt et al. (2006) claim that the regional stress field was oriented NW-SE during the Santonian-Campanian time before switching to the current NE-SW orientation.

Baker Atlas GEOScience (1999) analysed Field M *in situ* stresses in 9 wells. The analysis included the identification of breakouts derived from the differential formation micro image (FMI) and formation micro scanner (FMS) caliper measurements. They followed the assumption that breakouts occur perpendicular to the maximum *in situ* stress direction. Breakouts were only detected in 6 wells. Figure 2.5 summarises the results obtained for the 6 wells. The five well measurements in the Nahr Umr show a consistence NE-SW maximum stress orientation, which is consistent with the regional maximum stress orientation in North Oman (Figure 2.4). The one well breakout measurement in the Natih formation shows N-S maximum stress orientation. It is worth mentioning that this single well measurement was taken at deep depth close to the Nahr Umr and the *in situ* stress direction might be different at shallow depths of the Natih formation.

In another study by Hodder (2004), using FMI techniques, hydraulic fractures were observed in the Natih A7 submember striking ENE-WSW (66°). Drilling induced hydraulic fractures are believed to have strike parallel to the maximum horizontal stress direction (e.g., Bell, 1990).

Al-Anboori (2006) estimated the stress directions and the type of fault movements in the Field M lithological units using focal mechanism analysis on some large events recorded by the deep microseismic network (see Chapter 3 for description of the network). The analysis assumed pure double-couple sources and found that the maximum compressive stress direction is horizontal E-W in the Fiqa cap rock, horizontal NNE-SSW in the Natih A gas reservoir, subhorizontal E-W in the Nahr Umr shale and subvertical in the Shuaiba oil reservoir. Moreover, the study revealed a transition in faulting regime from strike-slip in the Fiqa shale to pure thrusting in the Natih A chalk carbonate and a transition from strike-slip in the Nahr Umr shale to normal faulting in the Shuaiba chalk reservoir.

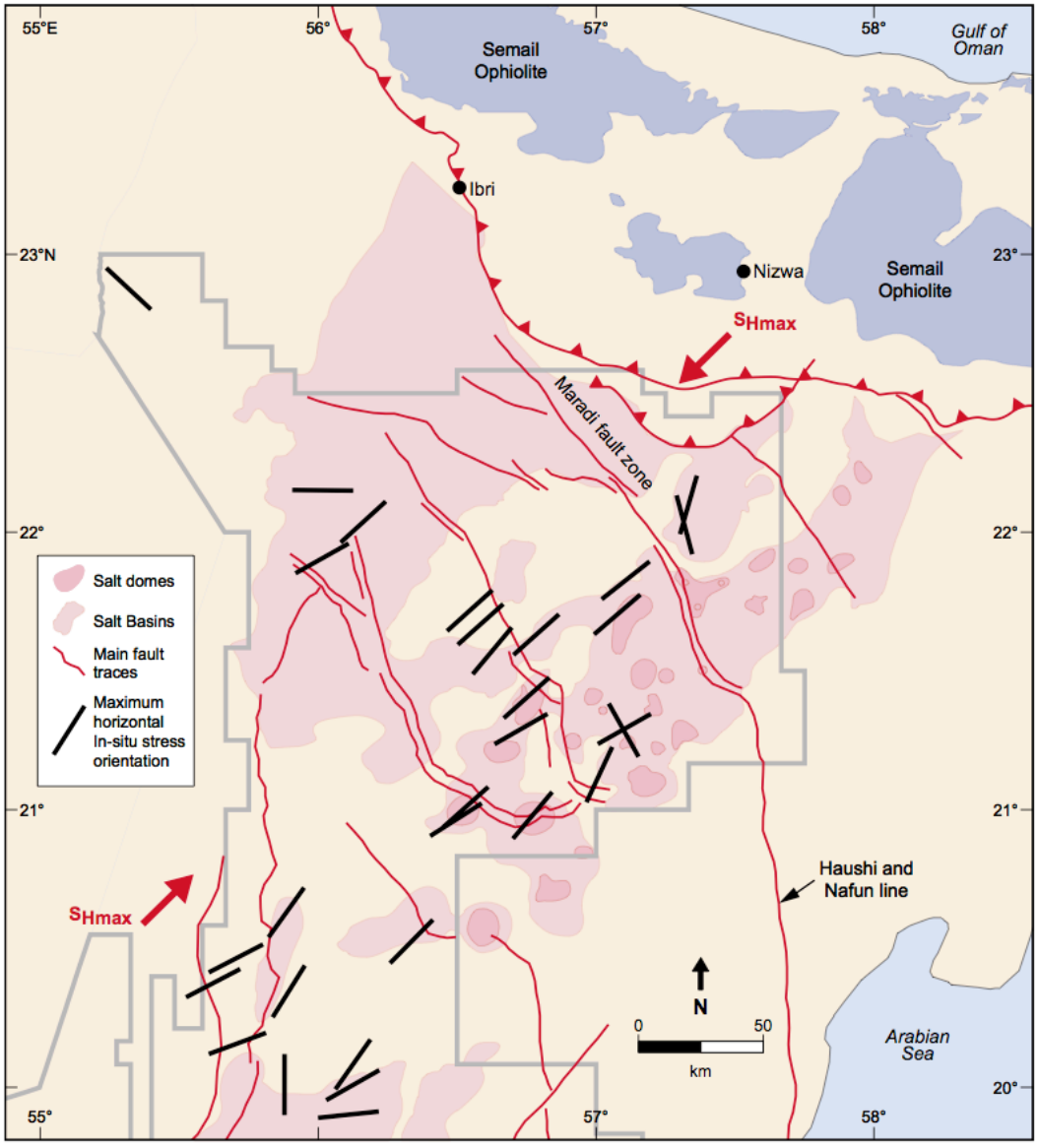

Figure 2.4: Maximum horizontal *in situ* stress orientations in North Oman estimated from borehole breakouts and induced fracture orientations (after Filbrandt et al., 2006). The mean orientation is NE-SW.

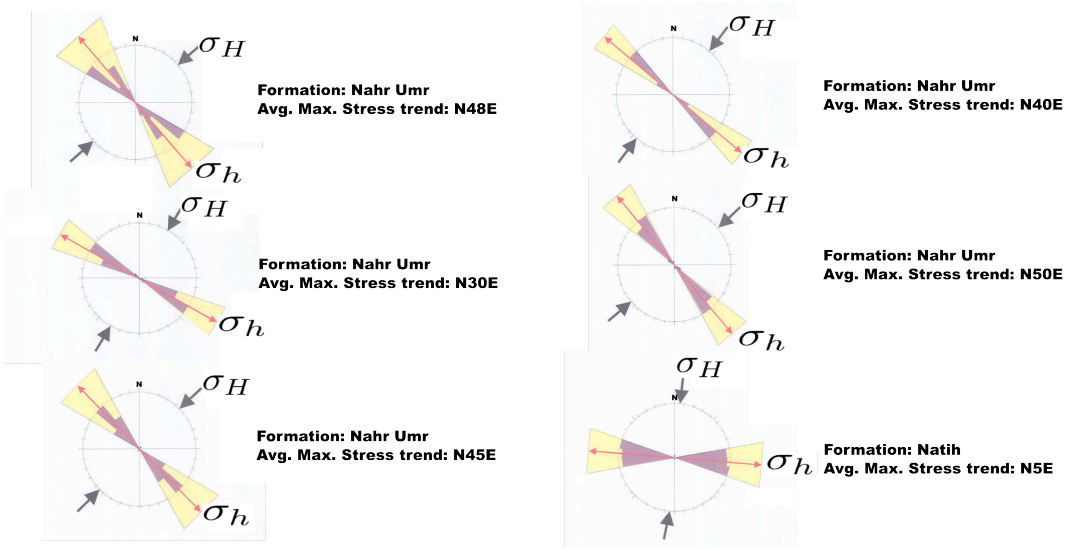

Figure 2.5: Orientations of the maximum (σ_H) and minimum (σ_h) *in situ* stresses obtained from wellbore breakouts derived from differential FMI and FMS caliper measurements. Results from the Nahr Umr are consistent and indicate NE-SW maximum horizontal stress orientation. Results from only one well available for the Natih formation show N-S oriented maximum horizontal stress (after Baker Atlas GEOScience, 1999).

2.5 Fracture system

2.5.1 Borehole observations

Hydrocarbon production from the Natih and Shuaiba reservoirs relies heavily on fracture-induced permeability. Several techniques have been applied to characterise the fracture system of Field M in both reservoirs.

Borehole image logs from 15 horizontal wells have been analysed by Al-Busaidi (1997) to characterise fractures at the Shuaiba level. A rose diagram of the fracture orientations is shown in Figure 2.6a. The predominant trend of fractures is NW-SE with a minor number of fractures oriented NE-SW. Al-Busaidi (1997) attributed these fracture orientations to the Late Cretaceous emplacement of ophiolite thrust sheets in the Oman Mountains. The fracture orientations are consistent with fault patterns interpreted from Field M 3D seismic data (Figure 2.2) and their densities vary between different reservoir units and appear to be a function of lithology. In addition, Al-Busaidi (1997) analysed image logs at the Shuaiba level from a nearby field that shares a similar deposition and tectonic history as Field M. It is located about 100 km to the NW of

Field M. The fractures were observed to have one main orientation, NW-SE. Moreover, cemented fractures, filled with calcite, have been also identified in both fields. They have similar trend as the open ones. They are subvertical and mostly located in the less porous facies.

In 2002, the fracture system at the Shuaiba level was further investigated using FMI logs. The study involved higher well density coverage compared to the one by Al-Busaidi (1997). Fractures were observed to strike predominantly in the NE-SW and NW-SE directions (Figure 2.6b). The crest and southern flank of the field are fractured more extensively than the northern flank. This trend agrees with the lateral variation in density of minor faults mapped using 3D seismic data, as illustrated in Figure 2.2.

An integrated study of core and FMI logs from five vertical and horizontal wells have been conducted by Hodder (2004) to study the Natih A fracture system. Few fractures were observed within the vertical wells compared to the horizontal wells. Fractures are dispersed throughout the Natih A with little evidence for clustering. Figure 2.7a shows rose diagrams of strike for the five wells studied at the Natih A level. The observed fractures are divided into conductive and resistive (cemented) fractures. Similar to the Shuaiba fracture network, the predominant fracture orientations (NE-SW, NW-SE and NNW-SSE) are consistent with the trends of major faults mapped from the field 3D seismic data (Figure 2.2).

A further detailed analysis was carried out by Ozkaya et al. (2004) to study the fracture system and karstic zones at the Natih A reservoir. The study was based on observations from borehole images, openhole logs and cores from two horizontal wells located in the NW part of the field (referred to as W1 and W2, Figure 2.7b). A common aspect of both W1 and W2 wells is the apparent sparse fracturing, which is in sharp contrast to the Shuaiba formation. In well W1, fractures are oriented in a NW-SE direction parallel to the NW-SE fault system, even though the well is close to the NE-SW graben. Half of the fractures are cemented and the average conductive fracture spacing is 20 m. Fractures in this well seem to be slightly more abundant in the Natih A2 and A3 submembers than in the Natih A4 submember. In well W2, fractures are striking parallel to the NE-SW and NW-SE trending faults. The average conductive fracture spacing is 50 m. For both wells the average fracture dip is 70°. This subvertical fracture dip supports the finding by Hodder (2004) that less fractures were observed in vertical wells compared to horizontal wells. Furthermore, Ozkaya et al. (2004) identified karstic disrupted zones within the Natih A with thicknesses ranging from 0.1 to 2 m. The study also revealed that the Natih A is densely populated by high permeability fracture corridors and mega-fractures. A more quantitative measure of their

size is not available. Similar observations from nearby fields have shown that these mega-fractures are characteristic of the Natih A and absent in the Shuaiba and the lower members of Natih formation.

2.5.2 Surface observations

The surface observations of fractures mainly come from the Natih formation outcrops exposed in the Salakh arch (located 130 km east of Field M). The Salakh arch consists of five well-exposed thrust-related anticlines.

Mercadier & Mäkel (1991) collected fracture measurements from the Salakh arch aiming to integrate them with subsurface data from the Natih reservoir in a nearby field. Two groups of fractures have been identified in the outcrops: (1) cross-axial fractures striking sub-perpendicular to the fold axis and (2) longitudinal fractures striking sub-parallel to the fold axis. The fractures are extensional or shear in nature and all dipping subvertically. The cross-axial extensional fractures are up to several hundreds of meter long with fracture spacing between one and several tens of meters. The cross-axial shear fractures have a length of one to several tens of meters and a spacing of 0.1 to 2 m. In contrast, the longitudinal fractures are more dependent on bed curvature and lithology. Their length is several tens of meters, with fracture spacing between 0.5 and 5 m. The fracture aperture varies from 100 microns (shear) to 5 cm (extensional).

De Keijzer et al. (2007) conducted a more focused fracture study on one of the Salakh arch anticlines called Madmar. Two dominant fracture sets have been observed. They are oriented in the NE-SW and NW-SE directions. The NE-SW fractures are oriented at high angle to bedding. The density of these fractures is high, with spacing often down to the centimetre-scale. Evidences of NE-SW fracture corridors have been also reported. The NW-SE trending fractures are more heterogeneously distributed and longer compared to the NE-SW trending fractures. In addition, WNW-ESE trending normal faults are common in the Madmar anticline.

In a more intensive study, Al-Kindi (2006) gathered a large dataset of fracture parameters in order to assess the relationship between small-scale structures (fracture patterns) and large-scale structures (folds and faults) presenting in the Salakh arch. The study included gathering fracture measurements from the five mountains forming the arch. The results indicate that the five mountains have fractures with different trends, which suggest that they were primarily formed by local stresses. The three predominant fracture orientations are NNE-SSW, NW-SE and E-W. They run parallel or perpendicular to fold axes. Generally, the fracture trend and density are

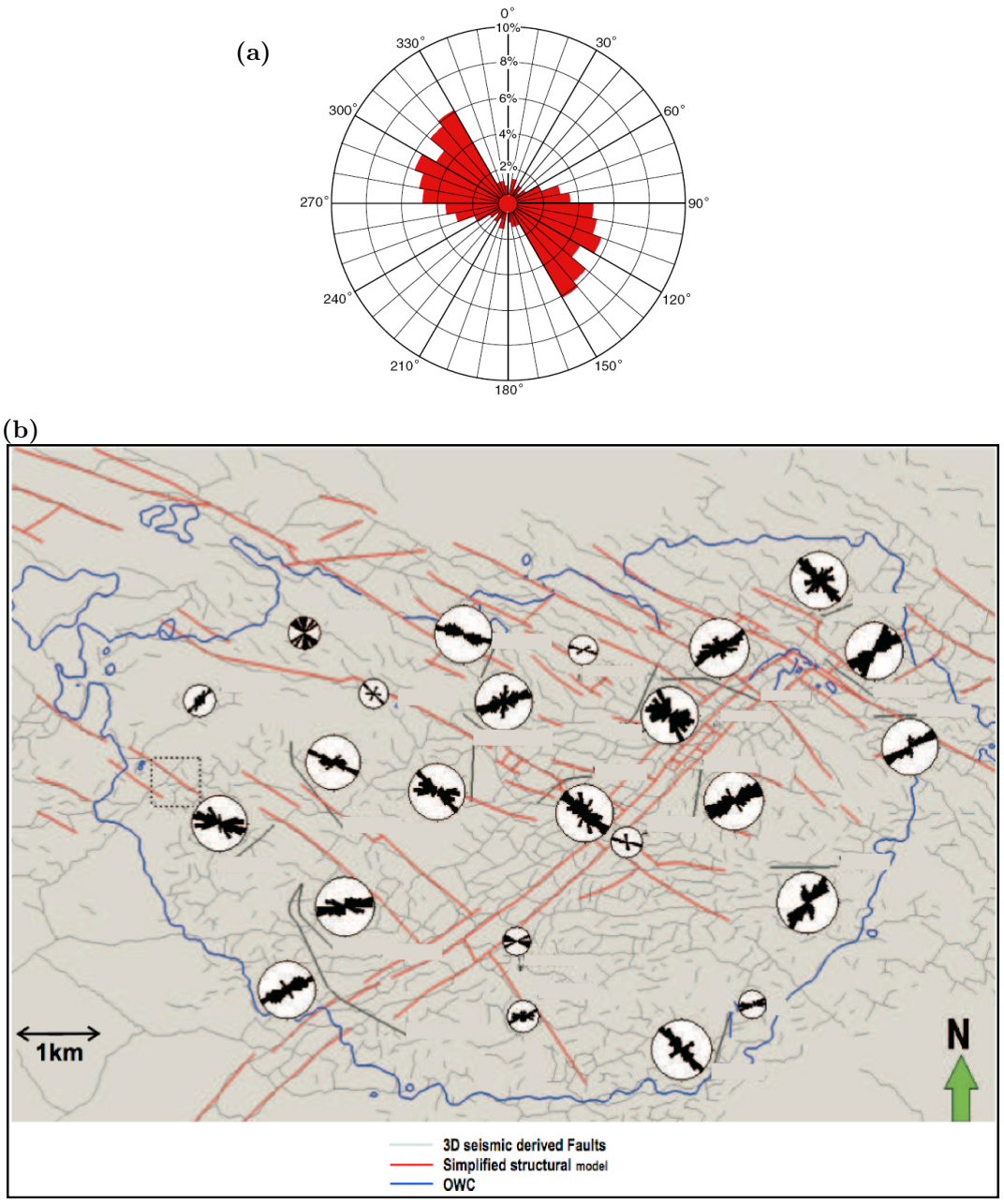

Figure 2.6: The Shuaiba fracture system. (a) The Shuaiba open fracture orientation rose diagram obtained from borehole image logs (after Al-Busaidi, 1997). The predominant fracture strike is NW-SE. (b) Results from an FMI study using dense well coverage at the Shuaiba level. There is a clear consistency between the fracture strikes and the fault patterns (Figure courtesy of PDO).

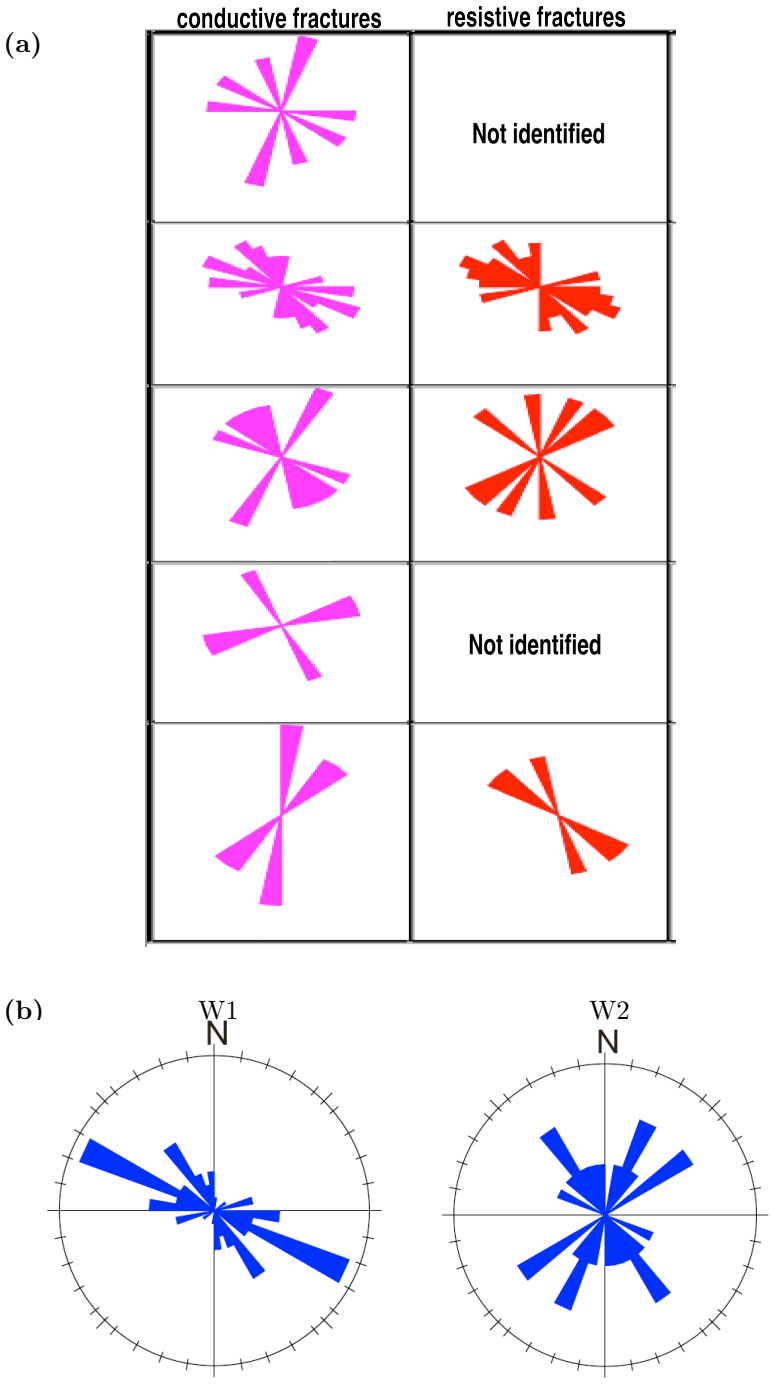

Figure 2.7: The Natih fracture system. (a) Rose diagrams of the Natih A conductive and resistive fracture orientations estimated from integrated core and FMI borehle image data from five vertical wells (shown in each row; after Hodder, 2004). (b) The Natih A open and cemented fracture orientation rose diagrams for wells W1 and W2 obtained from borehole images, openhole logs and cores. In well W1, fractures are oriented NW-SE. In well W2, fractures are oriented in two directions: NE-SW and NW-SE (after Ozkaya et al., 2004).

highly influenced by fold-axis bending and any geometrical irregularities. Cemented fractures are filled with calcite. Furthermore, significant increase in fracture density has been observed towards fault planes. Al-Kindi (2006) also collected measurements of fracture sizes from the Qusaibah anticline (part of the Salakh arch). He observed fractures with lengths in the range 4-22 m with fracture aperture between 3 and 14 mm. The Qusaibah anticline is mostly covered by the Natih A rocks.

2.6 Anisotropy

Al-Anboori (2006) estimated the percentage difference between the fast and slow shear wave velocities (δV_s) using dipole shear sonic logs. Minimum estimates of vertical δV_s within the field inferred from such logs show a decrease with depth from 4% in the Fiqa, to 2% in the Natih A and Natih B-G1, to 1% in the Natih B-G2.

Sze (2005) performed shear-wave splitting (SWS) analysis on microearthquakes recorded by the shallow passive seismic network (see Chapter 3 for description of the network). The results from 125 microearthquakes generally indicate normalised delay time (δt) ranging from 0.6 to 5.8 ms/km. The fast polarisation orientations (Φ) indicate predominant NE-SW fracture strike, with a few measurements indicating NW-SE strike. The average fracture dip is greater than 70°.

Al-Abri (2003) analysed four days of Field M microseismic data acquired using the deep microseismic network (see Chapter 3 for description of the network). The estimated δt was in the range 0-26 ms, corresponding to δV_s varying between 0% and 3%. The estimated mean fast strike was E-W ($\sim 96°$). Al-Anboori (2006) studied 22 days of data ($\sim$ 600 events) from the same network to get more detailed picture of the field anisotropy. This study showed that δV_s declines from 5-10% in the SE footwall of the eastern-most graben fault to about 1% in the NW part of the field and 2-3% in the region between the two graben faults. δV_s also varies with depth: the highest magnitudes (5%) are found in the highly fractured Natih A gas reservoir and decreases to about 1% in the non-producing lower part of Natih B-G. The Fiqa shale exhibits moderate anisotropy (3%). Al-Anboori (2006) also performed frequency-dependent anisotropy analysis on a subset of the data and found that fractures have sizes of less than 0.1 μm in the Fiqa cap rock and about 2 m in the Natih A reservoir. Both studies by Al-Abri (2003) and Al-Anboori (2006) were performed using manual SWS analysis.

Potters et al. (1999) performed an anisotropy study in a nearby field which shares the same geological history as Field M. Anisotropy was determined using observations of SWS in a nine-component three-dimensional (9C3D) experiment. In the Fiqa shale, δt was observed to be generally small (0-8 ms) and Φ was oriented N-S over the north-east part of the survey and NE-SW in the south-east part. In the Natih carbonate rocks, Φ is oriented NE-SW with high δt and δV_s values exceeding 30 ms and 15%, respectively. The splitting magnitudes are higher at the crest (at the Natih and the Fiqa) than on the flanks of the field. The observed NE-SW fast strike agrees with the orientation of open fractures, preferential flow direction and present-day *in situ* maximum horizontal stress. Tichelaar & Hatchell (1997) confirmed the NE-SW fast direction using an inversion of 4-C borehole flexural waves.

2.7 Compaction and subsidence

Compaction and subsidence in Field M are due to pore-collapse caused by production from the Natih and Shuaiba reservoirs. The geomechanical behaviour of the field is monitored using microseismic monitoring, continuous GPS measurements and InSAR satellite images (Bourne et al., 2006; Klemm et al., 2010). Bourne et al. (2006) integrated measurements from the three techniques to show that large-scale fault reactivation is occurring above, within and below the depleting Natih A gas reservoir. The InSAR satellite maps indicate higher rates of subsidence occurring in the NW part of the field compared to the SE part (Figure 2.8). The fastest compacting units are the Natih A2 and the Natih A4. Both units are soft and hetrogeneous. Compaction in the Shuaiba is much less than in the Natih, presumably due to water injection maintaining formation pressure.

2.8 Summary

Field M is a dome shaped anticline with faults trending NE-SW and NW-SE cutting the stacked shale and carbonate formations. The NE-SW striking faults form a graben system in the centre of the field. Gas is produced from the topmost Natih A reservoir by pressure depletion, whereas oil is produced from the deeper Shuaiba reservoir, where pressure is maintained by water injection.

The *in situ* compressive stress at the Nahr Umr level, estimated from breakout measurements, is oriented NE-SW, agreeing with current North Oman regional stress direction. In contrast, the *in situ* stress is oriented N-S within the Natih formation, but with low confidence as one

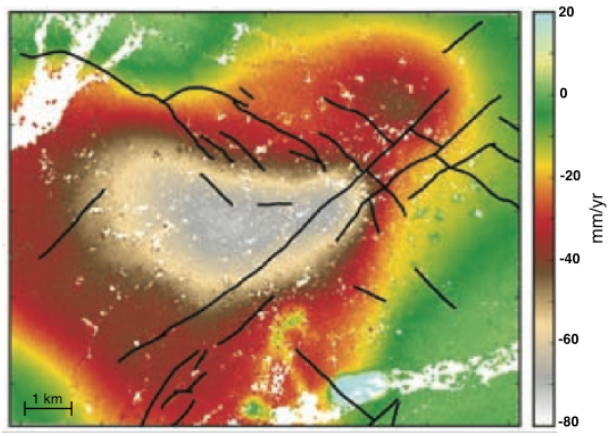

Figure 2.8: Subsidence rates from InSAR satellite images overlaid with major faults at the base of Fiqa (after Klemm et al., 2010). The highest rates of subsidence occurs in the NW part of the field.

measurement is only available. Focal mechanisms of the microearthquakes revealed E-W and NNE-SSW maximum compressive stress directions in the Fiqa and Natih A, respectively.

Fractures imaged by borehole techniques show two predominant NE-SW and NW-SE strikes that are consistent with the major fault trends. The average fracture dip is 70°. The Natih A reservoir is populated with mega-fractures and fracture corridors. Observations of fractures in the Natih A outcrops indicate increase in fracture density towards fault planes.

There is a spatial variation in anisotropy estimated from SWS analysis. The highest magnitudes are found to the SE of the eastern-most graben fault and decrease in the NW direction. The highly fractured Natih A reservoir exhibits higher amounts of anisotropy compared to the cap rock shale and the non-producing part of the Natih formation.

3
Field M microseismic monitoring, data processing and event statistics

3.1 Introduction

Chapter 2 introduced the two reservoirs monitored by the microseismic network: the Natih and Shuaiba. In this chapter I outline the acquisition and processing of Field M microseismic data and I perform a statistical analysis of the recorded seismicity. First, I describe the Field M microseismic monitoring network. Second, I outline the preliminary processing steps applied to the data prior to the analysis. Third, I explain the methodology used in locating the events and then explore the spatial and temporal distributions of events and how they are linked to the field production and injection activities. Fourth, I describe the technique used to measure the source parameters (seismic moment, moment magnitude, source radius and stress drop) and I investigate their statistical distribution and their variations with lithology. Finally, I estimate b-values for the Field M microearthquakes using the Gutenberg-Richter relation (Gutenberg & Richter, 1944) and the maximum likelihood method (Utsu, 1965; Aki, 1965).

As discussed in Chapter 1, microseismic events occur as a consequence of stress perturbation. Thus, by studying the spatial and temporal distributions of event locations and their associated parameters, we gain insights into the geomechanical properties of rocks. Observations of seismicity in mining environments show that induced seismic events follow the same statistical behaviors as those seen with natural earthquakes (e.g., Gibowicz & Kijko, 1994). Events induced in hydrocarbon reservoirs are expected to obey the same rules of thumb because they are induced by similar mechanisms to those observed in mines.

3.2 Field M passive seismic monitoring

West-central Oman, where Field M is located, is generally an aseismic region. The closest active seismic zone is the boundary between the Arabian and the Euroasian plates in the Gulf of Oman. Nevertheless, seismic tremors have been felt by staff working in Field M since 1995. In addition, surface subsidence has been observed in the centre of the field (see Figure 2.8 in Chapter 2). The seismic events were small in magnitude and they were not detected by the Omani and regional

seismic networks. It was later realised that the seismicity is occurring within the field due to perturbations in the stress field caused by production and injection activities. These observations of seismicity and subsidence have increased concerns about the integrity of wells and risks facing surface facilities.

In 1999, the Field M compaction monitoring program was initiated in order to: (1) understand the causes of the observed microearthquakes, (2) quantify the compaction of the Natih and Shuaiba reservoirs and (3) upgrade the infrastructure to withstand the movements caused by the induced seismic activities. The project included installing a shallow passive seismic monitoring network, followed by the deployment of borehole network at the Natih A level.

3.2.1 Shallow network

The shallow network, which is still functioning, consists of five continuously monitoring borehole arrays (Figure 3.1). Four three-componet geophones were installed in each borehole, located at depths 135 m, 140 m, 145 m and 150 m. The system was only able to detect large magnitude events. More information about the shallow network and the detected events can be found in Sze (2005).

3.2.2 Deep network

The demand to have better insight into the geomechanical behaviors of the field reservoirs led to the deployment of a deep microseismic network in 2002. The project, known as the High Impact Project (HIP), was a collaborative research experiment between ABB Offshore Systems Limited (now VetcoGray) and Petroleum Development Oman (PDO), with technical support from Shell E & P Technology and Research (SepTAR). The intent of the project was to assist in reservoir management decision making by: understanding compaction processes, monitoring water front movement, identifying compartmentalisation due to faulting and evaluating fracture dominated flow (Jones et al., 2004). The total monitoring period was 18 months (from February 2002 to August 2003).

The experiment involved five suspended oil wells (Figure 3.1), where each well was instrumented with an eight-level geophone array. Well 2 is located at the centre of the field with the other four wells forming a parallelogram-like shape of 2 km by 2 km in dimension. The detectable monitoring area was about 10 km^2. The network was designed to monitor microseismic activity in the Natih and Shuaiba reservoirs and the surrounding formations. The final design was achieved using a

	Phase-I					Phase-II				
Well	**1**	**2**	**3**	**4**	**5**	**1**	**2**	**3**	**4**	**5**
Station	1.1	2.1	3.5	4.1	5.1	1.1	2.1	3.1	4.1	5.1
	1.6	2.2	3.7		5.3		2.2	3.5	4.2	5.3
		2.4			5.5		2.4	3.7		5.5

Table 3.1: List of the microseismic stations with known tool orientations for Phase-I and Phase-II of the Field M microseismic experiment.

combination of numerical modelling and logistical constraints imposed by availability of wells and their completions (Jones et al., 2004). The seismic stations are named using well number and level number from top to bottom. For example, station 3.5 refers to well 3 and level 5 from the top.

In each well, each level consists of 4 sensors arranged in tetrahedral shape. In tetrahedral geophone configuration, sensors are arranged along the vectors joining the centre of the tetrahedra to its four vertices (the angle between each pair of sensors is 109°). The tetrahedral geophone arrangement provides data redundancy and allows for performance checking of the system during its operational life (Jones & Asanuma, 2004). Moreover, it has the advantage that 3 orthogonal components can be constructed even if one sensor is dead or malfunctioning. The geophones were cemented in the tubing/casing to ensure good sensor-formation coupling and to reduce noise from tube waves propagating down the wells (Raymer et al., 2003).

The downhole geophones were continuously recording signals, digitised at 2 kHz. Out of 160 channels (4 channels per station), 120 channels could be connected at any time to the acquisition system. After the initial selection, the connected geophones remained the same for about six months. Then, on the 9^{th} of July 2002 the system was rewired and some channels were switched off (Raymer et al., 2003). The period of the experiment before the rewiring is called Phase-I and the one after the rewiring is called Phase-II. Only particular channels were allowed to trigger. For each trigger, one second of data before the trigger and three seconds after the trigger were recorded. Data were time-stamped using a GPS clock.

Throughout the experiment, most of the geophones were dead or badly functioning. The failure of the majority of the geophones was linked to the leakage of electrical signals across the geophone string. Only data from 13 stations (listed in Table 3.1 and shown in Figure 3.1b) can be used in the processing, as they have known tool orientations obtained using check-shots generated by a vibroseis truck (Raymer et al., 2003).

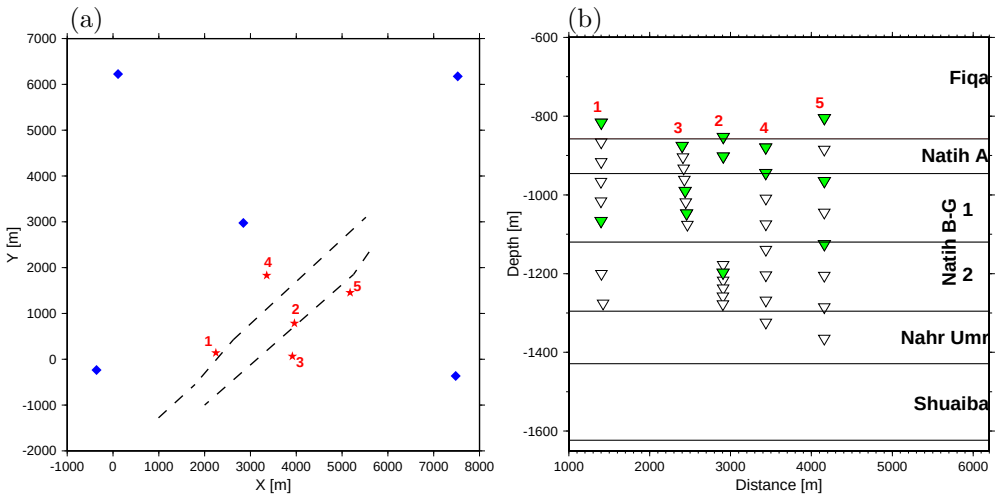

Figure 3.1: Passive seismic monitoring in Field M. (a) Map view of the monitoring wells used for the shallow network (blue diamonds) and the deep network (red stars). Dashed lines are the two graben faults cutting the field reservoirs. (b) Cross-section parallel to the main graben faults showing the seismic stations of the deep network. Stations with known tool orientations are marked in green.

3.3 Preliminary data processing

Originally the data were delivered for this study in *stwf*[1] (containing waveforms and acquisition information), *xml* (containing P- and S-wave time picks), and *ascii* (containing event information such as location, magnitude ... etc.) formats. The challenge was to convert all these file formats, which are used mainly by oil companies, to SAC[2] format. Figure 3.2 shows the workflow for data reformatting. The programs and scripts which have been used in the data reformatting are listed in Table A.1 in Appendix A.

I used the microseismic processing software XMETAL[3] to carry out the initial processing steps. The raw data (in *stwf* format) were first filtered using a predictive filter (part of the XMETAL package) to eliminate the 50 Hz electrical noise and its harmonics. The source of electrical noise is the electrical signals transmitted down wells to prevent corrosion (cathodic protection). Figure 3.3 shows an example of seismogram before and after applying the predictive filter. The second step was to convert the 4 component records (tetrahedral configuration) to a 3 component orthogonal set (one vertical and two horizontal). Then, the two horizontal components were rotated and

[1]Simple Triggered Waveform interchange Format (STWF) consists of two files: a one-line waveform binary file and an ascii table containing information about each waveform file.

[2]Seismic Analysis Code (SAC) is a program used widely in global seismology (Goldstein, P., 2005, SAC: Seismic Analysis Code, http://www.llnl.gov/sac/). It can be adapted to be used with microseismic data.

[3]The X-windows version of the Microseismic Event Timing And Location. It is owned by Schlumberger.

aligned with the geographical Cartesian coordinates (north-south and east-west). Finally, the data were exported from XMETAL in *stwf* binary format. The XMETAL program also outputs *stwf ascii* tables which contain information about the seismograms stored in the *stwf* binary files (one *stwf ascii* table for each *stwf* binary file).

The arrival time picking was performed by ABB Offshore System Limited. The P- and S-wave absolute arrival time picks were supplied in *xml* format. These were extracted from the *xml* files in order to calculate the relative arrival times and were then written to *ascii* tables (Figure 3.2). Furthermore, a single file per event containing information about location, magnitude and origin time was created from the original *ascii* file containing information about all located events. The resultant four files for each event (*stwf* binary, *stwf ascii*, time pick file and event information file) were then combined and converted to SAC format.

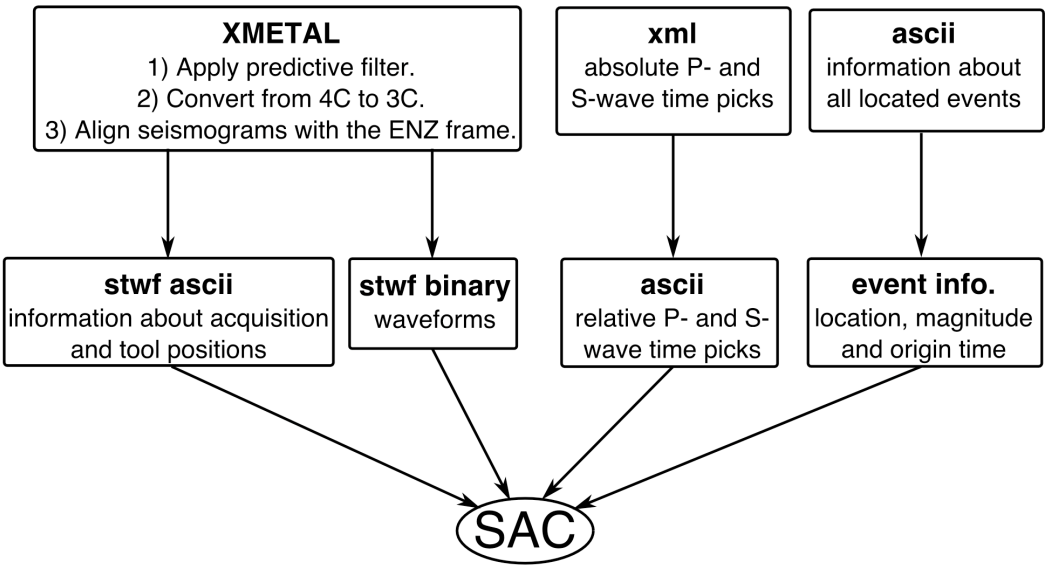

Figure 3.2: Workflow of Field M microseismic data reformatting.

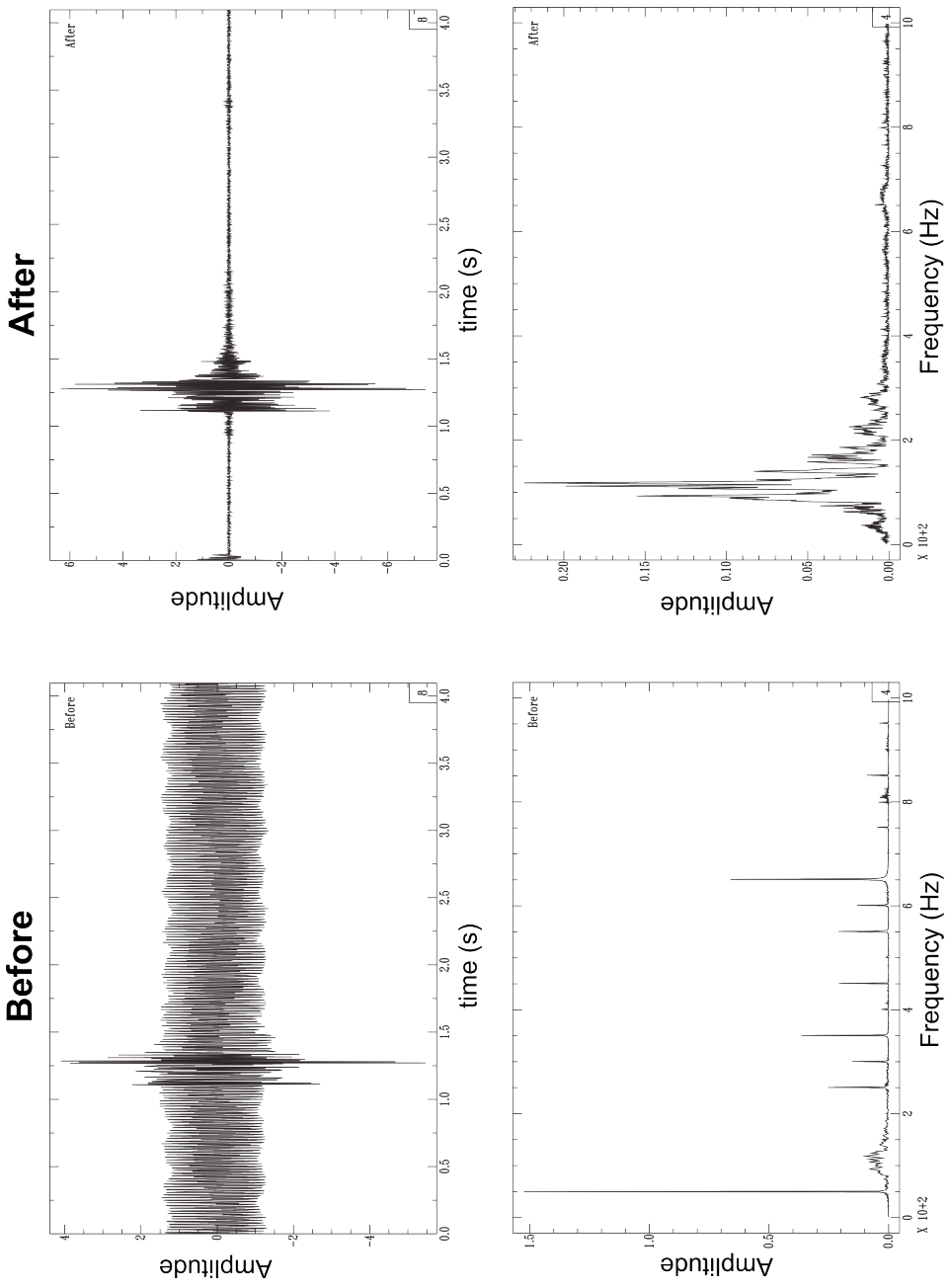

Figure 3.3: Application of a predictive filter to remove electrical noise. [Left panel] Seismogram before applying the predictive filter and its frequency spectrum plot. [Right panel] The same seismogram after applying the predictive filter and its frequency spectrum plot. Time is in seconds. Note the sharp 50 Hz noise and its harmonic tones before filttering.

3.4 Event locations

3.4.1 Methodology

The detected microearthquakes were located by ABB Offshore System Limited using the XMETAL processing package (Raymer et al., 2003; Raymer & Jones, 2004). A 3D velocity model of Field M, based on seismic logs, was used to locate the events. Figure 3.4 illustrates a simplified 1D 21-layer velocity model extracted from the 3D velocity volume of the field. Event origin times and locations were determined using P- and S-wave arrival times and P-wave particle motion. The location methodology is based on Geiger's method, which solves for the event location (x, y and z) and the origin time (t) simultaneously (description of the Geiger's method can be found in Buland (1976)). The optimum location is chosen such that the root mean square (RMS) error is minimum.

The total number of located events during Phase-I of the experiment is 3096, with an average rate of 14 events per day. In the second phase of the experiment, events were located every other day giving a total of 4657 events (28 events per day). Only 13 months of data from the 18 months of monitoring are available for this research (from February 2002 to May 2003 with no data available for December 2002, March 2003 and part of January 2003). The available dataset for this research is 3397 located events, distributed unevenly over a period of 457 days.

In the next two sections I analyse the spatial and temporal distribution of events located by ABB Offshore Systems Limited.

3.4.2 Spatial distribution of events

The distribution of events in space is shown in Figure 3.5. Events are generally clustered along the two main graben faults cutting the field formations. Sze (2005) located the events recorded by the shallow network and reported similar observations of clustering along the graben faults.

In the Fiqa shale, the events do not show a clear clustering (Figure 3.5b). These events were likely caused by thrust faulting in response to the contraction of the depleting Natih A reservoir (see for example the modelling of Segall (1989)). The high proportion of seismicity clustered close to the monitoring well 3 and centered in the Natih A reservoir (Figure 3.5c) was due to gas production from a nearby well (Raymer et al., 2003). A region of high seismicity was also detected around monitoring well 5. This region was mostly active during summer and is called

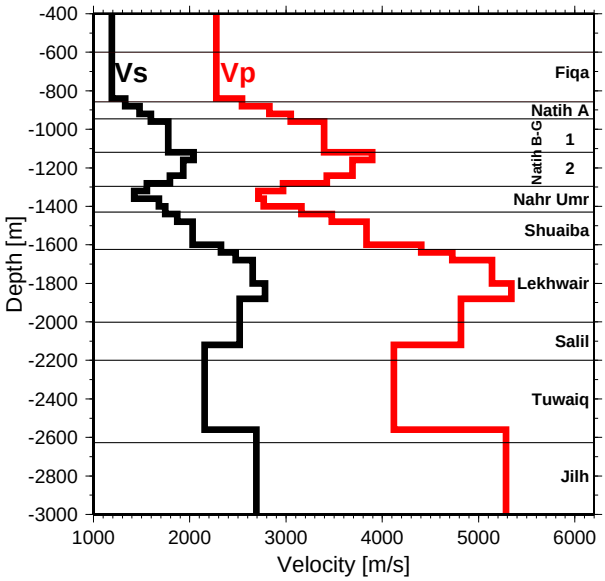

Figure 3.4: Field M 21-layer V_p and V_s velocity models. The model was extracted from the field 3D velocity volume.

the Horseshoe due to its horseshoe-like shape in plan view (Figure 3.5c). This feature is thought to be a reservoir compartment (Raymer & Jones, 2004). Microseismicity surrounding the feature is driven by pressure differential caused by depletion of the rock volume outside the feature. This is supported by the focal mechanism analysis of Raymer & Jones (2004) which indicated normal faulting along the sides of the compartment. In the non-producing Natih B-G unit, events are mostly clustered along the two graben faults (Figure 3.5d). The reactivation of the faults was thought to be driven by water injection into the Shuaiba formation (Raymer et al., 2003). However, the fault reactivation might also be due to the contraction of the Natih A or both the contraction of the Natih A and the inflation of the Shuaiba (see for example Segall (1989)). Events within the Nahr Umr and the Shuaiba are randomly distributed (Figure 3.5e). Figure 3.6 displays the vertical distribution of events. It can be clearly seen that the highest rate of seismicity occurred in the compacting Natih A reservoir. The low seismicity level at the Shuaiba reservoir is not necessarily due to the formation being seismically quiet but could be due to the limited coverage of the network (Figure 3.1), not allowing to detect small deep events. Better insights into the mechanisms behind the observed seismicity at Field M can be obtained by undertaking more detailed analysis of the event focal mechanisms.

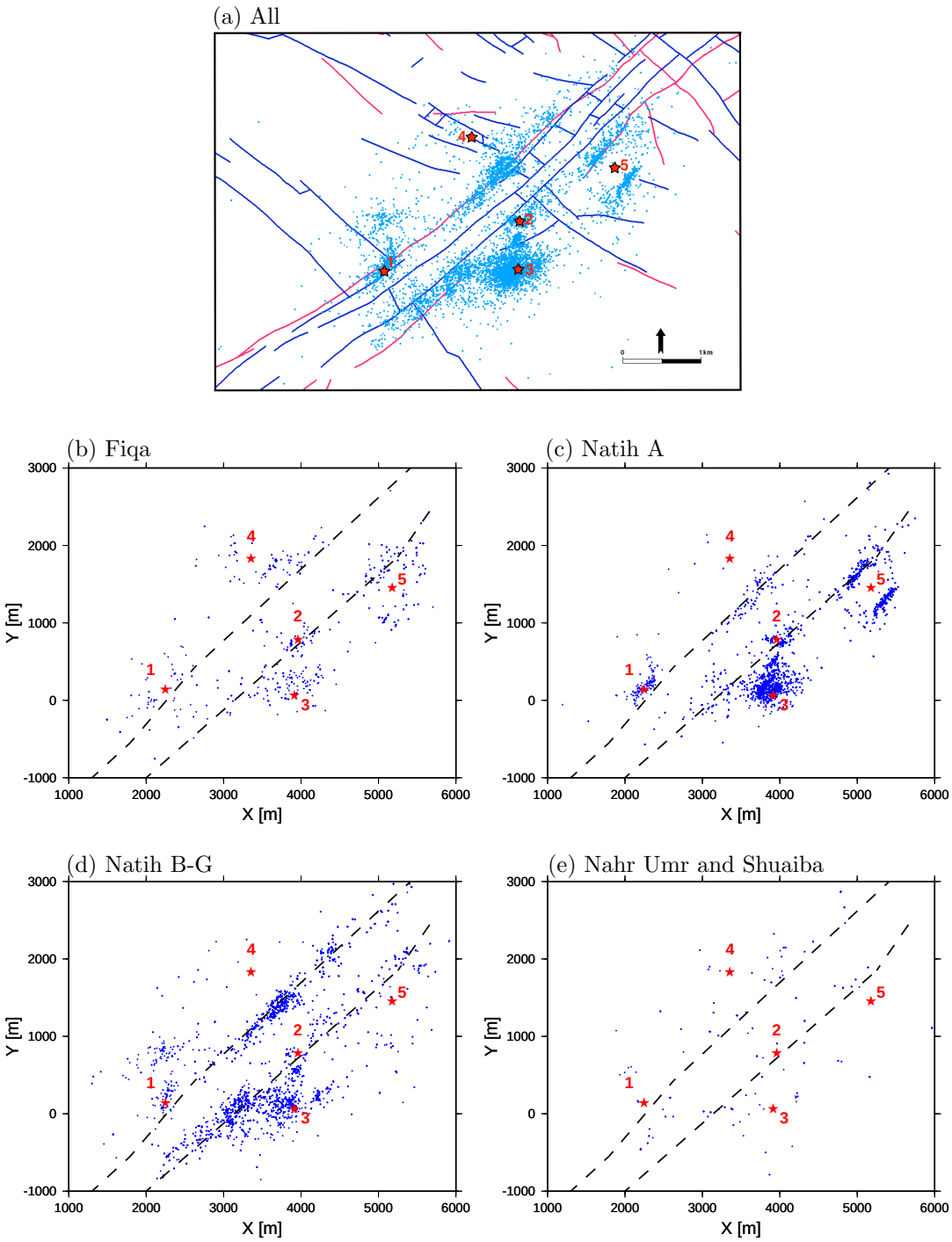

Figure 3.5: Map views of Field M microearthquake locations. (a) All located events shown in a map view with faults cutting the base of the Fiqa shale (red lines) and faults at mid-Shuaiba (blue lines). Events shown in depth slices: (b) the Fiqa; (c) the Natih A; (d) the Natih B-G and (e) the Nahr Umr and Shuaiba (see Figure 3.4 for depth ranges). The monitoring wells are denoted by red stars. The main graben faults are shown by dashed lines in (b) to (e).

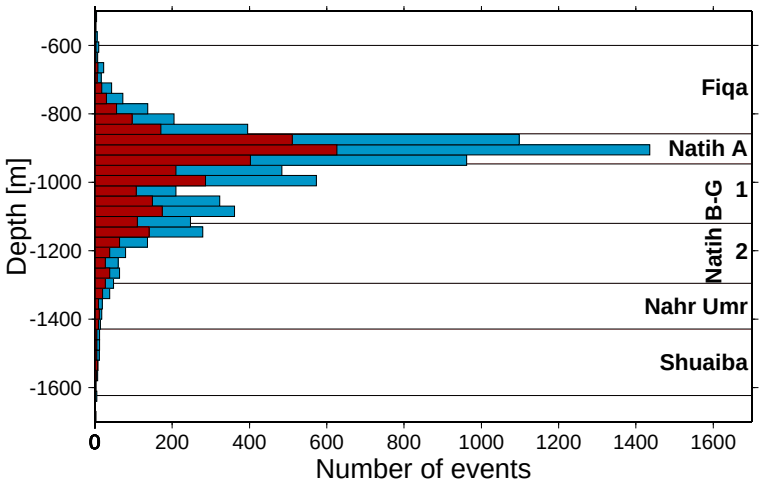

Figure 3.6: Histogram of event distribution with depth (30 m bin size). Most events occurred within the highly compacting Natih A reservoir. Blue bars are all the located events, whereas red bars are events available for this research.

3.4.3 Temporal distribution of events

Figure 3.7 shows the distribution of events over time, together with the fluid production and injection rates. The microseismicity level is reasonably well correlated with the field production and injection activities. Seismicity increases during the summer when gas production from the Natih A increases to meet the high demand for electricity to operate air conditioning systems. The correlation between seismicity level and gas production rates becomes clearer when considering events that occurred entirely within the producing Natih A reservoir (Figure 3.8). It should be noted that events were located every other day during Phase-II of the experiment (i.e., after 9^{th} of July 2002, vertical dashed line in Figures 3.7 and 3.8), hence, seismicity level should be higher than it appears in Figures 3.7 and 3.8 for the second part of the experiment.

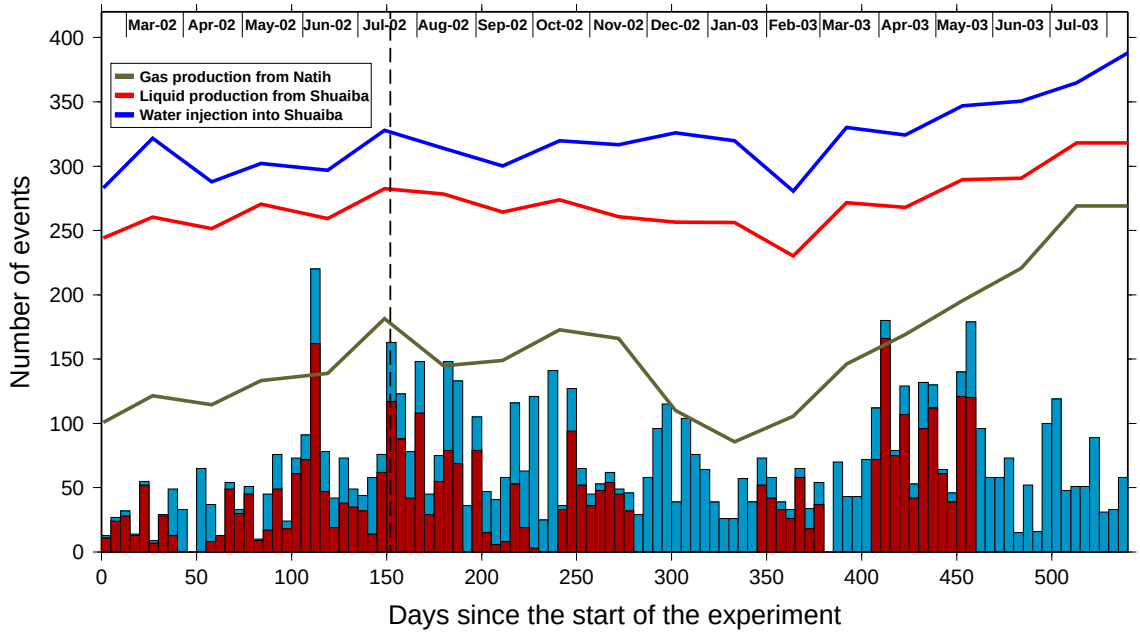

Figure 3.7: Histogram of seismicity level with time and field production/injection rates (5 days bin size). Vertical dashed line marks the start of Phase II of the experiment. Seismicity was high during summer 2002 and 2003, when gas production from the Natih reservoir reached maximum. Water injection and liquid production into and from the Shuaiba reservoir remained almost constant over the time of the experiment. Blue bars show all the located events and red bars show located events available for this research. Production and injection rates are not to scale for confidentiality reasons. Only relative variation is shown.

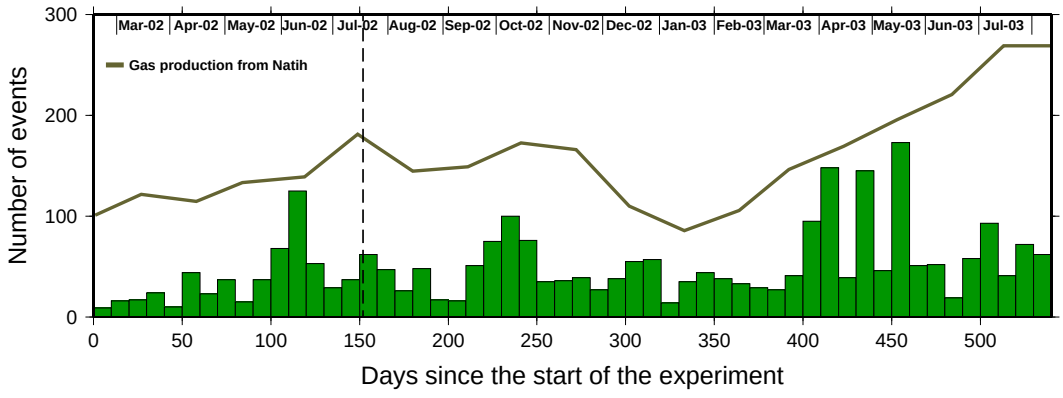

Figure 3.8: Histogram of seismicity level with time for events that occurred within the Natih A reservoir (10 days bin size). Vertical dashed line marks the start of Phase II of the experiment. There is a clear correlation between seismicity rate and gas production from the Natih A reservoir. Gas production rate is not to scale for confidentiality reason. Only relative variation is shown.

3.5 Source parameters

3.5.1 Methodology

ABB Offshore Systems Limited measured the source parameters of the events using spectral analysis of the seismic records (Raymer et al., 2003; Raymer & Jones, 2004). The seismic moment ($M_\circ$) was obtained directly from the low-frequency spectral level ($\Omega_\circ$) of the far-field displacement spectra of the P- and S-waves following the relations of Brune (1970):

$$M_\circ(p) = \frac{\Omega_\circ(p) 4\pi\rho D V_p^3}{R_\theta(p)}, M_\circ(s) = \frac{\Omega_\circ(s) 4\pi\rho D V_s^3}{R_\theta(s)}, \tag{3.1}$$

where D is the source-receiver distance, ρ is the rock density, R_θ is an angle dependent radiation correction factor, V_p and V_s are the P- and S-wave velocities, respectively. The relation is independent of the detailed slip processes along the fault surface. The moment magnitude (M) was then derived from the seismic moment ($M_\circ$) using an empirical relation.

Another quantity which can be obtained from the spectral analysis is the corner frequency (f_c) which is related to the rupture duration of the seismic source. f_c describes the source dimension along which the rupture occurs. Hanks & Wyss (1972) related the source radius (r) to f_c using:

$$r = \frac{K V_r}{f_{cr}}, \tag{3.2}$$

where K is a constant, V_r is the average P- or S-wave velocity and accordingly f_{cr} is the corner frequency of the P- or S-wave. Raymer et al. (2003) used K values of 0.32 and 0.21 when using P- and S-waves in the spectral analysis, respectively. Having computed $M_\circ$ and r, the average static stress drop ($\Delta\sigma$) assuming circular fault can be estimated using (Brune, 1970):

$$\Delta\sigma = \frac{7 M_\circ}{16 r^3}. \tag{3.3}$$

3.5.2 Statistical distribution of source parameters

Source parameters are only available for 4221 events out of the total located 7753 microearthquakes. In this section I analyse the statistical distribution of the source parameters and how they vary with lithology.

Seismic moment ($M_\circ$)

Histograms of $M_\circ$ estimates for the entire dataset, Fiqa, Natih A and Natih B-G are shown in Figure 3.9. $M_\circ$ is mainly clustered between 0 and 0.2 GNm in the Fiqa and Natih A with a broader variation in the Natih B-G formation. The median of $M_\circ$ varies from 0.05 GNm in the Fiqa, to 0.02 GNm in the Natih A, to 0.09 GNm in the Natih B-G.

Moment magnitude (M)

The variation in M is shown in Figure 3.10. When considering the entire dataset, most of the events have magnitudes between -1.5 and -0.5 with the minimum being -2.2 and the maximum being 0.85. The median is -0.9. The median of M decreases from -0.9 in the Fiqa shale to -1.1 in the fractured Natih A reservoir. The Natih B-G has the relatively highest median estimate of M (-0.7).

The spatial variation in M is also analysed by plotting the M magnitudes in map view and cross-section (Figure 3.11). The data were gridded to get bulk estimate of the spatial variation in M. Figure 3.11 shows that large magnitude events occurred along the graben faults and mostly clustered within the Natih B-G formation. In contrast, small magnitude events occurred either side of the graben system, and generally confined to the gas producing Natih A reservoir.

Source radius (r)

Histograms of the variation in r are shown in Figure 3.12. For the entire dataset, r varies between 1.1 m and 6.7 m with a median of 2.6 m. Similar to the variation of $M_\circ$, events with large r are found in the Natih B-G formation with a median of 3.2 m. The median of r decreases from 2.9 m in the Fiqa cap rock, to 2.2 m in the Natih A reservoir.

Stress drop ($\Delta\sigma$)

$\Delta\sigma$ describes the difference between the average initial and final shear stresses on the fault. The variation in $\Delta\sigma$ is displayed in Figure 3.13. Since the two parameters are linked by Equation (3.3), the variations in $\Delta\sigma$ and $M_\circ$ look similar. When considering the entire dataset, $\Delta\sigma$ mainly ranges between 0.02 and 10 MPa with a median of 1.1 MPa. The same estimate of $\Delta\sigma$ median is

observed in the Fiqa shale which decreases with depth to 0.9 MPa in the Natih A reservoir. Higher amounts of stress release are observed for events that occurred within the Natih B-G formation with a median of 1.3 MPa.

3.5.3 Frequency-magnitude relation

One of the most important statistical laws in seismology is the relation between the frequency and magnitude of earthquakes which occur during a certain period of time in a specific region. The most commonly used equation to study the frequency-magnitude distribution is the Gutenberg & Richter (1944) relation (Log$N$=A-bM), where N is the number of events with magnitude M, A is a parameter indicating the level of seismicity and b describes the relative proportion of small and large magnitude events. A low value of b indicates that the occurrence of high magnitude events is more frequent compared to the case of large b-value. In this section I estimate the frequency-magnitude relation for the events detected in Field M.

The b-value is estimated by plotting the log of the cumulative number of events with moment magnitude equal or greater than a given value against M. Then, the value of b is obtained by finding the gradient of the best-fit straight line to the curve of Log$N$ against M using a linear regression technique (Figure 3.14). The b-value has been estimated for the entire dataset, the Fiqa, the Natih A and the Natih B-G (Figure 3.14). The results are summarised in Table 3.2.

It is worth noting that the frequency-magnitude curves in Figure 3.14 are linear only in the middle. This is most likely because the catalogue of events is incomplete (i.e., missing significant portion of small and large magnitude events). This is quite often seen in studies of microearthquakes (e.g., Lahaie & Grasso, 1999; Chun-lai et al., 2009). In passive seismic monitoring, very small events are often beyond the detectability limit of networks. Also, we need to record for longer time and/or expand the area of network coverage to detect more large magnitude events.

In the cases of incomplete earthquake catalogue it becomes more appropriate to use the maximum likelihood method of Utsu (1965) and Aki (1965) to estimate the magnitude of b. The maximum likelihood procedure assumes that magnitudes are continuous and unlimited from the top. It gives more robust estimates of b-value and is asymptotically unbiased (Gibowicz & Kijko, 1994). In the maximum likelihood method b is defined as

$$b = \frac{log_{10}(e)}{(\bar{M} - (M_c - M_{bin}/2)}, \tag{3.4}$$

where $\bar{M}$ is the mean magnitude, M_c is the magnitude of completeness and M_{bin} is the binning width of the catalogue. M_c is defined as the minimum magnitude in which the catalogue is

complete. To estimate M_c, I follow the maximum curvature method (e.g., Wiemer & Katsumata, 1999) which defines M_c as the point of maximum curvature by computing the maximum value of the first derivative of the frequency-magnitude curve. Furthermore, I use the bootstrapping technique described by Woessner & Wiemer (2005) to estimate the uncertainties in M_c and b. The software package ZMAP of Wiemer (2001) is used to perform the analysis. The results are summarised in Table 3.2.

The estimates of b-values from the maximum likelihood method are lower than those from the Gutenberg-Richter relation. This is most likely because the magnitude of M_c from the maximum curvature method is often underestimated especially for gradually-curved frequency magnitude distributions (e.g., Woessner & Wiemer, 2005). However, both techniques indicate decrease in the magnitude of b with depth. In the subsequent interpretation I base the analysis on the results from the maximum likelihood method.

	Gutenberg-Richter		Maximum likelihood		
Dataset	b	A	M_c	b	A
All	1.2	2.4	-0.94±0.15	0.86±0.1	2.54
Fiqa	0.83	1.6	-0.99±0.17	0.77±0.09	1.62
Natih A	1.1	1.7	-1.2±0.08	0.85±0.05	2.07
Natih B-G	1.2	2.1	-0.68±0.1	1.05±0.08	2.19

Table 3.2: Estimates of the b and A parameters using the Gutenberg-Richter relation and the maximum likelihood method. M_c is the magnitude of completeness. Uncertainties in M_c and b are estimated using bootstrapping technique.

3.5.4 Interpretation

Generally, the source parameters appear to correlate with lithology in Field M. The highest estimates of $M_\circ$, M, r and $\Delta\sigma$ are observed in the Natih B-G formation. In this formation events are believed to be generated by fault reactivation driven by water injection into the deep Shuaiba reservoir. In contrast, the magnitudes of the source parameters are relatively low in the soft Natih A reservoir where events are thought to be caused by fracture generation and closure due to fluid flow. The shale cap rocks show moderate source parameter magnitudes. Similar lithology-related variations in source parameters have been reported by Feignier & Grasso (1991), using induced seismicity recorded at the Lacq gas field in France. The seismicity in the Lacq field is driven by pressure depletion. The source radius (r) decreases sharply from the overburden (reef limestone

and marly layer, r>50 m) to the underlying gas reservoir (limestone, r<50 m). This is comparable with the variation in r at Field M (maximum in the non-producing Natih B-G and minimum in the Natih A reservoir). Moreover, Feignier & Grasso (1991) showed that the maximal stress drops ($\Delta\sigma$) within each geological unit at the Lacq field are correlated with the rock mechanical strength. In section 2.3.1 of Chapter 2, we have discussed the fact that the Natih A is mechanically weaker compared to the underlying Natih B unit (Herz, 2004). This corroborates the observation that $\Delta\sigma$ is low in the Natih A compared to the Natih B-G.

The studies of global earthquakes have shown that the b-value is typically close to 1 (e.g., Frohlich & Davis, 1993; Stein & Wysession, 2003). In contrast, a deviation from unity has been reported in studies of b-value in local earthquakes (e.g., Mori & Abercrombie, 1997; Gerstenberger et al., 2001), volcanic tremors (e.g., Wiemer et al., 1998; Wyss et al., 2001; Bridges & Gao, 2006; Farrell et al., 2009) and induced seismicity in mines (e.g., Chun-lai et al., 2009; Kwiatek et al., 2010) and hydrocarbon reservoirs (e.g., Lahaie & Grasso, 1999; Urbancic et al., 2010). Furthermore, several studies have shown that the magnitude of b can vary in space (e.g., Bridges & Gao, 2006; Wiemer et al., 1998; Wyss et al., 2001) and time (e.g., Wiemer et al., 1998; Chun-lai et al., 2009). The factors which control the magnitude of b include temperature (Warren & Latham, 1970), state of stress (e.g., Scholz, 1968; Amitrano, 2003) and medium heterogeneity (e.g., Mogi, 1962). Warren & Latham (1970) observed an increase in b-value with increasing thermal gradient. In the vicinity of volcanos, the magnitude of b is observed to increase close to magma chambers. This increase is attributed to either or both the decrease in effective stress, caused by increase in pore pressure by intrusion of magma, and the increase in heterogeneity by intensive fracturing (e.g., Wiemer et al., 1998; Wyss et al., 2001). In California, Mori & Abercrombie (1997) observed a systematic decrease in the magnitude of b with depth and suggested the increase in ambient stress as a possible explanation. In the Lacq field in France, Lahaie & Grasso (1999) reported a decrease in b-value when increasing loading rate by pressure depletion (i.e., gas production). Gas production will reduce pore pressure and consequently increase effective stress. A detailed review of studies in b-value and the factors controlling its magnitude can be found in Wiemer & Wyss (2002).

From Table 3.2, it can be seen that the Fiqa shale exhibits a lower b-value (0.77) compared to the carbonate Natih A and Natih B-G rocks (0.85 and 1.05, respectively). The high b-values within the carbonate rocks are likely due to high pore fluid pressure (low effective stress) or strong heterogeneity caused by extensive fracturing or perhaps it is due to both factors. To confirm such conclusions more information about the field rocks and state of stress are required. For example,

the effect of stress on the magnitude of b can be investigated by monitoring the variation in the b-value over several years of pressure depletion by production. Thermal gradients in Field M are not likely to be significant and thus not controlling the magnitude of b.

Overall, the results show that the study of source parameters and b-value using microseismic data has the potential of delivering valuable information for reservoir characterisation and management, and hazard assessment. Such potential has been already highlighted, for example, by Feignier & Grasso (1991), Lahaie & Grasso (1999) and Urbancic et al. (2010). Feignier & Grasso (1991) found a correlation between the magnitudes of source parameters and the rock mechanical properties at the Lacq field in France. In the same field, Lahaie & Grasso (1999) were able to link the variation in the magnitude of the b parameter with the rate of pressure depletion. Finally, Urbancic et al. (2010) found a relation between the magnitude of b and the nature and complexity of fracturing (obtained from focal mechanisms) during reservoir stimulation.

3.6 Summary

With the advantage of five monitoring wells, the Field M microseismic dataset offers unique possibilities for reservoir imaging. Furthermore, the length of the experiment was long enough to monitor and understand the behaviour of the field over time. Unfortunately, tool orientations are only available for 13 stations out of the originally deployed 40 stations. Nevertheless, the dataset is unprecedented in the oil industry.

Prior to the analysis, several essential pre-prosessing steps were applied to the microseismic dataset. This includes: (1) removal of harmonic noise, (2) construction of 3C orthogonal seismograms from tetrahedral geophone configuration and (3) alignment of the orthogonal records with the geographic Cartesian coordinates north-south, west-east and vertical.

The majority of the events in Field M are located within the compacting Natih A reservoir. These microearthquakes were generated by the perturbation in the local stress field caused by gas production, which is reflected by the increase in seismicity levels during summer months when gas production increases. The events within the Natih B-G formation have high magnitudes and they are mostly clustered along the two graben faults that cross-cut the field, indicating that the seismicity is due to the reactivation of faults. Events within the cap rock shale show variable magnitudes and they were probably generated by seal arching in response to compaction in the underlying Natih A reservoir.

The magnitudes of source parameters (seismic moment, moment magnitude, source radius and stress drop) are dependent on lithology. The highest estimates are within the mechanically stable Natih B-G, whereas the lowest estimates are observed within the soft compacting Natih A reservoir. b-value increases from 0.77 in the Fiqa shale to 0.85 and 1.05 in the Natih A and Natih B-G, respectively, possibly reflecting an increase in heterogeneity with depth and/or increase in pore pressure (decrease in effective stress).

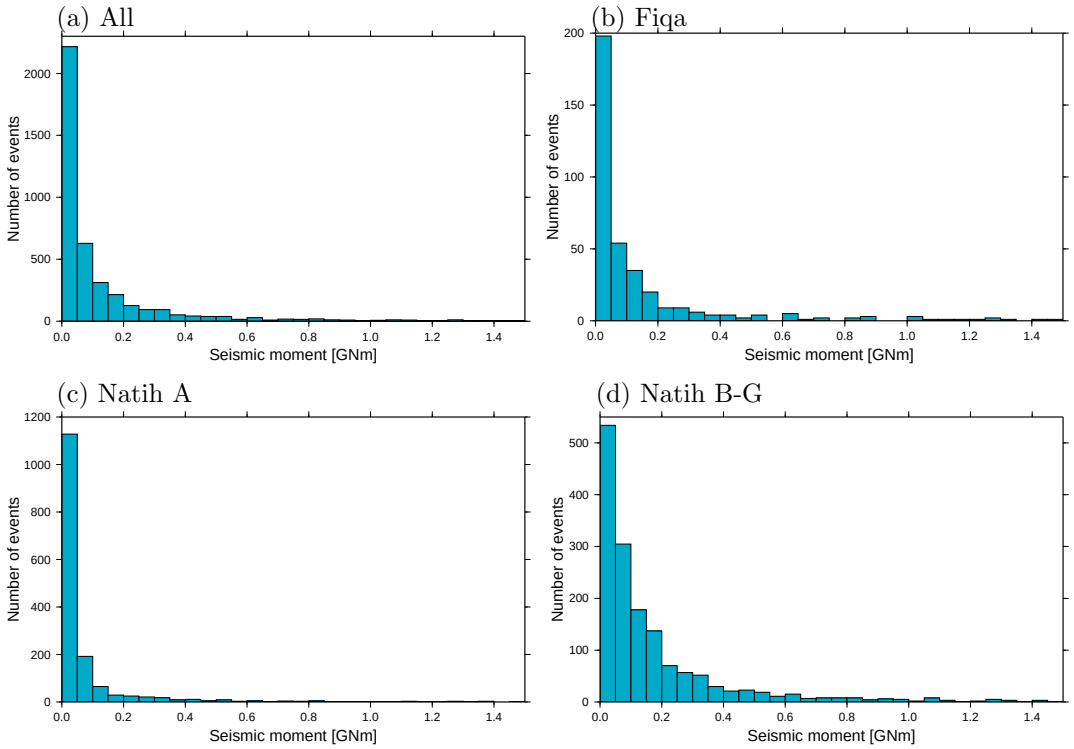

Figure 3.9: Histograms of variations in seismic moment ($M_\circ$) for (a) the entire dataset, (b) events within the Fiqa, (c) events within the Natih A and (d) events within the Natih B-G. The Natih B-G estimates show a broader range in $M_\circ$ compared to the Fiqa and Natih A.

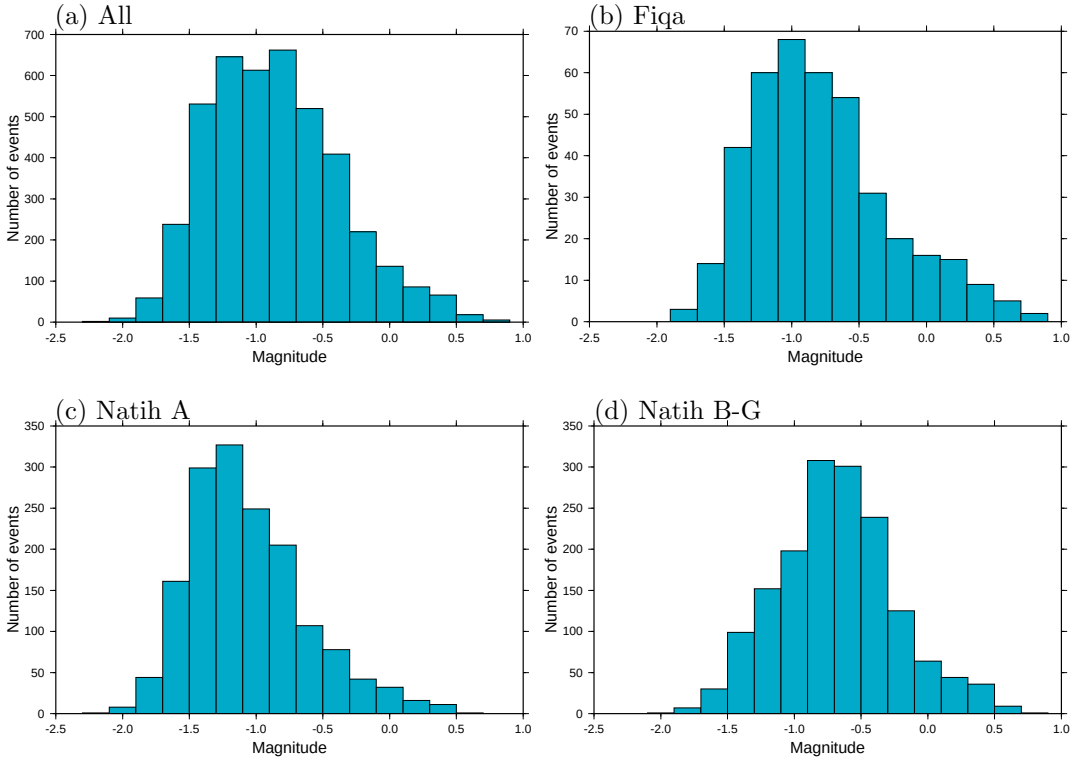

Figure 3.10: Histograms of variations in seismic moment magnitude (M) for (a) the entire dataset, (b) events within the Fiqa, (c) events within the Natih A and (d) events within the Natih B-G. M generally ranges between -1.5 and -0.5. Most of the highest magnitude events occurred within the Natih B-G.

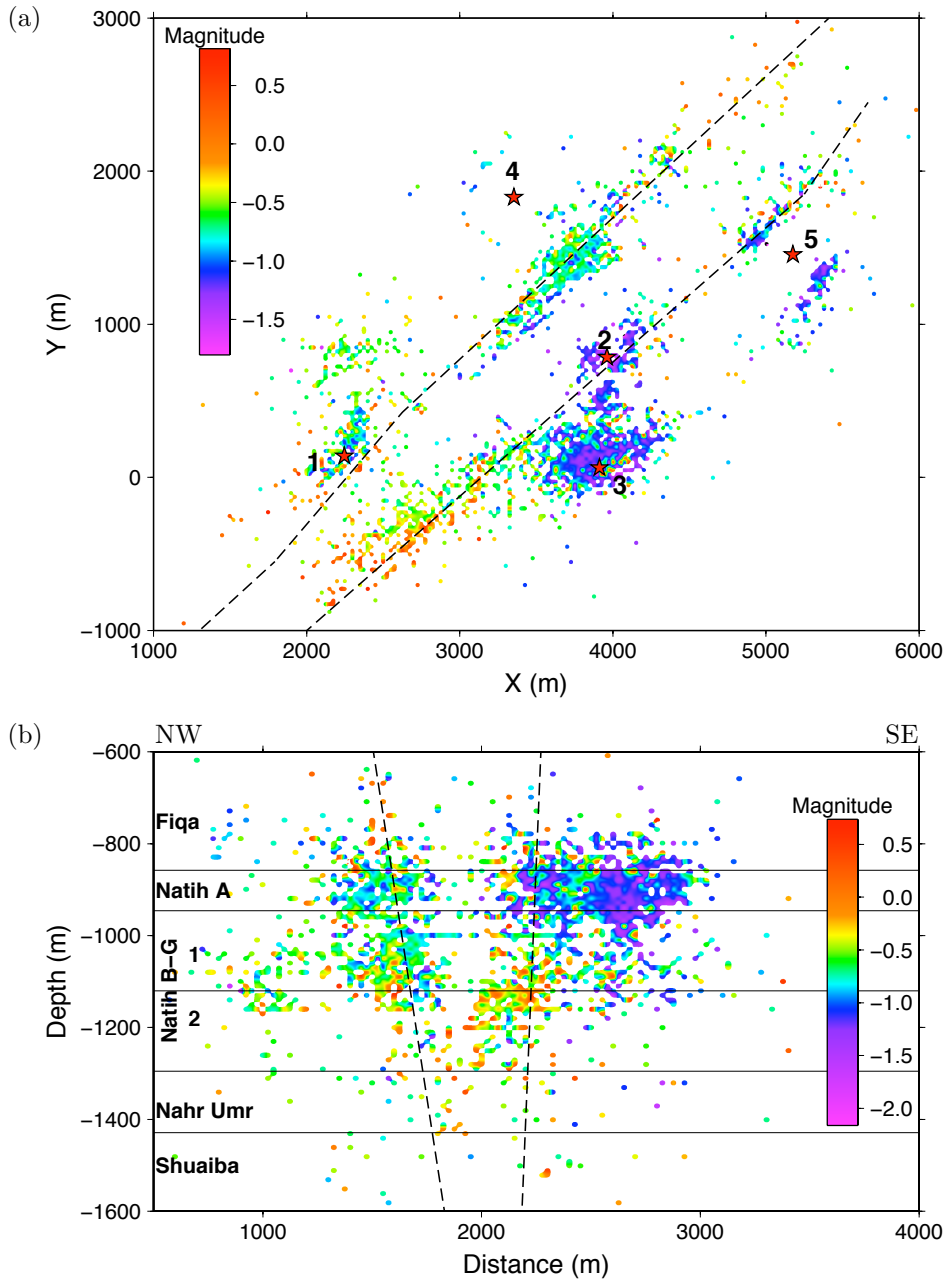

Figure 3.11: Spatial variation of moment magnitude displayed in (a) map view and (b) NW-SE cross-section. The graben faults are shown by dashed lines. The five monitoring wells are marked by red stars. When girding the data cell sizes of 25×25 m and 25×10 m were used with the map view and the cross-section, respectively. Note that relatively high magnitude events (yellow and orange) are located close to the graben faults and mostly clustered in the Natih B-G formation.

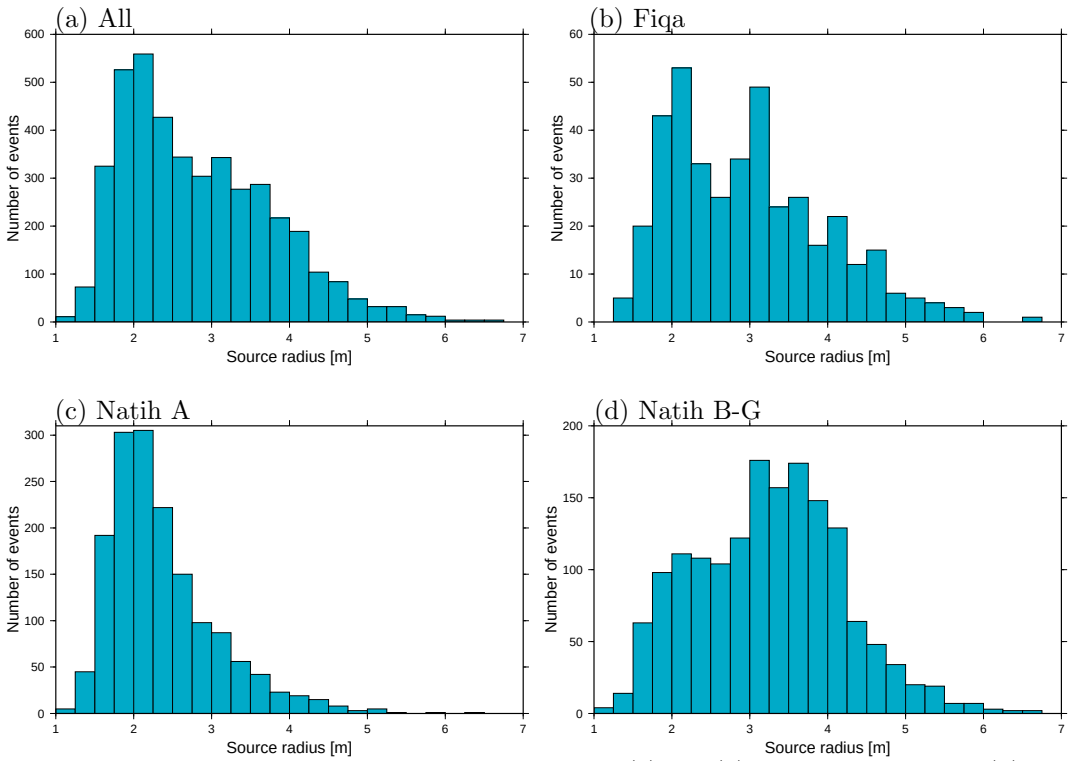

Figure 3.12: Histograms of variations in source radius (r) for (a) the entire dataset, (b) events within the Fiqa, (c) events within the Natih A and (d) events within the Natih B-G.

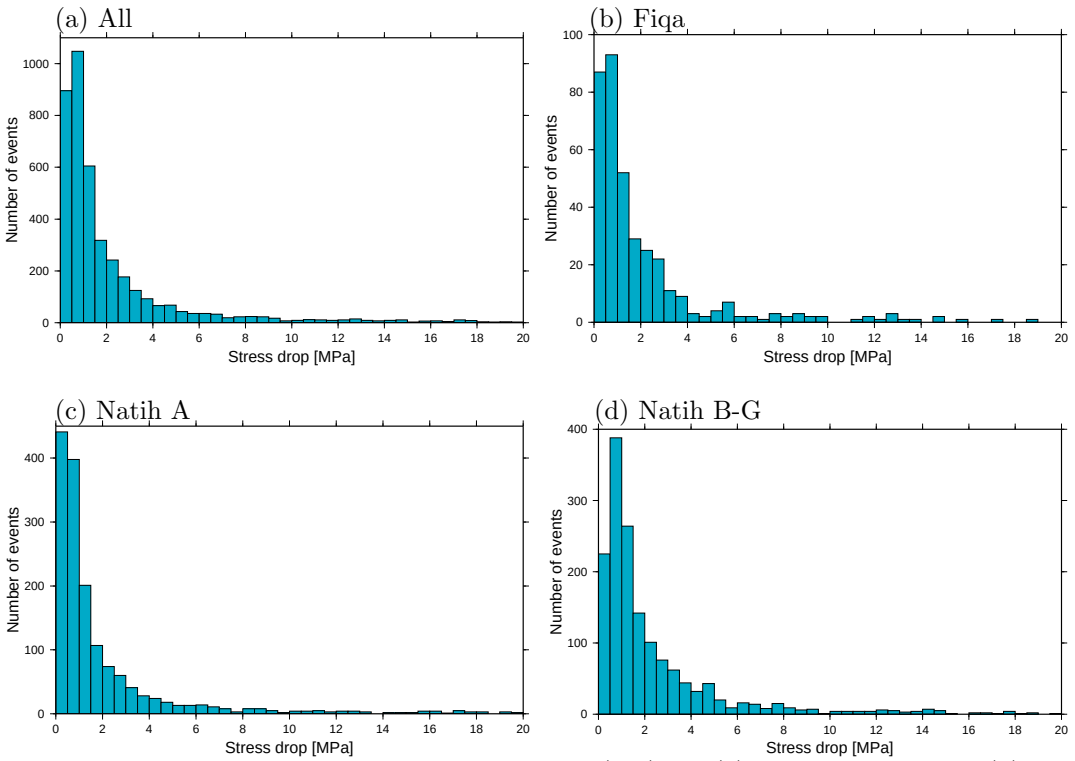

Figure 3.13: Histograms of variations in stress drop ($\Delta\sigma$) for (a) the entire dataset, (b) events within the Fiqa, (c) events within the Natih A and (d) events within the Natih B-G..

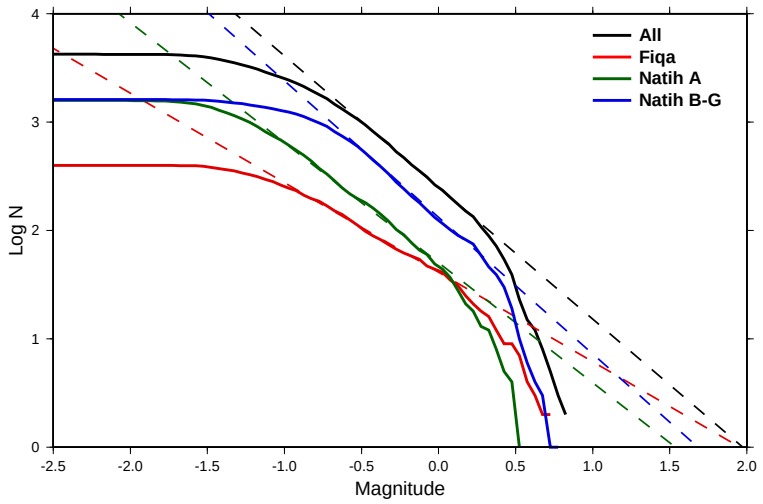

Figure 3.14: Frequency-magnitude relations for the entire dataset and the Fiqa, Natih A and Natih B-G formations. The b-values are estimated by fitting straight lines to the curves using linear regression.

4
Shear-wave splitting analysis: automated quality control and null detection

4.1 Introduction

Shear-wave splitting (SWS) analysis is a widely used tool in seismology to quantify and describe anisotropy in the Earth. When a shear-wave enters an anisotropic medium, it is split into two independent and orthogonally polarised components travelling at different speeds. Seismic anisotropy is described by the polarisation direction of the leading component (Φ) and the delay time between the two components (δt). There are several techniques that can be used to estimate the two splitting parameters. The two most common techniques used in SWS analysis, and those which I will use in this study, are minimisation of the covariance matrix describing the S-wave ellipticity (e.g., Silver & Chan, 1988, 1991) and cross-correlation of S-wave components (e.g., Fukao, 1984; Bowman & Ando, 1987). The minimisation of the covariance matrix, also known as the eigenvalue method (EV), performs grid search over a range of Φ_{EV} and δt_{EV} that best minimise the second eigenvalue of the covariance matrix describing the ellipticity of the S-wave in the anisotropic medium. After removing the anisotropy effect by rotating the fast and slow components of the S-wave by Φ_{EV} and time shifting one of them by δt_{EV}, the S-wave elliptical particle motion is linearised. In contrast, the cross-correlation method (XC) derives the splitting parameters (Φ_{XC} and δt_{XC}) by rotating and cross-correlating the S-wave components in the S-wave plane to find the orientation with the highest cross-correlation coefficient.

The use of robust automated or semi-automated techniques for SWS analysis becomes crucial with fast growing microseismic and teleseismic data volumes, especially with long deployments and large monitoring networks. Manual analysis becomes too time consuming in such cases. Furthermore, the splitting result accepted by one researcher may not be considered reliable by another, making the definition of reliable splitting measurement subjective. Inconsistency is therefore another issue with manual splitting analysis. On the other hand, automated techniques maximise

objectivity and minimise human interaction. Moreover, they help with handling large seismic data volumes in a rapid and convenient way.

There have been several attempts to automate SWS analysis in the past both using global and microseismc datasets. For example, Levin et al. (2004) in their automated technique used both the XC and EV methods to study SWS observations from the Kamchatka Peninsula, Russia. The misfit in the splitting parameters from the two methods is used to rank the quality of the measurements. Evans et al. (2006) investigated the SWS beneath the permanent broad-band stations in Canada using SKS phases from 20,000 station-event combinations. They used the EV and transverse energy (TE) methods described in Silver & Chan (1991) with a multi-step QC system to determine reliable splitting measurements. The TE method grid searches over splitting parameters that minimise energy on the S-wave transverse component. Teanby et al. (2004b) used a semi-automated approach based on the EV method to analyse microseismic data from the Valhall field in the North Sea. The method removes the subjectivity of choosing an S-wave analysis window by performing cluster analysis to determine the most stable window.

The biggest challenge when trying to automate the splitting process is defining the constraints that must be satisfied in order to accept the measurements. Errors in splitting measurements can arise, for example, from the inclusion of secondary phases, low signal-to-noise ratio, low energy and complexity of the waveform. Automation can be optimized by visual checking of diagnostic plots (plot inspection of seismograms, particle motion and error surfaces) or by imposing stringent selection criteria. Teanby et al. (2004b), for example, used manual quality control by inspecting the splitting diagnostic plots after the cluster analysis. Crampin & Gao (2006) in a review of the techniques used to measure SWS in signals from local earthquakes concluded that none of the existing automated techniques are fully satisfactory.

Automation methods are used with the price of rejecting most of the data. For example, Teanby et al. (2004b) ended with 40%-less reliable measurements when using their automated technique, compared to using manual analysis. However, the problem of loosing some good events is not significant when handling large datasets.

In this chapter I describe a step-by-step approach to automating SWS analysis and then apply it to the Field M dataset. The automated technique combines the use of the cluster analysis method of Teanby et al. (2004b), together with the SWS quality control suggested by Wüstefeld & Bokelmann (2007). The success of the technique is assessed by visually examining the diagnostic plots. Finally, I test the effect of filtering prior to the SWS analysis on the splitting magnitudes.

This automated approach has been successfully tested on synthetic data (Wüstefeld et al., 2010). It has also been tested on datasets from the Valhall (Wüstefeld et al., 2010) and Ekofisk (Jones, 2010) oil fields and microseismic data from a mine in Australia (A. Wüstefeld, Uni. of Bristol. pers. comm. March 2010).

4.2 Methodology

4.2.1 Rotation to the ray frame and filtering

Unlike global seismology, with microseismic monitoring raypaths are not always near vertical, which means significant amount of S-wave energy can be on the vertical component. To improve the clarity of the S-wave arrivals and to get more accurate splitting measurements the seismograms are rotated from the east, north and vertical geographical coordinates (ENZ) into the ray frame which is defined by the a, b and c axes (Figure 4.1a). Axis c is along the ray direction and, a and b are orthogonal to c. The longitudinal P-wave arrivals are maximised on the c component after rotation. Axis a is pointing horizontally and contains the S-wave arrivals in the horizontal plane (S_h), whereas axis b contains the S-wave arrivals in the sagittal plane (S_v).

The rotation to the ray frame is performed based on the P-wave particle motion. P-wave particle motion is polarised parallel or near-parallel to the ray direction in isotropic/weakly anisotropic media. Hence, it can be used as ray direction proxy. The data are first filtered using low pass 350 Hz filter to remove high-frequency noise. Second, the P-wave window is chosen manually to construct hodograms. A robust estimation based on least absolute residuals (L1 norm) is used to obtain the rotation angles in the horizontal and vertical planes (azimuth and inclination). A bootstrap technique (Press et al., 1989) is used to measure the uncertainties of the rotation angles. Figure 4.1b shows an example of seismograms before and after rotation based on P-wave particle motion. When the P-wave is poorly defined or contaminated by other phases, a straight line raypath is assumed to determine the rotation angles. After the rotation, the data are low pass filtered using a Butterworth filter with a corner frequency of 100 Hz following the previous studies by Al-Abri (2003) and Al-Anboori (2006). However, this value is modified to 200 Hz at the end when analysing the effect of filtering on splitting magnitudes.

The manual picking of the P-wave window to construct hodograms is a time consuming process. I found that for events with clear and impulsive P-wave arrivals, it is possible to automate the rotation process by defining a fixed P-wave window relative to the P-wave time pick and then

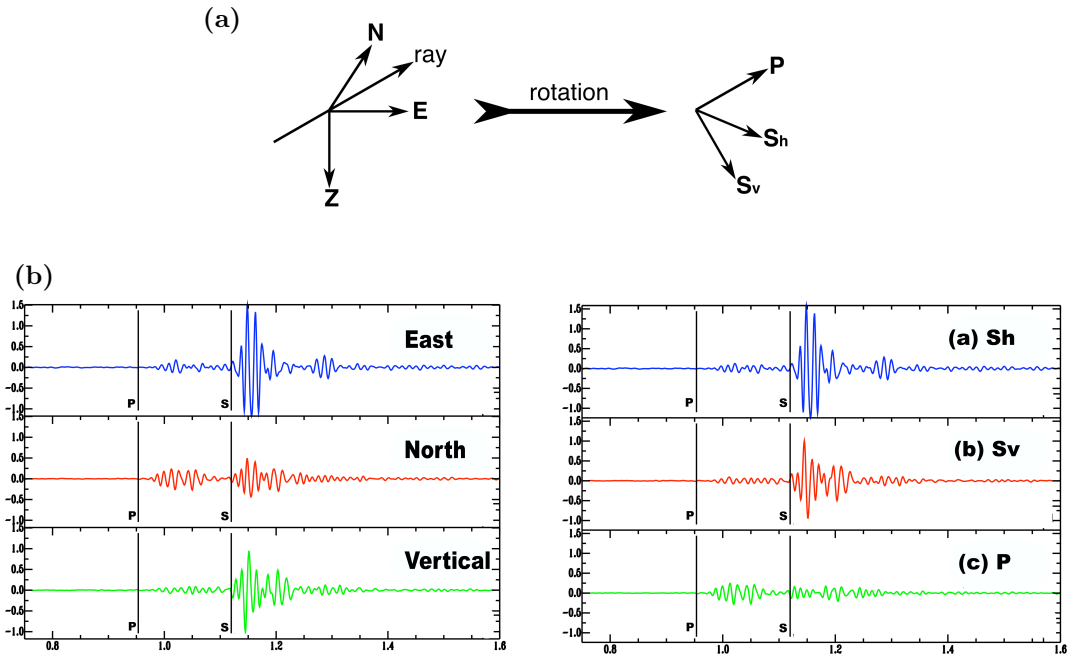

Figure 4.1: Rotation from geographic to ray coordinates. (a) Schematic illustration of the rotation. (b) Seismograms before and after rotation to ray frame. Notice the increase in S-wave energy in a and b, which contain the horizontal and vertical component arrivals of the S-wave, respectively. P-wave energy is maximised on component c. The P- and S-wave onsets are marked in the two plots.

constructing the hodograms by looping over the chosen events. This is illustrated in Figure 4.2 using a subset of events that have clear P-wave arrivals. Note the good match between the rotations angles when using manual and automated P-wave picking. Following this recipe, Wüstefeld et al. (2010) were able to rotate the seismograms of the Valhall dataset in an automated way.

4.2.2 Cluster analysis

One of the issues when performing SWS is to choose an S-wave window that provides a robust estimate of the anisotropy along the raypath. It has been recognised that different analysis windows in size and location relative to the S-wave pick can result in significantly different splitting parameters. Manual selection of S-wave window is subjective and often lead to biased results. Teanby et al. (2004b) removed this subjectivity by incorporating a cluster analysis technique in SWS analysis.

The automation technique of Teanby et al. (2004b) performs splitting analysis for a range of windows around the S-wave and then applies a cluster analysis to find the Φ and δt values that are most stable over many different windows. The first step of the automation technique

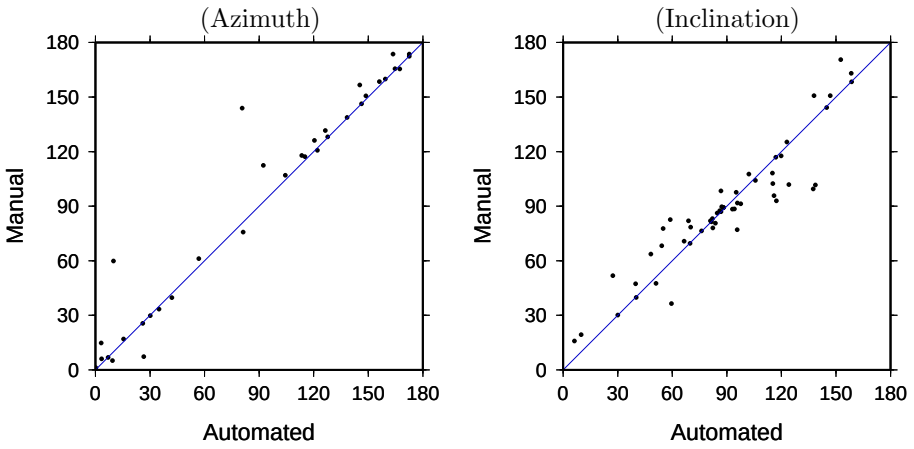

Figure 4.2: Comparison between manual and automated approaches when determining rotation angles to the ray frame. These measurements were obtained for a subset of events with clear impulsive P-wave arrivals.

is to construct a grid of analysis windows (multi-windows with different lengths). A schematic illustration of analysis grid is illustrated in Figure 4.3. The grid is set by choosing a starting window (extending from T_{beg_0} to T_{beg_1}) before the S-wave time pick (T_s) and an ending window (extending from T_{end_0} to T_{end_1}) after several S-wave cycles. The analysis window starts at T_{start} and ends at T_{stop}. T_{start} is allowed to vary with N_{beg} steps of Δt_{beg} between T_{beg_0} and T_{beg_1}. In a similar way, the end of the analysis window (T_{stop}) is allowed to vary between T_{end_0} and T_{end_1} with N_{end} steps of Δt_{end}. The two boundaries of the S-wave analysis window (T_{start} and T_{stop}) are defined by:

$$T_{start} = T_{beg_1} - (i-1)\Delta t_{beg} \qquad for: i = 1.....N_{beg} \tag{4.1}$$

$$T_{stop} = T_{end_0} + (j-1)\Delta t_{end} \qquad for: j = 1.....N_{end} \tag{4.2}$$

T_{beg_0}, T_{beg_1}, T_{end_0} and T_{end_1} are defined relative to T_s. The total number of analysis windows is $N{=}N_{beg}{\times}N_{end}$.

The splitting results from all windows will generally coalesce into clusters on a 2D plot of Φ against δt (Figure 4.4). The best cluster is chosen based on the number of points and the variance within the cluster. Finally, the optimum splitting measurement is the measurement with the smallest error from within the best cluster.

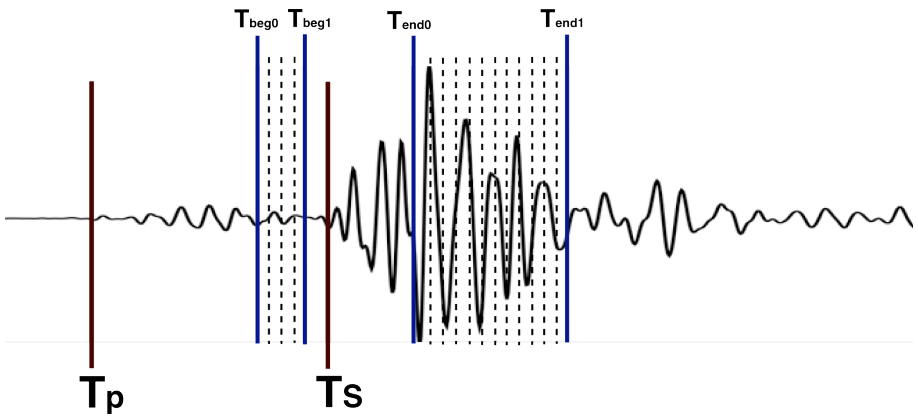

Figure 4.3: Grid of S-wave analysis windows. T_p and T_s mark the start of the P- and S-waves, respectively. The start of the analysis window is allowed to vary between T_{beg_0} and T_{beg_1} and, the end of the analysis window between T_{end_0} and T_{end_1}.

4.2.3 Choice of automation parameters

According to Teanby et al. (2004b), when choosing the automation parameters (N_{beg}, N_{end}, T_{beg_0}, T_{beg_1}, T_{end_0}, T_{end_1}, Δt_{beg} and Δt_{end}) the following guidelines must be considered:

- The analysis window should be representative of the S-wave and includes several periods of the dominant frequency to reduce the influence of noise and prevent cycle skipping. The window should include a minimum of one wavelength of the dominant period of the S-wave.
- The analysis window should not be so long as to include spurious secondary phases which appear later in the waveform. It also should not overlap with the P-wave. Inclusion of such phases will degrade splitting estimates.
- The results are often more stable when choosing the start of the window slightly before the onset of the S-wave. This also reduces cycle skipping effects.
- Large N and small Δt give the most detailed exploration of the window space. N_{beg} can be smaller than N_{end}, and Δt_{beg} can be larger than Δt_{end} because splitting measurements are usually more sensitive to the window end than the window start. However, large N requires more computational time.
- T_{beg_1} is chosen such that it starts slightly before the S-wave onset, by an amount greater than the S-wave pick (T_s) uncertainty.

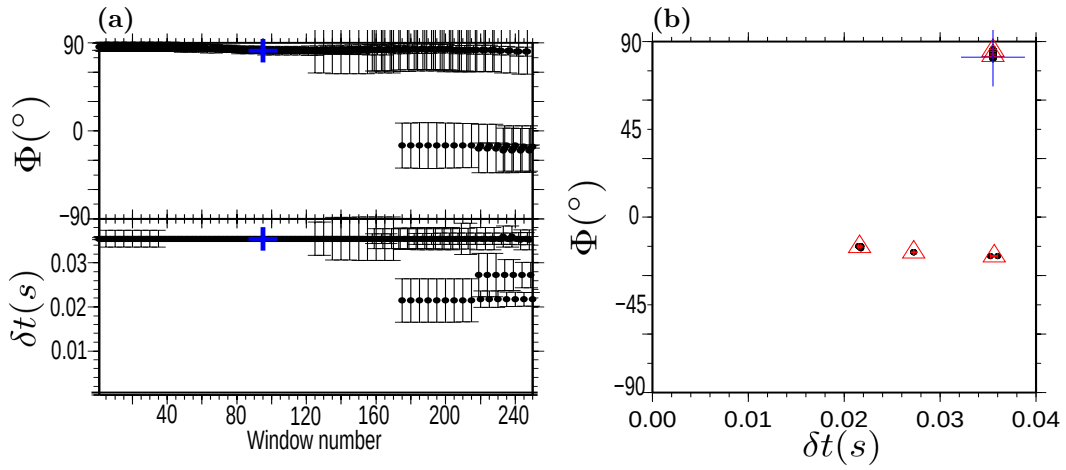

Figure 4.4: Shear-wave splitting cluster analysis. (a) Measurements of δt and Φ estimated from 250 different analysis windows. (b) 2D plot of Φ versus δt. The different measurements shown on (a) condense into tight clusters of points in (b). Clusters are automatically identified using cluster analysis (denoted by red triangles). The best splitting parameters are marked by blue crosses in both figures.

According to the work of ABB, the error in the S-wave arrival time picks is in the order of 5 ms for Field M dataset. Therfore, T_{beg_1} is set to be at 5 ms before T_s to account for the uncertainty in the time pick. T_{end_0} is set to be at 40 ms after T_s, corresponding to the maximum expected delay time. N_{beg} and N_{end} are set to be 5 and 50, respectively. I have tested two approaches to setting the S-wave analysis windows. In the first test I use fixed window parameters and in the second I use adaptive parameters as follow:

Test 1

In this test T_{beg_0} is chosen to be at 25 ms before T_s and T_{end_1} is chosen to be at 50 ms after T_s. The windows are kept small in length and only the first few cycles of the S-wave envelope are used in the splitting analysis.

Test 2

In the case of the Field M microseismic dataset, events have a wide range of hypocentral distances (D) ranging from tens of metres to few kilometers, causing significant variations in the P- and S-wave time pick separation (ΔT) and the S-wave envelope duration (t_{env}). In this test T_{beg_0} and T_{end_1} are chosen such that T_{beg_0} is at an appropriate length before T_s but does not overlap with P-wave arrivals and T_{end_1} is positioned at the end of the S-wave envelope. The time separation (ΔT) between P-wave onset (T_p) and T_s is a function of source-receiver distance (D). Figure 4.5a shows the variation of ΔT with D for the entire dataset. The relation between ΔT and D is linear and can be written as ΔT=0.3×D where ΔT is in ms and D in m. T_{beg_0} is chosen to be at $\frac{1}{4}\Delta T$

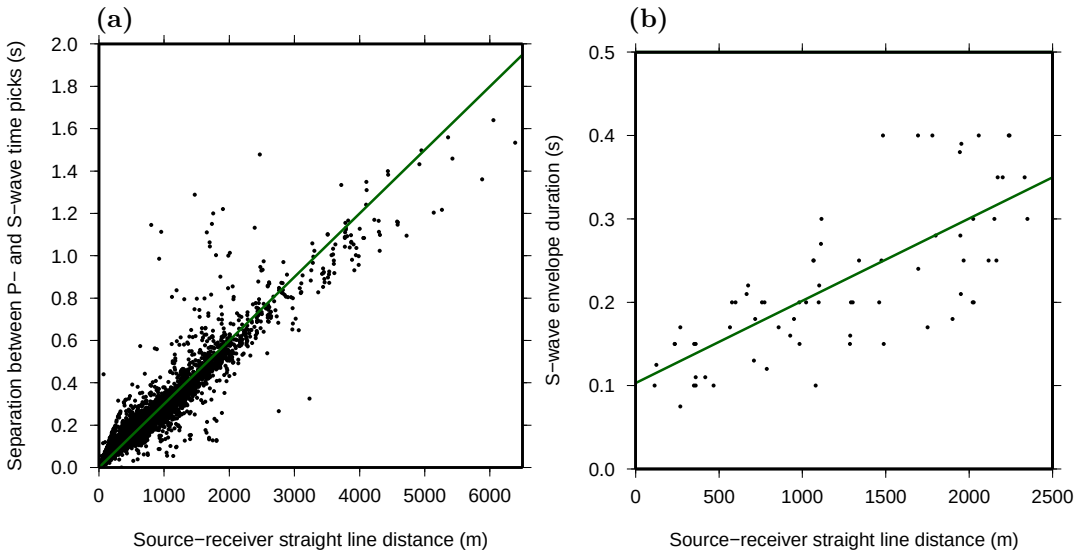

Figure 4.5: Variations of P- and S-wave onset separation and S-wave envelope duration with hypocentral distance. (a) Variation in the separation between P and S-wave time picks (ΔT) with the source-receiver straight line distance (D). (b) Variation of the S-wave envelope duration (t_{env}) with distance (D). Green lines are the best-fit straight lines.

before T_s. This gives a wide enough analysis window and avoids overlapping with the P-wave arrivals. However, when ΔT is less than 20 ms, T_{beg_0} is set to be at 5 ms before T_s which means it is the same as T_{beg_1}.

The S-wave envelope duration (t_{env}) is dependent on travel distance and frequency (Saito et al., 2002). In this test, for simplicity, I ignored the effect of frequency on envelope size and considered only the variation with D. I manually calculated the variation of t_{env} with D for various events with different hypocentral distances. The relation is illustrated in Figure 4.5b. When D exceeds 2500 m, secondary phases start appearing in the seismograms and it becomes difficult to accurately measure t_{env}. For events having hypocentral distances less than 2500 m, the relation between t_{env} and D is roughly linear and it can be expressed as t_{env}=0.098×D+103.26 where t_{env} is in ms and D in m. Hence, t_{env} as a function of ΔT in ms becomes t_{env}=0.327×ΔT+103.26. For events with D less than 2500 m, T_{end_1} is set to be at T_s+t_{env} to ensure that the whole S-wave envelope is encompassed in the splitting analysis. For events with D greater than 2500 m, T_{end_1} is set to be at 350 ms after T_s (corresponding to D = 2500 m). Also, converted P-wave phases are often observed for events with distances greater than 2500 m, thus T_{beg_0} is set to have a maximum of 188 ms before T_s. Any degradation in the results caused by the inclusion of phases other than the direct S-wave can be observed when inspecting the diagnostic plots.

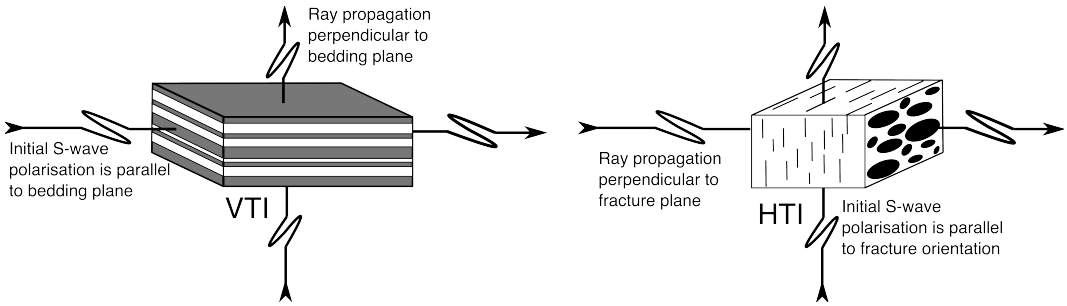

Figure 4.6: Examples of null SWS in the cases of VTI and HTI media. There is no splitting when the S-wave is polarised parallel to the bedding or fracture planes before entering the anisotropic medium. The second case is when the raypath is perpendicular to the bedding and fracture planes.

4.2.4 Quality of the splitting measurements

Automated quality control

Grading the results is a crucial step in SWS analysis, as generally less than 10% of the data give reliable results. In the approach to automating Field M SWS analysis, I use the eigenvalue method (EV) together with the cross-correlation method (XC). Both methods are automated using the cluster analysis technique of Teanby et al. (2004b). In the case of the Field M dataset, a grid search over $0< \delta t_{EV} \leq 40$ ms and $-90° \leq \Phi_{EV} \leq 90°$ is used with the EV method.

Wüstefeld & Bokelmann (2007) used the systematic differences in the outputs from the EV method (Φ_{EV} and δt_{EV}) and the XC method (Φ_{XC} and δt_{XC}) to classify the quality of the splitting measurements and to detect the so-called SWS null measurements. Null measurements occur either if the wave propagates through an isotropic medium or if the initial S-wave polarisation is (near-) parallel or perpendicular to the fast direction of anisotropy (Figure 4.6). In the case of nulls, the S-wave is not split into two components or one of the split S-waves is too weak to be observed. Wüstefeld & Bokelmann (2007) showed that both XC and EV methods give identical splitting parameters if the fast and slow polarisation axes are far away from null direction and they show a systematic deviation close to it. Figure 4.7 shows splitting parameter estimates for different angles relative to the null direction. δt_{XC} diminishes systematically in near null directions and Φ_{XC} shows deviation of about 45° compared to Φ_{EV}. In contrast, the EV method is relatively stable, except near null direction where it shows considerable scatter in results. Φ_{EV} deviates around $\pm 90°$ from the true fast polarisation axis and δt_{EV} shows considerable scatter often reaching the maximum value in the grid search. Null measurements can also result from low signal-to-noise ratio. This is because the S-waveforms are not clear (Wüstefeld & Bokelmann, 2007).

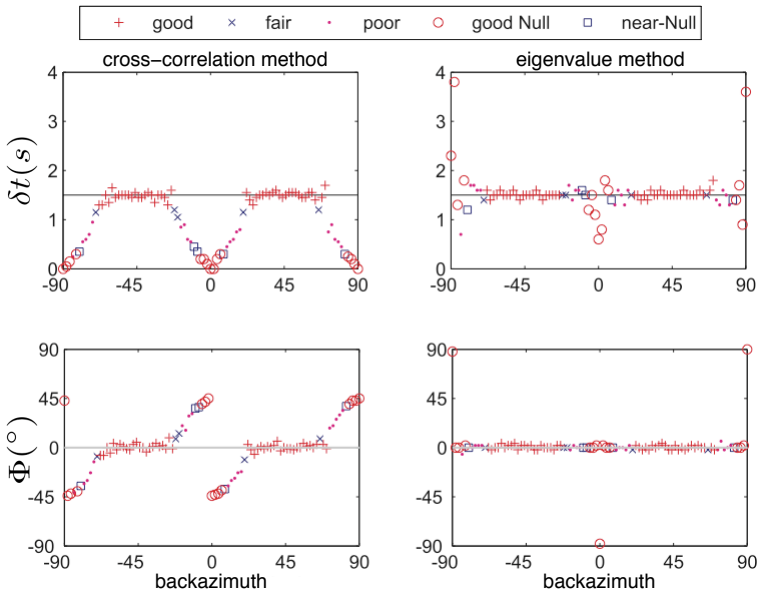

Figure 4.7: Behaviour of the XC and EV methods tested on synthetic seismograms. Upper panel illustrates variation in δt with backazimuth and lower panel shows estimates of Φ. The input δt and Φ are 1.5 s and 0°, respectively (indicated by horizontal lines). The EV method is stable over a wide range of backazimuths, whereas the XC method fails close to null directions. The systematic differences between the two method are used to classify the splitting results (after Wüstefeld (2007)).

The ratio between the delay time from the XC method to the delay time from the EV method ($R = \delta t_{XC}/\delta t_{EV}$) and the normalised misfit between the fast polarisation direction from the two methods (Ω=Φ_{EV}-Φ_{XC}/45°) are used to classify splitting measurements. R has a range between 0 and ∞, whereas Ω ranges between 0 and 1. Splitting measurements are classified as good, poor and good null based on the values of R and Ω. Ideal good measurements are characterised by both the XC and EV methods yielding identical Φ and δt estimates (i.e., R=1 and Ω=0). On the other hand, ideal good null measurements are characterised by δt_{XC}=0 (R=0) and misfit of 45° in Φ (Ω=1). When plotting Ω versus R, splitting measurements are typically distributed along the extreme points R=1 and Ω=1 (see Figure 4.11 later). The splitting measurement quality (q) is determined from how far it is from these two extreme points. Wüstefeld et al. (2010) defined d_{null} as the distance from the extreme point Ω=1 and d_{good} as the distance from the extreme point R=1 as follow:

$$d_{null} = \sqrt{2(R^2 + (\Omega - 1)^2)}$$

$$d_{good} = \sqrt{2((R - 1)^2 + \Omega^2)} \tag{4.3}$$

$$q = \begin{cases} -(1 - d_{null}) & : \quad for \quad d_{null} < d_{good} \\ (1 - d_{good}) & : \quad for \quad d_{null} \geq d_{good}. \end{cases}$$

The value of q ranges from +1 (good) to 0 (poor) to -1 (good null). Additionally, fair and fair-null quality categories can be defined subjectively to be close to the good and good null quality ranges, respectively. In Equation (4.3), distances greater than one are set to one, so they directly result in Q=0 which corresponds to poor measurement. When using the cluster analysis method as described in section 4.2.2, each single analysis window is assigned a quality measure (Q_{wind}). The final quality of the splitting measurement (Q) is computed using (Wüstefeld et al., 2010):

$$Q = \omega_1 \frac{\sum Q_{wind}}{N} + \omega_2 Q_{best}, \tag{4.4}$$

where Q_{best} is the quality of the best analysis window from the cluster analysis (see Figure 4.4), and $\omega_{1,2}$ are weighting factors. The values of ω_1 and ω_2 in Equation (4.4) and the ranges of Q defining each quality category are chosen empiricaly. For the case of Field M microseismic data, I chose ω_1 and ω_2 to be $\frac{1}{3}$ and $\frac{2}{3}$, respectively. I also define the ranges of each quality category as: good ($Q \geq 0.75$), fair ($0.75 > Q \geq 0.25$), poor ($0.25 > Q \geq -0.25$), fair null ($-0.25 > Q \geq -0.75$) and good null ($-0.75 > Q$). Figure 4.8 illustrates examples of good and null splitting measurements.

Diagnostic plot inspection

In addition to the automated quality control, I further classify the splitting measurements by inspecting the diagnostic plots from the EV method. The aim of this step is to validate the success of the automation. Splitting measurements are considered reliable by inspecting the output plots if:

- The S-wave is well defined and distinct from the P-wave.
- Energy on the corrected transverse component is minimsed.
- The fast and slow S-wave components have similar waveforms.
- The elliptical S-wave particle motion is linearised after the splitting correction.
- The grid search gives unique 95% confidence solution without any cycle skipping.

A measurement is classified as class A if it satisfies all the above five criteria and it is classified as class B if it meets only four of them. An observation is classified as class C if it fails to satisfy two or more of the constraints. Figure 4.9 shows an example of class A measurement.

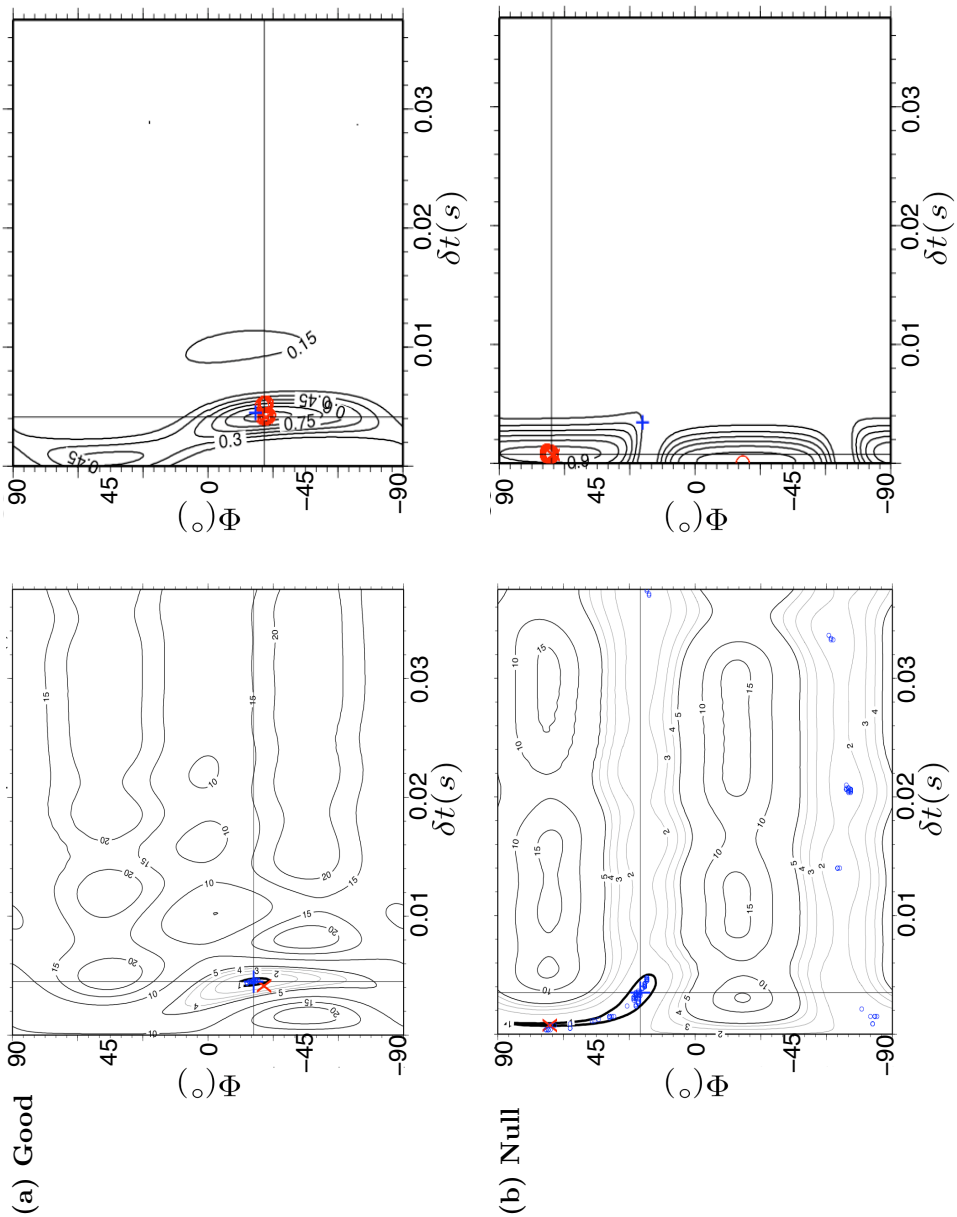

Figure 4.8: Examples of good and null splitting measurements. Left panel shows grid search over δt_{EV} and Φ_{EV} with the results from all analysis windows marked by blue circles. Right panel shows grid search over δt_{XC} and Φ_{XC} with the results from all analysis windows marked by red circles. For comparison, the best splitting measurement from the XC method is denoted by red cross in the left panel and the best splitting measurement from the EV method is denoted by blue plus sign in the right panel. The thick contour in the left panel is the 95% confidence interval calculated using an F-test. Note the tight clustering of measurements in (a) and the elongated 95% confidence interval in the null example (b).

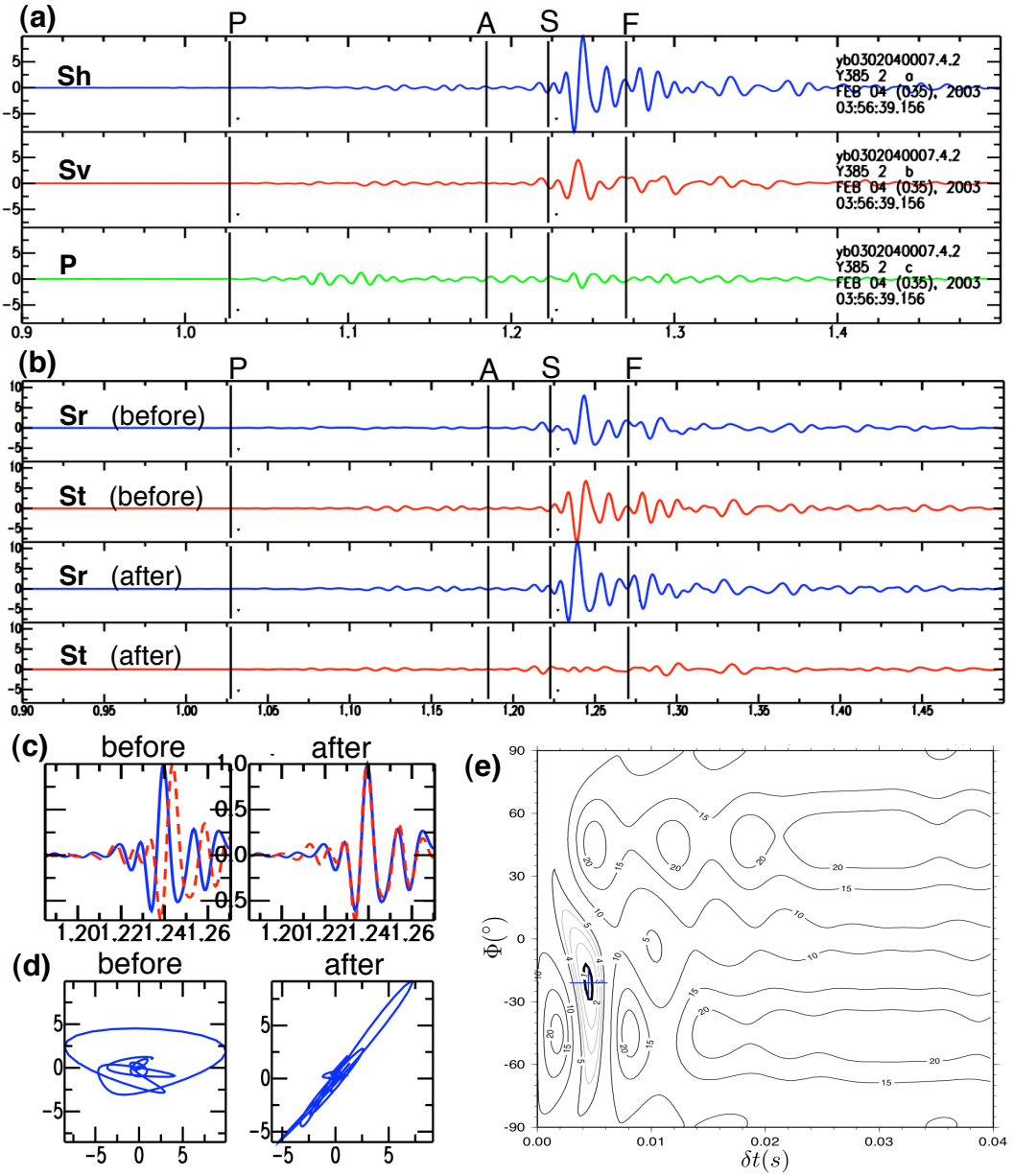

Figure 4.9: Example of class A splitting measurement. (a) Seismograms in ray coordinates (S_h, S_v and P) low pass filtered with a 100 Hz corner frequency. (b) Radial (S_r) and transverse (S_t) shear-wave components before and after splitting correction. (c) Fast and slow shear-wave components before and after splitting correction. (d) S-wave particle motion before and after splitting correction. (e) A grid search over Φ and δt. The blue cross is the solution and the thick contour is the 95% confidence interval. In (a) and (b), P is P-wave pick, S is S-wave pick and, A and F are the begin and end of the best S-wave analysis window determined from the cluster analysis.

4.3 Results

I analysed 3397 microseismic events acquired by a maximum of 13 stations deployed in 5 monitoring wells. The dataset provides 8545 splitting measurements. Figure 4.10 shows histograms of the measurement qualities. The first test, using fixed splitting window parameters, yields 3819 poor measurements and 474 good measurements. The second test, using adaptive splitting window parameters, yields 2772 and 736 poor and good measurements, respectively. The number of null measurements remains approximately the same for both tests. Obviously, the second test gives more good measurements and less poor measurements than the first test. Then, I visually examine the diagnostic plots of the results from the second test. Table 4.1 summarizes the results from the second test after the automated quality control and after the plot inspection. A plot of Ω versus R for the same results is shown in Figure 4.11.

Class	Good	Fair	Poor	Fair null	Good null
A	94	35	21	5	34
B	364	282	297	107	328
C	278	592	2454	612	2942

Table 4.1: Shear-wave splitting results of the second test with the adaptive splitting window parameters sorted into quality categories (good, fair, poor, fair null and good null) using the automated quality control and classes (A, B and C) using the manual plot inspection.

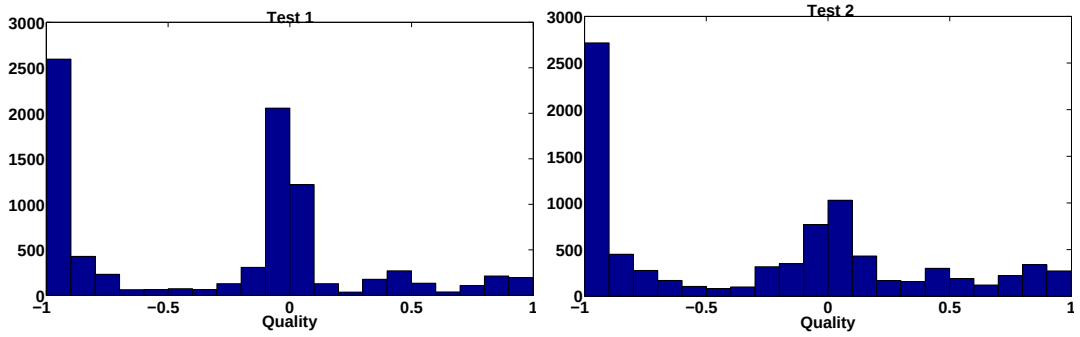

Figure 4.10: Histograms of measurements quality using the automated quality control for Test 1 (fixed window parameters) and Test 2 (adaptive window parameters).

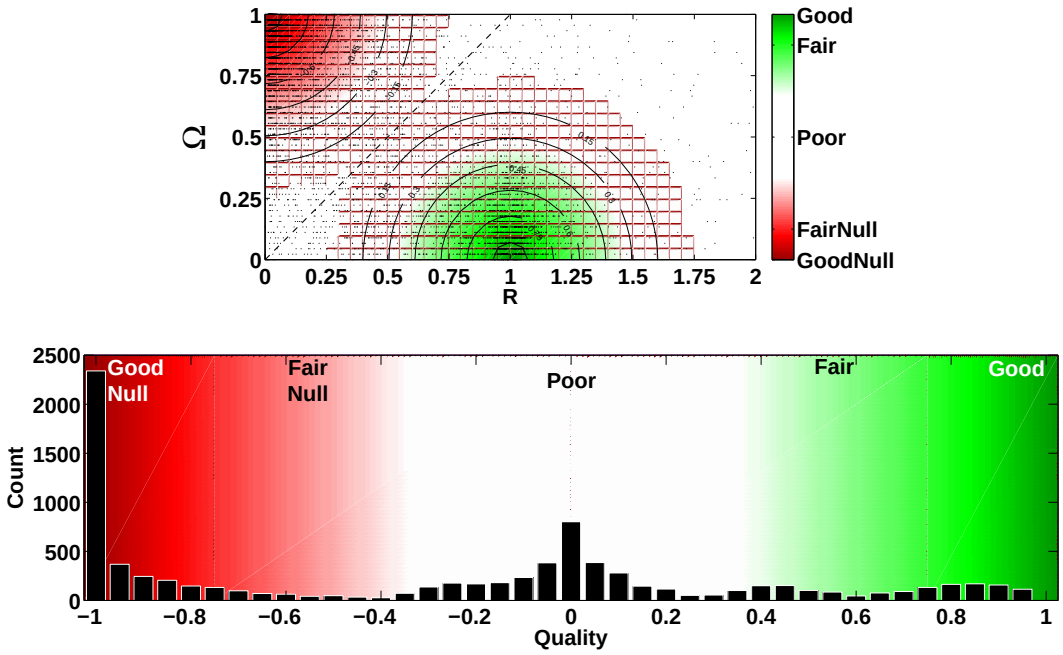

Figure 4.11: Distribution of splitting measurement qualities. [Top] Misfit of the fast-axis (Ω) against the delay time ratio (R) between the XC and EV methods calculated for the Field M microseismic dataset (total of 8545 measurements). [Bottom] Histogram of the splitting measurement quality distribution.

4.4 Discussion

Fixed versus adaptive automation parameters

The analysis of the S-wave coda revealed that the separation between the P- and S-wave onsets and the duration of the S-wave envelope correlate systematically with hypocentral distance. The quality of the splitting measurements improved significantly by using adaptive automation parameters (T_{beg_0} and T_{end_1}). The number of poor measurements decreased by 25% and the number of good measurements increased by 55%. For simplicity, I considered only the variation of S-wave envelope duration with distance and I ignored other factors like frequency. The method can be further improved by observing the S-wave envelope build-up and decay in a mathematical way (see for example Saito et al. (2002)). Moreover, ray tracing techniques can be used to predict when the secondary phases start contaminating the S-wave coda (see for example Guest & Kendall (1993)).

Automated versus manual quality control

In Table 4.1, 68% of class A measurements are in the categories good and fair, and 11% in the category poor. 89% of the poor measurements are of class C, but only 13% of the good measurements

are of class A. This implies that the approach is successful in detecting unreliable measurements. However, a final plot inspection remains necessary, but it can be limited to the good and fair measurements which account for only 19% of the total measurements. Figure 4.12 shows histograms of measurement quality (Q) for the results in the good category. It can be seen that class A results show a general increasing trend towards Q=1 and vice versa for class C results. I suggest that if the processed data are of good signal-to-noise ratio and the S-wave coda is clear enough or the data volume is very large, then the threshold of the good category (Q) can be shifted to be 0.8, or perhaps even 0.9, instead of 0.75. This would help making the process fully automated without the need to do the visual examination of the diagnostic plots. The same approach has been applied to a large microseismic dataset (about 40000 splitting measurements) from a mine in Australia in a fully automated way (A. Wüstefeld, Uni. of Bristol, pers. comm.). The mine dataset is of good signal-to-noise ratio and the S-wave coda is much more clear compared to the Field M dataset. Measurements with the highest quality (10% of the total) were considered reliable without conducting visual examination of diagnostic plots. In a similar way, Jones (2010) applied the approach to a microseismic dataset from the Ekofisk field in the North Sea. Also, Wüstefeld et al. (2010) applied the technique to the Valhall microseismic dataset and they were able to replicate the results of the manual approach of Teanby et al. (2004a).

Equation (4.4) allows characterising events with problematic S-wave windows by incorporating the quality of the best window (Q_{wind}) together with a mean quality from all analysis windows in the cluster analysis. Alternatively, one could omit the cluster analysis and define the best measurement simply as the one with the highest quality (Q), but such definition must exclude null measurements (Wüstefeld et al., 2010). Furthermore, the weighting factors ($\omega_{1,2}$) in Equation (4.4) can be adopted according to the quality of the dataset (e.g., how clear and impulsive is the S-wave coda).

In the case of the Field M dataset, measurements of class A that are in categories good and fair are considered reliable (Table 4.1). Measurements in category good but classified as class B are also considered reliable as they show high tendency towards Q=1 (Figure 4.12). In addition, splitting measurements are only accepted if they have error of less than 10° in Φ and error of less than 2 ms in δt.

Null measurements

The other advantage of the automated approach is the detection of null measurements. In particular near-null observations could be mistaken for reliable anisotropy measurements. For instance, in

Table 4.1 21% of class A measurements are in reality null measurements. The null measurements possess valuable information about the anisotropic symmetry of the medium. However, they need to be interpreted carefully because null measurements can be also due to low signal-to-noise ratio or the case where the polarisation of the fast or slow S-wave component coincides with the initial source polarisation direction.

Figure 4.13 illustrates the distribution of Q against the difference between the initial source polarisation and Φ. It can be seen that the technique is overall successful in detecting null measurements. Reliable measurements require separation of more than 20° from the null direction (Figure 4.13). The large number of null measurements in Field M dataset can be attributed to the low signal-to-noise ratio in most cases which is visible when performing the diagnostic plot inspection. It also can be due to the waveform dissimilarity of the fast and slow split S-wave components. Slow split S-waves are observed to be more attenuated and less impulsive than fast split S-waves (Crampin & Gao, 2006). In Chapter 2 we have seen that the Natih formation is populated with fractures. Heavy fracturing can cause high attenuation to the slow shear-waves, rendering them difficult to detect (Mueller, 1991; Kendall & Kendall, 1996).

Perhaps, one can further classify null measurements into: noise nulls, nulls due to isotropic medium and nulls due to proximity to null direction (see also Wüstefeld et al. (2010)). Figure 4.13 can be used as a guide. However, this is outside the scope of this study, thus I ignore the null measurements.

Examining the filtering effect on anisotropy magnitudes

The automated technique allows allows testing many input parameters quickly. Here, I test changing the filter used prior to the analysis and how it affects the final estimates of anisotropy. The percentage difference between the fast and slow shear-wave velocities along the raypath (δV_s) is computed using $(100 \times V_{s(avg)} \times \delta t)/\mathrm{D}$, where D is the straight line source-receiver raypath and $V_{s(avg)}$ is the average S-wave velocity along D based on the 1D velocity model of the field (Figure 3.4). The anisotropy is assumed to be averaged uniformly over D. When interpreting anisotropy, magnitudes of δV_s are plotted at the source-receiver mid-points.

Al-Abri (2003) and Al-Anboori (2006) low pass filtered the data with a corner frequency of 100 Hz prior to SWS analysis, when they used subsets of Field M microseismic dataset. However, close inspection of the S-wave frequency content reveals that the dataset has a broader S-wave frequency bandwidth, which mostly ranges from 10 to 200 Hz and it can reach up to 400 Hz (this is discussed in more detail in Chapter 7). Figure 4.14 illustrates the dominant S-wave frequency

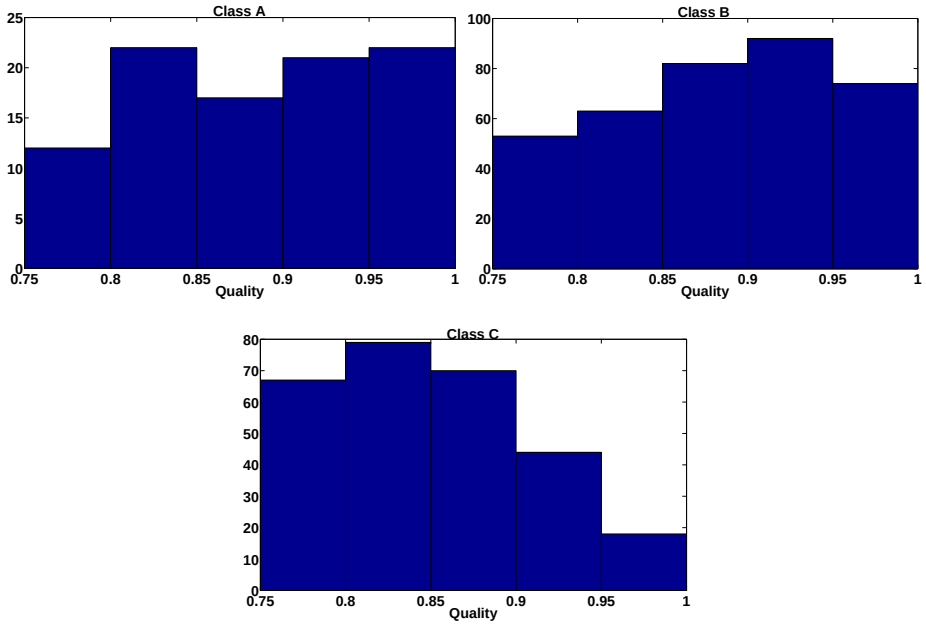

Figure 4.12: Comparison between manual and automated quality controls. Histograms show the quality distribution of the good results ($Q \geq 0.75$) for classes A, B and C (see Table 4.1).

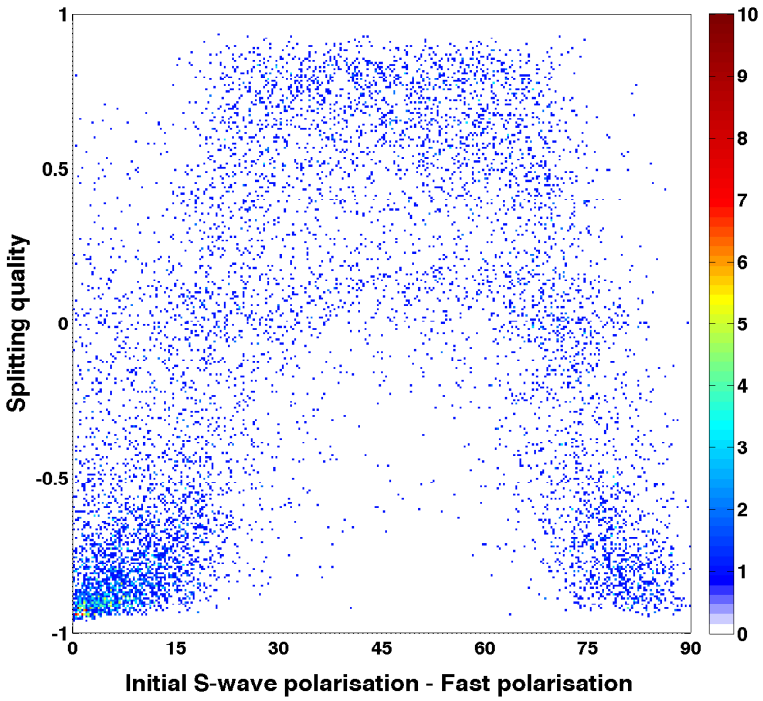

Figure 4.13: Density map of splitting quality versus difference between initial source polarisation and fast S-wave polarisation (Φ) for the Field M dataset. Colour indicates density of measurements.

for the cases when using 100 Hz and 200 Hz low pass filters. For the case of a 100 Hz filter the dominant frequency has a skewed distribution. In contrast, the dominant frequency has Gaussian-

like distribution centred around 110 Hz for the case of 200 Hz filter. Thus, I repeat the same automation workflow described above but using data low pass filtered with a 200 Hz low pass filter to examine the effect on the magnitudes of δV_s.

This time I limited the plot visual examination to the measurements in the quality categories fair and good. Figure 4.15 shows the variation of δV_s with distance for results from both filters. It can be seen that generally the magnitudes of δV_s are less when using a 200 Hz low pass filter than when using a 100 Hz low pass filter, especially for short distance events ($D<$ 500 m). Events with short hypocentral distances often have a dominant frequency above 100 Hz (less attenuated compared to distant events). When these seismograms are filtered with a 100 Hz low pass filter (harsh filter), the S-wave signal is partly destroyed and the waveform becomes more sinusoidal-shaped, resulting in a relatively large δt. Moreover, filtering below 100 Hz introduces the effect of frequency-dependent anisotropy (described with more details in Chapter 7) which should be avoided at this stage. Hence, I use the results from the second test with the 200 Hz low pass filter for subsequent interpretation in Chapter 5. Additionally, magnitudes of δV_s over 20% are considered unreliable as the maximum δV_s observed in a nearby field, with similar lithological column, using 3D-9C data is approximately 20% (Potters et al., 1999).

The effect of filtering prior to the SWS analysis has been also addressed by Vecsey et al. (2008) using teleseismic data and by Wüstefeld et al. (2010) using microseismic dataset from the Valhall oil field in the North Sea. Both references highlighted the importance of using a proper filter prior to the SWS analysis to avoid biased results.

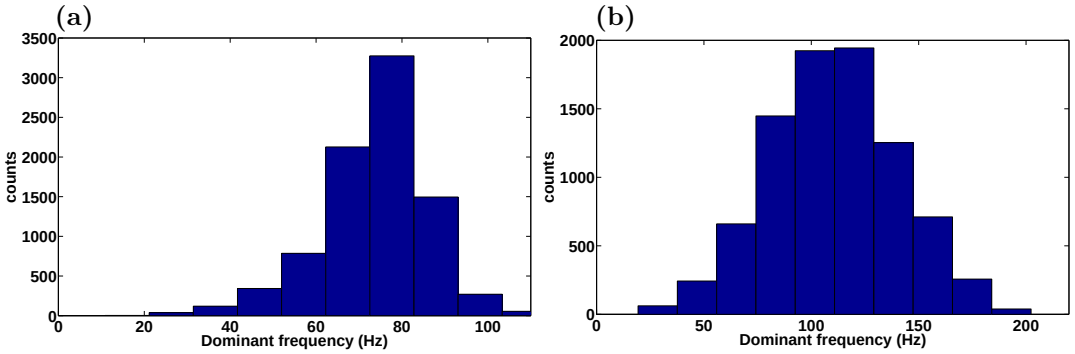

Figure 4.14: Histograms of dominant S-wave frequency for the cases when using (a) 100 Hz low pass filter and (b) 200 Hz low pass filter. The majority of the data show dominant frequency around 110 Hz, thus the use of 200 Hz low pass filter is more appropriate.

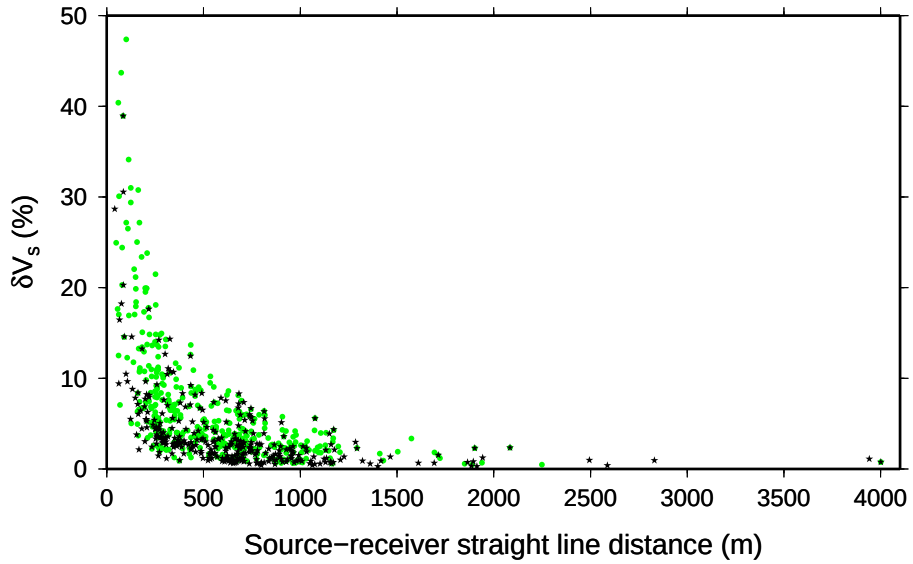

Figure 4.15: Variation of δV_s with distance when low pass filtering the data using a corner frequency of 100 Hz (green circles) and 200 Hz (black stars). Generally, the anisotropy is higher and the scatter is more when filtering the data with 100 Hz filter compared to 200 Hz filter, especially for the first 500 m.

4.5 Conclusion

I have presented a complete workflow for automating the SWS analysis of large microseismic datasets. I have shown the importance of using adaptive window lengths when using the cluster analysis technique when solving the subjectivity of choosing the S-wave analysis window. The suggested automated quality control has the probability of being fully automated, depending on the clarity of the S-wave coda and the signal-to-noise ratio. For noisy datasets with complex waveforms (e.g., Field M dataset), the automated quality control helps limit the manual visual examination of the diagnostic plots to measurements in quality categories good and fair. The other advantage of the approach is the detection of so-called null measurements. Human interaction is usually not capable of distinguishing between reliable and null measurements. The automated approach can be applied to other microseismic datasets including those acquired from mines, geothermal fields and volcanoes or datasets from local and global earthquakes.

I have also shown the importance of using the right filter prior to SWS analysis. A poor choice of filter can result in the introduction of noise or destruction of the S-wave signals, consequently yielding biased splitting results.

5
Spatial and temporal variations of anisotropy

5.1 Introduction

In Chapter 4 I described the approach used to automate the shear-wave splitting (SWS) analysis of the Field M microseismic dataset. In this chapter I explain how to use the splitting parameters, fast shear-wave polarisation direction (Φ) and delay time (δt), to describe and quantify anisotropy in Field M. δt is normalised by the raypath length to yield the percentage difference between the fast and slow shear-wave velocities along the raypath (δV_s) (see section 4.4 in Chapter 4). The anisotropy is interpreted in terms of aligned fractures or cracks superimposed on an intrinsic VTI rock fabric. The anisotropic symmetry strike and dip can be estimated from Φ. In contrast, δV_s provides information about fracture density or strength of sedimentary fabric. It should be noted that each δV_s value describes seismic shear-wave anisotropy in a certain ray propagation direction. The medium's overall anisotropy can be then estimated by averaging δV_s measurements from different ray propagation directions. Also, the splitting is assumed to be uniformly averaged along the raypath. Thus, the δV_s values should be considered as minimum estimates of anisotropy in the direction of propagation, and the anisotropy may be more concentrated in certain regions along the raypath.

In Chapter 2 we have seen that the Natih A and Shuaiba are highly fractured carbonate reservoirs. Therefore, the anisotropy caused by the HTI symmetry is expected to be dominant over the background intrinsic anisotropy of the rocks. Consequently, in the carbonate rocks the obtained δV_s measurements will reflect fracture density and Φ will describe fracture orientations. The cap rock shales (the Fiqa and the Nahr Umr) are expected to exhibit VTI symmetry due to mica alignment. However, usually it is not that simple to make such assumptions because hydrocarbon reservoirs are very dynamic and complicated environments, and as such the observed SWS will be the bulk effect of past and present geological and geomechanical processes.

Prior to the interpretation I perform synthetic modelling to predict SWS response in some rock models embedded with cracks and sedimentary fabric. The results from the modelling are used to guide the interpretation of the real data. Then, I investigate the spatial distribution of anisotropy

in Field M and how it varies with location and lithology. I also study the temporal variation of anisotropy and how it is linked to the stress changes caused by gas production from the Natih A reservoir.

5.2 Shear-wave splitting modelling

Due to the variety of causes of anisotropy (described in Chapter 1), the interpretation of SWS results is not easy and can be non-unique. Estimating SWS with downhole-recorded microseismic data is more complicated than in teleseismic earthquake SWS analysis (e.g., Kay et al., 1999; Wüstefeld et al., 2010). In this section I predict SWS in different rocks using rock physics modelling. The models mainly focus on the seismic response due to the inclusion of vertical cracks and horizontally-aligned sedimentary fabrics. I consider the cases of a single crack set, two crack sets, VTI sedimentary fabric and superposition of a single crack set and VTI sedimentary fabric. Modelling is crucial prior to the analysis of real data in order to understand the limitations in SWS analysis. It also helps in distinguishing between fracture-induced anisotropy and the intrinsic anisotropy of rocks.

5.2.1 Model building

I follow the approach outlined by Verdon et al. (2009) to build a series of rock physics models. For each model the full stiffness tensor is computed in order to model SWS in any direction of ray propagation. First, the isotropic tensor of the background rock is built and then the compliance of the fractures is added to the rock frame compliance using the method of Schoenberg & Sayers (1995)(see also Hall & Kendall, 2003, in appendix). The effects of sedimentary fabric can be added to the rock frame compliance in a similar way. I model the fracture compliance using the low frequency approximation for a penny shaped fracture set in matrix of equant porosity (Pointer et al., 2000), where the key variables are the crack density (ξ) and strike (α). This approximation is appropriate because the dominant frequencies in the data range mainly from 50 to 150 Hz. I also assume high permeability medium. A transient wave at low frequency can induce differential compaction on the fracture and pore space. In highly permeable rock the associated pore pressure gradients are accommodated by fluid flow. The high permeability assumption might not be true for carbonate reservoirs. However, I made it to focus on the key first order parameter, ξ, and avoid the need to consider other parameters to which SWS is less sensitive, like fracture aperture

(Verdon et al., 2009). I use a P-wave velocity of 3500 ms^{-1}, an S-wave velocity of 1800 ms^{-1} and a rock density of 2400 kg/m^3 when building the isotropic rock frame. I assume ξ of 0.05 for each set of vertical cracks and a crack aspect ratio of 0.001. The rock physics modelling approach is explained in further detail when performing SWS inversion in Chapter 6, section 6.2.

After computing the elastic stiffness tensor, I solve the Christoffel equation to calculate δV_s and Φ for different propagation angles. To better understand the results I display the output from the modelling using lower-hemisphere projection plots (Figure 5.1). The calculated Φ in the ray frame is then mapped into the geographic (east-north-vertical) frame to yield two parameters, strike and dip, that describe the orientation of the fast shear-wave polarisation in 3D. The azimuthal variations in δV_s, fast strike and fast dip are illustrated for ray inclination angles of 0°, 30°, 60° and 90° from vertical (Figure 5.2).

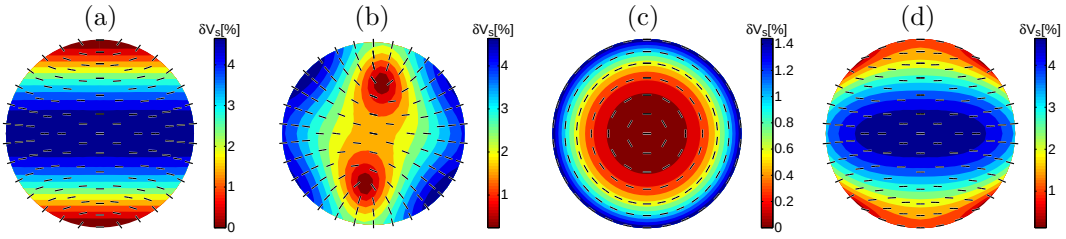

Figure 5.1: Shear-wave splitting in synthetic rock models. Lower-hemisphere projection plots of δV_s and fast shear-wave polarisation for the cases of (a) single crack set striking E-W, (b) two crack sets having strikes of 55° and 135°, (c) VTI medium and (d) VTI medium with a single crack set striking E-W. Horizontally propagating rays are plotted at the perimeter, whilst vertically propagating rays are plotted at the centre. The magnitude of δV_s is indicated by colour and the fast shear-wave orientations are denoted by the orientation of the black bars.

5.2.2 Synthetic models

Isotropic medium with a single set of cracks

The lower-hemisphere projection plot of SWS for the case of a single vertical crack set with an E-W strike is shown in Figure 5.1a. Maximum amounts of δV_s are encountered when rays travel parallel to the crack plane and reach a minimum when rays travel perpendicular to the crack plane. Thus, the azimuthal variation of δV_s can be used to estimate crack strike in HTI media. This is clearly illustrated in Figure 5.1a and in Figure 5.2a in the case with a 90° ray inclination. The estimated fast strike recovers the crack strike (90°) very accurately except for the case of horizontal ray propagation (Figure 5.2b). In contrast, the fast dip retrieves the crack dip accurately when

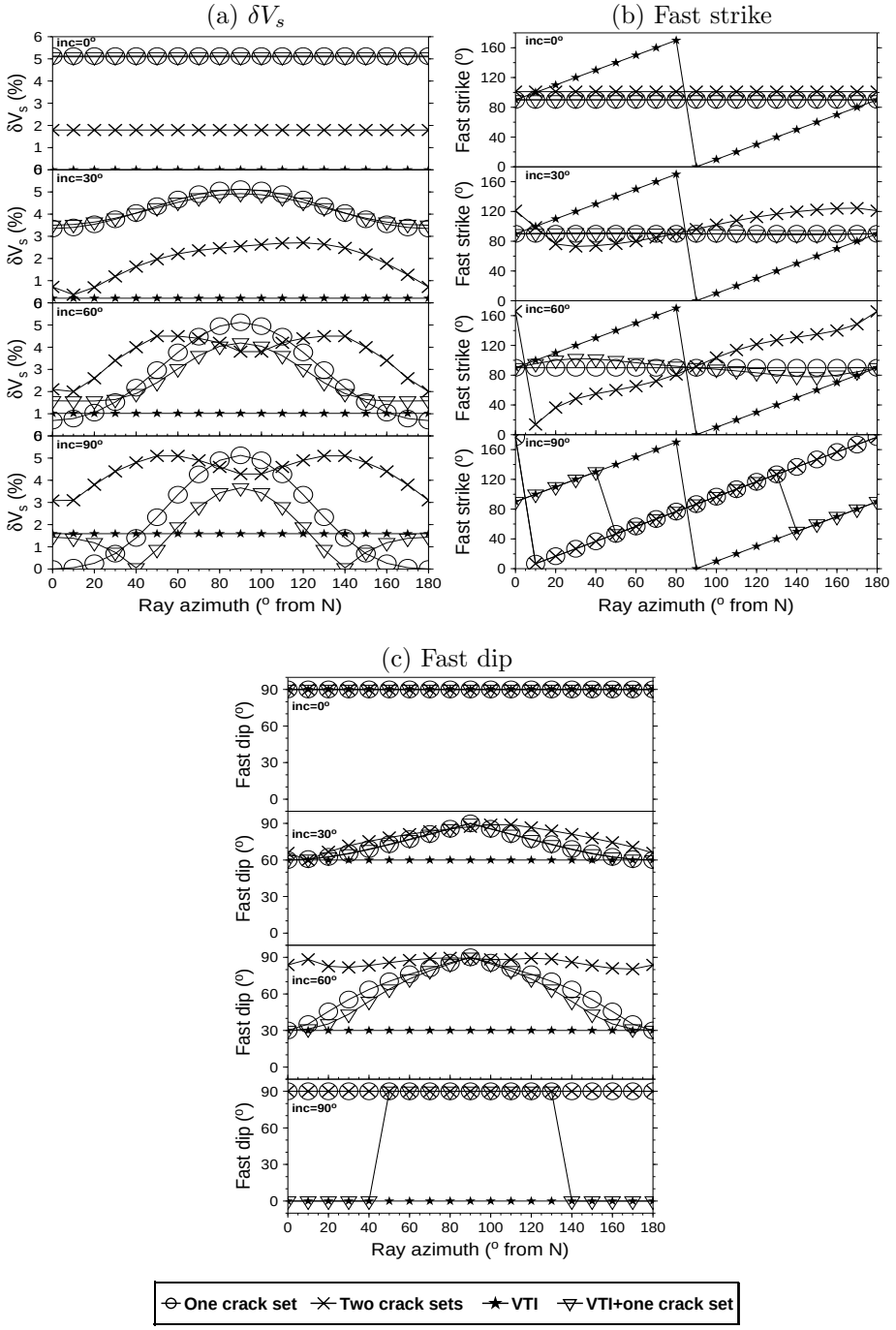

Figure 5.2: Azimuthal variations in (a) δV_s, (b) fast strike and (c) fast dip for the cases of single crack set, two crack sets, VTI and VTI plus one crack set (see Figure 5.1). The variations are presented for 0°, 30°, 60° and 90° inclination angles from vertical. Fast strike is measured from north and fast dip from horizontal.

rays travel horizontally. The estimated fast dip is always at 90° from horizontal for ray inclination of 0° because the S-wave fast plane is always dipping vertically in the case of normal incidence.

Isotropic medium with two sets of cracks

In this model, I consider a monoclinic medium formed by two vertical crack sets having strikes of 55° and 135° embedded in an isotropic background. Both crack sets have crack density of 0.05. The lower-hemisphere projection plot is shown in Figure 5.1b. The azimuthal variations of δV_s, fast strike and fast dip are displayed in Figure 5.2. The interpretation of the results from the model with two crack sets is more complicated compared with the case of single crack set. The low amounts of δV_s encountered by subvertical rays can be explained by the geometry of the two crack sets being almost orthogonal with identical crack density. Thus, the split S-waves polarised in any arbitrary orthogonal directions in the horizontal plane sense similar physical properties leading to low δV_s. For subhorizontal rays in Figure 5.2a, the azimuths where δV_s shows peaks correlate well with the two crack strikes (55° and 135°). Therefore, similar to the case of HTI media above, the azimuthal variation of δV_s can be used to estimate crack strikes in monoclinic media. Rays travelling at normal incidence reveal a crack strike of 95°, which lies between the two strikes of the crack sets (Figure 5.2b). This agrees with the prediction of Liu et al. (1993) and MacBeth (1996), that the fast strike is given by the crack-density-weighted average direction between the conjugate sets in monoclinic media. The two crack strikes can be roughly recovered in the case of 60° ray inclination, but within about ±10° ray azimuth from the true crack strikes (Figure 5.2b). Similar to the case of a single crack set, the crack dip can be only accurately recovered for rays travelling subhorizontally (Figure 5.2c).

VTI medium

Here, I study the seismic response purely due to the inclusion of sedimentary fabrics that cause a VTI symmetry. For illustration, I assume a weak rock intrinsic anisotropy having a magnitude of about 30% of the magnitude of anisotropy caused by a single crack set. In terms of Thomsen's parameters (Thomsen, 1986), the VTI medium has γ of 0.02 and δ of 0.04. The variation in SWS character of the VTI medium is displayed in Figure 5.1c. The azimuthal variations of δV_s, fast strike and fast dip are shown in Figure 5.2. The estimated δV_s and fast dip are dependent on ray inclination. δV_s gradually increases from zero at vertical incidence to maximum in horizontal direction (Figures 5.1c and 5.2a). The estimated fast strike is meaningless and it remains perpendicular to the propagation direction for all incidence angles (Figure 5.2b). The dip of the fast shear-wave

due to the sedimentary fabric (0° in this case) can be recovered accurately using horizontal rays (Figure 5.2c). The accuracy in estimating this dip decreases as the ray inclination varies from horizontal to vertical.

VTI medium with a single crack set

In this model I superimpose a single crack set striking E-W onto the previously described VTI medium, yielding a superposition of HTI and VTI symmetries (orthorhombic). The seismic response is shown using lower-hemisphere projection plot in Figure 5.1d. The variations of δV_s, fast strike and fast dip with azimuth are illustrated in Figure 5.2. The vertically propagating S-waves are not affected by the inclusion of sedimentary fabric, but rather by the alignment of cracks. The opposite occurs when rays travel horizontally and perpendicular to the crack strike orientation, where the SWS is caused by the sedimentary fabric. The contribution from the sedimentary fabric on the overall δV_s increases with the increase in the ray inclination from vertical (Figure 5.2a). The crack strike (90°) can be recovered accurately from the estimates of fast strike, but the accuracy decreases with the increase of ray inclination (Figure 5.2b). The fast strike becomes meaningless for horizontal rays. The crack dip can be retrieved from the estimates of fast dip using horizontal rays but with ray azimuths close to the true crack strike (i.e., ray azimuth of 90°±45° for this model). In contrast, the sedimentary fabric dip can be recovered using estimates of fast dip but for ray azimuths away from the true fracture strike (Figure 5.2c). Note that in this model the contamination of VTI anisotropy is relatively moderate (a VTI/HTI ratio of roughly 1/3). The observed variations in δV_s, fast strike and fast dip will change with the increasing strength of sedimentary fabric, but the model established some rules of thumb that can be used for interpretation purposes.

5.2.3 Guidelines from modelling

The successful identification of the nature of anisotropic media is highly dependent on ray coverage. Good ray coverage in the horizontal and vertical planes is required in order to distinguish between HTI and VTI symmetries, and single or multiple crack sets. In HTI media, δV_s, fast strike and fast dip are dependent on ray azimuth and inclination, whereas in VTI media the three variables are only dependent on ray inclination.

In HTI media caused by the alignment of cracks, vertically travelling rays can be used to recover crack strike and horizontally propagating rays can be used to retrieve crack dip. Al-Anboori (2006) showed that for HTI medium with about 40% VTI background contamination, the fast strike can

be reliably used to recover crack strike for ray inclinations up to 60°. In similar way, rays travelling within ±15° from horizontal are useful to reliably estimate crack dip. For horizontally propagating rays in HTI and monoclinic media caused by aligned cracks, the number of azimuthal peaks in δV_s indicates the number of crack sets and the corresponding azimuths can be used to estimate their strikes.

5.3 Results

I analyse 3397 located events covering a period of 457 days. The data were recorded using 13 stations with known tool orientations, yielding 8545 splitting measurements. Out of 8545 source-reciver combinations there are 325 reliable measurements (∼4%), after using the quality controls outlined in Chapter 4. Unfortunately, there are no SWS measurements available for the Nahr Umr shale and Shuaiba oil reservoir. Thus, the subsequent analysis and interpretation will be limited to the Fiqa shale and the Natih carbonate formation.

Figure 5.3 shows ray coverage in the vertical and horizontal planes. There is a good azimuthal coverage with a poor coverage in the vertical plane. The majority of the rays travel subhorizontally. Since fracture dip is estimated using rays travelling subhorizontally (±15° from horizontal) and fracture strike is estimated using rays travelling subvertically (up to 60° from vertical), fracture dip is much better constrained than fracture strike.

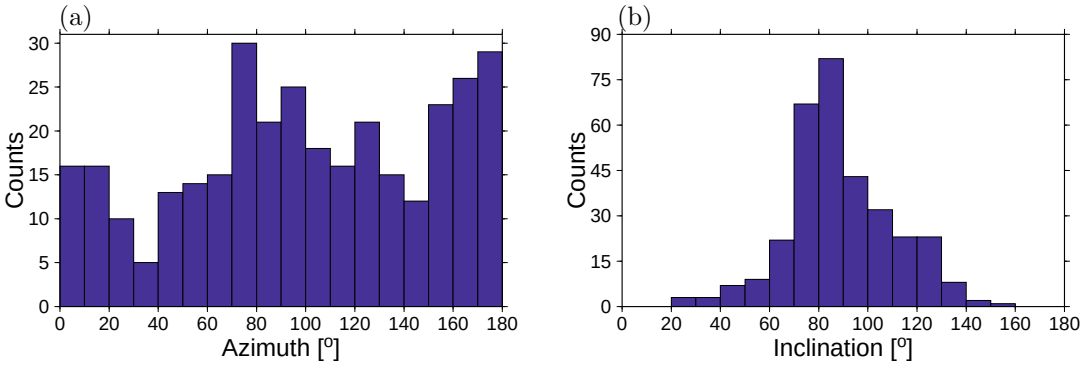

Figure 5.3: Horizontal and vertical ray coverage of the reliable splitting measurements. (a) Azimuth from north calculated assuming straight source-receiver raypath. (b) Inclination from vertical (up) calculated assuming straight source-receiver raypath. There is a good azimuthal coverage but poor vertical coverage.

5.4 Spatial variation of anisotropy

In this section I explore the spatial variations in the SWS results within Field M. I first analyse the results from the entire dataset. Then, I subdivide the results into groups by confining source-receiver paths into blocks, clusters and lithologic units.

5.4.1 Entire dataset

Histograms of δt and δV_s are displayed in Figure 5.4. δt ranges between 0 and 34 ms which corresponds to δV_s generally ranging from 0% to 10% with a maximum of 18%. Figure 5.5a shows δV_s as a function of azimuth and inclination. δV_s together with fast shear-wave polarisation direction are plotted in Figure 5.5b using a lower-hemisphere projection plot. Generally, vertically propagating rays encounter higher magnitudes of anisotropy (average 5%) than horizontally propagating rays (average 3%), which probably means that an HTI symmetry is more dominant than a VTI symmetry (see Figure 5.1).

The magnitudes of δV_s are displayed in Figure 5.6 in both a map view and in a NW-SE cross-section across the main graben faults. To better illustrate the spatial variation in anisotropy the estimates of δV_s are gridded and displayed in Figure 5.7. In general, δV_s decreases from about 3-10% in the SE part of the field and close to the eastern-most graben fault to about 2% in the NW flank, but there are considerable variations on a more localised scale. These localised variations are investigated later when subdividing the results into smaller groups. Figure 5.8 shows the variation in δV_s with depth. Anisotropy is weak to moderate in the Fiqa shale. The highest anisotropy magnitudes are in the gas producing Natih A reservoir. The lowest amounts of anisotropy occur within the Natih B-G2 formation.

Similar to what I have done in the synthetic modelling, the estimates of Φ in the ray frame are mapped into the geographic (east-north-vertical) frame to yield the fast shear-wave polarisation strike and dip. When estimating the fast strike and dip, I calculate the average of those angles forming clear peaks in rose diagrams and histograms, respectively.

A rose diagram of the fast strike is depicted in Figure 5.9a. There are three predominant fast strike orientations: NE-SW (43°), ENE-WSW (74°) and NW-SE (117°). Figure 5.9b displays an example of azimuthal variation of anisotropy for the data from 120°±15° inclination. The two peaks of δV_s coincides roughly with the two predominant fast polarisation strikes: NE-SW and NW-SE (Figure 5.9a). The spatial variation in fast strike is shown in Figure 5.10 using cross-section

and map view. Most of the fast strike orientations correlate very well with the major fault trends. The measurements close to and between the two main graben faults show fast strike orientation consistent with the NE-SW trend of the graben system, especially those close to monitoring wells 2 and 5. In contrast, the fast strike orientation either side of the graben agrees with the NW-SE trend of the minor faults located either side of the main graben system (see Figure 2.2 in Chapter 2).

A histogram of the fast dip is shown in Figure 5.11. The fast dip ranges mostly between 50° and 90° with the average being near-vertical (69°). The fast dip orientations are illustrated in depth section in Figure 5.12. The same measurements are displayed in NW-SE and SW-NE cross-sections in Figure 5.13. The fast dip is subvertical in all the lithology units except the deep Natih B-G2 unit which shows a more subhorizontal fast dip.

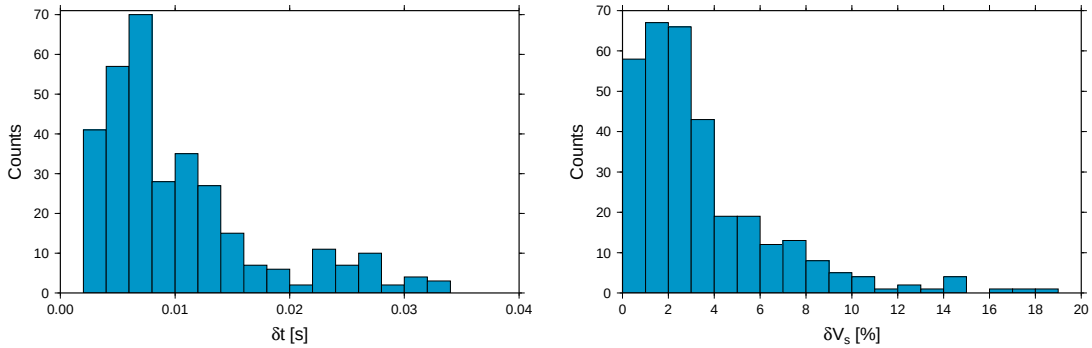

Figure 5.4: Histograms of δt and δV_s for the entire dataset (325 splitting measurements).

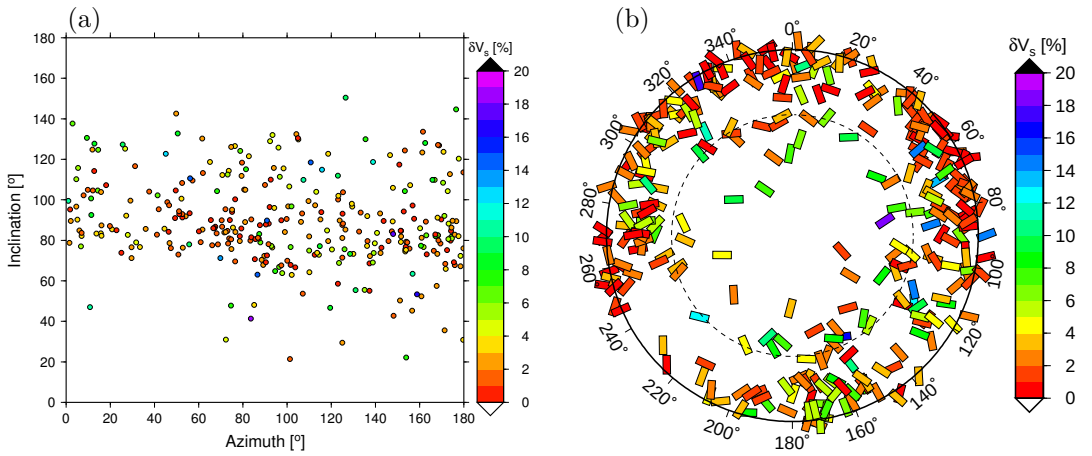

Figure 5.5: Directional variation of anisotropy. (a) Plot of δV_s as a function of ray inclination and azimuth. (b) Plot of δV_s and fast shear-wave polarisation orientation using lower-hemisphere projection. In (b), vertically propagating rays are plotted at the centre and horizontally propagating rays are plotted at the perimeter. The colour of the small rectangles represents δV_s magnitude whereas their long axis orientation indicates fast shear-wave polarisation. The dashed circle marks the 60° ray inclination angle. Generally vertically propagating rays encounter higher anisotropy than horizontally propagating rays. In both figures, the horizontal ray coverage is better than the vertical ray coverage.

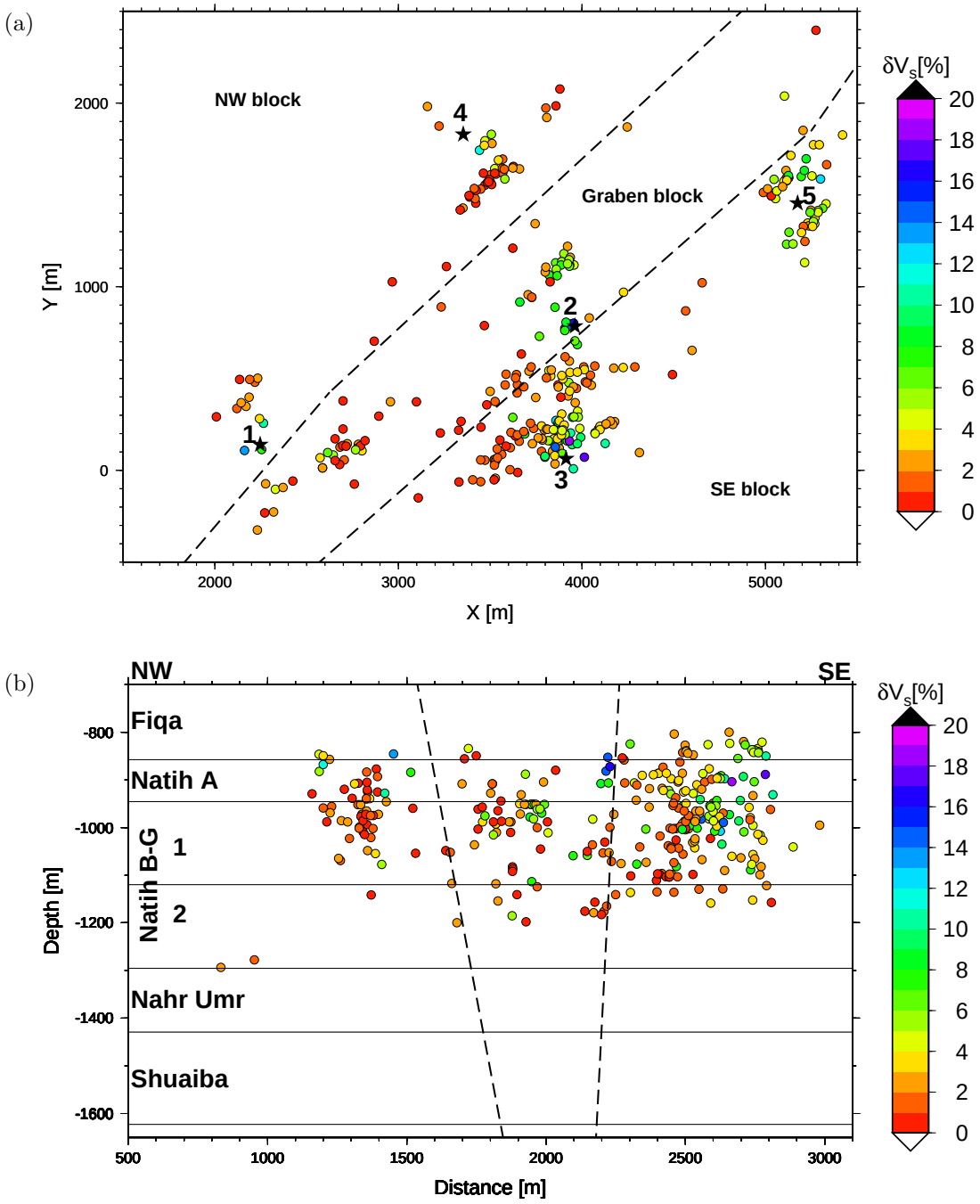

Figure 5.6: Spatial distribution of Field M anisotropy. Estimates of δV_s are plotted at source-receivr mid-points. (a) Map view and (b) NW-SE cross-section cutting the major graben faults and oriented at 45° clockwise from east. Faults are shown by dashed lines. The anisotropy magnitudes decrease dramatically as moving from the SE part to the NW part of the field and crossing the main graben faults. Also, there is a general decrease in anisotropy with depth.

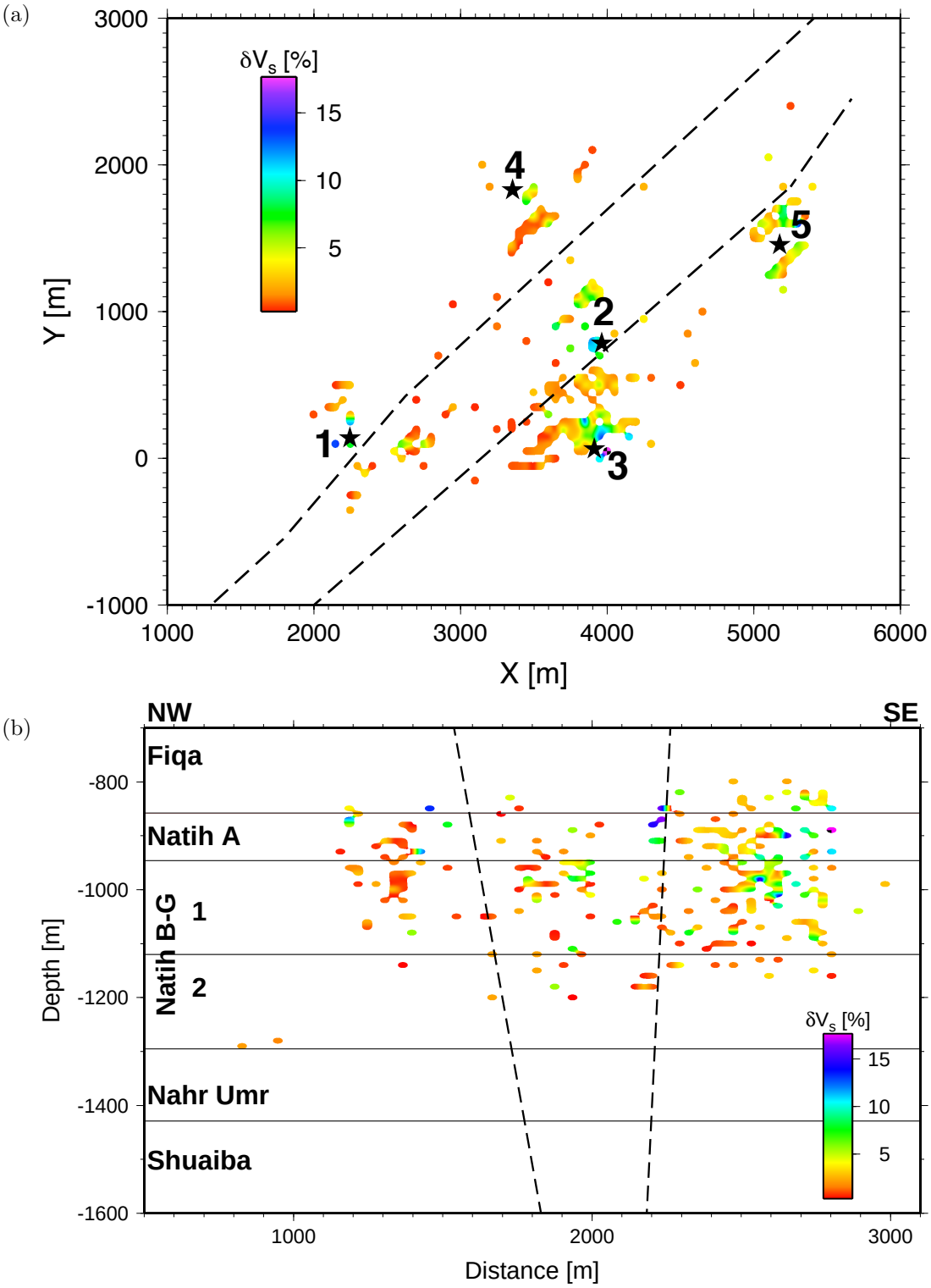

Figure 5.7: Spatial variation of Field M anisotropy. These are the same estimates of δV_s in Figure 5.6 but after gridding. The decay of anisotropy as crossing the graben faults in the NW direction becomes clearer.

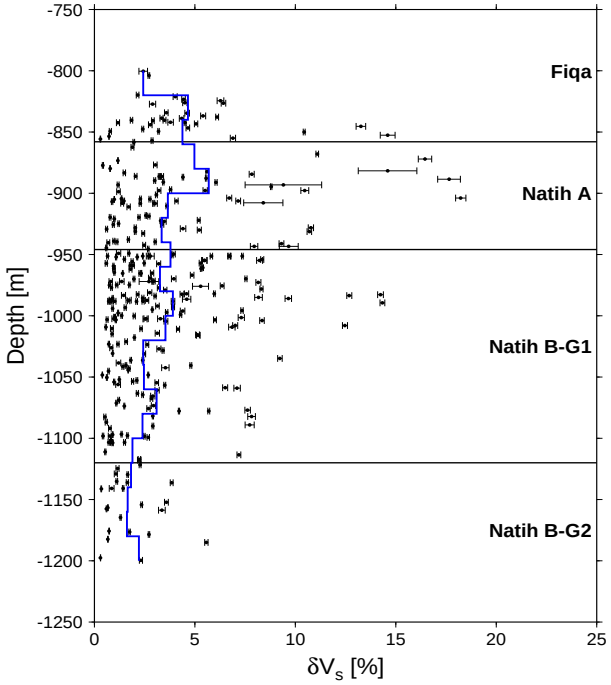

Figure 5.8: Variation of δV_s with depth. Measurements are averaged every 20 m depth (blue line). There is a general decrease in anisotropy with depth. The highest magnitudes of anisotropy are within the highly fractured gas producing Natih A reservoir.

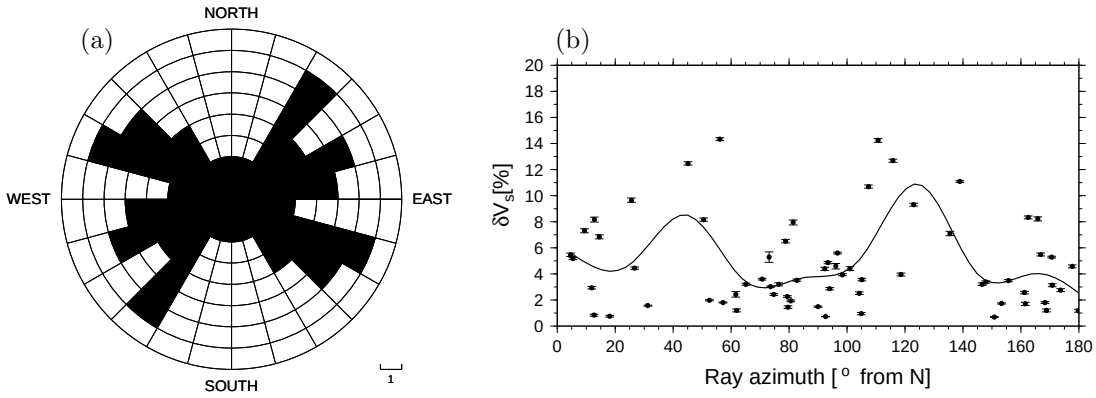

Figure 5.9: Fast shear-wave polarisation strike and azimuthal variation of anisotropy. (a) Rose diagram of the fast strike obtained from subvertically propagating rays, having inclination less than 60° from vertical. The predominant fast strike trends are NE-SW (43°), ENE-WSW (74°) and NW-SE (117°). (b) δV_s variation with azimuth for rays travelling at inclination of $120° \pm 15°$ from vertical. The thick line is a moving average estimate with damping factor of 1 and spacing of 20°. The two peaks at 45° and 125° roughly correlate with the NE-SW and NW-SE strikes in (a).

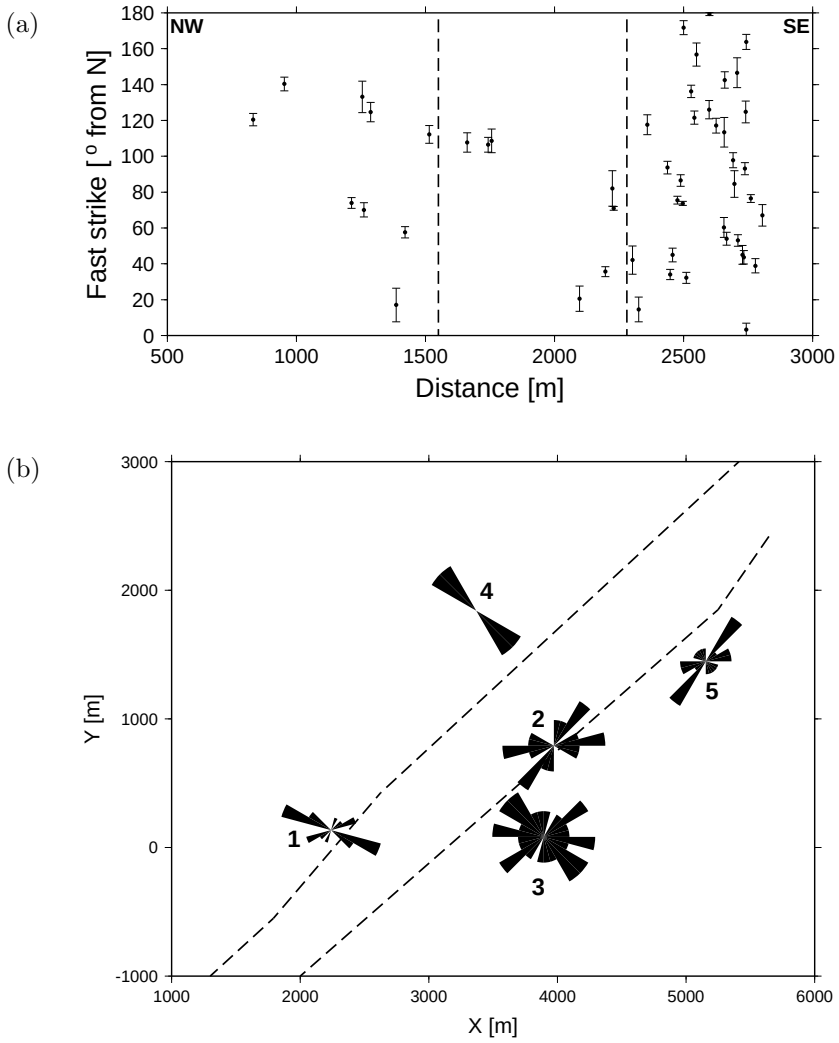

Figure 5.10: Spatial distribution of fast strike orientations. (a) NW-SE cross-section showing the variation of strike with distance. Dashed lines indicate the approximate location of the graben faults. (b) Map view of the fast strike. The rose diagrams are centred at the monitoring well heads and they represent fast strike orientation recorded at each well. There is a transition from NE-SW fast strike orientation close and between the graben faults to NW-SE fast strike orientation either side of the graben system.

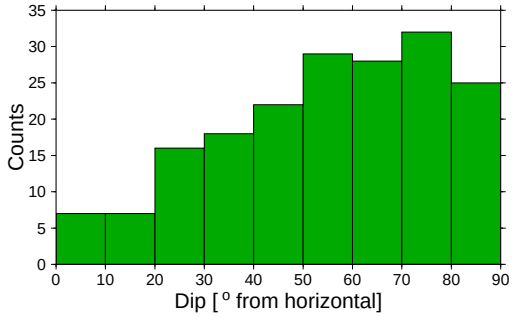

Figure 5.11: Histogram of the fast shear-wave dip obtained from subhorizontally propagating rays, traveling within ±15° from horizontal. The average fast dip is near-vertical (69°).

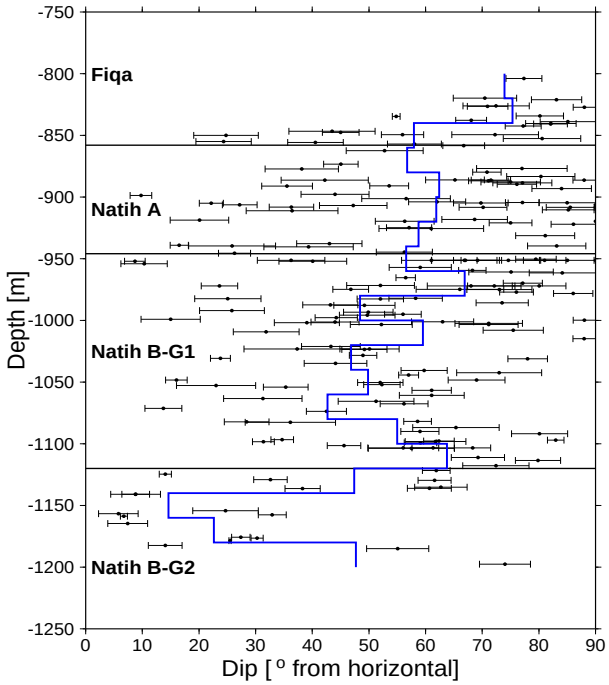

Figure 5.12: Variation of fast dip with depth. Measurements are averaged every 20 m depth (blue line). There is a clear transition from subvertical dip in the Fiqa, Natih A and Natih B-G1 to subhorizontal dip in the Natih B-G2.

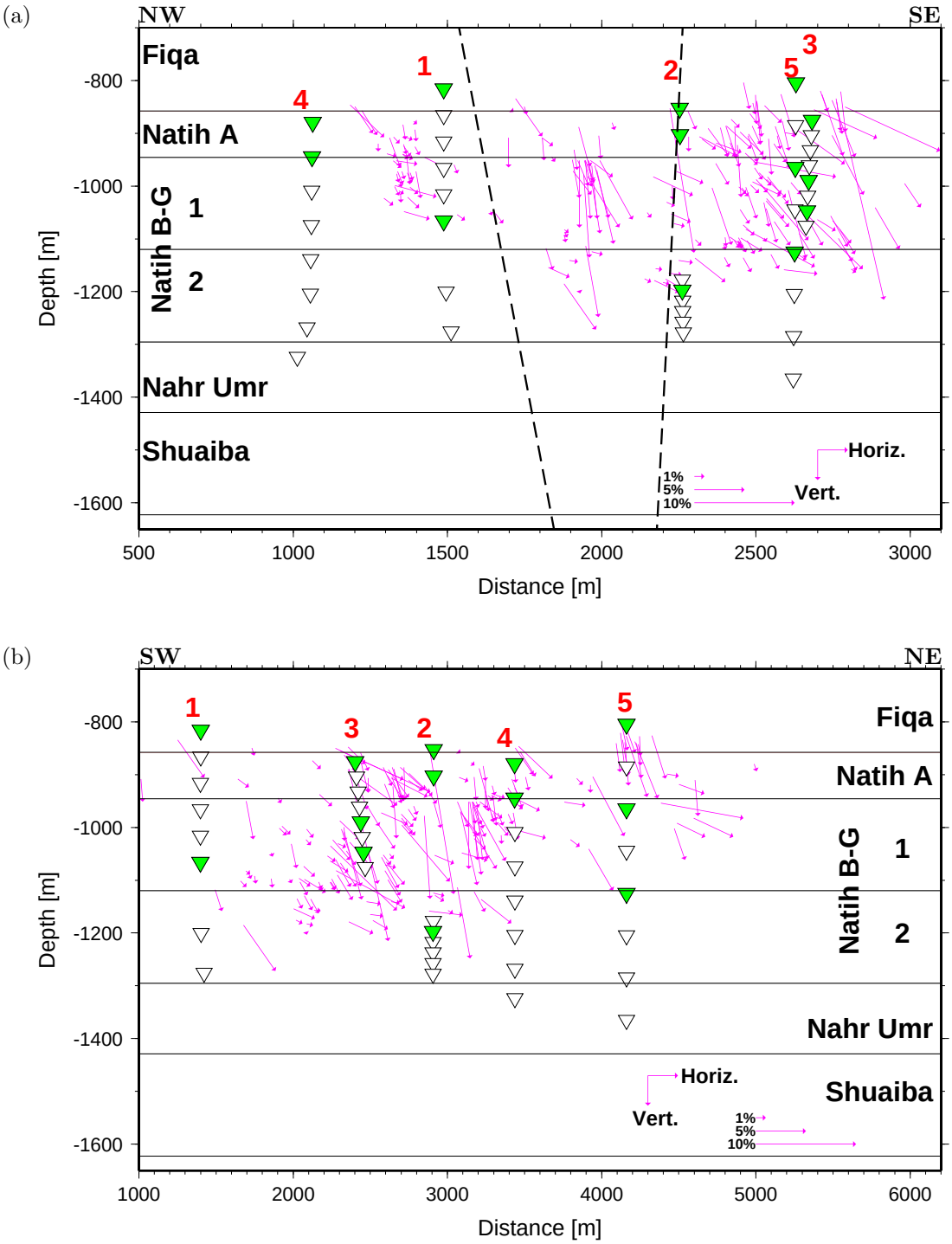

Figure 5.13: Spatial variation of fast dip. (a) NW-SE oriented cross-section cutting the main grabe faults and (b) SW-NE oriented cross-section parallel to the main graben faults. The majority of the rays show subvertical dip (>50°), especially those between the two graben faults and close to well 5. Most of the subhorizontal dip measurements are located in the Natih B-G2 unit.

5.4.2 Anisotropy variation between field blocks

In this section I investigate the variation in anisotropy magnitudes, fast strike and dip and how they are linked to geological structures. I subdivide the field into three main blocks separated by the two main graben faults. These are the SE, Graben and NW blocks (see Figure 5.6a). Measurements from rays crossing the graben fault planes are excluded. The SE block is the footwall of the eastern-most graben fault. There are 132 splitting measurements entirely confined to this block and recorded by stations installed in wells 3 and 5. The measurements in the Graben block (17 measurements) are entirely confined to the rock volume between the two graben faults cutting the field and recorded by well 2 stations. The NW block measurements come from events that occurred to the NW of the western-most graben fault and recorded by stations deployed in wells 1 and 4. There are 58 reliable splitting measurements confined entirely to this block.

The lower-hemisphere projection plots of SWS for the SE, Graben and NW blocks are displayed in Figure 5.14. The average δV_s decreases from about 4.6% in the SE block and 5.2% in the Graben block to about 2.4% in the NW block. Rose diagrams of the fast strike orientation are shown in Figure 5.15. The predominant fast strike is NE-SW (39°) for the SE block and NNE-SSE (27°) for the Graben block. These two strikes are sub-parallel to the trend of the graben faults. There is a secondary minor fast strike trend oriented NW-SE (132°) in the SE block dataset. In the NW block the predominant fast strike is NW-SE (119°). The fast dip is subvertical (73°) in the NW block, whereas it is clustered around 55° and 75° in the SE block. In contrast, the Graben block dataset shows a subhorizontal fast dip with an average of 25°. However, the estimated fast dip in the Graben block is not well constrained due to the poor ray coverage in the horizontal plane (Figure 5.14b). A better estimate of the fast dip is obtained later when analysing splitting results from the F1-W2 measurement group.

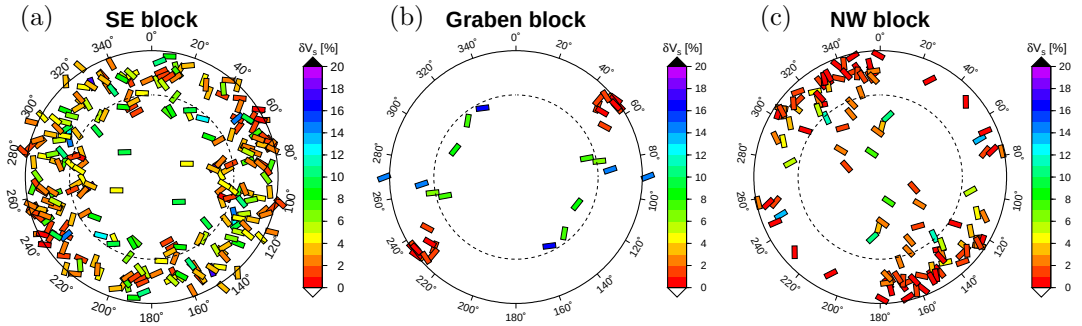

Figure 5.14: Shear-wave splitting observations represented using lower-hemisphere projection plot for (a) SE block, (b) Graben block and (c) NW block (see Figure 5.5b caption). Note the decrease in anisotropy as moving from the SE part to the NW part of Field M. The results are reflected through origin point for illustration purposes. Dashed circles mark the 60° ray inclination angle.

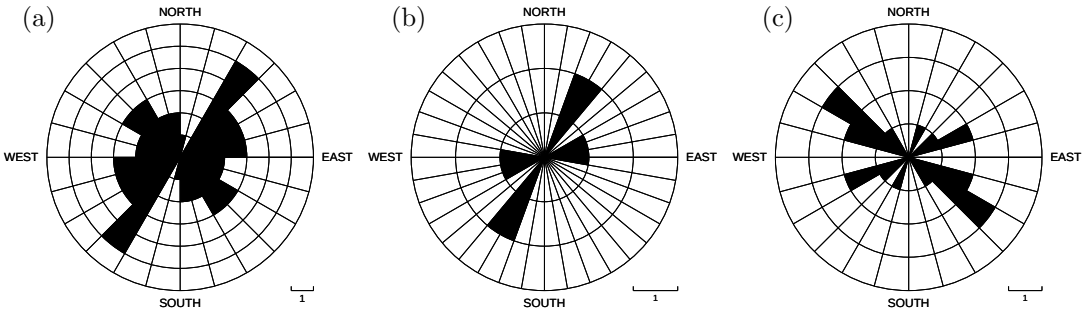

Figure 5.15: Rose diagrams of fast strike orientations for (a) SE block, (b) Graben block and (c) NW block. The fast strike orientations correlate well with the fault trends in each of the three blocks. Due to the small number of measurements available for the Graben block, bin size of 20° is used in (b).

5.4.3 Anisotropy variation between event clusters

In this section I explore the variation of anisotropy with location. Six event clusters, shown in Figure 5.16, were chosen yielding seven groups of measurements. Event clusters are subdivided into two categories: event clusters around monitoring wells and event clusters caused by major faults reactivation. The first category includes the Well-1, Well-2 and Well-3 clusters. The second category includes the F1 and F2 clusters. In addition, I study the measurements from the cluster of events surrounding the Horseshoe feature (Figure 5.16). Table 5.1 summarises cluster dimensions and recording stations used with each cluster.

The Well-1 cluster includes events surrounding well 1 and recorded by stations 1.1 and 1.6 (Figure 5.16). Measurements from this cluster reveal the anisotropy nature to the west of the western-most graben fault. The Well-2 cluster includes events surrounding well 2 and recorded by stations 2.1, 2.2 and 2.4 (Figure 5.16). Events in this cluster were most likely caused by the reactivation of the eastern-most graben fault. The Well-3 cluster of events is located to the SE of the eastern-most graben fault (Figure 5.16). It was likely caused by gas production from a nearby well (Raymer et al., 2003). The intensity of events is very high inside this cluster. The lower-hemisphere projection plots of SWS for the Well-1, Well-2 and Well-3 clusters are shown in Figures 5.17(a,b,c). δV_s is high inside the Well-2 and Well-3 clusters with average estimates of 9.7% and 7%, respectively, and it decreases to an average of 3.9% in the Well-1 cluster. δV_s is high in both the horizontal and vertical planes in the Well-3 cluster. Rose diagrams of fast strike orientation for the Well-1, Well-2 and Well-3 clusters are shown in Figure 5.18. The Well-2 dataset shows a single fast strike trending NE-SW (32°). The Well-1 and Well-3 datasets show two predominant fast strike trends. These are ENE-WSW (66°) and NW-SE (123°) for the Well-1 cluster and, E-W (90°) and NNW-SSE (151°) for the Well-3 cluster. The average fast dip is subvertical for the Well-3 cluster with an average of 75°. The fast dip cannot be estimated for the Well-1 and Well-2 clusters due to the limited horizontal ray coverage.

The F1 event cluster yields the F1-W2 and F1-W4 measurements, which were recorded by monitoring wells 2 and 4, respectively. The F2-W1 dataset comes from the source-receiver combination between events in cluster F2 and stations 1 and 6 of monitoring well 1. The F1-W2 and F2-W1 measurement groups are used to constrain the anisotropy between the two graben faults as the ray-paths are confined to the rock volume inside the graben system. The F1-W4 measurements reveal the anisotropy magnitudes to the NW of the western-most graben fault. The lower-hemisphere projection plots are displayed in Figures 5.17(d,e,f). δV_s decreases dramatically from an average of

Cluster name	Size	Recording stations
Well-1	X45 = 272 : 1577 Y45 = 490 : 2719 Z = 600 : 1623	1.1 and 1.6
Well-2	X = 3700 : 4350 Y = 600 : 1150 Z = 600 : 1623	2.1, 2.2 and 2.4
Well-3	X = 3600 : 4100 Y = -150 : 400 Z = 858 : 1295	3.1, 3.5 and 3.7
F1-W2	X45 = 1523 : 1849 Y45 = 2719 : 5003 Z = 600 : 1295	2.1, 2.2 and 2.4
F1-W4	X45 = 1523 : 1849 Y45 = 2719 : 5003 Z = 600 : 1295	4.1 and 4.2
F2-W1	X45 = 1958 : 2447 Y45 = 1958 : 2447 Z = 600 :1623	1.1 and 1.6
Horseshoe	X = 4600 : 5800 Y = 850 : 2200 Z = 750 : 970	5.1 and 5.3

Table 5.1: Event cluster sizes and recording stations used when investigating variation in anisotropy with location. X45 and Y45 are the x-axis and the y-axis, respectively, rotated clockwise by 45°.

4.3% for the F1-W2 group to an average of 1.6% for the F1-W4 group. This further confirms the decrease in δV_s across the western-most graben fault when moving from the Graben to the NW block (Figures 5.14(b,c)). However, δV_s decreases to about 2.1% in the SW part of the Graben block as shown by the measurements of the F2-W1 group (Figure 5.17f). The ray coverage in the vertical plane is poor for all the three groups of measurements, rendering the estimation of the fast strike orientation impossible. The average fast dip is 84°, 73° and 74° for the F1-W2, F1-W4 and F2-W1 measurement groups, respectively.

The Horseshoe feature extends from the mid-Fiqa to the bottom of the Natih A reservoir. Only measurements having their raypaths within the depth range of the feature and recorded by stations 1 and 3 of monitoring well 5 are used. The lower-hemisphere projection plot of SWS in this area is shown in Figure 5.17g. δV_s is moderate, with an average of 3.9%, and the average fast dip is 83°.

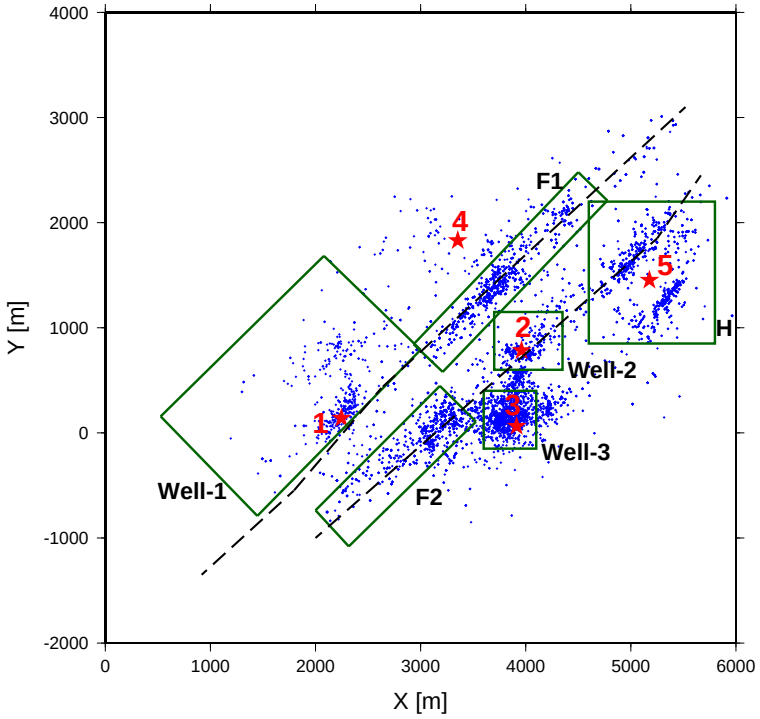

Figure 5.16: Map view of event locations (blue dots) with the clusters used in the analysis bounded by green rectangles (H=Horseshoe cluster). Monitoring well heads are denoted by red stars.

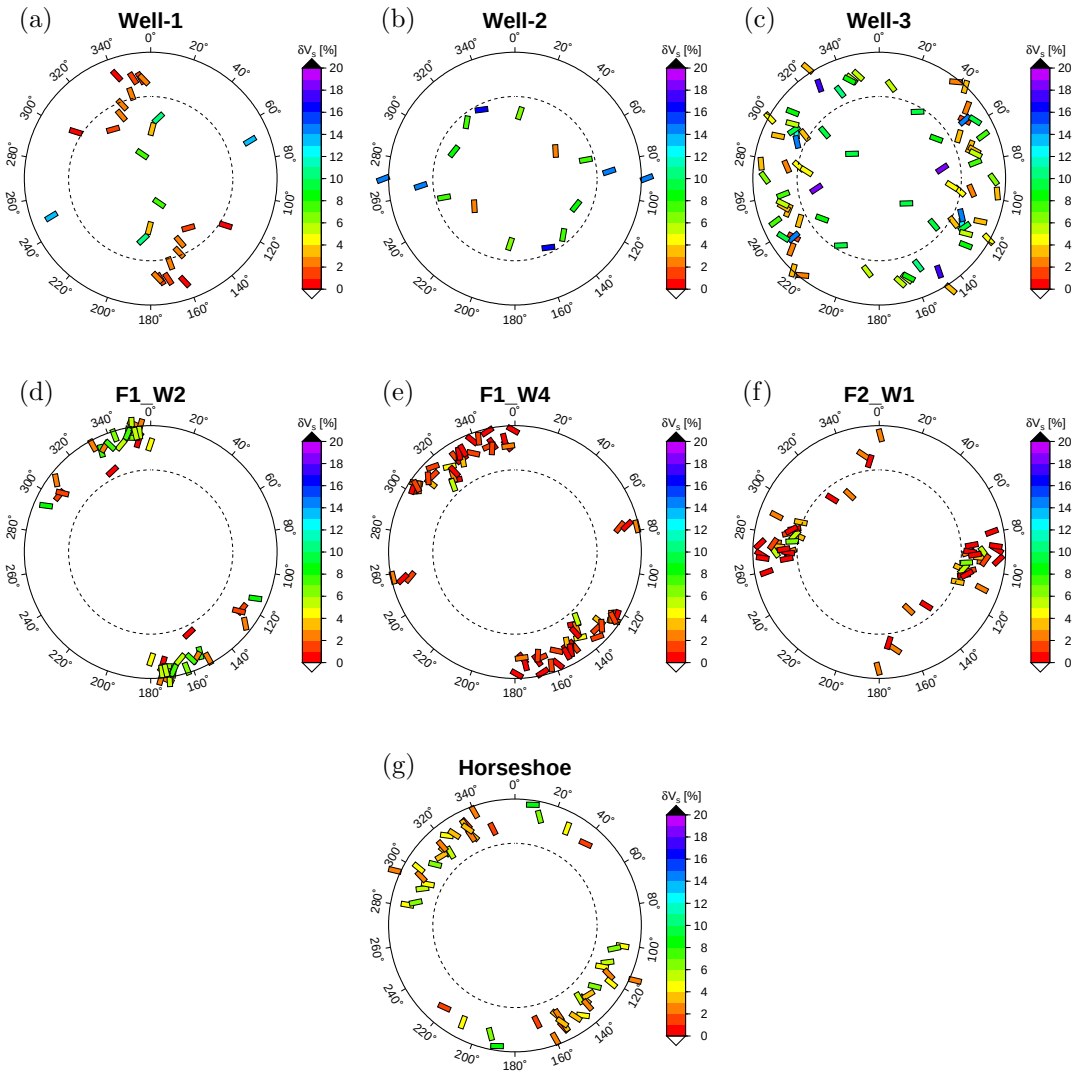

Figure 5.17: Shear-wave splitting variation based on location (see Figure 5.5b caption). Note the high amounts of δV_s in the SE part of the field (c and g) and between the two graben faults (b and d) compared to the NW part (a). The results are reflected through the origin point for illustration purposes. Dashed circles mark the 60° ray inclination angle.

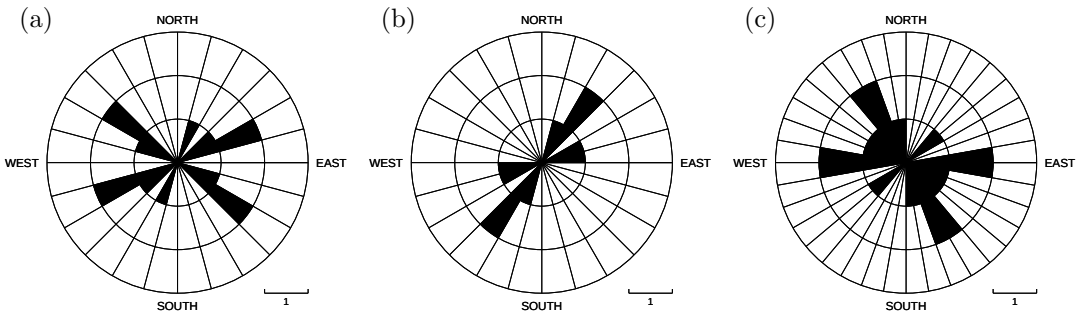

Figure 5.18: Rose diagrams of fast strike for events around (a) well 1, (b) well 2 and (c) well 3 (see Figure 5.16). The predominant strike in (b) is sub-parallel to the trend of the main graben faults (NE-SW). The NW-SE fast strike in (a) and (c) matches with the trend of minor faults located either side of the graben system.

5.4.4 Anisotropy variation between lithological units

In this section I study the variation in anisotropy between the field lithological units. This is done by considering source-receiver pairs bounded by the formation boundaries. Such measurements would help observing the variation in anisotropy due to lithology by ensuring that rays do not cross different lithological units. Table 5.2 defines event depth ranges and recording stations when sorting results based on lithology. There are no measurements confined to the deep Shuaiba reservoir and its overlying cap rock (Nahr Umr).

Formation	**Event depth range (m)**	**Recording stations**
Fiqa	600 - 858	1.1, 2.1 and 5.1
Natih A	858 - 946	2.1, 2.2, 3.1, 4.1, 4.2 and 5.3
Natih B-G	946 - 1295	1.6, 2.4, 3.5, 3.7, 4.2, 5.3 and 5.5
Natih B-G1	946 - 1120	1.6, 3.5, 3.7, 4.2, 5.3 and 5.5
Natih B-G2	1120 - 1295	2.4 and 5.5

Table 5.2: Depth ranges and stations used when sorting and confining raypaths to lithological units. The Natih B-G1 is the upper part of the Natih B-G formation and Natih B-G2 is the lower part. Stations which lie in or near the formation boundaries are used for the formation above and below it (e.g., station 2.1 is used with events occured in the Fiqa and Natih A units).

Fiqa shale

There are only 8 source-receiver pairs confined entirely to the Fiqa shale. The lower-hemisphere projection plot of the Fiqa subset (Figure 5.19a) displays δV_s in the range 2-6% with an average of 3.9%. The average fast dip is 72°. There are no subvertical rays available to estimate the fast

strike orientation. Contrary to expectation, anisotropy in the Fiqa shale is not dominated by the intrinsic anisotropy but rather by the vertical alignment of cracks (compare Figure 5.19a with Figure 5.1c).

Natih A carbonate

There are 44 reliable splitting measurements available for the Natih A reservoir. The lower-hemisphere projection plot for the Natih A dataset (Figure 5.19b) shows high amounts of δV_s. δt varies mostly between 2 and 32 ms with a peak at 8 ms, corresponding to variation in δV_s between 0% and 18%. The average δV_s is 4.5%. The average fast dip for subhorizontal rays is 73°. The predominant fast strike is trending ENE-WSW (62°) and NNW-SSE (146°). However, these estimates are poorly constrained as they come from three measurements only.

Natih B-G carbonate

Raypaths entirely confined within the Natih B-G formation yield 92 good splitting measurements. δt in this carbonate formation varies mostly from 2 to 15 ms. The range of δV_s is between 0% and 5% with an average of 2.3% (Figure 5.19c). The ray coverage is good in the horizontal plane but poor in the vertical plane. The two predominant fast strikes, estimated from subvertical rays, are NNE-SSW (14°) and NW-SE (120°). The fast polarisation dip is near vertical with an average of 63°.

The anisotropy in the Natih B-G unit is further investigated by subdividing the formation into upper part (Natih B-G1) and lower part (Natih B-G2). Raypaths crossing the boundary between the lower and upper parts are excluded (see Table 5.2). There are 47 good splitting measurements for the Natih B-G1 and 6 measurements for Natih B-G2. The Natih B-G1 has higher δV_s magnitudes with an average of 2.5% (Figure 5.19d) compared to the underlying Natih B-G2 with an average of 1.2% (Figure 5.19e). The ray coverage in the vertical plane is poor for both units, rendering the estimation of fast strike orientation difficult. The fast dip in the Natih B-G1 is clustered around 54° and 73°. The fast dip direction is subhorizontal (average 26°) in the Natih B-G2.

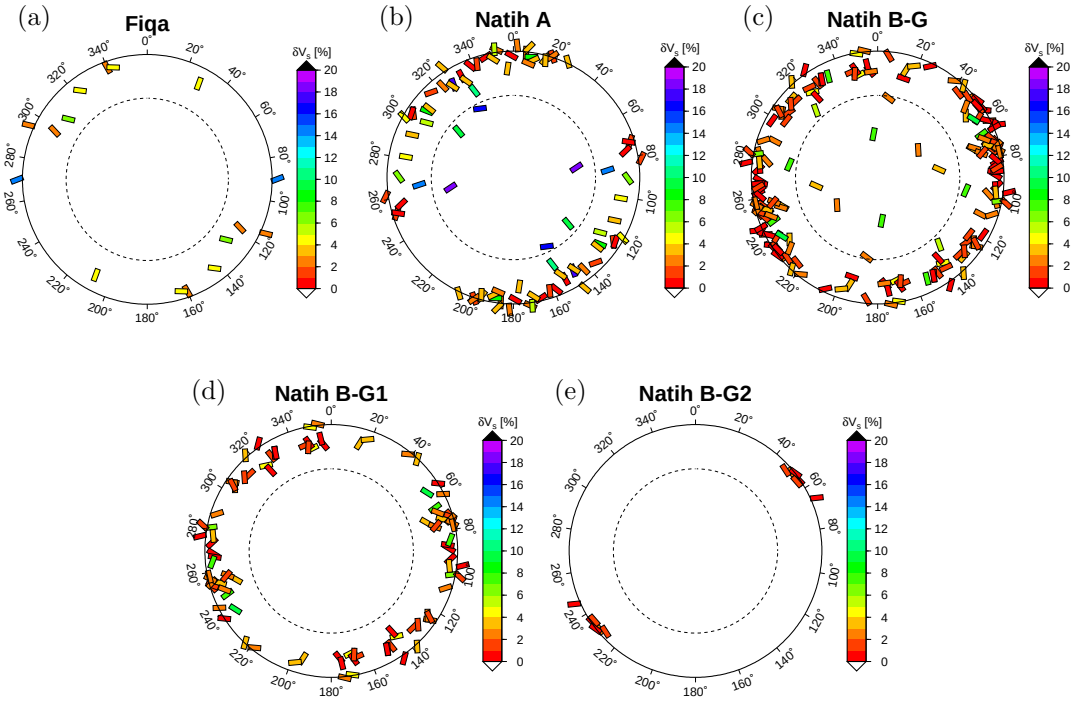

Figure 5.19: Shear-wave splitting variation based on lithology (see Figure 5.5b caption). Measurements are entirely confined to (a) the Fiqa shale cap rock, (b) the Natih A gas reservoir, (c) the Natih B-G carbonate formation, (d) the upper part of Natih B-G and (e) the lower part of Natih B-G. The highest amounts of δV_s (average 4.5%) are observed in the highly fractured Natih A reservoir. δV_s decreases dramatically with depth reaching an average of 1% in the lowest part of the Natih B-G formation. The Fiqa shale has moderate δV_s (average 3.9%). The results are reflected through the origin point for illustration purposes. Dashed circles mark the 60° ray inclination angle.

5.5 Temporal variation of anisotropy

The long deployment of the Field M microseismic monitoring network allows for performing some temporal analysis on the results. It has been already shown in Chapter 3 that the seismicity level correlates well with the rate of gas production from the Natih A reservoir. In this section I investigate the variation of anisotropy in relation to the seismicity level and production activities. Figure 5.20 depicts the temporal variation of δV_s together with the variations in seismicity level and gas production while the network was active. The time-δV_s relation is only plotted for datasets with good distribution of measurements over time. These include the entire dataset, SE block, Well-3, Natih A and Natih B-G subsets. No systematic temporal variations in the fast strike and dip have been observed.

The entire dataset does not show clear correlation between δV_s and the field activities. Similar thing is observed for measurements from the non-producing part of the Natih formation (Natih B-G). In contrast, measurements from the SE block, Well-3 cluster and the Natih A subset display a reasonable correlation with the gas production rates and seismicity level. The maximum amounts of δV_s are observed during summer (May to August) when the gas production is maximum. The correlation is well illustrated by measurements from Well-3 cluster. We have seen in Chapter 3 that the seismic activity within this cluster was caused by gas production.

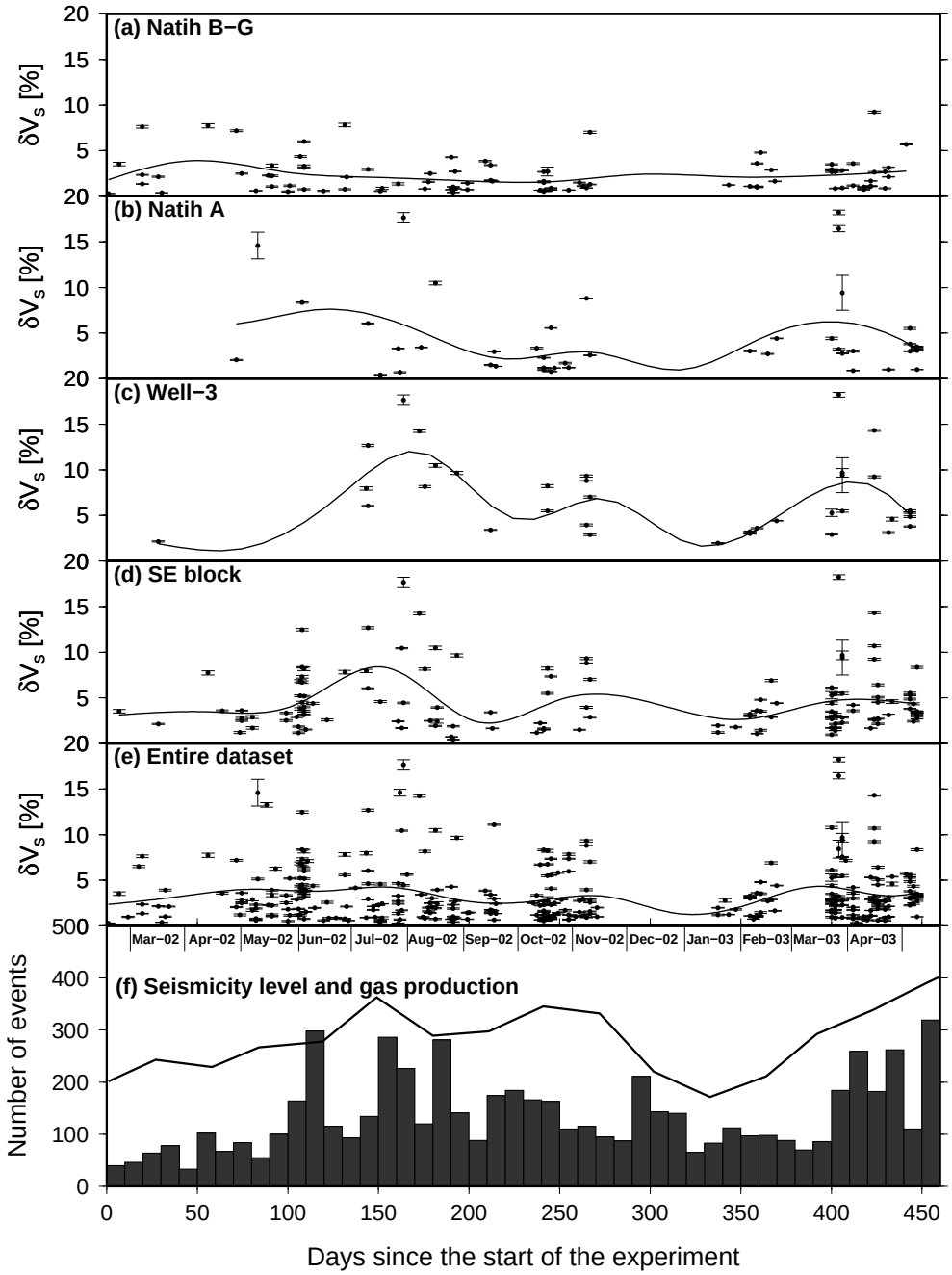

Figure 5.20: Temporal variation of δV_s for different datasets. Lines in (a) to (e) represent moving average estimates. (f) Histogram of seismicity and monthly gas production from the Natih A reservoir. Gas production is not to scale for confidentiality reason. Note the increase in δV_s during summer in (b), (c) and (d). This increase fairly correlates with the increase in seismicity level and gas production.

5.6 Summary of key observations

Table 5.3 summarises the key observations of variations in δV_s, fast strike and fast dip between the field blocks, event clusters and lithological units.

Group	**Average δV_s**	**Fast strike**	**Fast dip**
All	3.5%(325)	43°±8°(11), 74°±7°(11) & 117°±8°(13)	69°±11°(118)
SE block	4.6%(132)	39°±5°(6) & 132°±9°(6)	55°±3°(14) & 75°±3°(12)
Graben block	5.2%(17)	27°±8°(2)	25°±1°(3)
NW block	2.4%(58)	119°±9°(5)	73°±2°(6)
Well-1	3.9%(13)	66°±7°(3) & 123°±9°(3)	-
Well-2	9.7%(8)	32°±9°(3)	-
Well-3	7.0%(37)	90°±7°(2) & 151°±5°(2)	75°±2°(4)
F1-W2	4.3%(23)	-	84°±3°(7)
F1-W4	1.6%(34)	-	73°±2°(6)
F2-W1	2.1%(25)	-	74°±3°(3)
Horseshoe	3.9%(25)	-	83°±3°(6)
Fiqa	3.9%(8)	-	72°±3°(4)
Natih A	4.5%(44)	62°±8°(2) & 146°±0°(1)	73°±3°(10)
Natih B-G	2.3%(92)	14°±0°(1) & 120°±4°(2)	63°±3°(16)
Natih B-G1	2.5%(47)	-	54°±3°(9) & 73°±2°(9)
Natih B-G2	1.2%(6)	-	26°±1°(2)

Table 5.3: Summary of the observed spatial variation in δV_s, fast strike and fast dip for the different clusters and formations. Numbers between brackets are numbers of measurements. The standard deviation is calculated for each estimate of strike and dip.

5.6.1 Lateral variation in fracture density

Figures 5.6 and 5.7 show well defined fault-bounded lateral variation in the magnitude of anisotropy. The average δV_s decreases dramatically from about 5% in the SE part and the graben block to about 2% in the NW part of the field. The trend is also highlighted by the change from high anisotropy in the SE block clusters (Well-3 (Figure 5.17c) and Horseshoe (Figure 5.17g)) to low

anisotropy in the NW block clusters (Well-1 (Figure 5.17a) and F1-W4 (Figure 5.17e)). The fault-related lateral variation in anisotropy is clearly observed in the Fiqa, the Natih A and the Natih B-G1 units, but is much less significant in the Natih B-G2 unit (Figure 5.6b). High amounts of δV_s are observed close to the eastern-most graben fault, especially the region close to monitoring wells 2 and 5 (Figure 5.6).

5.6.2 Vertical variation in fracture density

The anisotropy also seems to correlate with the nature of the rock (Figure 5.8). The Fiqa shale is a moderately anisotropic medium with an average δV_s of 3.9%. The gas-producing Natih A is strongly anisotropic reservoir with δV_s ranges between 0% and 18% (average 4.5%). δV_s decreases to 2.5% in the Natih B-G1 and 1.2% in the Natih B-G2.

5.6.3 Temporal variation in stress and fracture density

Significant increase in δV_s is observed during summer when gas production from the Natih A rservoir is at its maximum rate. The relation is clearly observed in the SE block, the Natih A reservoir and the Well-3 cluster, especially in the latest one where seismicity is believed to be caused by gas production. Magnitudes of δV_s remain approximately constant in the non-producing Natih B-G unit.

5.6.4 Fracture geometry

Fracture strike

The majority of the splitting measurement groups show two predominant fracture strikes (Table 5.3). The subvertically propagating rays for the entire dataset (Figure 5.9a) indicate three fracture strikes: NE-SW, ENE-WSW and NW-SE. The fracture strikes appear to follow the major fault trends (NE-SW and NW-SE). Measurements close and between the two graben faults have NE-SW fracture strike (e.g., Graben block and Well-2 cluster (Table 5.3)). Measurements outside the graben indicate two fracture strikes, which in most cases trend NE-SW and NW-SE. Fractures striking ENE-WSW and E-W are inferred within the Well-1, Well-3 clusters and the Natih A gas reservoir.

Fracture dip

The majority of the results show average fast dip greater than 70° (Table 5.3). The average fast dip from the entire dataset is 69°. The average fracture dip decreases with depth from about 70° in the Fiqa and the Natih A reservoir to 26° in the lower part of the Natih B-G unit.

5.7 Discussion and interpretation

The lateral variation in anisotropy can be explained by the observations that the crest and the southern flank are faulted and fractured more extensively than the northern flank (see Figure 2.2 in Chapter 2). The second explanation of the lateral variation in anisotropy can be compaction rates and pore pressure. The highest rates of compaction (maximum in Natih A) and subsidence are in the NW block (see Figure 2.8 in Chapter 2) and most of the gas producers are located in this part of the field. Gas production reduces pore pressure and increases effective vertical stress, resulting in reservoir compaction. Compaction can destroy fractures and decrease their sizes and consequently decreases the amount of splitting.

The faults appear to have a significant influence on fracturing and compartmentalisation. The highest anisotropy magnitudes observed close to the eastern-most graben fault may reflect a high fracture density caused by movement along the fault plane. Al-Kindi (2006) reported an increase in fracture density towards fault planes in the Natih A outcrop in the Salakh arch (located 130 km east of Field M, see Chapter 2).

The obtained results for the Natih A reservoir (δt (2-32 ms) and δV_s (0-18%)) match with the results of Potters et al. (1999) (maximum of 30 ms and 15%) for the same lithology unit in a nearby field sharing the same geological history. Furthermore, the anisotropy results in the Fiqa (3.9%), Natih B-G1 (2.5%) and Natih B-G2 (1.2%) are in a good agreement with those inferred from dipole-shear logs (4%, 2% and 1%, respectively). In contrast, anisotropy in the Natih A reservoir (average 4.5%) is higher than that inferred from dipole-shear logs (2%). This may reflect large-scale fractures in the Natih A that cannot be imaged by high frequency tools that probe short distances (often significantly shorter than fracture spacing) and fine-scale fractures in the other formations. Such conclusion will be assessed later in Chapter 7 when performing frequency-dependent anisotropy to estimate fracture sizes. The large amounts of anisotropy in the Natih A reservoir are consistent with the high amounts of fracturing observed in the reservoir (Ozkaya et al., 2004). Furthermore, the anisotropy magnitudes are in a good agreement with those estimated by

Al-Anboori (2006) using manual SWS analysis (3% Fiqa, 5% Natih A, 2.7% Natih B-G1 and 1% Natih B-G2).

Temporal variation in anisotropy, generally, reflects variation in the *in situ* stress conditions and number of opened fractures (e.g., Teanby et al., 2004a; Crampin & Peacock, 2008). In Field M, anisotropy increases with the increase in gas production rate. This relation is clearly observed in the SE block, the Natih A reservoir and the Well-3 cluster, whereas anisotropy remains approximately constant in the non-producing part of the Natih formation (Natih B-G). These observations can be explained by the opening of new fractures by gas flow during production. When gas production decreases, the effective stress returns to its equilibrium state, resulting probably in randomly oriented and almost closed fractures.

However, the temporal variation in anisotropy has to be interpreted in a more careful way because the scatter in the splitting parameters over time can evolve, for example, from: (1) spatial migration of seismicity, (2) estimating splitting parameters along different raypaths from different source locations and (3) change in source focal mechanisms (see discussions in Volti & Crampin, 2003; Liu et al., 2004; Seher & Main, 2004; Crampin & Peacock, 2008). Furthermore, the temporal observations have to be analysed statistically to judge their reliability before withdrawn any conclusion. For example, Seher & Main (2004) used the objective Bayesian information criterion (BIC; Leonard & Hsu, 1999) to evaluate the results of Crampin et al. (1999) who claim that they were able to predict the occurance of M=5 earthquake in Icelend by monitoring temporal variations in δt measurements. Seher & Main (2004) using their statistical analysis concluded that the measurements of Crampin et al. (1999) are not yet adequate to make forecasts of individual earthquakes. Finally, a more frequent production rates (probably daily or weekly rather than monthly) and estimates of pore fluid pressure are required to withdraw a conclusion about the reason behind the observed temporal variation.

The estimated predominant fracture strikes (NE-SW and NW-SE) are consistent with the major fault patterns (see Figure 2.2 in Chapter 2). The same consistency in trends between fractures and faults was reported at the Shuaiba level by Al-Busaidi (1997). The NE-SW and NW-SE fracture trends were also observed in 5 wells at the Natih A reservoir (Hodder, 2004). The strike trend matching between the majority of fractures and faults suggests that the fractures imaged by SWS analysis are of tectonic origin. The NE-SW fracture strike agrees with North Oman present-day regional maximum stress orientation (Filbrandt et al., 2006). The third fracture strike oriented ENE-WSW (74°) is in a good agreement with the *in situ* stress direction (66°) estimated from

the drilling induced hydraulic fractures (Hodder, 2004). The ENE-WSW fracture strike is also observed in the Natih A gas reservoir, but with less confidence, indicating that these fractures are probably opened by gas flow in the direction parallel to the *in situ* stress direction. Furthermore, close inspection of the Field M tectonic map (Figure 2.2) reveals the existence of E-W minor faults, especially close to monitoring well 3. Interestingly, the results indicate E-W fracture strike inside the Well-3 cluster (Table 5.3).

The average fast dip (73°) in the Natih A agrees with the fracture dip (70°) estimated by Ozkaya et al. (2004) for the same formation using formation micro images (FMI) and core samples. The decrease in anisotropy and fracture dip with depth indicates transition from fracture-induced anisotropy (Fiqa, Natih A and Natih B-G1) to a more intrinsic anisotropy (Natih B-G2). Similar near-vertical fracture dip is observed in the Natih formation outcrop in the Salakh arch (Mercadier 1989). The subvertical average fracture dip in the Fiqa shale indicates that the seal is fractured and the observed anisotropy is caused by fractures rather than thin layering of mica. This highlights the importance of SWS in assessing seal integrity.

Collectively, the observations when compared with the rock models in section 5.2 suggest a model where fracture-induced anisotropy dominates a weaker background intrinsic anisotropy.

5.8 Conclusion

I used a total of 325 reliable SWS splitting measurements to investigate the nature of anisotropy in Field M. The results provide good spatial and temporal coverage. They offer valuable information about the field fracture system. The interpretation of the results were guided using synthetic modelling to distinguish between fracture-induced anisotropy and the intrinsic anisotropy of the rocks.

The SWS observations show that anisotropy within the field is controlled by both rock type and proximity to major faults. The highest anisotropy values (3-10%) lie to the SE part of the field and between the two major graben faults. Anisotropy decreases to an average of 2% in the NW part. The lateral variation in anisotropy is explained by the observations that the crest and the southern part are fractured more extensively than the northern part. The deformation and closure of fractures caused by high compaction rates in the NW part provide a possible cause of the low anisotropy magnitudes.

The shallow parts of the field display high anisotropy and subvertically polarised shear-waves that are attributed to fractures and cracks. In contrast, the deeper parts of the field show low amounts of anisotropy and subhorizontally polarised fast shear-waves that are attributed to the intrinsic anisotropy of the rocks. The highest amounts of anisotropy (average 4.5%), as expected, are observed within the highly fractured Natih A reservoir. The mapped fractures have strikes parallel to the NE-SW and NW-SE oriented faults. The consistency in strike trends between faults and fractures implies that fractures in Field M are of tectonic origin.

Overall, the results agree with those obtained from shear-dipole logs, FMI and core samples. Collectively, the outputs from the study suggest that anisotropy in carbonate rocks can serve as a proxy for reservoir quality and consequently it can help in reservoir evaluation and management. For example, fractures are dipping vertically, therefore production can be maximised by drilling horizontal wells. Drilling activities should be directed to regions with high fracture density (large amounts of anisotropy in this case). The results can also be used in term of risk assessment and seal integrity. For instance, the anisotropy inferred within the Fiqa cap rock is primarily caused by subvertivally dipping fractures rather than by mica horizontal alignment. This indicates that the seal is fractured and fluid leakage may happen.

6
Shear-wave splitting inversion using rock physics modelling

6.1 Introduction

In Chapter 5 I presented evidence of spatial and temporal variations in anisotropy in Field M. The results represent different mechanisms of anisotropy, ranging from a single fracture set to multiple fracture sets superimposed on an intrinsic VTI rock fabric. However, inverting for the optimum subsurface model directly from shear-wave splitting (SWS) observations can be non-unique because of the different potential causes of anisotropy. The splitting parameters, fast polarisation direction (Φ) and delay time (δt), are highly dependent on the direction of ray propagation with respect to fracture orientation (e.g., Crampin & Peacock, 2008). In seismology, Φ and δt measurements are traditionally treated independently. It is common to directly assume that Φ corresponds to the strike of the fractures and/or the maximum horizontal stress orientation, and that δt reflects fracture intensity. However, these assumptions are limited to cases where the S-waves propagate subvertically, for example, in 3D and VSP seismic surveys. In the case of microseismic monitoring using downhole geophones, 3D ray coverage is more feasible and thus the interpretation of the splitting measurements becomes far less intuitive (Verdon et al., 2009). Furthermore, in sedimentary settings subsurface sedimentary fabrics can contribute to the overall estimated anisotropy making it even harder to interpret the results assuming aligned fractures as the only cause of anisotropy. In reality, both δt and Φ are controlled by the overall subsurface rock architecture and thus they must be used simultaneously to investigate the causes of anisotropy (Yang et al., 2005).

In this chapter I investigate the possible causes of anisotropy in Field M via the use of SWS inversion. I apply the inversion approach proposed by Verdon et al. (2009) to estimate the best-fit fracture geometries and strength of sedimentary fabrics that match with the results obtained in Chapter 5. I start by describing the rock physics modelling and how the inversion works. The approach of Verdon et al. (2009) assumes that a single aligned fracture set embedded in a VTI sedimentary fabric is controlling the rock anisotropy. However, for the case of Field M, some of the results in Table 5.3 show two dominant fracture strikes. Hence, I have modified the inversion code to deal with the case of two aligned fracture sets. The limitation of the inversion in imaging the

possible range of anisotropic symmetries is studied using synthetic modelling. Finally, I compere the results from the SWS inversion with those previously obtained in Chapter 5.

6.2 Method

6.2.1 Model building

The SWS inversion technique of Verdon et al. (2009) begins by constructing realistic rock physics models that can simulate the rock architecture. For each model the full stiffness tensor (C) or its inverse compliance ($S{=}C^{-1}$) is calculated in order to model SWS in any direction of propagating. First, the isotropic elastic tensor of the background rock (C_I) is constructed using the Lamé parameters λ and μ, which are based on the seismic velocities (V_p and V_s) and the rock density (ρ),

$$\mu = \rho V_s^2, \qquad \lambda = \rho V_p^2 - 2\mu. \tag{6.1}$$

The isotropic elastic tensor can be described using Voigt notation as

$$C_I = \begin{pmatrix} \lambda+2\mu & \lambda & \lambda & 0 & 0 & 0 \\ \lambda & \lambda+2\mu & \lambda & 0 & 0 & 0 \\ \lambda & \lambda & \lambda+2\mu & 0 & 0 & 0 \\ 0 & 0 & 0 & \mu & 0 & 0 \\ 0 & 0 & 0 & 0 & \mu & 0 \\ 0 & 0 & 0 & 0 & 0 & \mu \end{pmatrix}. \tag{6.2}$$

In the presence of horizontal layering or many sedimentary fabric the rock frame compliance becomes anisotropic (VTI symmetry). The stiffness matrix of such system has the form

$$C = \begin{pmatrix} C_{11} & (C_{11}-2C_{66}) & C_{13} & 0 & 0 & 0 \\ (C_{11}-2C_{66}) & C_{11} & C_{13} & 0 & 0 & 0 \\ C_{13} & C_{13} & C_{33} & 0 & 0 & 0 \\ 0 & 0 & 0 & C_{44} & 0 & 0 \\ 0 & 0 & 0 & 0 & C_{44} & 0 \\ 0 & 0 & 0 & 0 & 0 & C_{66} \end{pmatrix}. \tag{6.3}$$

The strength of the VTI anisotropy is quantified using Thomsen's γ and δ parameters (Thomsen, 1986), where

$$\gamma = \frac{C_{66} - C_{44}}{2C_{44}} \tag{6.4}$$

and

$$\delta = \frac{(C_{13} - C_{44})^2 - (C_{33} - C_{44})^2}{2C_{33}(C_{33} - C_{44})}. \tag{6.5}$$

Finally, the additional compliance due to a set of fractures is added to yield the overall rock compliance using the approach of Schoenberg & Sayers (1995). I follow Verdon et al. (2009) in using the low frequency approximation for penny shaped fractures in a matrix with equant porosity as described by Pointer et al. (2000), where the key variables are the fracture density (ξ) and strike (α) (see the discussion in section 5.2.1 in Chapter 5).

6.2.2 Inversion

The SWS inversion workflow is outlined in Figure 6.1. The inversion starts by performing a grid search over α, ξ, γ and δ in an iterative way. In each loop, the elastic stiffness tensor (C_{ijkl}) is computed. For each generated model, the velocities and polarisations of all three body waves (P, S_{fast} and S_{slow}) are estimated using ray theory. This is done by solving the Christoffel equation,

$$(C_{ijkl}p_j p_k - \rho\delta_{il})g_l = 0, \tag{6.6}$$

where p_i is the i-th component of slowness, g_l is the l-th component of polarisation, and ρ is the rock density. The Christoffel equation is used to compute the percentage difference between the fast and slow shear-wave velocities (δV_s=S_{fast}-S_{slow}/(S_{fast}-S_{slow}/2)) and Φ for each propagation direction that is present in the observed dataset (i.e., for each azimuth and inclination angle). The modelled δV_s and Φ are then compared with the observed ones (real data) and the root mean square (RMS) misfit is computed. The misfits for δV_s and Φ are then normalised by their respective minima to yield two misfit surfaces, which are then summed to give the overall misfit surface. The values of α, ξ, γ and δ which minimise the overall misfit are chosen as the optimum solution. Finally, the 90% confidence interval of the solution is computed using an F-test (e.g., Silver & Chan, 1991).

6.2.3 Inversion assuming two fracture sets

As mentioned earlier, the SWS inversion code of Verdon et al. (2009) is limited to cases with a single vertically aligned fracture set embedded in a VTI medium. According to Table 5.3 in Chapter 5, the majority of the SWS results show two predominant fracture strikes. To investigate this possibility, I modified the original inversion code of Verdon et al. (2009) to incorporate two vertically aligned fracture sets instead of one. However, this is done at the expense of excluding

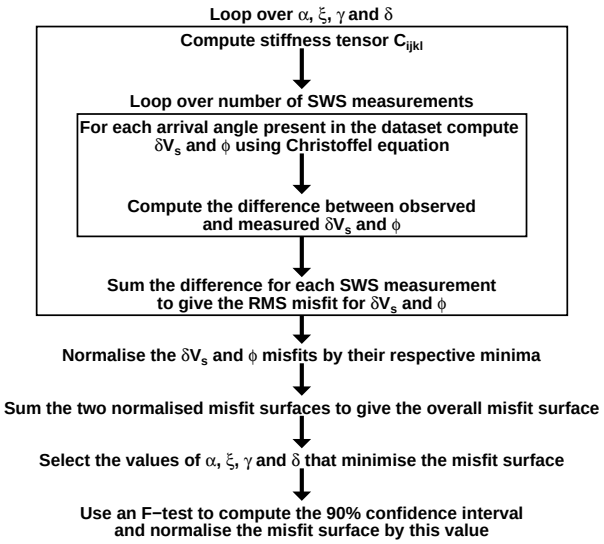

Figure 6.1: Shear-wave splitting inversion workflow (reproduced from Verdon et al. (2009)).

the inversion for the VTI parameters (γ and δ). The exclusion is aimed to reduce the degree of freedom by minimising the number of parameters in the inversion. Perhaps, if a priori knowledge about the VTI anisotropy strength is available, then γ and δ can be inputted into the inversion while constructing the stiffness tensor (Figure 6.1).

The workflow of the new code looks identical to the one shown in Figure 6.1 but this time the grid search is performed over ξ_1, α_1, ξ_2 and α_2 which are the density and strike of the first and second fracture sets, respectively. Throughout this chapter, I will refer to the inversion scheme of Verdon et al. (2009) as *MISHED* (Modelling and Inverting SHEar wave Differences) and the new inversion scheme, assuming two fracture sets, as *2Frac*.

6.2.4 Assumptions

The modelled fractures and sedimentary fabrics are assumed to be uniformly distributed with the fractures having vertical dip. *MISHED* and *2Frac* work under the assumption that the entire rock mass through which the seismic rays travel has uniform physical properties. In the case of significant spatial variation in anisotropy, the two inversion schemes may breakdown and fail to find minima in the grid search. Such failure, if it occurs, can be used to support the finding in Chapter 5 that there is a significant spatial variation in anisotropy within Field M.

The input velocities and densities are summarised in Table 6.1. I use average estimates of V_p and V_s obtained from the Field M 21-layer 1D model (see Figure 3.4 in Chapter 3). Estimates of

dataset	V_p (ms^{-1})	V_s (ms^{-1})	ρ (kgm^{-3})
Field-wide	3000	1560	2400
Fiqa	2300	1200	2200
Natih A	2800	1500	2400
Natih B-G	3500	1800	2400

Table 6.1: P- and S-wave velocities and rock densities used in the inversion of Field M SWS measurements.

Parameter	α	ξ	γ	δ	α_1	ξ_1	α_2	ξ_2
minimum	0°	0	-0.1	-0.3	0°	0	90°	0
maximum	180°	0.2	0.3	0.3	180°	0.2	180°	0.2
step size	5°	0.01	0.02	0.02	10°	0.01	10°	0.01

Table 6.2: Ranges of the SWS inversion parameters.

ρ were obtained from density logs (PDO in-house reports). When performing the inversion using measurements from the entire dataset, blocks and event clusters the density of the carbonate rocks (ρ=2400 kgm^{-3}) is used, as the field is mostly comprised of carbonate rocks.

The ranges and step sizes when searching for the optimum estimates of α, ξ, γ, δ, α_1, ξ_1, α_2 and ξ_2 are listed in Table 6.2. Assuming a maximum δV_s of 20% (see Chapter 4) and following the assumption of Crampin (1994) that fracture density is roughly equal to one hundredth of δV_s magnitude, I set the maximum fracture density to be 0.2. Wang (2002) carried out laboratory experiments on gas-saturated carbonate rock samples from Canada and the Gulf Coast and found that γ and δ ranges are approximately -0.044–0.12 and -0.20–0.22, respectively. The ranges change to -0.049–0.14 for γ and -0.16–0.15 for δ when the rocks are brine-saturated. Thomsen (1986) reported higher estimates of γ and δ in shales. To explore wider ranges of estimates, I set γ to vary between -0.1 and 0.3 and δ to vary between -0.3 and 0.3 (Table 6.2).

6.3 Synthetic modelling

In the SWS synthetic modelling in Chapter 5 we have seen the importance of having good ray coverage in order to describe any anisotropic symmetry. Here, I perform synthetic modelling to test the ability of the inversion in imaging the different ranges of anisotropic symmetries (HTI,

VTI, orthorhombic and monoclinic) based on the available ray coverage. Furthermore, I test the behaviour of the inversion when the anisotropy varies spatially.

A range of plausible ray propagation directions are chosen for each test. The Christoffel equation is used to compute δV_s and Φ for each propagation direction. Furthermore, random noise[1] of up to 0.3% and 10° is added to δV_s and Φ, respectively. These are typical error ranges for real microseismic splitting measurements (e.g., Al-Harrasi et al., 2010a; Verdon et al., 2009). The modelled data are then fed to the inversion codes: $MISHED$ and $2Frac$. The success of the inversion is assessed by comparing the input parameters, used in constructing the elastic model, with those revealed by the inversion. In addition, the misfit surfaces are inspected to see how well the solution is constrained.

6.3.1 VTI, HTI and orthorhombic media

Verdon et al. (2009) used synthetic modelling to examine the sensitivity of the inversion (*MISHED* code) to γ and δ. They performed three inversions at different raypath inclination ranges: subvertical (0°-30°), oblique (30°-60°) and subhorizontal (60°-90°). In each of the three inclination ranges there is a full range of arrival azimuths (i.e., 0°-180°). A VTI medium embedded with a single fracture set is assumed. Verdon et al. (2009) observed the following:
- For subhorizontal rays, γ is significant and δ is not well constrained. However, δ can be ignored in this case because the splitting of subhorizontal shear-waves is not significantly affected by the magnitude of δ.
- For subvertical arrivals neither γ nor δ can be imaged accurately.
- At oblique arrivals both γ and δ can be imaged.

Verdon et al. (2009) also investigated the capability of the inversion to recover γ, α and ξ in the case of limited ray coverage by simulating the geometry of a real microseismic dataset acquired from frac monitoring. The dataset consists of subhorizontal rays with arrivals limited to the NE-SW direction. They found that:
- When assuming a pure VTI medium, it is possible to estimate γ.
- When assuming a pure HTI medium with fracture strike perpendicular to ray propagation direction (i.e., NW-SE in this case), it is possible to recover α but not ξ.

[1]Random noise is generated using `rand(0)` command in FORTRAN 77.

- When placing the fracture set such that it is oblique to the ray propagation direction, it becomes possible to recover α and ξ.

Now, I repeat the procedure described above using the Field M microseismic data to understand the limitation of the inversion with this dataset (i.e., what can and cannot be imaged). First, I use the ray coverage shown by the entire dataset (325 measurements). I model five different anisotropic symmetries. These are VTI symmetry (γ=0.02 and δ=0.04), HTI symmetry (α=40° and ξ=0.05), HTI symmetry (α=120° and ξ=0.05), orthorhombic symmetry (α=40°, ξ=0.05, γ=0.02 and δ=0.04) and orthorhombic symmetry (α=120°, ξ=0.05, γ=0.02 and δ=0.04). The 40° and 120° account for the NE-SW and NW-SE fracture strikes revealed by the entire dataset in Chapter 5 (Table 5.3). The inversion results for the five cases are displayed in Figures 6.2-6.4 . The inversion is capable of recovering the input parameters except for the cases of orthorhombic symmetry, where ξ is not recovered accurately and shows elongated misfit contours (Figure 6.4). This can be explained by the limited ray coverage in the vertical plane. The accuracy in estimating ξ is expected to decrease with increased contamination from the VTI anisotropy. Similar observations (not plotted here) have been seen when simulating the ray coverage confined to the Natih A reservoir. It should be noted that the entire dataset and the Natih A subset show fairly good azimuthal coverage.

I also tested the case of limited azimuthal coverage. For this, I have chosen the F1-W4 subset (34 measurements) which shows subhorizontal rays limited to the azimuth range between 260° and 360° (Figure 6.5). I considered the same five anisotropic symmetries tested with the entire dataset. The results are displayed in Figures 6.5-6.7. Similar to what we have seen with the entire dataset, the inversion is able to recover the input parameters except for the cases of orthorhombic symmetry. However, in the case of HTI symmetry (Figure 6.6) the inversion is able to recover the 0.05 fracture density but the misfit surface is elongated along the ξ-axis, indicating a poorly constrained solution. In the case of orthorhombic symmetry with α=40°, the inversion does not recover ξ accurately and shows elongated misfit contours (Figure 6.7a). Things becomes even worse when the orthorhombic symmetry has α=120° (Figure 6.7b). In this case, the inversion fails to detect the presence of VTI anisotropy (γ=δ=0) and gives the wrong estimate of fracture density (ξ=0.04). The failure to accurately determine ξ is not surprising given the limited vertical ray coverage, whereas the failure to detect the VTI anisotropy is explained by the limited azimuthal coverage. To successfully detect the VTI anisotropy, horizontal rays propagating oblique and/or

perpendicular to the fracture plane are required (see Figure 5.1d and discussion in section 5.2.2, Chapter 5).

6.3.2 Monoclinic media

In this section I repeat the same recipe as above but this time for the case of isotropic media with two fracture sets and using the *2Frac* inversion code. I assume two fracture sets with strikes of α_1=40° and α_2=120°, and having the same fracture density (ξ_1=ξ_2=0.05). First, I test the inversion at different inclination ranges: subvertical (0°-30°), oblique (30°-60°) and subhorizontal (60°-90°). Again, full azimuth range of arrivals is used (i.e., 0°-180°). The results are shown in Figure 6.8. The inversion of the subhorizontal arrivals gives well constrained results (Figure 6.8c). As moving towards normal incidence, clear trade-offs in the estimates of fracture strike and density are observed (Figures 6.8a,b). In the second step, I repeat the inversion but this time simulating the ray coverage shown by the entire dataset and the F1-W4 subset. The results are shown in Figure 6.9. For both datasets, the input parameters are recovered accurately. However, for the case of the F1-W4 subset, there is a clear trade-off in the estimate of ξ_1 which corresponds to α_1=40°. This fracture set is almost perpendicular to the ray propagation direction in this example. In contrast, the estimates of ξ_2 and α_2 are well constrained. The second fracture set is trending almost parallel to the ray propagation direction.

In the case of subhorizontal arrivals, rays sense the effect of each fracture set individually. In contrast, in the case of oblique and subvertical arrivals, rays start sensing the bulk effect of the two fracture sets making the resultant effect more complicated (see discussion in section 5.2.2, Chapter 5). Such complexity is expected to increase in the case of two fracture sets with different fracture density. Analysis of Φ for near-vertical ray propagation in the presence of two fractures (e.g., Liu et al., 1993; MacBeth, 1996) found that the effective fast polarisation (Φ_{eff}) is equal to the fracture-density-weighted average direction between the conjugate sets,

$$\Phi_{eff} = \frac{\alpha_1\xi_1 + \alpha_2\xi_2}{\xi_1 + \xi_2}. \tag{6.7}$$

We have already seen such effects with the SWS modelling in section 5.2.2 of Chapter 5. This is highlighted here by the appearance of clear trade-offs in the misfit plots of α_1 versus α_2 (Figures 6.8 and 6.9). In these examples, any combination of fracture strikes around the mean strike direction (80° in this case) would explain the modelled Φ as long as they have the right combination of densities to satisfy Equation (6.7). This also might be a problem when inverting for two fracture

sets (i.e., using *2Frac* code) for the case of one fracture set. In such a situation, from the inversion we expect to either get one of the fracture with negligible density and the other one with the true input strike and density or two fracture strikes having similar separation from the true input strike and have exact density or two fracture strikes having separation from the true input strike weighted by their corresponding densities. In fact, this might be an issue when inverting the real data, expecting large trade-offs in the estimates of α_1 and α_2.

6.3.3 Spatial variation in anisotropy

Early in section 6.2.4 we speculated that the two inversion approaches (*MISHED* and *2Frac*) might breakdown in the presence of significant spatial variation in anisotropy. Here, I test the success of the inversion in the case of spatial variation in anisotropy using synthetic examples that are analogous to the nature of anisotropy in Field M.

In the first example, I consider the transition with depth from VTI anisotropy (Fiqa shale) to HTI anisotropy (fractured Natih formation). I generate two synthetic models separately (i.e., two subsets). The first subset comes from pure VTI medium with γ=0.02 and δ=0.04, and the second one comes from HTI medium with α=40° and ξ=0.05. In both models, full ranges of inclination (0°-90°) and azimuths (0°-180°) are considered as to avoid the effect of ray coverage. The two subsets are then merged to create one dataset. To some extent, this is now analogous to gathering SWS measurements from the Fiqa and Natih formation simultaneously (i.e., the entire dataset in Table 5.3). Finally, the measurements are fed into the *MISHED* code. The results are shown in Figure 6.10 . The outputs (α=50°, ξ=0.03, γ=0 and δ=0.02) do not match with the inputs and trade-offs are clearly shown by the misfit surfaces. We conclude that the inversion fails in the case of variation in anisotropy with depth.

In the second example, I consider the lateral variation in anisotropy. This example is analogous to the case of recording SWS measurements from the Graben block and the NW block. For the Graben block, I consider a fracture set with strike of α_1=40° (parallel to the graben faults) and density of ξ_1=0.05. In contrast, the NW block has α_2=120° (parallel to the minor faults in this part of the field) and ξ_2=0.05. Again, to avoid the effect of ray coverage, a full range of propagation angles is considered but this time the Graben block is imaged by rays in the azimuth range 0°-180° whereas, the NW block is imaged by rays in the azimuth range 180°-360° (i.e, two different subsets with two different azimuth ranges). Then, the two subsets are merged to form one dataset. To some extent, this now simulates the transition in the fracture strike as moving from the Graben

block to the NW block. Finally, the measurements are fed into the *2Frac* code. The results are displayed in Figure 6.11. Again, the outputs (α_1=60°, ξ_1=0.02, α_2=100° and ξ_2=0.04) are not well constrained and do not agree with the original inputs. We conclude that the inversion fails in the existence of lateral variation in anisotropy.

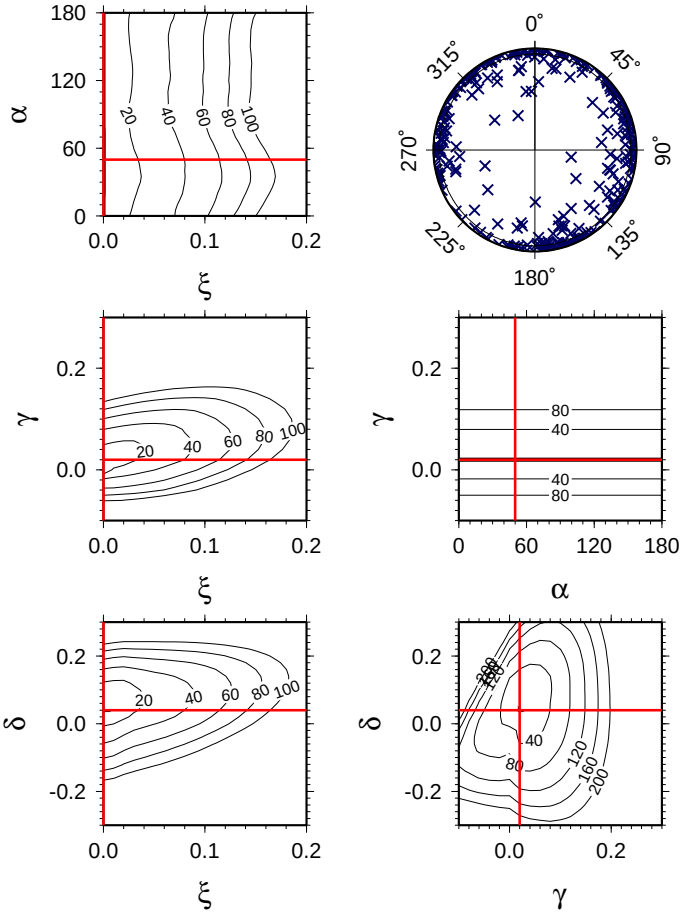

Figure 6.2: Shear-wave splitting inversion for fracture strike (α), fracture density (ξ) and VTI parameters (γ and δ) assuming a VTI medium (γ=0.02 and δ=0.04). The ray coverage, top-right circle, is that for the entire dataset. The red lines mark the inversion results. The misift contours are normalised such that 1 indicates the 90% confidence limit.

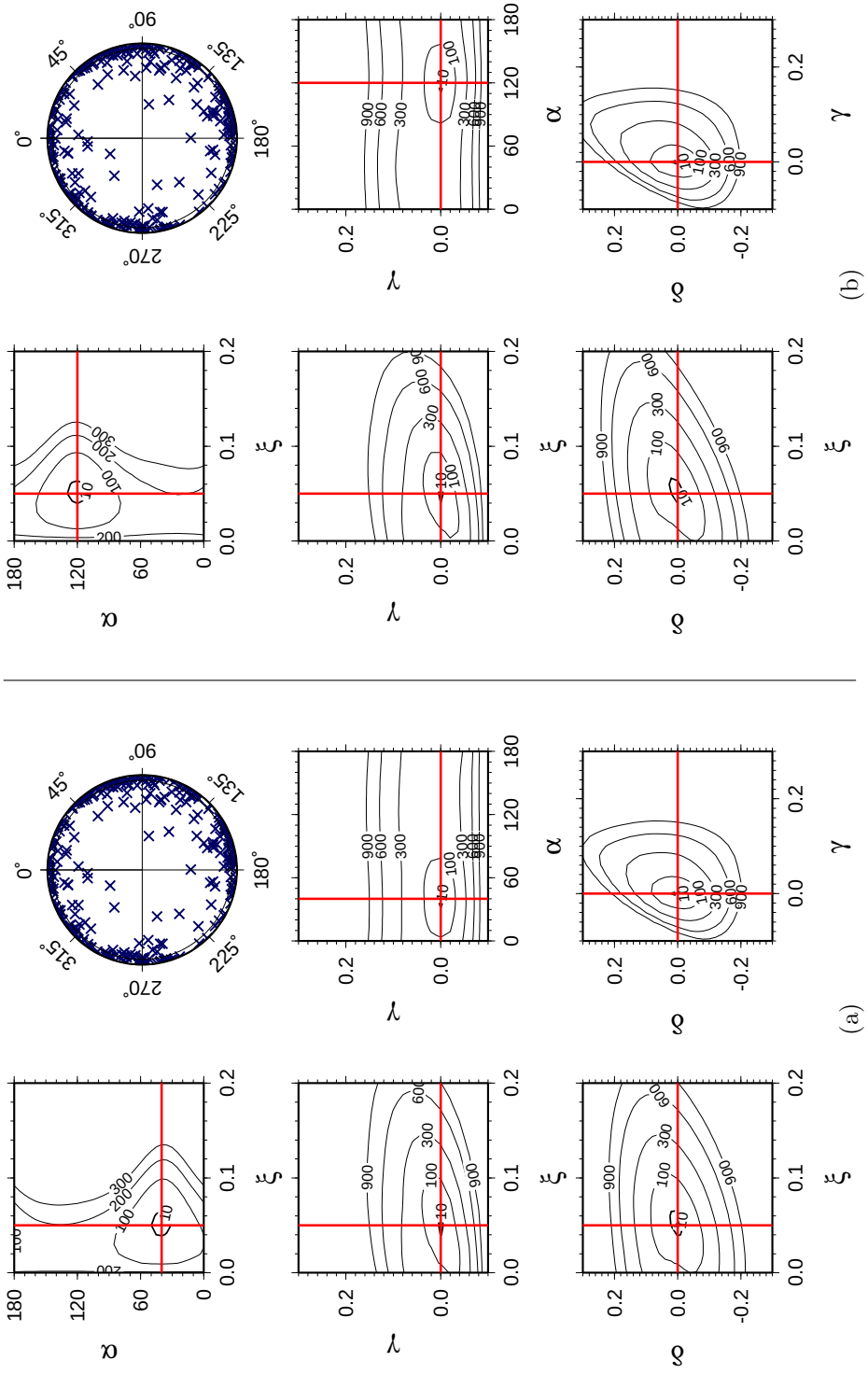

Figure 6.3: Shear-wave splitting inversion assuming an HTI medium with fracture strike of (a) 40° and (b) 120° (see Figure 6.2 caption). The fracture density is 0.05 in both models. The ray coverage, top-right circle, is that for the entire dataset.

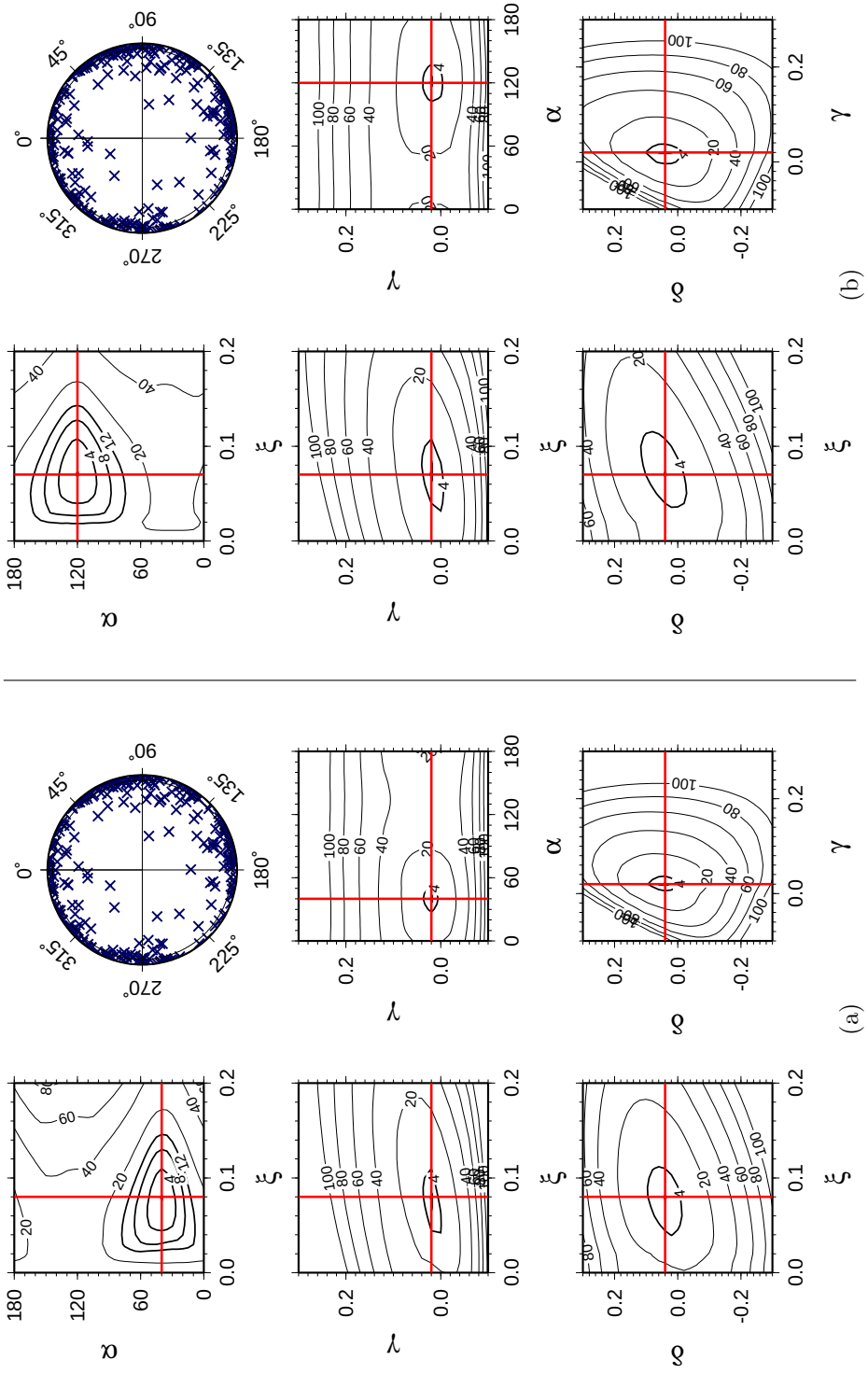

Figure 6.4: Shear-wave splitting inversion assuming a superposition of VTI symmetry (γ=0.02 and δ=0.04) and HTI symmetry with fracture strike of (a) 40° and (b) 120° (see Figure 6.2 caption). The fracture density is 0.05 in both models. The ray coverage, top-right circle, is that for the entire dataset.

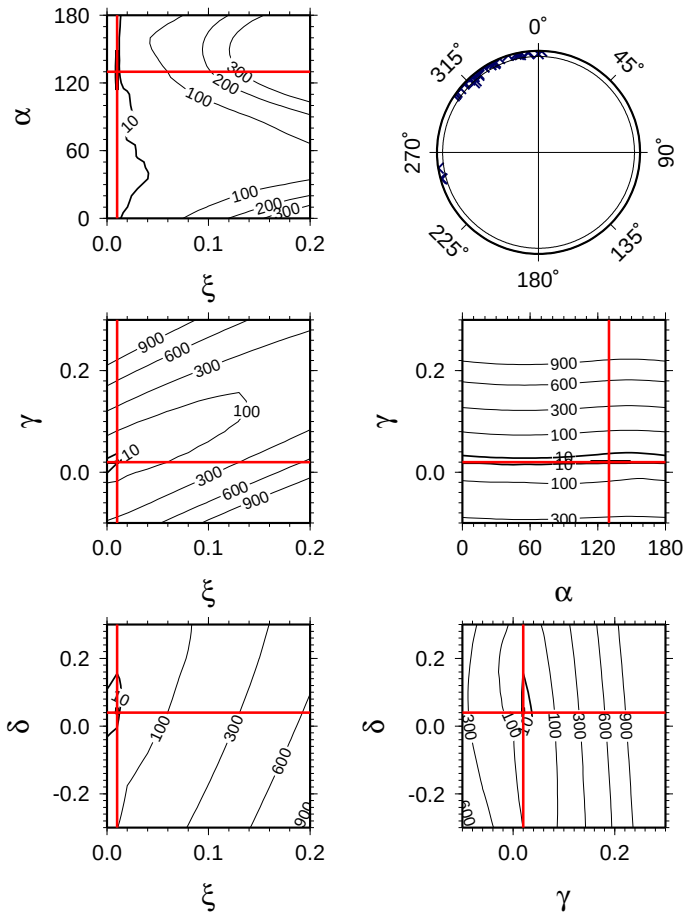

Figure 6.5: Shear-wave splitting inversion assuming a VTI medium (γ=0.02 and δ=0.04) (see Figure 6.2 caption). The ray coverage, top-right circle, is that for the F1-W4 subset.

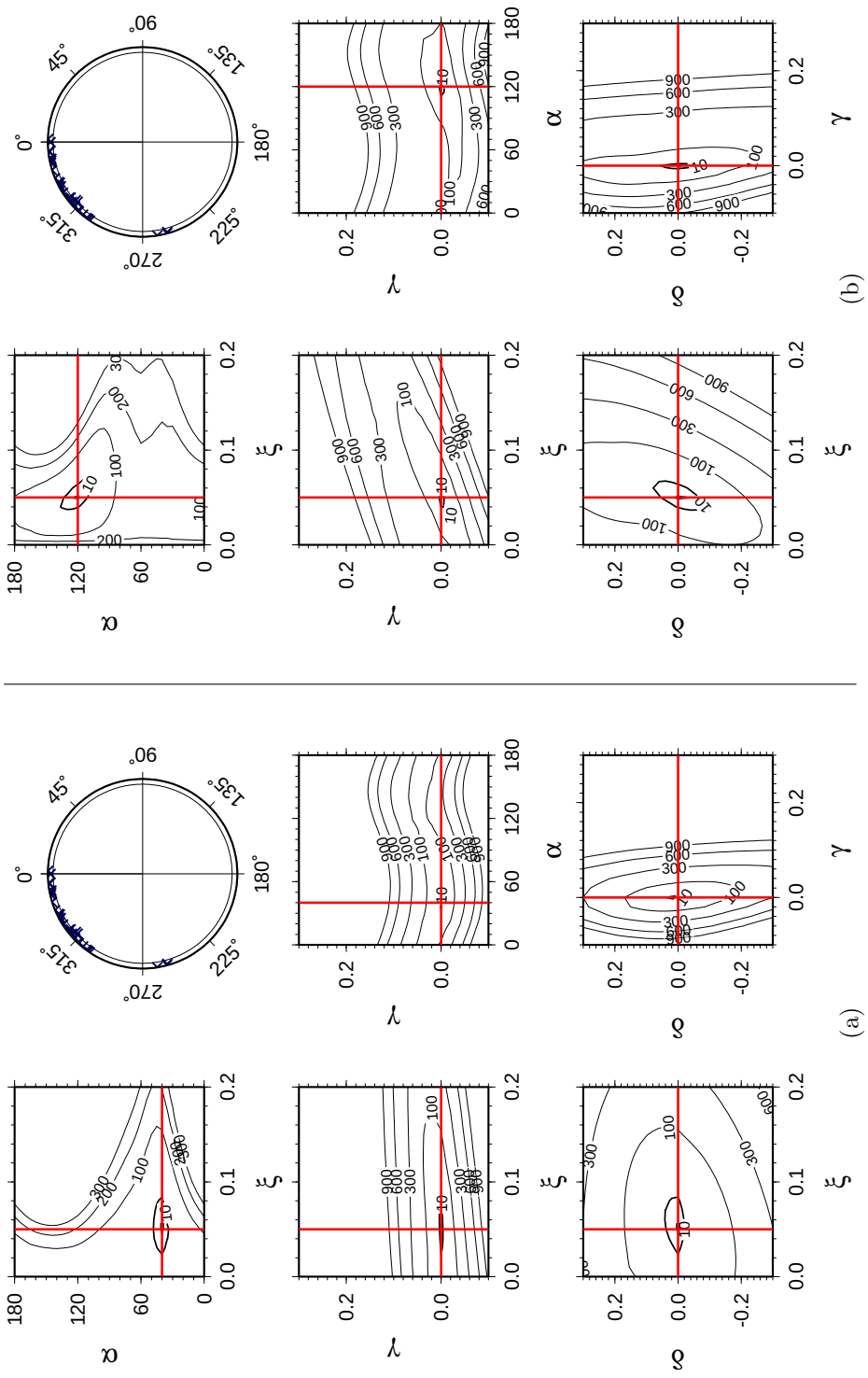

Figure 6.6: Shear-wave splitting inversion assuming an HTI medium with fracture strike of (a) 40° and (b) 120° (see Figure 6.2 caption). The fracture density is 0.05 in both models. The ray coverage, top-right circle, is that for the F1-W4 subset.

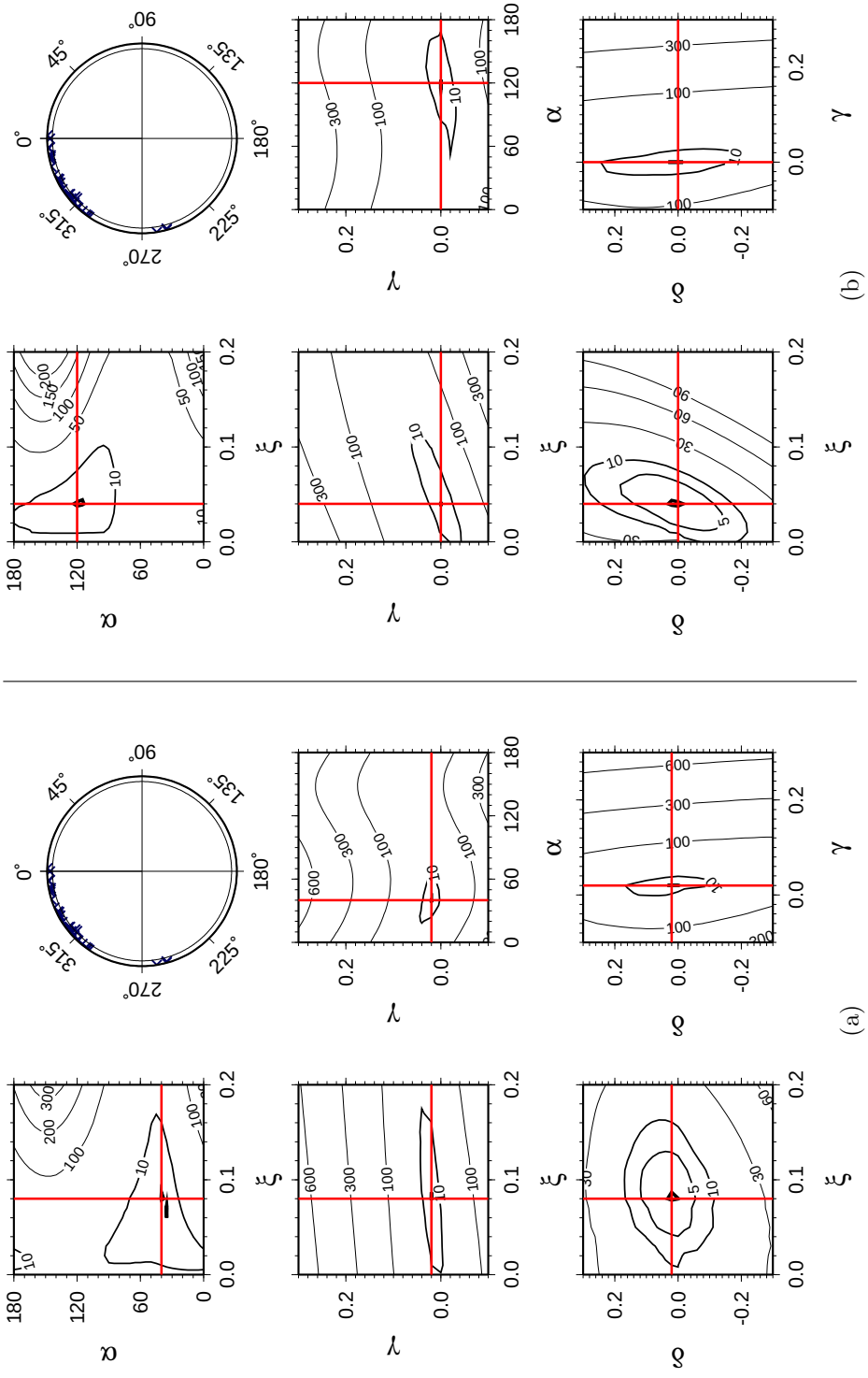

Figure 6.7: Shear-wave splitting inversion assuming a superposition of VTI symmetry (γ=0.02 and δ=0.04) and HTI symmetry with fracture strike of (a) 40° and (b) 120° (see Figure 6.2 caption). The fracture density is 0.05 in both models. The ray coverage, top-right circle, is that for the F1-W4 subset.

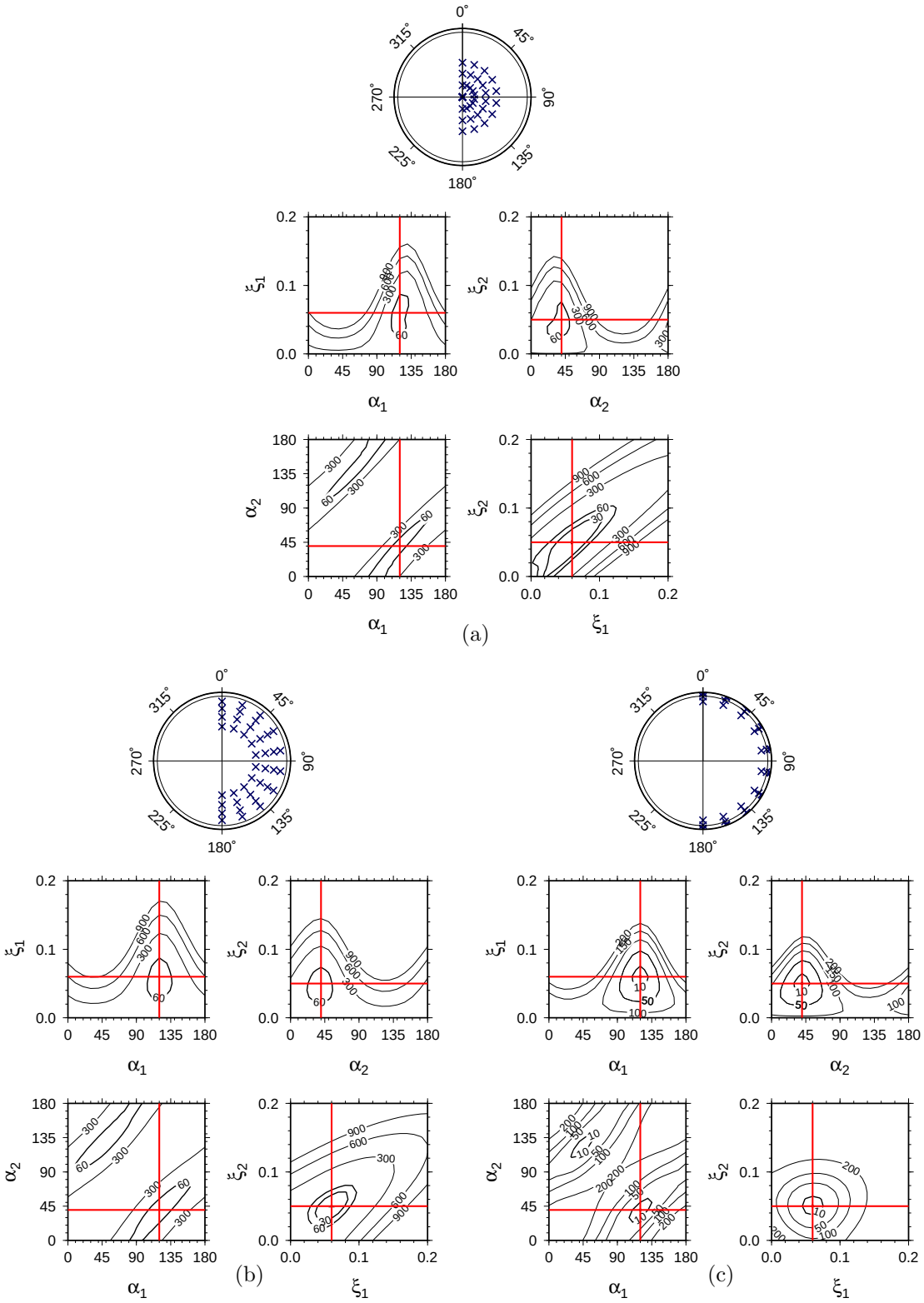

Figure 6.8: Shear-wave splitting inversion assuming a medium with two fracture sets (α_1=40°, α_2=120° and ξ_1=ξ_2=0.05). The inversion is performed assuming different ray inclination ranges from vertical: (a) 0°-30°, (b) 30°-60° and (c) 60°-90°. The red lines mark the inversion results. The misift contours are normalised such that 1 indicates the 90% confidence limit.

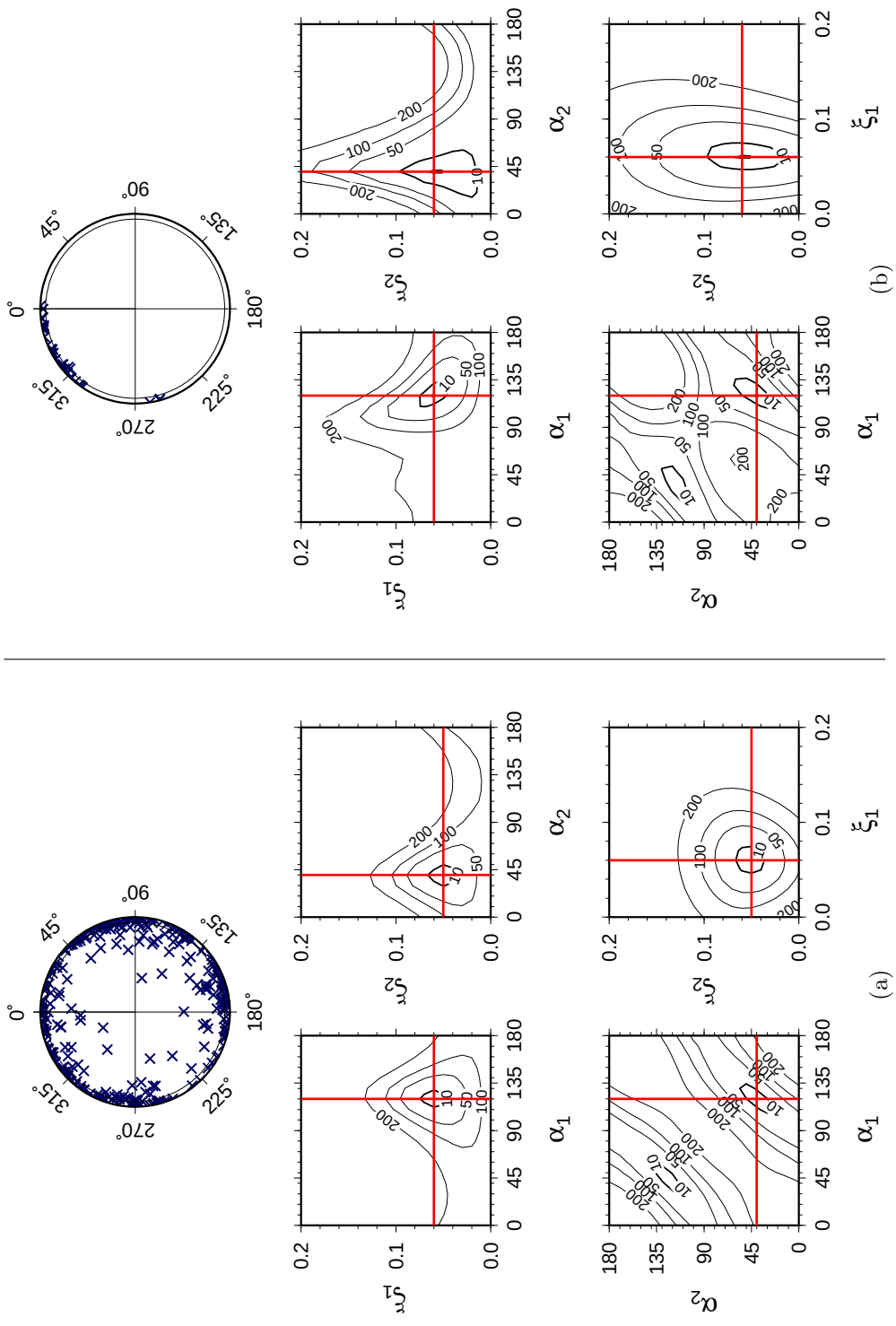

Figure 6.9: Shear-wave splitting inversion assuming a medium with two fracture sets (α_1=40°, α_2=120° and ξ_1=ξ_2=0.05) (see Figure 6.8 caption). The inversion is performed assuming the ray coverage of (a) the entire dataset and (b) the F1-W4 subset.

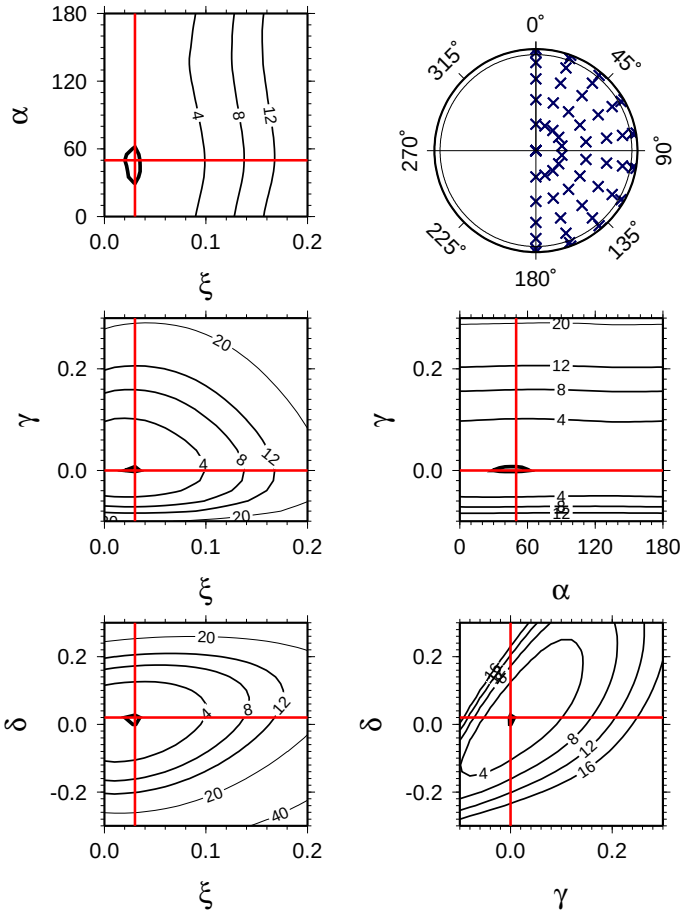

Figure 6.10: Shear-wave splitting inversion assuming a transition in depth from VTI anisotropy (γ=0.02 and δ=0.04) to HTI anisotropy (α=40° and ξ=0.05) (see Figure 6.2 caption). The VTI and HTI models were constructed separately. The results are then merged to form one dataset. The outputs (α=50°, ξ=0.03, γ=0 and δ=0.02) do not match any of the original inputs.

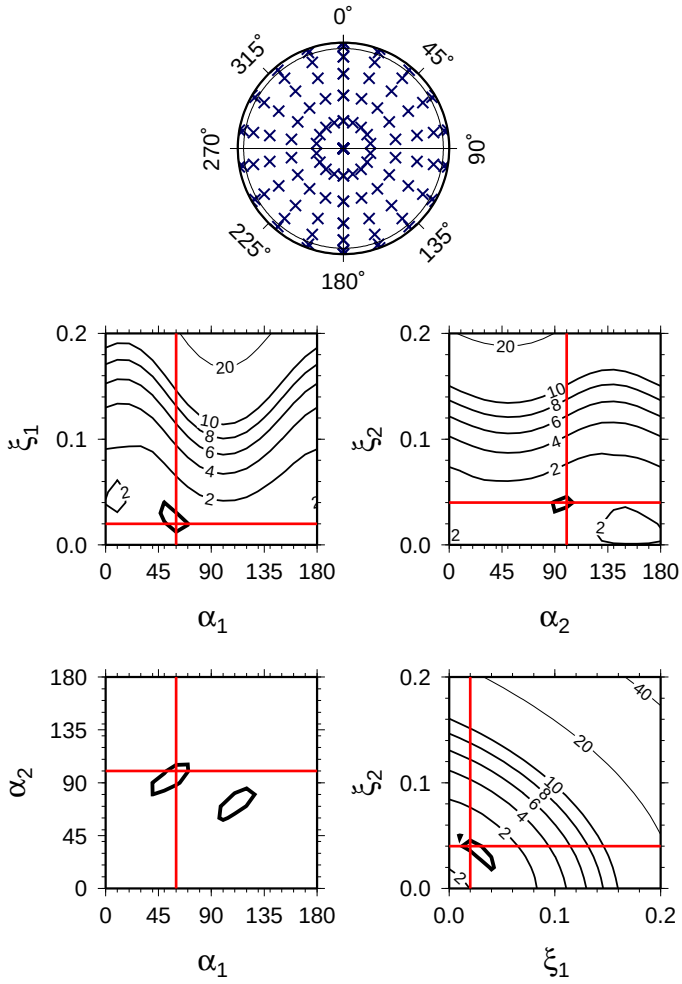

Figure 6.11: Shear-wave splitting inversion assuming a lateral transition from HTI symmetry with α_1=40° (azimuth from 0° to 180°) to HTI symmetry with α_2=120° (azimuth from 180° to 360°). ξ_1=ξ_2=0.05. The outputs (α_1=60°, α_2=100°, ξ_1=0.02 and ξ_2=0.04) do not match any of the original inputs.

6.4 Results

The groups of measurements listed in Table 5.3 (Chapter 5) are used to invert for anisotropy parameters. A detailed description of these groups can be found in Chapter 5. For each group of measurements, I tested inversions for two cases: (1) VTI plus a single vertical fracture set using the *MISHED* code and (2) two vertical fracture sets using the *2Frac* code. The results are summarised in Table 6.3. The misfit surfaces from the F-tests are shown in Figures 6.12 to 6.27. These are used to assess confidence in the inversion outputs.

Since the magnitude of δ does not significantly affect the SWS of subhorizontal arrivals, which is the case with most of the Field M measurements, the strength of the VTI anisotropy is inter-

dataset	number of measurements	Orthorhombic				Monoclinic			
		α (°)	ξ	γ	δ	α_1 (°)	ξ_1	α_2 (°)	ξ_2
All	325	130	0.01	-0.02	-0.08	0	0.04	100	0.04
SE block	132	140	0.02	-0.02	-0.08	30	0.06	120	0.06
Graben block	17	95	0.2	0.1	0.28	170	0.1	110	0.12
NW block	58	90	0.03	0	-0.06	40	0.03	120	0.03
Well-1	13	65	0.11	0.02	-0.04	140	0.07	60	0.14
Well-2	8	70	0.13	-0.04	0	90	0.2	170	0.16
Well-3	37	140	0.03	-0.02	-0.12	140	0.08	80	0.06
F1-W2	23	60	0.1	-0.04	-0.06	70	0.15	0	0.05
F1-W4	34	135	0.04	0.02	0.04	30	0.01	120	0.02
F2-W1	25	45	0.03	0	-0.04	140	0.01	60	0.03
Horseshoe	25	130	0.09	0.06	0.04	110	0.05	20	0.05
Fiqa	8	75	0.15	0.02	-0.24	70	0.15	160	0.04
Natih A	44	35	0.01	-0.02	-0.2	110	0.07	170	0.02
Natih B-G	92	135	0	0.02	0.08	110	0.03	20	0.03
Natih B-G1	47	55	0.01	-0.02	-0.08	40	0.04	120	0.02
Natih B-G2	6	120	0.11	0.02	0.16	20	0.01	30	0.01

Table 6.3: Results from the SWS inversion of real data assuming orthorhombic symmetry (α, ξ, γ and δ) and monoclinic symmetry (α_1, ξ_1, α_2 and ξ_2).

preted based on the magnitudes of γ only. However, no independent estimate of γ for Field M is available. Instead, for comparison purposes, I use the estimates obtained by Wang (2002) for gas-saturated carbonate samples (max=0.123, min=-0.044, median=0.005 and average=0.013) and brine-saturated carbonate samples (max=0.136, min=-0.049, median=0.004 and average=0.014). Based on the average estimates of γ, the expected VTI anisotropy in the gas-saturated Natih A reservoir and the non-producing Natih B-G unit (assumed brine-saturated) would be in the order of 0.01. γ is expected to be higher in the shale (e.g., Thomsen, 1986). However, it is worth mentioning that the results by Wang (2002) generally show large scatter. The experiments were carried out using very tight limestone and dolomite samples with low porosity ($\sim$0.5–10%) and under pressures of 6.9 MPa and 55 MPa. For the Field M rocks, the average porosity in the Natih A and Natih B-G is 30% and 24%, respectively, and the pressure conditions might be different. Thus, the magnitudes of γ by Wang (2002) may not reflect the VTI anisotropy in Field M.

Entire dataset

The inversion of measurements from the entire dataset (Figure 6.12a) yields a predominant fracture strike in the NW-SE direction (130°). This strike direction is in a good agreement with the 117° strike obtained from ordinary SWS analysis (Figure 5.9a). However, there is a trade-off in this estimate of fracture strike (Figure 6.12a), reflecting probably the existence of more than one fracture set. A similar trade-off is also observed when assuming two fracture sets (Figure 6.12b). The estimated fracture density is low, both when assuming one fracture set (ξ=0.01) and two fracture sets (ξ_1=ξ_2=0.04). The magnitude of γ is -0.02.

SE block

The inversion results for the SE block measurements are shown in Figure 6.13. The inversion for one fracture set shows a NW-SE (140°) predominant fracture strike that is in a good agreement with the fracture strike obtained from ordinary SWS analysis (132°; Table 5.3). A similar fracture strike (120°) is revealed when assuming two fracture sets. The second fracture set has a strike of 30°, which is in a good agreement with the 39° strike estimated from ordinary SWS analysis (Table 5.3). The estimated fracture density is 0.02, which increases to 0.06 (for both) when assuming two fracture sets. The estimated strength of the VTI anisotropy is similar to that obtained for the entire dataset (γ=-0.02).

Graben block

The Graben block subset shows poor ray coverage, resulting in biased results both when assuming one and two fracture sets (Figure 6.14). Thus, the results from both inversions must not be used in any interpretation.

NW block

Although, the NW block subset shows fair ray coverage, the fracture strike and density remain unconstrained (Figure 6.15). The inferred 90° fracture strike was not observed when interpreting the fast strike independently from δV_s in Figure 5.15c. It also does not agree with the fault patterns in the NW block of the field. The misfit surface in Figure 6.15a shows a range of possible strikes ranging from NE-SW to NW-SE, rendering this estimate of strike doubtful. It is interesting that NE-SW (40°) and NW-SE (120°) fracture strikes are obtained when inverting for two fracture sets (Figure 6.15b), but with trade-offs in the solution. Fracture density of 0.03 is obtained from the two types of inversion. The magnitude of γ is zero, representing the absence of VTI anisotropy.

Well-1

The outputs from the SWS inversion of the Well-1 measurements (Figure 6.16) look better constrained compared to the previous four datasets, although the number of SWS measurements is smaller. When assuming one fracture set, the estimated fracture strike (65°) is consistent with the strike estimated from ordinary SWS analysis (66°; Figure 5.18a). In contrast, when assuming two fracture sets, NW-SE (140°) and NE-SW (60°) fracture strikes are obtained but suffering from clear trade-offs. The second fracture strike (60°) is better constrained than the first one, which supports the obtained strike (65°) when assuming a single fracture set. The estimated fracture density is high both when assuming one (ξ=0.11) and two fracture sets (ξ_1=0.07 and ξ_2=0.14). γ has a magnitude of 0.02.

Well-2

The limited number of measurements (8 measurements) results in poorly constrained outputs from the inversion of Well-2 subset, especially when assuming two fracture sets (Figure 6.17). Thus, the inversion outputs can not be used in any interpretation.

Well-3

The inversion of Well-3 measurements shows clear trade-offs in the estimates of fracture strike and density (Figure 6.18). However, the inferred NW-SE (140°) fracture strike both when assuming

one fracture set and two fracture sets agrees with the strike estimated from ordinary SWS analysis (151°; Figure 5.18c). Moreover, the second fracture set revealed by the inversion has strike of 80° which is in a good agreement with the 90° strike shown in Figure 5.18c. The fracture density is low when assuming one fracture set (ξ=0.03) and moderate to high when assuming two fracture sets (ξ_1=0.06 and ξ_2=0.09). The magnitude of γ is low -0.02.

F1-W2

The measurements in this subset show limited ray coverage (Figure 6.19). The poor ray coverage greatly affected the estimates of fracture density. The outputs from the second inversion, with the assumption of two fracture sets, are not usable due to the large trade-offs in the estimated parameters (Figure 6.19b). The estimated fracture strike (60°), when assuming a single fracture set, is sub-parallel to the NE-SW strike of the main graben faults that the rays travel between. The estimated fracture density is high (ξ=0.1), reflecting the high anisotropy magnitudes observed within the graben system (Figure 5.17d). The magnitude of γ is -0.04.

F1-W4

The outputs from the inversion are well constrained when assuming one fracture set and poorly constrained when assuming two fracture sets (Figure 6.20). Thus, the results from the second inversion with two fracture sets are not used. The fracture strike is oriented NW-SE (135°) which is consistent with the fault trends in the NW part of the field. The fracture density is low (ξ=0.04) which agrees with the low anisotropy in this part of the field. Similar to the Well-1 cluster (both estimates are for the NW part of the field), the measurements from the F1-W4 group reveal γ magnitude of 0.02.

F2-W1

Similar to the F1-W4 subset, the outputs from the inversion assuming one fracture set are much better constrained then when assuming two fracture sets (Figure 6.21). Therefore, the results from the later inversion are rejected. The 45° fracture strike is in a good agreement with the NE-SW trend of the graben faults. Remember, the rays of this subset travel within the rock volume between the two graben faults. The fracture density is low (ξ=0.03). The VTI anisotropy is negligible (γ=0).

Horseshoe

The inversion outputs are fairly well constrained both when assuming one and two fracture sets (Figure 6.22). In the case of one fracture set embedded in a VTI medium, the obtained fracture strike is NW-SE (130°) with high fracture density of 0.09. In the case of two fracture sets, the two strikes are 20° and 110° and the fracture density is 0.05 for both. In addition to the high fracture density, anisotropy within the Horseshoe is controlled by relatively high VTI strength (γ=0.06).

Fiqa

The size of the Fiqa subset is small (8 measurements), rendering the inversion outputs poorly constrained, especially in the second inversion with two fracture sets which are not useful (Figure 6.23). The estimated ENE-WSW (75°) fracture strike from the first inversion, assuming single fracture strike, is fairly well constrained, although, its corresponding fracture density (ξ=0.15) is poorly constrained. Identical fracture strike and density are obtained from the second inversion assuming two fracture sets. The shale shows relatively moderate VTI anisotropy (γ=0.02).

Natih A

The Natih A subset shows moderate azimuthal coverage, but poor coverage in the vertical plane (Figure 6.24). The estimates of fracture strike and density are poorly constrained in both inversions, especially with the case of two fracture sets, which can not be used for any interpretation. The first inversion, assuming one fracture set, reveals a NE-SW (35°) fracture strike with fracture density of 0.01, but with elongated misfit contours in the α-axis (Figure 6.24a). This strike does not agree with either strikes estimated from ordinary SWS analysis (62° and 120°, Table 5.3). However, both these fracture strikes are poorly constrained due to the few measurements of fast strike available, as discussed in Chapter 5. The magnitude of γ is -0.02.

Natih B-G

Due to the lack of subvertical rays, the estimates of fracture strikes and densities are poorly constrained for the Natih B-G subset (Figure 6.25). In contrast, γ and δ are well constrained because of the good ray coverage in the horizontal plane. When assuming one fracture set, the fracture density is zero indicating that fractures do not exist in this unit. This seems unrealistic. However, in the case of two fracture sets, the obtained 20° and 110° are in a good agreement with the strikes estimated from ordinary SWS analysis (14° and 120°, Table 5.3). The fracture density is 0.03 for both fractures.The magnitude of γ is 0.02.

The Natih B-G formation is further investigated by inverting the SWS measurements in the upper part of the formation (Natih B-G1; Figure 6.26) and the lower part of the formation (Natih B-G2; Figure 6.27). Due to the small number of measurements available for the Natih B-G2 unit, the results are biased and cannot be used. The estimated fracture strike and density in the Natih B-G1 are 55° and 0.01, respectively, when assuming one fracture set. However, the estimated fracture strike is poorly constrained. Similar strike (40°) but with higher density (0.04) is revealed when assuming two fracture sets. The second fracture set has strike of 120° and density of 0.02. The magnitude of γ is -0.02.

6.5 Discussion and interpretation

The frequently occurring trade-offs between anisotropy parameters in the inversion reflects either or both the limited ray coverage and the spatial variation in the anisotropy seen in Chapter 5. The spatial variation in anisotropy seems to have higher impact on the inversion because the groups with less number of measurements often give better constrained outputs compered to large subsets (e.g., compare Figure 6.12 with Figure 6.16). The trade-offs when inverting for two fracture sets can be attributed to the fact that any fast polarisation direction (Φ), especially for subvertical rays, is a strike of one fracture set or a fracture-density-weighted strike lying between two fracture sets (see early discussion in section 6.3.2). Overall, the results from the $MISHED$ code (assuming a single fracture set in a VTI medium) are better constrained in comparison to the results from the $2Frac$ code (assuming two fracture sets).

Despite the scatter in the results, the inversion allowed for the determination of the VTI anisotropy strength and the estimation of fracture strike and density which were not possible in some cases when using direct interpretation of Φ and δV_s (Table 5.3). For instance, for the first time we have estimates of fracture strike for the F1-W2 and F1-W4 subsets. In the following, I compare and contrast the variation in the fracture parameters (strike and density) and strength of the VTI anisotropy among the different subsets. The inversion parameters from the Graben block, the Well-2 cluster and the Natih B-G2 are not considered as they are too poorly constrained.

Fracture orientation

Generally, similar observations to those seen in Chapter 5 are obtained from the inversion in that fractures follow the major fault patterns. The trusted estimates of strike are summarised in Figure 6.28. It can be seen that rays travelling between the two main graben faults reveal NE-SW fracture

orientation, whereas rays travelling within the SE and NW parts of the field show predominant NW-SE fracture strike. This agrees with the results from ordinary SWS analysis (see Chapter 5). Measurement groups which show NE-SW fracture strike sub-parallel to the trend of the graben system are F1-W2 (60°, Figure 6.19a) and F2-W1 (45°, Figure 6.21a). Evidences of NW-SE fracture strike in the SE part of the field were observed using measurements from the SE block (140°, Figure 6.13a), the Well-3 cluster (140°, Figures 6.18a,b) and the Horseshoe cluster (130°, Figure 6.22a). In the NW part, the NW-SE fracture strike was observed for measurements from the Well-1 cluster (140°, Figure 6.16b) and the F1-W4 group (135°, Figure 6.20a). In addition, a NW-SE fracture strike is revealed when inverting the entire dataset but with trade-off (Figure 6.12a). There are also some evidences of NE-SW strike in the SE and NW parts of the field, but only when inverting for two fracture sets (see Figure 6.28).

Fracture orientation varies with lithology from 75° in the Fiqa shale (Figure 6.23a) to 35° in the Natih A reservoir (Figure 6.24a) to 55° in the Natih B-G1 unit (Figure 6.26a). Despite the large trade-off, these estimates are in a good agreement with the finding of Al-Anboori (2006) using a subset of Field M microseismic data. Al-Anboori (2006) showed that the strike of the fractures is E-W (90°) in the Fiqa cap rock, NNE-SSW (19°) in the Natih A and NE-SW (45°) in the Natih B-G1.

Fracture density

Except for the measurements around monitoring well 1 and within the Horseshoe feature (Table 6.3), the estimates of fracture density show a homogenous spatial distribution. For most cases the inversion reveals fracture density of around 0.03. This homogenous distribution of fracture intensity contradicts with our expectation that fracture density should correlate with the change in the δV_s magnitude. Similar contradiction is observed when comparing fracture density estimates for the Natih A and Natih B-G. Both units have fracture density of 0.01. However, it should be noted that fracture density is, generally, the least constrained parameter from the inversion. This is mainly due to the limited ray coverage in the vertical plane. Furthermore, this might be partly due to the oversimplification of restricting the analysis to the case of penny shaped fractures in a matrix with equant porosity (see section 6.2.1 above). Such assumption might not be appropriate for the Field M rocks. A better conclusion on the variation of fracture density with lithology and proximity to the graben faults is expected when performing frequency-dependent anisotropy analysis in the next chapter. Similar failures to constrain the estimates of fracture density have

been reported by Verdon et al. (2009) and Verdon et al. (2010), who applied the $MISHED$ code to microseismic datasets from frac job monitoring.

VTI anisotropy strength

Owing to the good ray coverage in the horizontal plane, the majority of the inversions give well constrained estimates of the VTI anisotropy strength (i.e., estimates of γ). In general, the magnitudes of γ are relatively close to the expected 0.01 for carbonate rocks (see discussion in section 6.4 above). However, it is interesting that measurements in the NW part of the field show positive γ (Well-1 (0.02) and F1-W4 (0.02)), whereas measurements within the SE part of the field (SE block (-0.02) and Well-3 (-0.02)) and between the graben faults (F1-W2 (-0.04)) show negative γ, except for the Horseshoe which shows unexpectedly high γ (0.06). Also, all the lithology units show the same magnitude of γ, but it is negative in the Natih A and positive in the Fiqa shale and Natih B-G formation. For horizontally propagating rays and in the case of weak anisotropy, the magnitude of γ represents the fractional difference between the vertical (S_v) and horizontal (S_h) shear-wave velocities ($\gamma \approx (S_h\text{-}S_v)/S_v$) (see for example Thomsen (2002)). In a very generalised way we can correlate the polarity of γ to the presence of VTI and HTI symmetries (i.e., positive γ indicates VTI symmetry, whereas negative γ indicates HTI symmetry). In this way we conclude that the VTI anisotropy is more dominant in the NW part of the field and within the Fiqa shale and the Natih B-G formation. It is less significant in the highly fractured regions (SE and Graben blocks, and the Natih A reservoir).

6.6 Conclusion

I demonstrated the use of rock physics modelling to invert SWS measurements in order to characterise the subsurface architecture. Two types of inversions were performed using two assumptions: (1) a single fracture set embedded in a medium with a VTI sedimentary fabric and (2) two conjugate fracture sets. The inversion allowed for characterisation of fractures and estimation of VTI anisotropy strength that was not possible using direct interpretation of the splitting parameters (Φ and δt). The limitation of the inversion is tested using synthetic examples of different anisotorpic symmetries. Plausible ray propagation directions were chosen to test and understand the effect of ray coverage on the success of the inversion. Moreover, the failure of the inversion in the presence of spatial variation in anisotropy has been illustrated using synthetic models.

The frequently observed trade-offs when inverting the real data are attributed to the spatial variation of the anisotropy in Field M and the limited ray coverage in some cases. Overall, the results agree with those obtained when interpreting Φ independently from δV_s as in Chapter 5. The majority of the fracture strikes are consistent with the fault patterns (NE-SW and NW-SE). Due to the limited ray coverage in the vertical plane, the estimates of fracture density are poorly constrained in most cases and they show homogenous spatial distribution which contradicts with the spatial variation in δV_s previously observed using ordinary SWS analysis. According to the values of Thomsen's γ, VTI anisotropy exists in the NW part of the field and within the Horseshoe feature. Also, it exists in the Fiqa shale and the Natih B-G formation but not in the highly fractured Natih A reservoir.

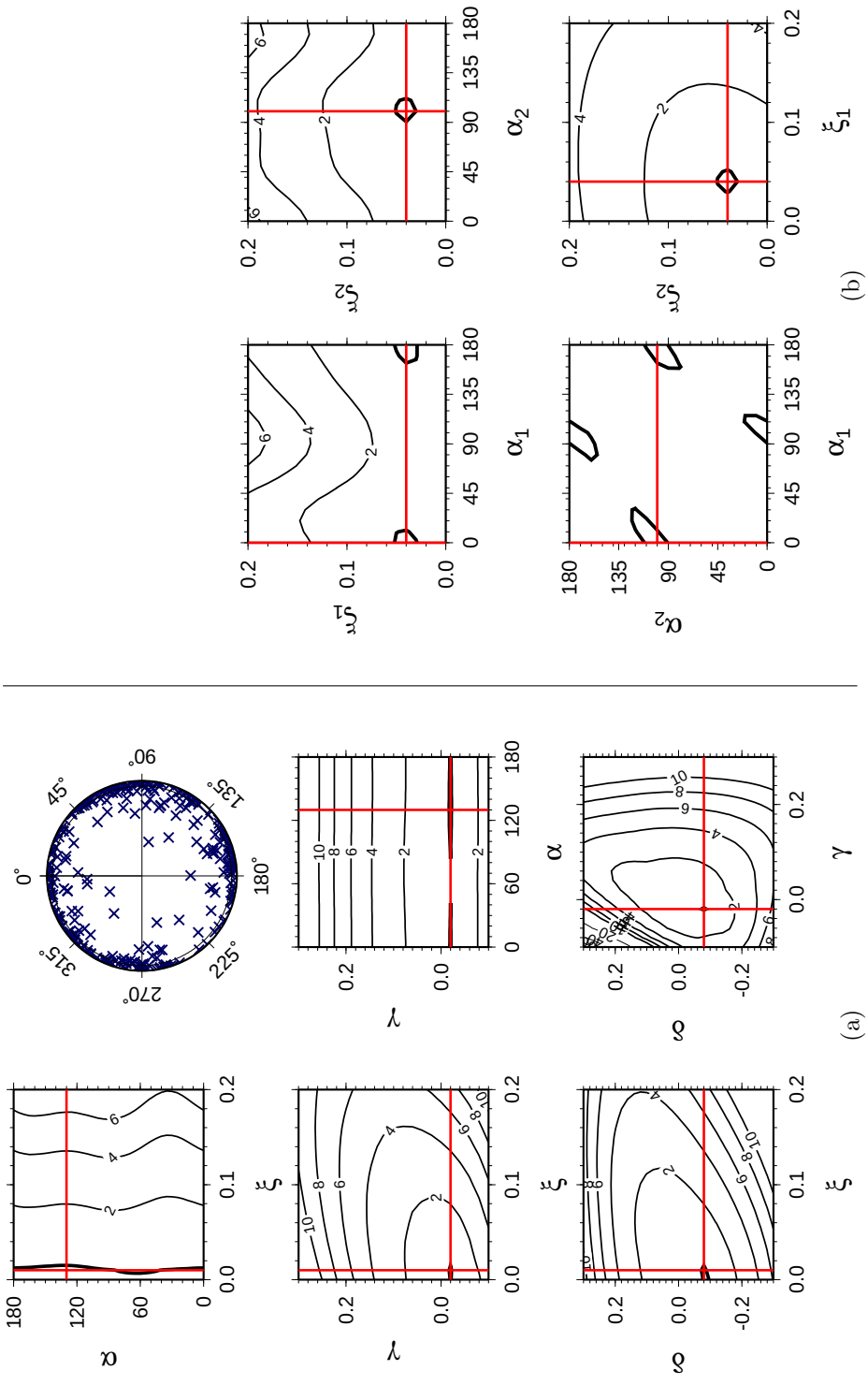

Figure 6.12: Shear-wave splitting inversion using the entire dataset. (a) Inversion for fracture strike (α), fracture density (ξ) and VTI parameters (γ and δ), assuming a single fracture set embedded in a medium with sedimentary fabrics. The top right circle shows the ray coverage. (b) Inversion assuming two fracture sets with strikes (α_1, α_2) and corresponding densities (ξ_1 and ξ_2). In (a) and (b), the red lines mark the inversion results. The misfit contours are normalised such that 1 (thick contour) indicates the 90% confidence limit.

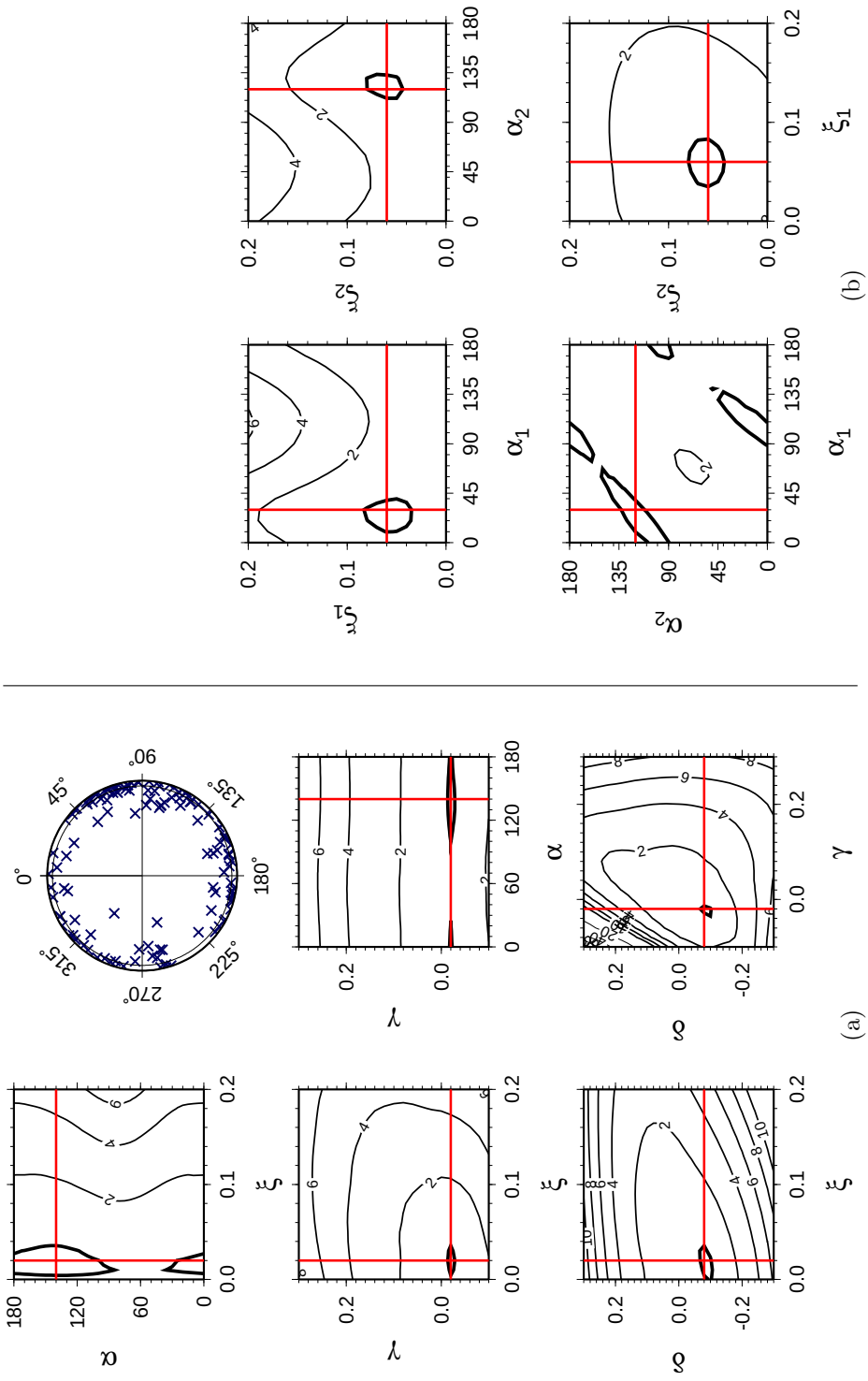

Figure 6.13: Shear-wave splitting inversion using the SE block subset (see Figure 6.12 caption).

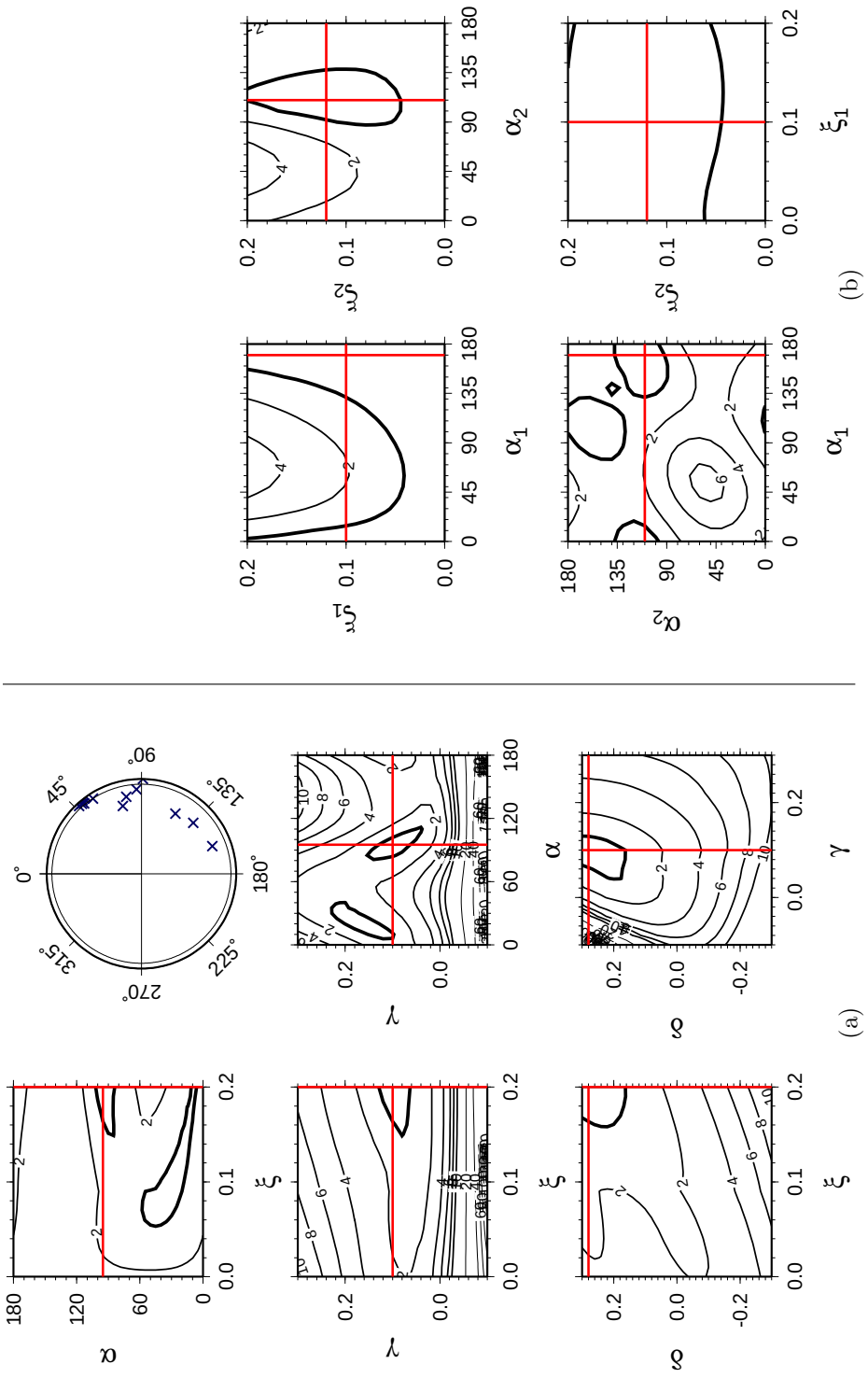

Figure 6.14: Shear-wave splitting inversion using the Graben block subset (see Figure 6.12 caption).

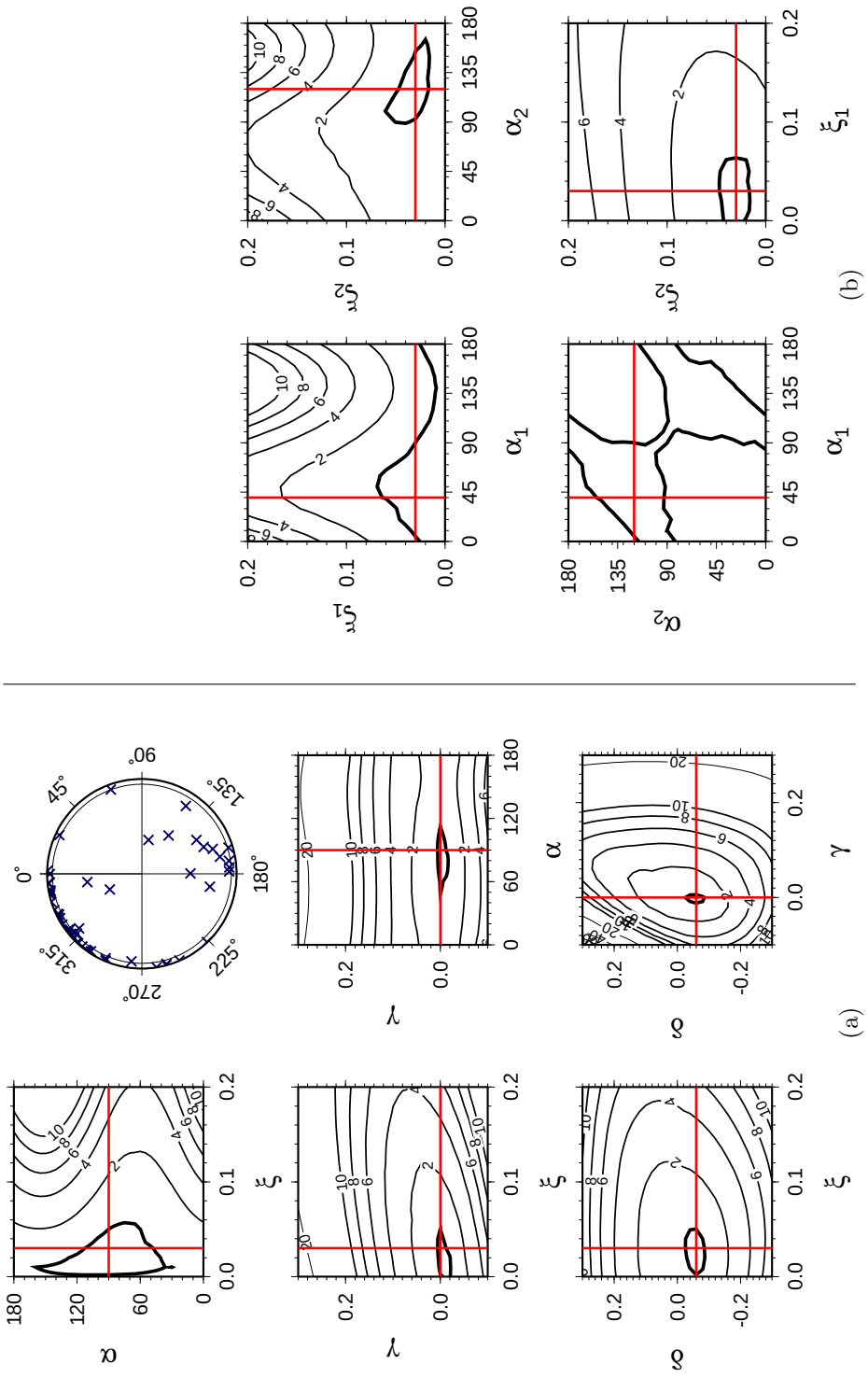

Figure 6.15: Shear-wave splitting inversion using the NW block subset (see Figure 6.12 caption).

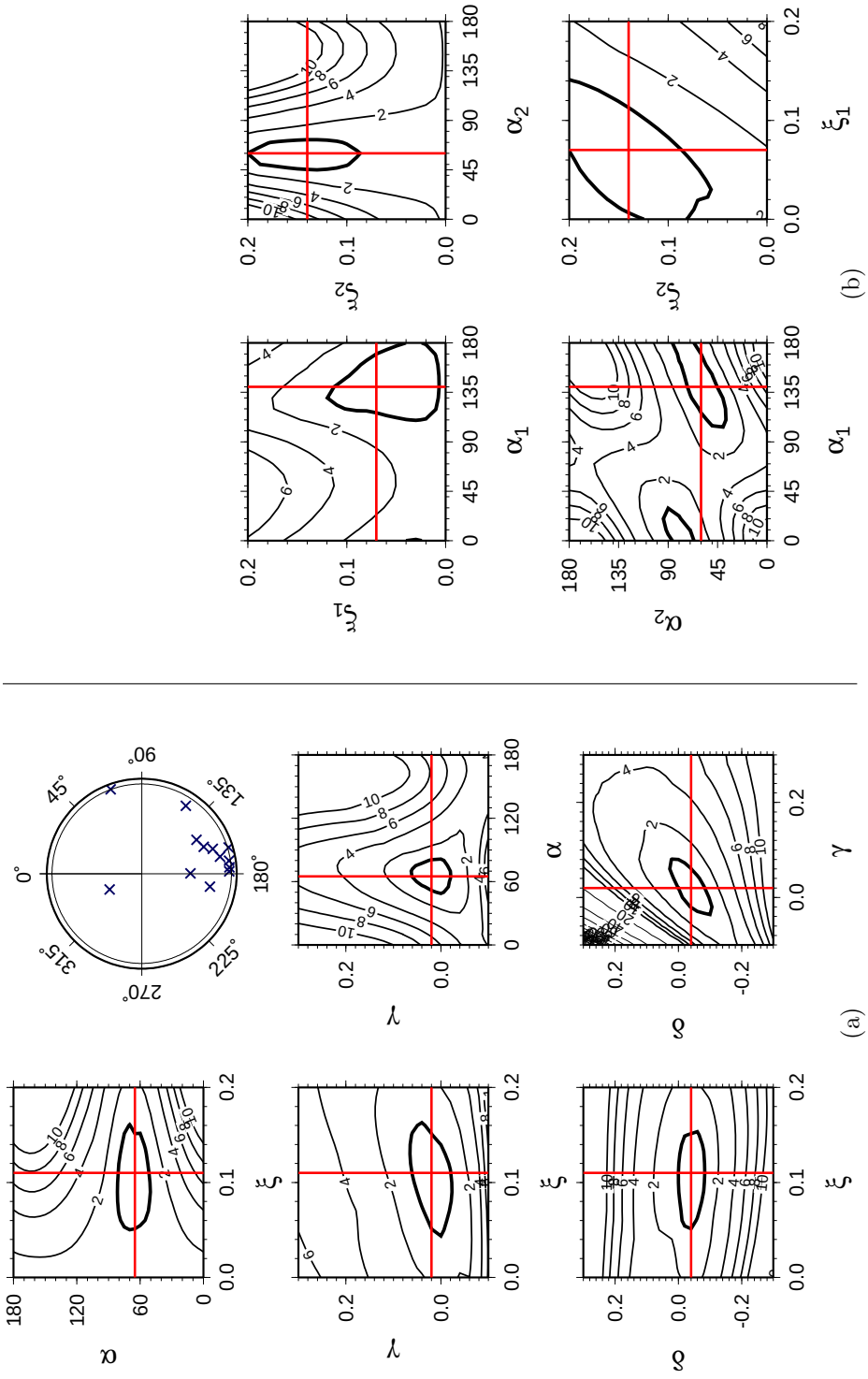

Figure 6.16: Shear-wave splitting inversion using the Well-1 subset (see Figure 6.12 caption).

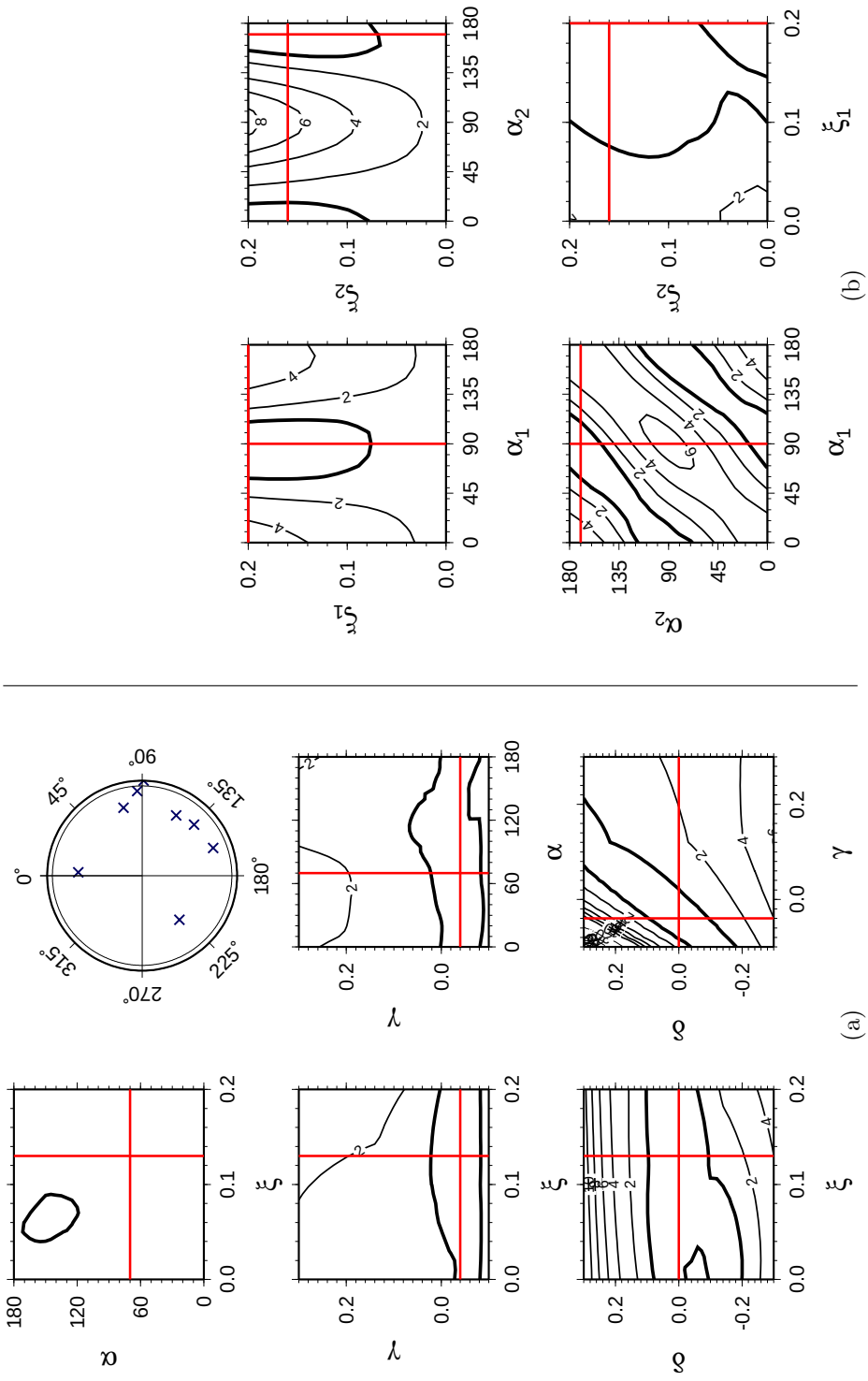

Figure 6.17: Shear-wave splitting inversion using the Well-2 subset (see Figure 6.12 caption).

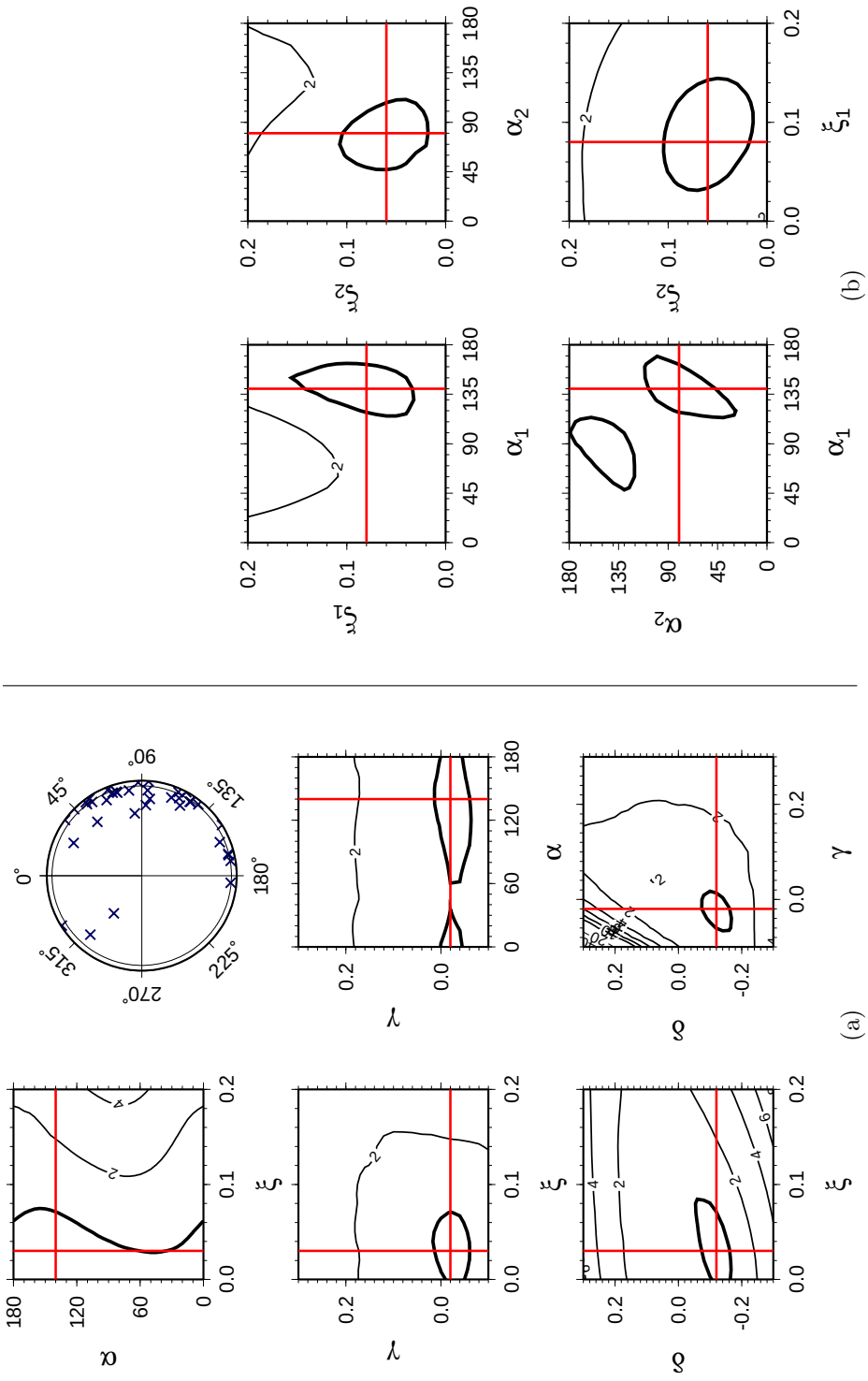

Figure 6.18: Shear-wave splitting inversion using the Well-3 subset (see Figure 6.12 caption).

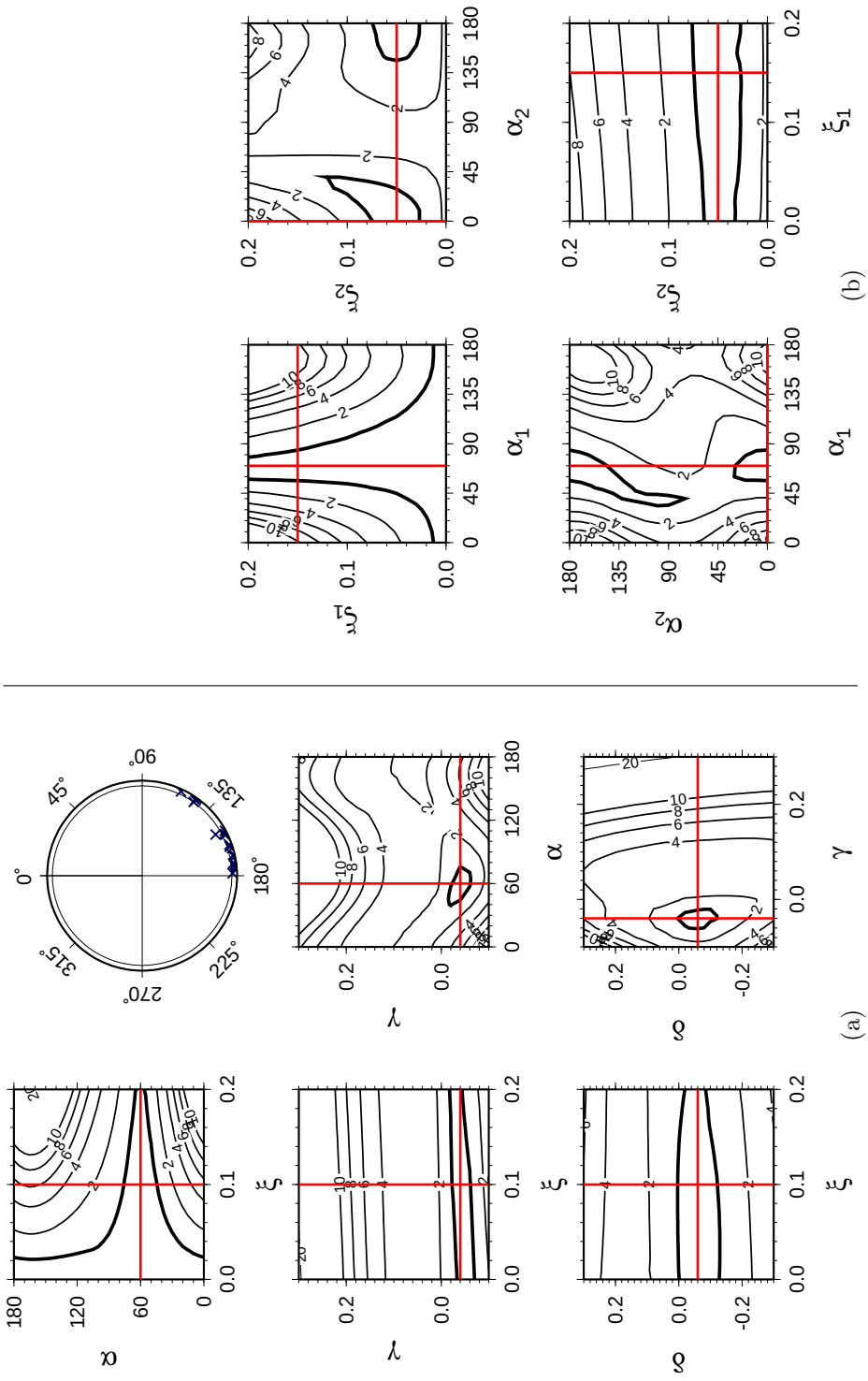

Figure 6.19: Shear-wave splitting inversion using the F1-W2 subset (see Figure 6.12 caption).

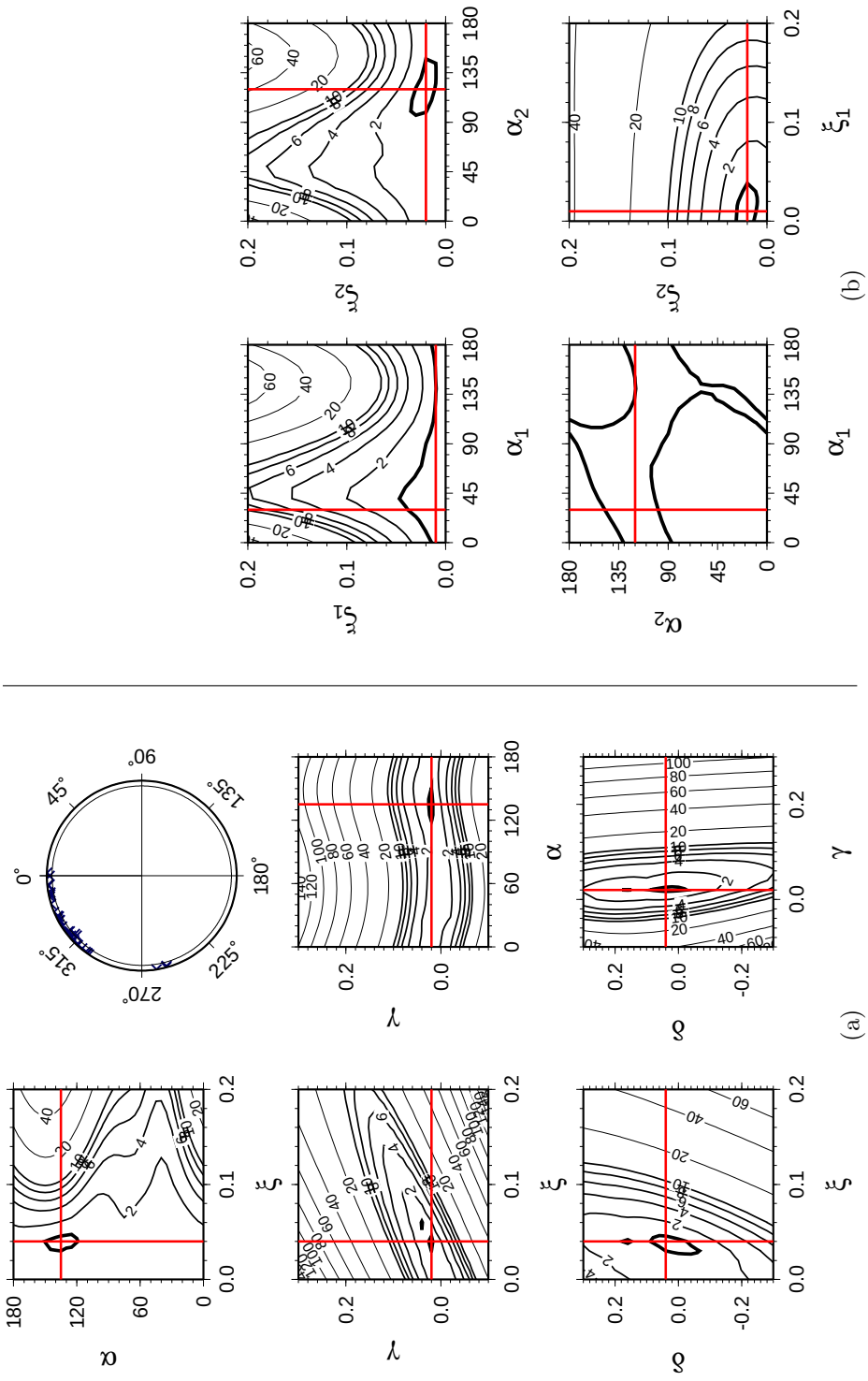

Figure 6.20: Shear-wave splitting inversion using the F1-W4 subset (see Figure 6.12 caption).

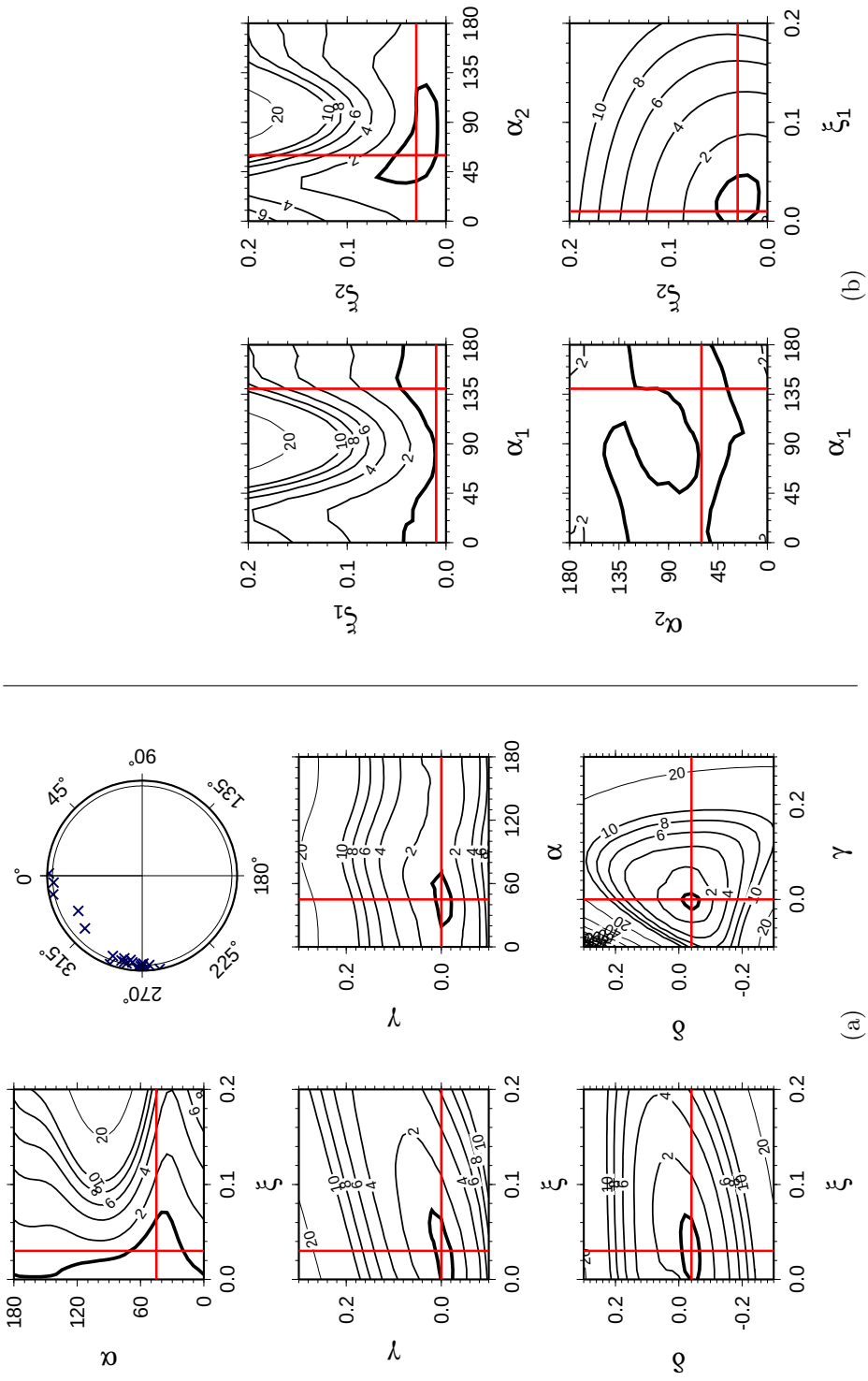

Figure 6.21: Shear-wave splitting inversion using the F2-W1 subset (see Figure 6.12 caption).

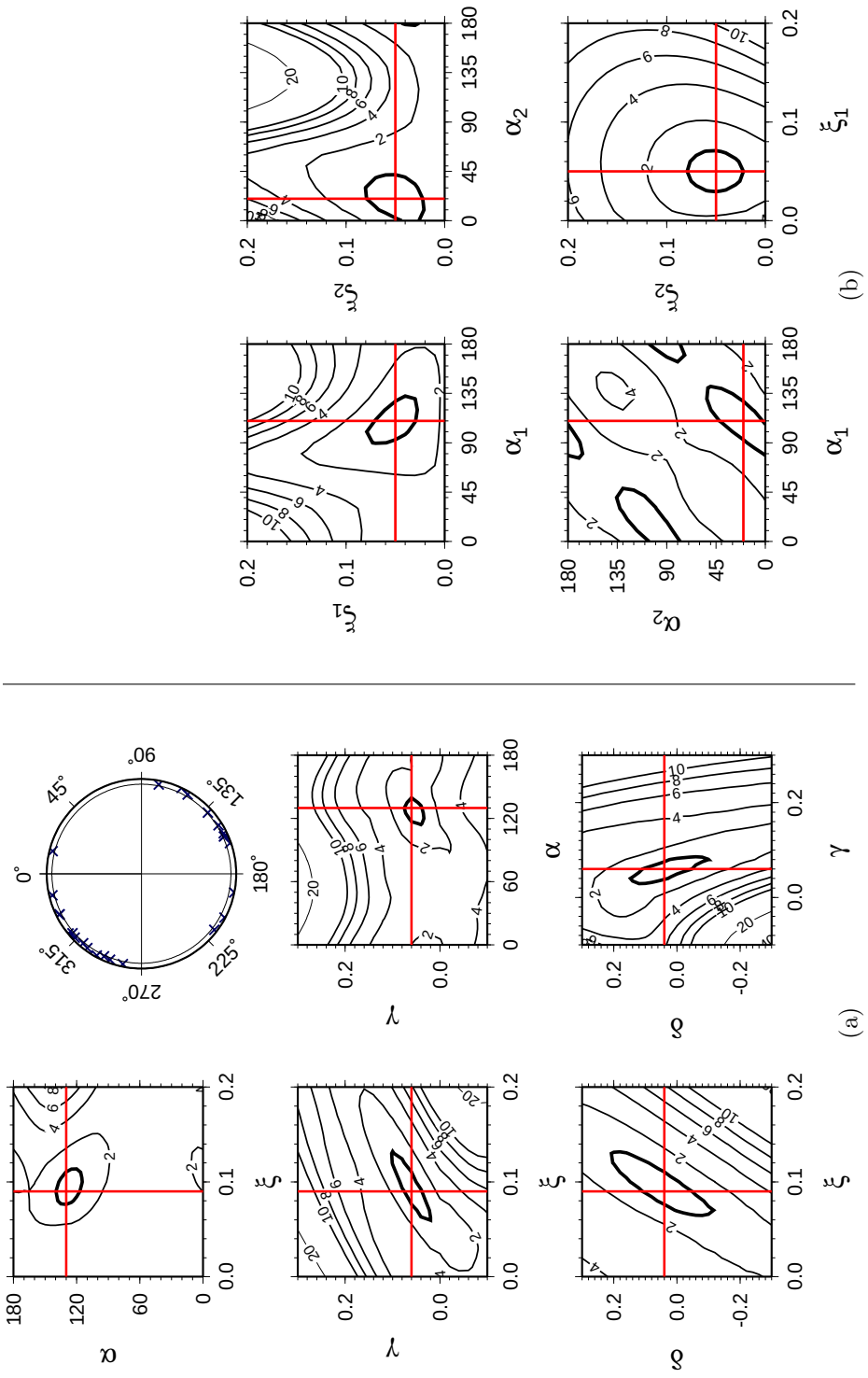

Figure 6.22: Shear-wave splitting inversion using the Horseshoe subset (see Figure 6.12 caption).

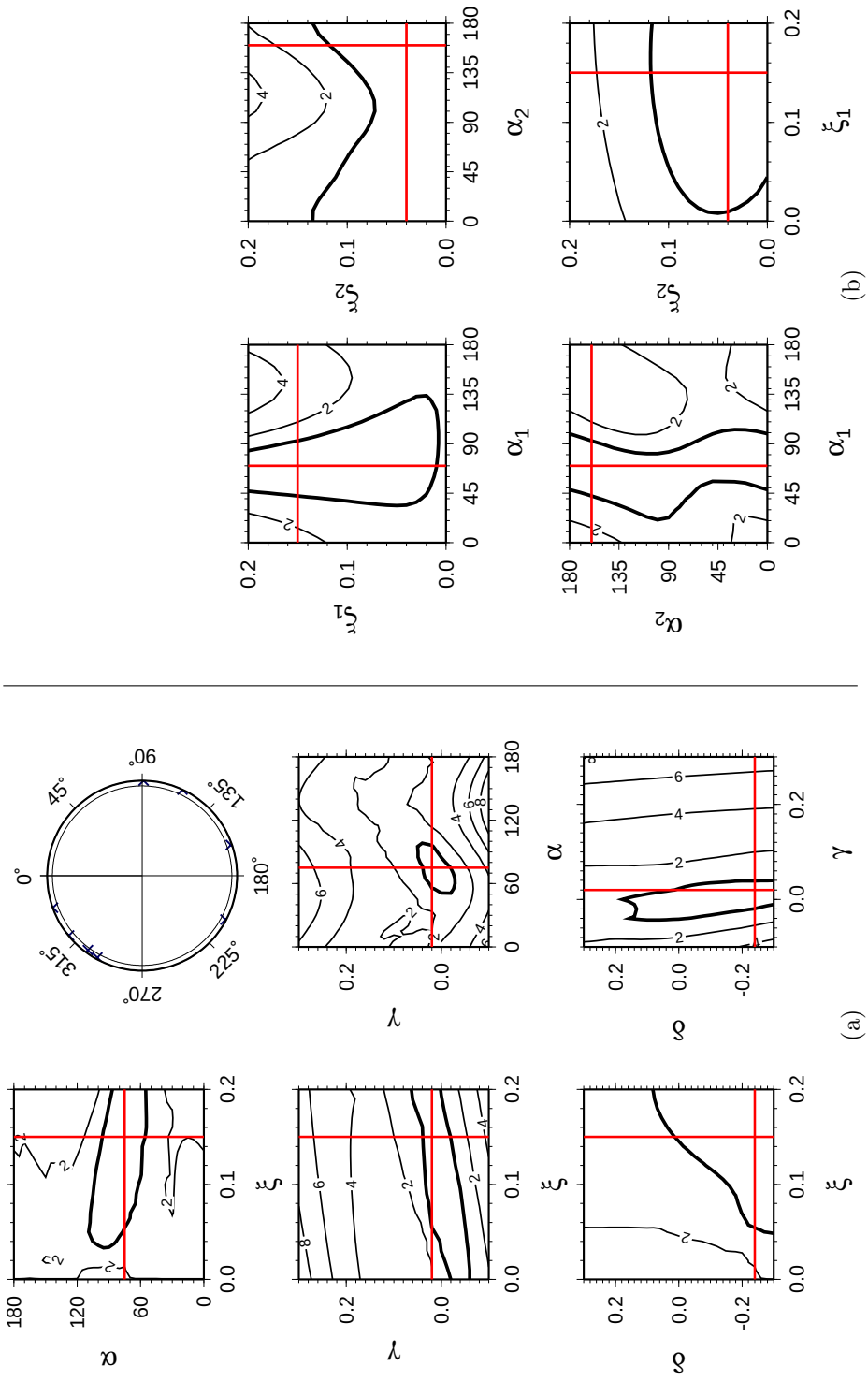

Figure 6.23: Shear-wave splitting inversion using the Fiqa subset (see Figure 6.12 caption).

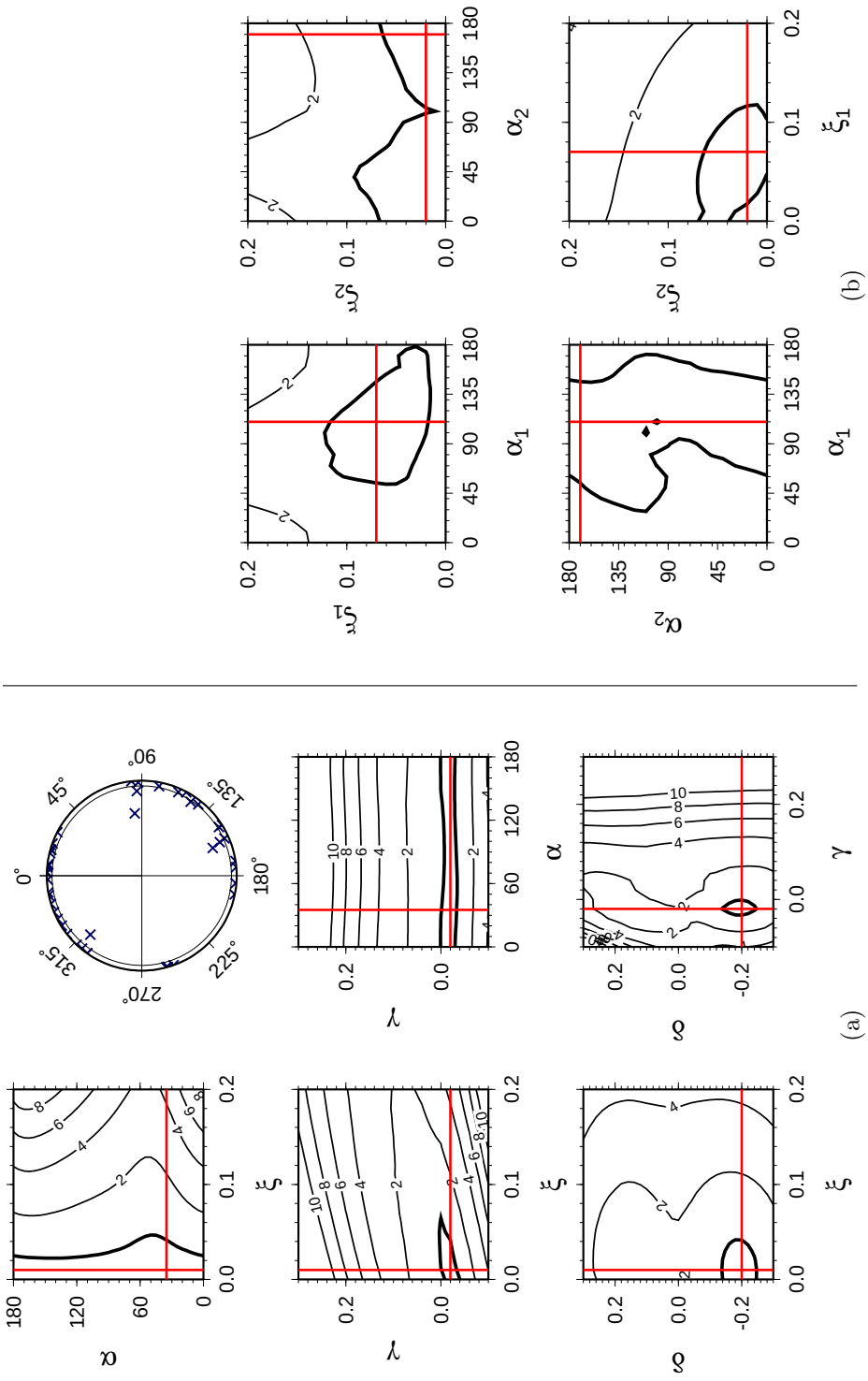

Figure 6.24: Shear-wave splitting inversion using the Natih A subset (see Figure 6.12 caption).

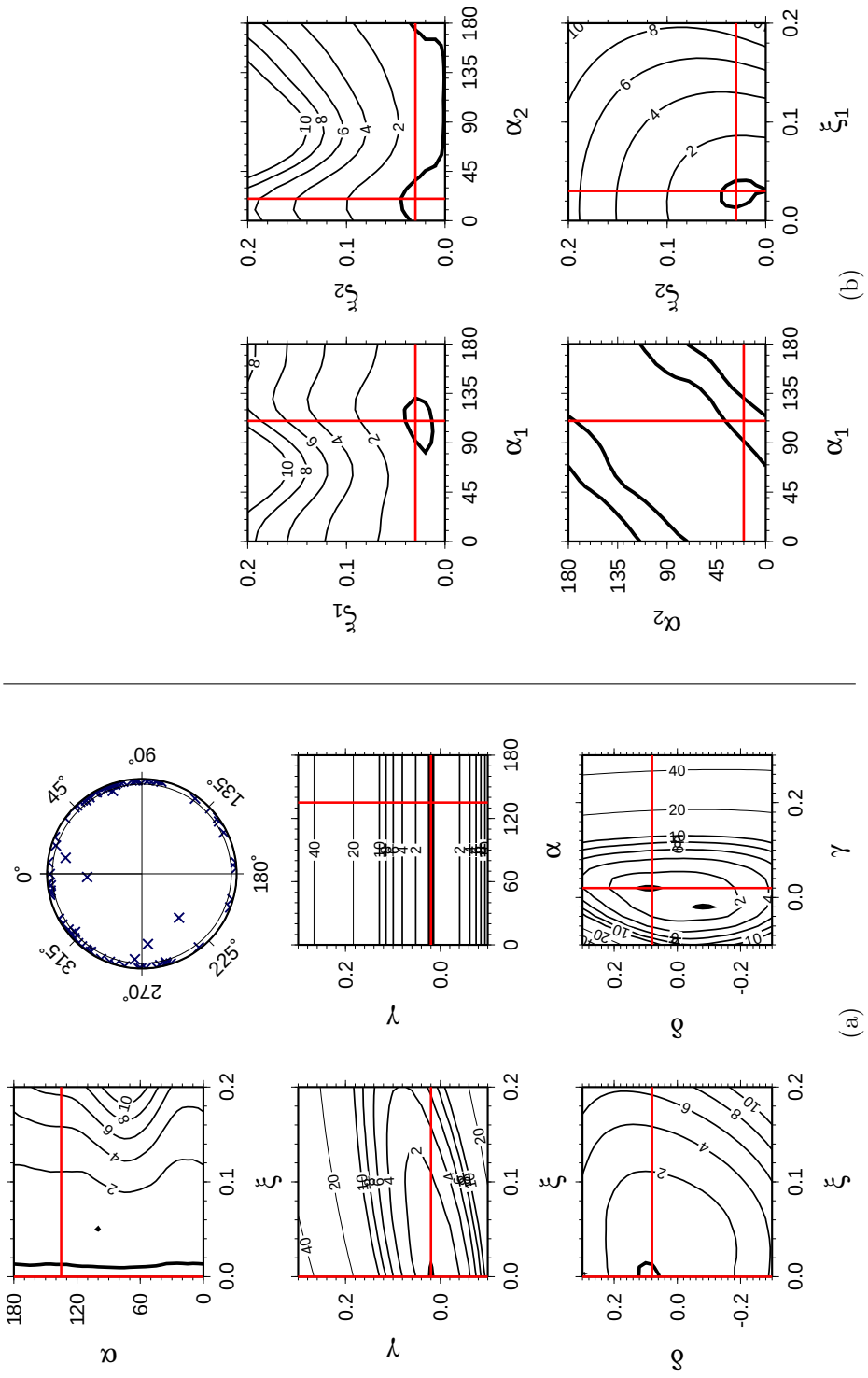

Figure 6.25: Shear-wave splitting inversion using the Natih B-G subset (see Figure 6.12 caption).

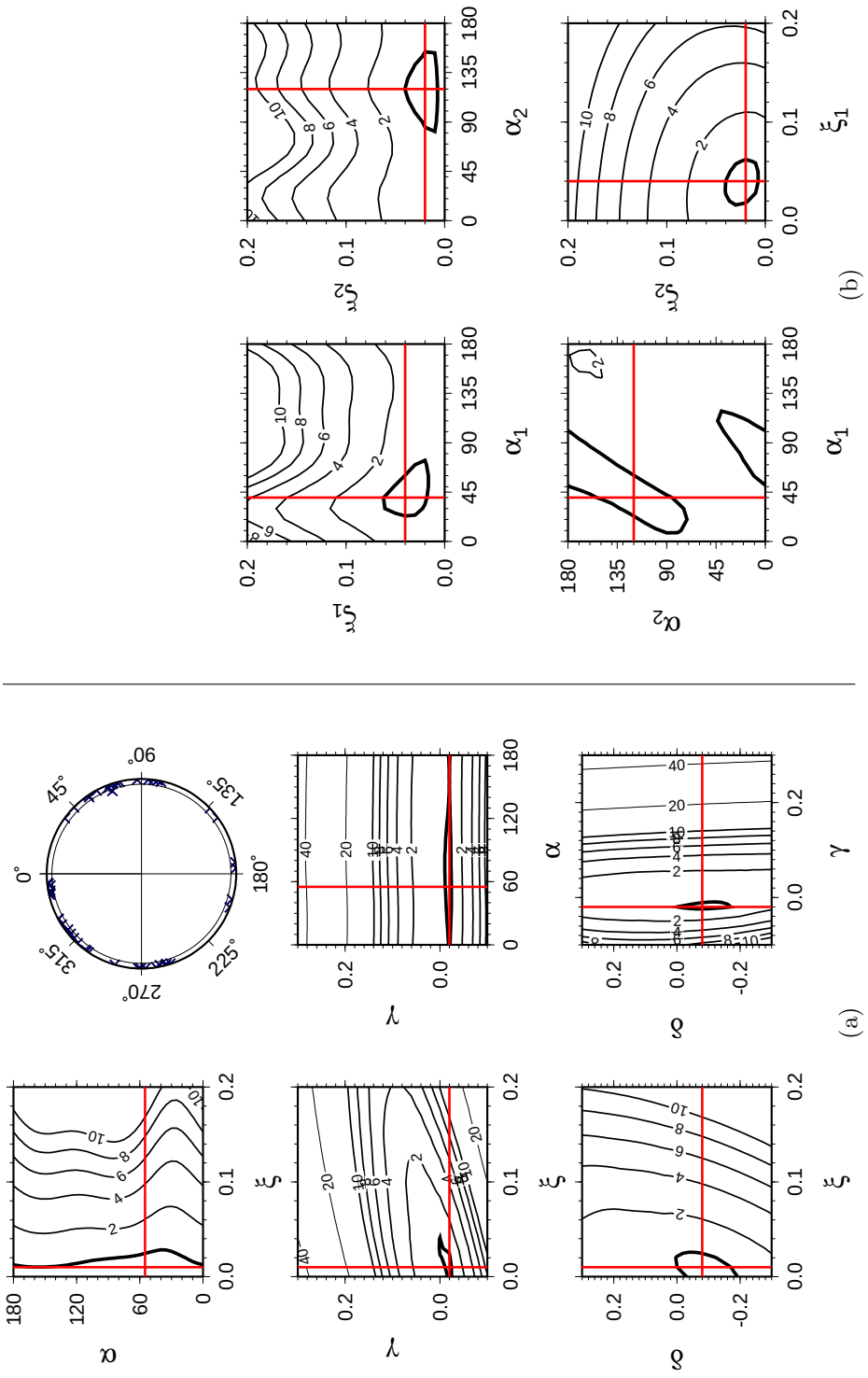

Figure 6.26: Shear-wave splitting inversion using the Natih B-G1 subset (see Figure 6.12 caption).

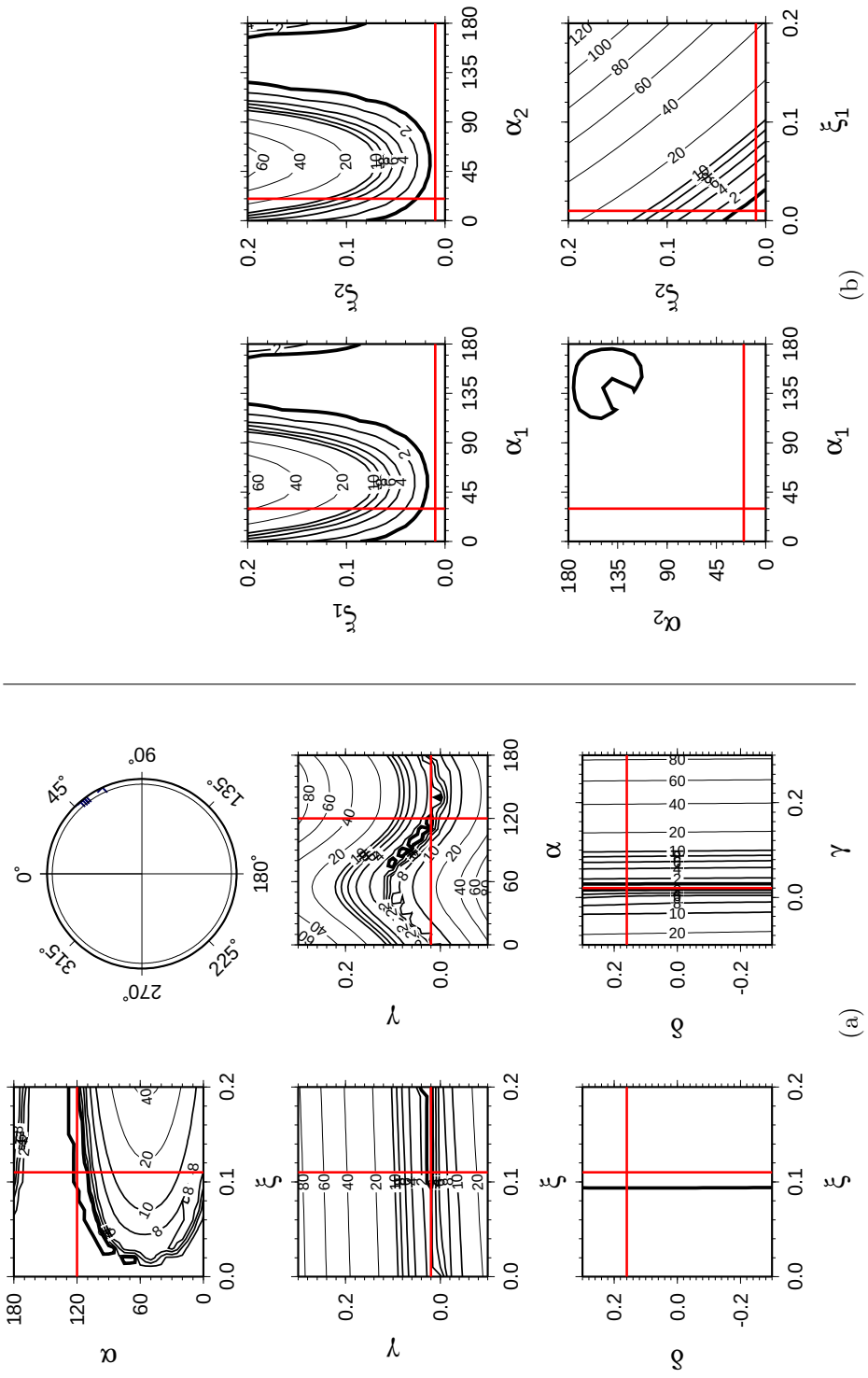

Figure 6.27: Shear-wave splitting inversion using the Natih B-G2 subset (see Figure 6.12 caption).

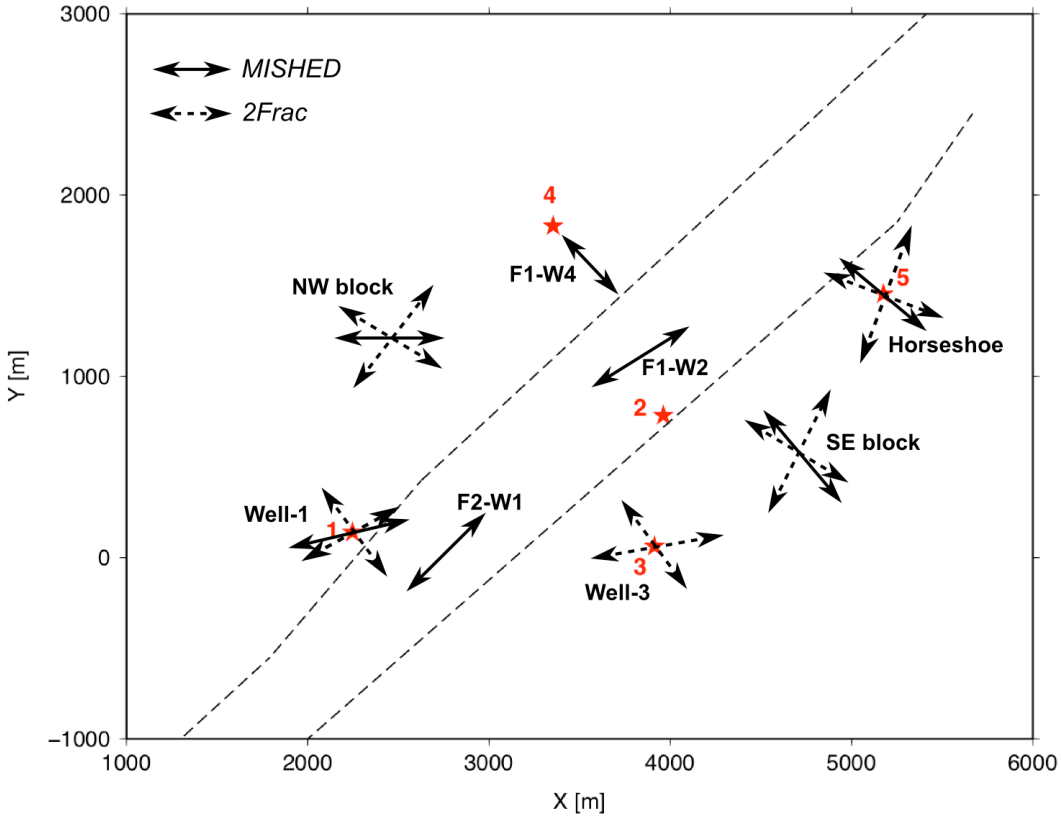

Figure 6.28: Summary of fracture strikes revealed by shear-wave splitting inversion. These are the results from using the two inversion codes: (1) $MISHED$ assuming a single fracture set and (2) $2Frac$ assuming two fracture sets. The subset names are indicated.

7
Frequency-dependent anisotropy

7.1 Introduction

Fractures play a crucial role in hydrocarbon production as they enhance porosity and permeability. Thus, fracture orientations, densities and sizes are of interest to reservoir engineers. However, when fracture systems are characterised using observations of seismic anisotropy, it is unknown whether the anisotropy is due to micro-scale cracks or macro-scale fractures. Reservoir engineers therefore do not generally use observations of seismic anisotropy as a routine method of fracture characterisation. Quantitative discrimination between the two scales (micro and macro) when characterising fractures is important because the latter controls reservoir storability and fluid flow.

Several studies have recently reported the dependence of anisotropy on frequency. Marson-Pidgeon & Savage (1997) observed evidence of frequency-dependent anisotropy (FDA) in earthquake data recorded in New Zealand using SKS and ScS phases. Rumpker et al. (1999) demonstrated the frequency-dependent nature of splitting parameters from such seismic phases in layered anisotropic media. Similar observations were shown by Chesnokov et al. (2001), Liu et al. (2003) and Maultzsch et al. (2003) using multicomponent VSP data and by Al-Anboori et al. (2006) using microseismic data. These observations were based on shear-wave splitting (SWS) analysis. Carter & Kendall (2006) observed frequency-dependent attenuation anisotropy in microseismic data acquired from the Valhal oil field, North Sea. They examined seismic attenuation anisotropy by comparing the relative frequency content of the fast and slow split shear-waves.

The two most likely mechanisms that can cause velocity dispersion, and consequently FDA, are scattering by inhomogenities and fluid flow in fractured porous rocks (Liu et al., 2003). Anisotropy induced by scattering occurs only when the seismic wavelength is longer than the size of the inhomogenities. A decrease in anisotropy and hence increase in scattering is observed with decreasing wavelength. A typical example of frequency-dependent scattering-induced anisotropy is wave propagation in finely layered media (e.g., Shapiro et al., 1994; Werner & Shapiro, 1999). Marson-Pidgeon & Savage (1997) suggested aligned heterogeneities as the likely cause of FDA observations in teleseismic data.

The second proposed mechanism for FDA accounts for fluid flow in fractured porous rocks. Seismic waves propagating through fractured porous rocks can induce pressure gradients that

cause fluid exchange between fractures and pore spaces to achieve pressure equalisation (e.g., Chapman, 2003). Thus, fluid-saturated fractured rocks are expected to show frequency-dependent velocity dispersion and attenuation and hence FDA effect. If FDA is detected it will be in the form of a decrease in percentage anisotropy with increasing frequency (e.g., Maultzsch et al., 2003; Al-Anboori et al., 2006).

In this Chapter I perform FDA analysis and modelling on the Field M dataset. First, I describe the Chapman (2003) model. Second, I explore the frequency content of the dataset and I describe the filtering technique that I use. Third, I conduct SWS analysis to estimate the splitting parameters (Φ and δt), with the later used to estimate the percentage raypath normalised difference between the fast and slow shear-wave velocities (δV_s). Finally, I model the results using the Chapman (2003) theory to invert for the fracture parameters: fracture radius (a_f), density (ξ) and strike (α).

7.2 Theoretical modelling of frequency-dependent anisotropy

7.2.1 Previous attempts

Traditional equivalent medium theories for fractured media (e.g., Hudson, 1981; Thomsen, 1995) do not consider the frequency-dependence of elastic response. Such models lack the sensitivity to fracture size. For example, a medium with a few large fractures will generate elastic constants equivalent to those produced by a medium containing many small cracks. In recent years, several frequency-dependent models have been proposed which incorporate the effect of wave-induced fluid motion (Hudson et al., 1996; Pointer et al., 2000; van der Kolk et al., 2001). However, these model do not explain the frequency-dependance of seismic anisotropy for the entire frequency range appropriately, especially with the presence of fluid saturated fractures.

There have been some attempts in the past few years to model the FDA effects observed in real data. For example, Chesnokov et al. (2001) suggested a model of FDA in fractured media that accounts for seismic scattering due to ordered heterogeneities (ellipsoidal inclusions). It was used to model the FDA effect measured in the Bluebell-Altamont field VSP data. To explain the observed FDA effect, Chesnokov et al. (2001) assumed a high concentration of large fractures (100 m in radius with aspect ratio of 0.06). Tod & Liu (2002) proposed a layer-bounded fracture model based on the equivalent medium theory of Hudson et al. (1996). The model describes the fluid flow between elliptical cracks (bed limited cracks in this case). It was used to simulate the FDA

observations in earthquake data by Marson-Pidgeon & Savage (1997). In this study I base my modelling on the poroelastic theory of Chapman (2003).

7.2.2 Chapman 2003 model

The poroelastic equivalent medium model of Chapman (2003) considers the case of a pore space which consists of a random isotropic collection of microcracks and spherical pores with aligned ellipsoidal fractures. It is an extension of the Chapman et al. (2002) model, which is restricted to squirt fluid flow within porous media (i.e., without fractures). The equant pores and microcracks in the Chapman (2003) model are on the scale of the grain size, whereas the aligned fractures are allowed to be much larger, as long as their size and spacing remain smaller than the seismic wavelength. Therefore, the model accounts for two different length scales and the resulting medium has hexagonal symmetry. The effective stiffness tensor can be expressed as:

$$C_{ijkl} = C^{\circ}_{ijkl} - \Phi_p C^1_{ijkl} - \varepsilon_c C^2_{ijkl} - \xi C^3_{ijkl}, \tag{7.1}$$

where C^0 is the isotropic elastic tensor of the matrix and, C^1, C^2 and C^3 are the additional contributions from pores, microcracks and fractures, respectively, multiplied by the porosity (Φ_p), the crack density (ε_c) and the fracture density (ξ). C^0 is constructed using Lamé parameters λ and μ. The Chapman (2003) model is restricted to low porosity and valid for low concentrations of inclusions. Thus, for the cases of high porosity, the use of the grain moduli λ and μ to calculate the effect of fractures can result in substantial errors. Chapman et al. (2003b) proposed a modified version which overcomes the restriction to low porosity. They suggested using λ° and μ° which are derived from the velocities V_p° and V_s° of the unfractured porous rock. λ° and μ° are defined as:

$$\mu^\circ = (V_s^\circ)^2\rho; \qquad \lambda^\circ = (V_p^\circ)^2\rho - 2\mu^\circ, \tag{7.2}$$

where ρ is the density of the saturated rock. Also, the isotropic tensor (C°) needs to be expressed in such away that the measured isotropic velocities are obtained by applying the pore and crack correction at a certain frequency $f_\circ$. The new Lamé parameters are defined as

$$\Upsilon = \mu^\circ + \Phi_{c,p}(\lambda^\circ, \mu^\circ, f_\circ); \qquad \Lambda = \lambda^\circ + \Phi_{c,p}(\lambda^\circ, \mu^\circ, f_\circ), \tag{7.3}$$

where $\Phi_{c,p}$ is perturbation function due to the presence of microcracks and pores. Now, $C^\circ(\Lambda,\Upsilon)$ is frequency independent and Equation (7.1) becomes

$$C_{ijkl}(f) = C^{\circ}_{ijkl}(\Lambda, \Upsilon) - \Phi_p C^1_{ijkl}(\lambda^\circ, \mu^\circ, f) - \varepsilon_c C^2_{ijkl}(\lambda^\circ, \mu^\circ, f) - \xi C^3_{ijkl}(\lambda^\circ, \mu^\circ, f), \tag{7.4}$$

where f is the frequency.

The Chapman (2003) model allows for fluid exchange between equant pore spaces and fractures. The model assumes that the pore spaces are fully saturated with one type of fluid. Chapman et al. (2003b) suggested that the model can be further simplified by ignoring ε_c for rocks with high Φ_p. Chapman et al. (2003b) argued that rocks with sufficient Φ_p can accommodate the expelled fluid from fractures. In contrast, for rocks with zero porosity, the expelled fluid is forced into the microcracks and the possibility for this to happen depends on ε_c. The porosity of the Field M rocks is high (Table 7.1) and thus the microcrack effect can be ignored.

The fluid flow in the model occurs at two scales: (1) the grain scale fluid flow described by the traditional squirt flow frequency (or relaxation time (τ_m)) and (2) the fracture scale fluid flow associated with larger time-scale constant (τ_f). The two time scales are related by the expression:

$$\tau_f = \frac{a_f}{\varsigma}\tau_m, \tag{7.5}$$

where a_f is the fracture radius (length of the major axis of a spheroid) and ς is the grain size. Equation (7.5) demonstrates that τ_f is directly proportional to a_f. As fracture radius increases, the ratio of surface area to volume decreases, meaning more volume of fluid has to move through an element of surface area to equalise the induced pressure, which requires more time (Maultzsch et al., 2003).

The model is sensitive to fracture size and pore fluid type, and able to explain attenuation and velocity dispersion at seismic frequencies. It can be used to invert for fracture parameters using frequency-dependent observations of δV_s (e.g., Maultzsch et al., 2003; Al-Anboori et al., 2006) or P-wave attenuation (e.g., Maultzsch et al., 2007).

7.3 Synthetic modelling

7.3.1 Model parameterisation

The construction of the Chapman (2003) model requires pre-defining the following parameters: V_p and V_s velocities, the frequency at which velcoities are estimated ($f_\circ$), saturated rock density (ρ), porosity (Φ_p), squirt flow relaxation time (τ_m), fluid bulk modulus (K_f) and fracture parameters (strike (α), dip (ϱ), density (ξ), radius (a_f) and aspect ratio). Following the work of Maultzsch et al. (2003) and Al-Anboori et al. (2006) the aspect ratio of fractures is assumed to be very small, so the model is not sensitive to it. The ray azimuth and inclination are defined with respect to the

fracture set strike (α) and dip (ϱ), respectively. Usually, the fracture density (ξ) and radius (a_f) are inverted for by modelling real data.

V_p and V_s are computed as average estimates along the raypath using the Field M 21 layers velocity model. These velocities were measured at $f_\circ$=40 Hz (Al-Anboori, 2006). Since there are no independent estimates of τ_m for the Field M rocks, they have to be estimated from other published laboratory data. Calibration is performed following the fact that τ_m is proportional to viscosity (η) divided by permeability (κ) (e.g., Chapman et al., 2003a). For calibration, I use the τ_m=20 μs estimated by Chapman (2001) for a rock sample with η and κ of $7.5\times10^{-3} Pa.s$ and 250 mD, respectively. The τ_m calibration equation takes the form:

$$\tau_m = \frac{2\times10^{-3}}{3}.(\frac{\eta}{\kappa}). \tag{7.6}$$

Table 7.1 lists the input parameters for the Fiqa, Natih A, Natih B-G1 and Natih B-G2 formations. The parameters were taken from the field's operator in-house reports (see Chapter 2). The fracture parameters (strike (α), density (ξ) and radius (a_f)) are inverted for using the real data as described below in section 7.5. The fracture strike (α) should be constrained in the model to limit the free parameters in the inversion to fracture density (ξ) and radius (a_f). However, I included it in the inversion because it is not well constrained from the observations of ordinary SWS in Chapters 5 and 6 due to the limited ray coverage in the vertical plane. The available observations show fractures oriented in multiple directions (mostly NE-SW and NW-SE), reflecting the structural complexity of Field M. These observations of variability in fracture orientation are supported by measurements from borehole techniques such as formation micro images (FMI, see Chapter 2).

Later in the inversion, for the Natih B-G2 dataset, I tested using fracture dips of 26° and 63°. The first fracture dip was estimated using measurements confined to the Natih B-G2 only whereas the latter was estimated using the entire Natih B-G subset (Table 5.3, Chapter 5). I found that the 63° fracture dip explains the FDA observations better than the 26° fracture dip.

7.3.2 Sensitivity of the model parameters

In this section, I use synthetic modelling to test the sensitivity of the Chapman (2003) model to varying each of the input parameters. The modelling also helps to visualise what we should expect to see in the real data. The Natih A parameters summarised in Table 7.1 are used to carry out the tests. Based on the field velocity model, the average V_p and V_s velocities for the Natih A formation

Parameter	**Fiqa**	**Natih A**	**Natih B-G1**	**Natih B-G2**
Density (kg/m^3)	2200	2400	2400	2400
Porosity (%)	30	30	24	24
Permeability (mD)	1×10^{-4}	10	1	1
Viscosity ($Pa.s$)	4.4×10^{-4}	1.42×10^{-5}	4.4×10^{-4}	4.4×10^{-4}
Relaxation time (s)	2.9	9.5×10^{-7}	2.9×10^{-4}	2.9×10^{-4}
Fluid type	Brine	Gas	Brine	Brine
Fluid bulk modulus (GPa)	2.3	0.0068	2.3	2.3
Fracture dip (° from horizontal)	72	73	73	63

Table 7.1: Model input parameters used in the inversion. V_p and V_s are computed using the field velocity model. Reference frequency ($f_\circ$) is 40 Hz.

are 2800 ms^{-1} and 1470 ms^{-1}, respectively. The aligned fracture set is assumed to have a_f of 1 m and ξ of 0.1, unless stated otherwise. I assume vertical fracture dip (ϱ=90°) with horizontal ray propagation. Horizontal ray propagation is assumed because the majority of the real data show subhorizontal ray propagation. The ray azimuth is 0° from north in all models. Note that varying α and ϱ is identical to varying ray azimuth and inclination, respectively. In the modelling, δV_s is calculated using ($100\times(S_p$-$S_q)/S_p$), where S_p is the pure-shear velocity and S_q is the quasi-shear velocity.

The synthetic modelling reveals that the Chapman (2003) model of FDA is sensitive to α or ray azimuth, ϱ or ray inclination, a_f, ξ and τ_m (Figure 7.1). The rest of the input parameters listed in Table 7.1 show no or minor sensitivity.

Fracture strike (α)

As expected there is no splitting and thus there is no FDA effect for rays propagating parallel and perpendicular to the fracture plane (Figure 7.1a). There are some cases where δV_s decays with increasing frequency until reaching zero and then starts increasing (cases of 45°, 60° and 75° in Figure 7.1a). These are cases of crossing shear-wave singularities, where the pure- and quasi-shear waves have the same velocity. The pure-shear wave has faster velocity than the quasi-shear wave before the singularity point but after that the quasi-shear wave is faster than the pure-shear wave for higher frequencies. This can not happen for near-vertical ray propagation (Mark Chapman,

Edinburgh Anisotropy Project, pers. comm., Dec. 2009). In the subsequent models, α is set to 30° as it shows a clear FDA effect without any singularity.

Fracture dip (ϱ)

There is no FDA effect when the fracture set is dipping horizontally (i.e., ray is travelling parallel to the fracture plane, Figure 7.1b). The decay in δV_s gets sharper as the separation between the raypath and fracture plane increases. Note that fracture dip is measured from horizontal.

Fracture radius (a_f)

For fractures with large radii, there is a pronounced drop in δV_s at low frequencies (Figure 7.1c). In contrast, the FDA effect is minor for the cases with small a_f and a drop in δV_s will occur at much higher frequencies.

Fracture density (ξ)

The case of varying ξ is slightly more complicated compared to the other parameters (Figure 7.1d). The FDA effect becomes more obvious with the increase in fracture density. However, for high ξ values (0.25 and 0.3), the model shows no FDA effect at lower frequencies and δV_s remains almost constant before showing a sharp drop with increasing frequency.

Relaxation time (τ_m)

Since τ_m and a_f are related by Equation (7.5), they show similar FDA responses (Figures 7.1c,e). The FDA effect is minor for small τ_m values. The model is very sensitive to τ_m and thus it has to be a highly accurate input to the model. Such accuracy can be probably obtained by observing frequency dispersion and attenuation using rock samples in laboratory experiments. Calibrating τ_m by extrapolating from one rock type to another, like what I did in section 7.3.1, can result in significant and unquantifiable error (Mark Chapman, Edinburgh Anisotropy Project, pers. comm., Dec. 2009). Such laboratory data are not available for Field M. Further suggestions for calibrating τ_m can be found in Maultzsch (2005) and Chapman et al. (2003a). For example, Maultzsch (2005) estimated τ_m by numerically fitting the Chapman (2003) model to the laboratory data of Rathore et al. (1995). This was done by modelling the velocity and attenuation measurements obtained by Rathore et al. (1995) for synthetic porous sandstone samples that were embedded with aligned fractures of known geometry.

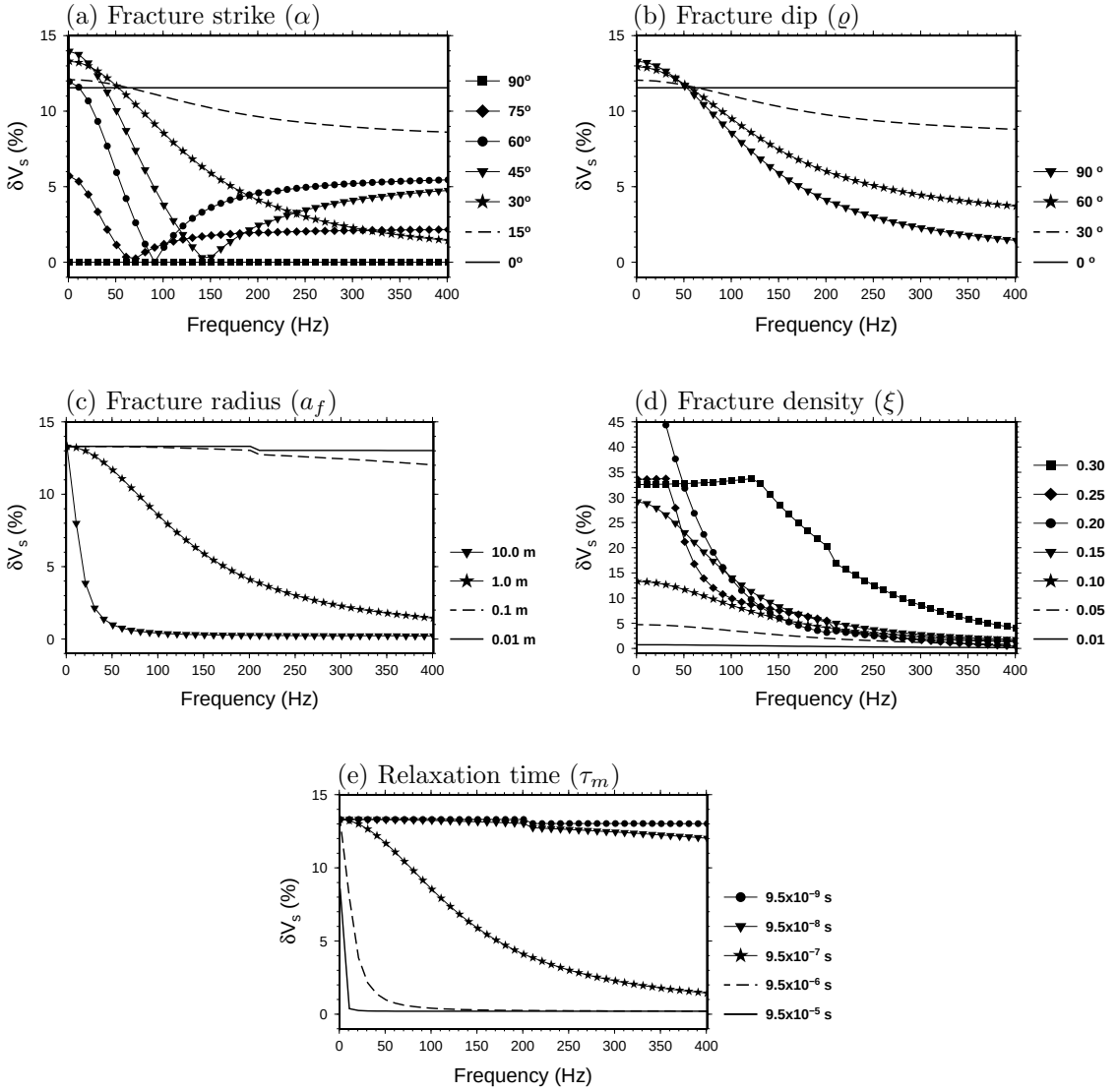

Figure 7.1: Synthetic modelling of frequency-dependent anisotropy. The models simulate the Natih A reservoir (see Table 7.1). In (b), (c), (d) and (e), α is 30° from north. In (a), (c), (d) and (e), ray inclination is 90° from vertical.

7.4 Frequency content and processing

In the FDA analysis, I use events which have their raypaths entirely confined to the Fiqa, Natih A, Natih B-G1 and Natih B-G2 (i.e., source and receiver within the specified formation). Rays crossing the formation boundaries are excluded. This is to ensure that seismic rays sense the same physical properties. Figures 7.2, 7.3, 7.4 and 7.5 show the S-wave frequency content for the Field M dataset sorted by formation and recording station. Generally, the Fiqa cap rocks show narrower frequency bandwidths (10-200 Hz; Figure 7.2) compared to the carbonate rocks (10-400 Hz; Figures 7.3, 7.4 and 7.5), suggesting that shale is more attenuative than limestone.

The FDA analysis involves filtering the data into different frequency bands and then for each band estimate the splitting parameters (Φ and δt). There are two views in term of the filter width: (1) fixed filter band and (2) increasing filter band with higher frequencies. The first type has been previously used with VSP data (e.g., Liu et al., 2003; Maultzsch et al., 2003), whereas the second type has been used with microseismic data (Al-Anboori et al., 2006). The VSP data analysed by Liu et al. (2003) and Maultzsch et al. (2003) have frequency content in the range 10-35 Hz, whereas microseismic data are often have frequency content which can reach up to 500 Hz, like the case of Field M dataset.

I tested a fixed filter width of 30 Hz and a filter with corner frequencies with a constant high to low frequency ratio of 2 (i.e., 1 octave). The low corner frequency of the first filter type is moved with 15 Hz steps starting from 10 Hz. The frequency bands in the second type overlay as follows: 10-20 Hz, 15-30 Hz, 20-40 Hz, 30-60 Hz etc.. Filtering continues until the S-wave signal is absent. For both types, I use Butterworth bandpass filter with 4 poles and 1 pass. One pass filters are used to minimise ringing effects. This should not affect the estimate of δt because we seek relative time rather than absolute time. Furthermore, the dominant S-wave frequency (f_d) for each frequency band is calculated following the definition of Barnes (1993):

$$f_d^2 = \frac{\int_0^\infty f^2 P(f) df}{\int_0^\infty P(f) df}, \tag{7.7}$$

where f is the frequency and $P(f)$ is the power spectrum.

Figure 7.6 shows an example of variation in δt with increasing frequency for the same source-receiver combination using the two filter types. The results from using the two types of filters show that there is high scatter in the estimates of δt when using filters with fixed frequency bandwidths compared to filters with increasing frequency bandwidths. Therefore, in the subsequent analysis I

use the second type of filtering with increasing frequency bandwidths. Liu et al. (2003), applying the first type of filtering, and Al-Anboori et al. (2006), applying the second type of filtering, used synthetic seismograms generated by frequency-independent models to show that the FDA observations are not artefacts of filtering.

With narrow frequency bands, SWS analysis is often prone to cycle skipping. This leads to fluctuation in Φ, even for events which show systematic decrease in δV_s with increasing frequency (Figure 7.7). The Chapman (2003) model predicts a decay in δV_s, but a constant Φ. Therefore, I fix Φ, a priori, to the value determined using the SWS analysis on the broadband data. δt is then estimated while searching over a narrow range of $\pm 10°$ from Φ. The $\pm 10°$ range accounts for the maximum acceptable error on Φ (see Chapter 4). The estimates of δV_s and shear-wave dominant frequencies (f_d) are then used to invert for the fracture parameters.

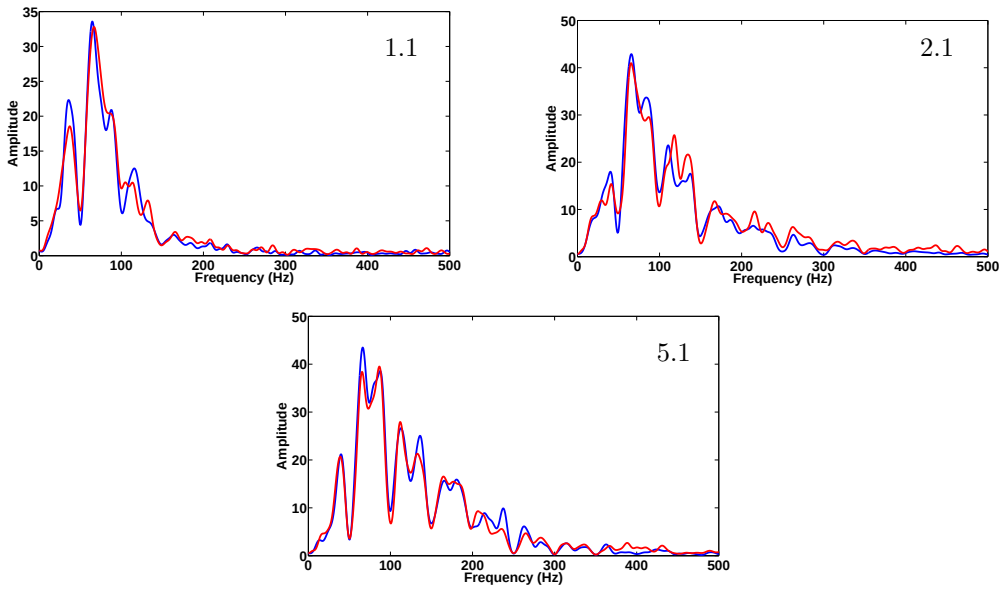

Figure 7.2: Frequency content of the Fiqa subset (stations 1.1, 2.1 and 5.1). A 100 ms S-wave window per event is used when analysing frequency spectrum of the horizontal (red) and vertical (blue) S-wave components. The frequency for each event is normalised and then the mean is computed from all the recorded events.

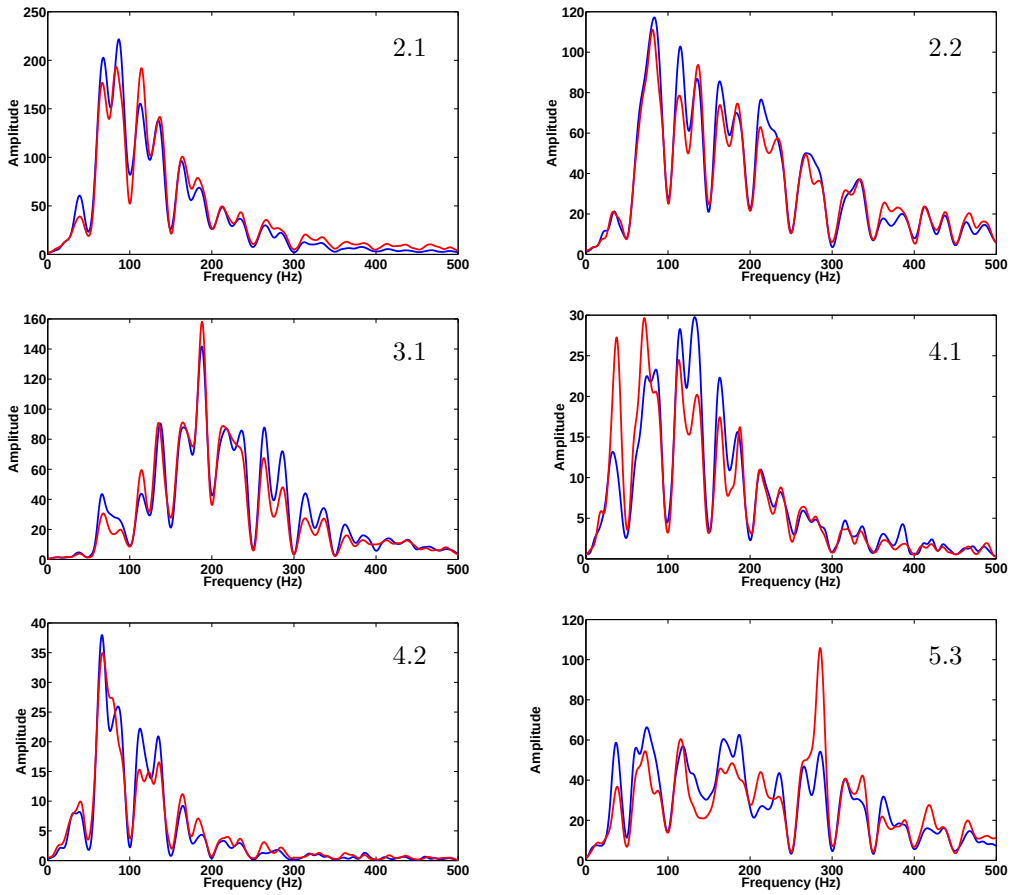

Figure 7.3: Frequency content of the Natih A subset (stations 2.1, 2.2, 3.1, 4.1, 4.2 and 5.3) (see Figure 7.2 caption).

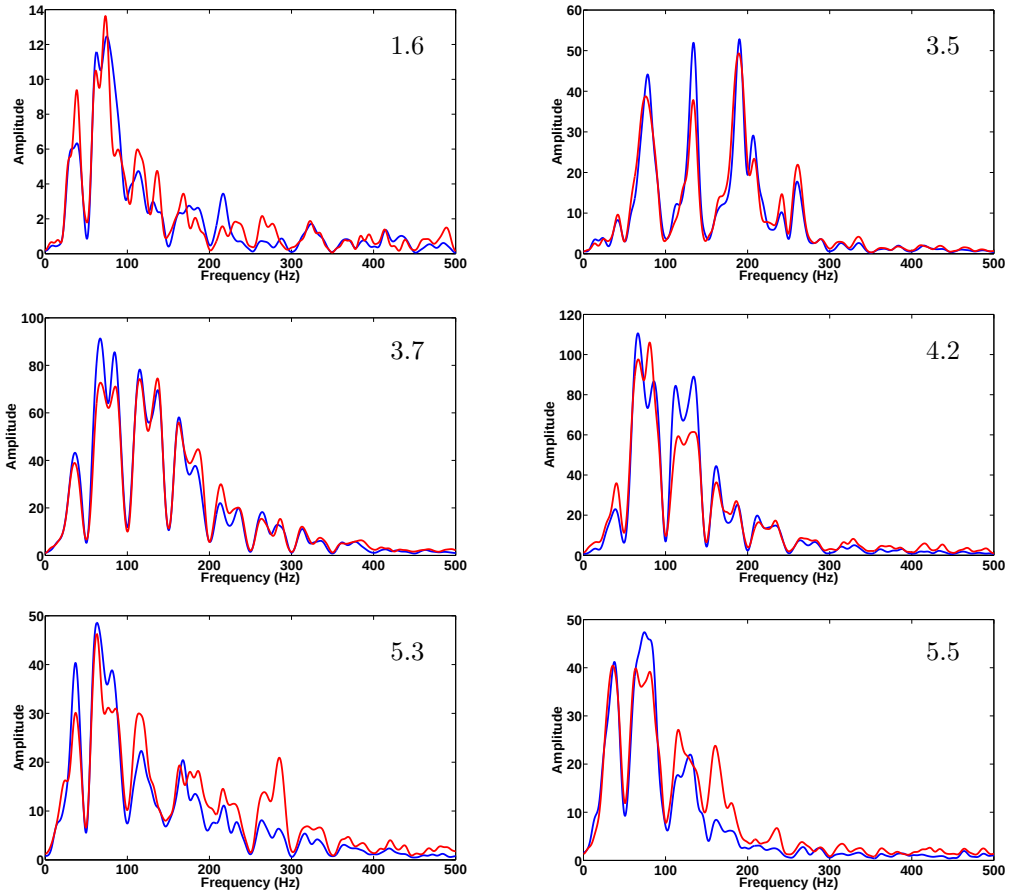

Figure 7.4: Frequency content of the Natih B-G1 subset (stations 1.6, 3.5, 3.7, 4.2, 5.3 and 5.5) (see Figure 7.2 caption).

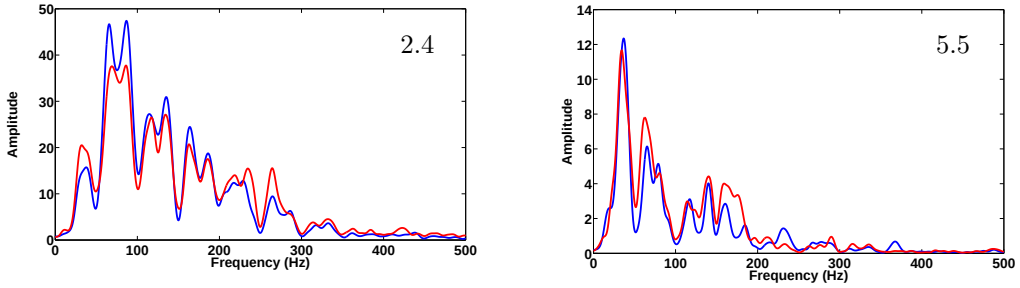

Figure 7.5: Frequency content of the Natih B-G2 subset (stations 2.4 and 5.5) (see Figure 7.2 caption).

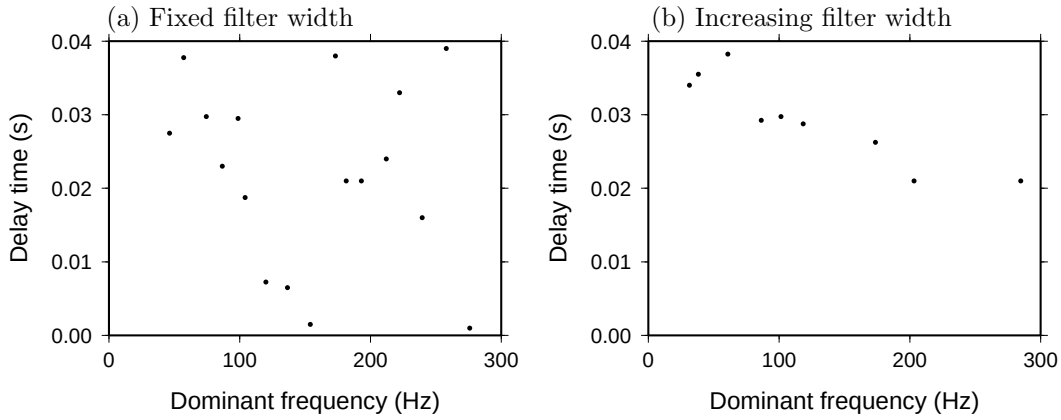

Figure 7.6: Comparison of two filtering techniques applied to the same source-receiver combination. (a) Fixed filter bandwidth of 30 Hz and (b) increasing filter bandwidth by 1 octave. Note the high scatter in δt when using filter with a fixed bandwidth.

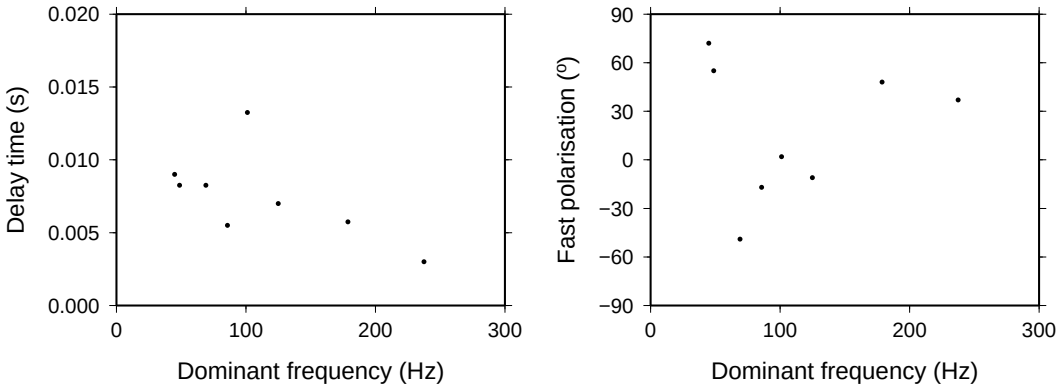

Figure 7.7: Variation of δt and Φ for the same source-receiver combination. Note the scatter in Φ although there is a clear decay in δt with increasing frequency.

7.5 Inversion

I invert for the fracture strike (α), fracture density (ξ) and fracture radius (a_f) that best matches the observations of FDA using the poroelastic model of Chapman (2003). A grid search is performed over the three fracture parameters to find the best combination that minimises the root mean square (RMS) misfit between the real and modelled data. It is performed in two steps. During the first step, while varying α with fixed steps of 5°, a_f and ξ are varied in power steps of 10^n to find in what order of magnitudes they fall. The second step is to search with shorter increments around a_f and ξ which were obtained from the first step. This allows searching over a wide range of possible fracture parameters in a fast and convenient way and without prior knowledge of the expected parameters. For example, the code searches for all possible values of a_f from the micro scale (10^{-6}) up to 100s of meters. Note that the grid search over α suffers 90° ambiguity (e.g., α of 45° and 135° generate identical FDA effect). Thus, the grid search over α is restricted to the range $0 \leq \alpha \leq 90°$.

The confidence on the results is assessed using an F-test (e.g., Silver & Chan, 1991). The 90% confidence interval is computed by normalising the RMS misfit surfaces. Also, the optimum fracture parameters from the inversion are used to generate the best fit model, which is then plotted with the real data to illustrate the match between them. Visual inspection of the plots is used to choose measurements with well constrained solutions.

To examine the robustness of the inversion, I generated a synthetic model using the Natih A parameters summarised in Table 7.1, with a vertically dipping fracture set having density of 0.1 and radius of 1 m. The fracture strike, ray azimuth and ray inclination are set to 30° from north, 0° from north and 90° from vertical, respectively. Noise is added to the estimates of δV_s using random distribution of δV_s magnitudes in the range 0% to 2%. The modelled data are then fed to the inversion code. The results are illustrated in Figure 7.8. It can be seen that the inversion is very robust and it gives estimates (α=30°, ξ=0.1 and a_f=0.83) which are very close to the original inputs, despite the addition of noise. The elongated shape of the RMS map of a_f against ξ in Figure 7.8 reveals interesting result that the minimum ($\sim$0.06) and maximum ($\sim$0.13) estimates of ξ correspond to what would be obtained if the frequency-independent models of Thomsen (1995) and Hudson (1981) are used, respectively. Both models are insensitive to fracture size. This highlights the importance of using frequency-dependent equivalent medium models. The same finding was reported by Maultzsch et al. (2003) using VSP data.

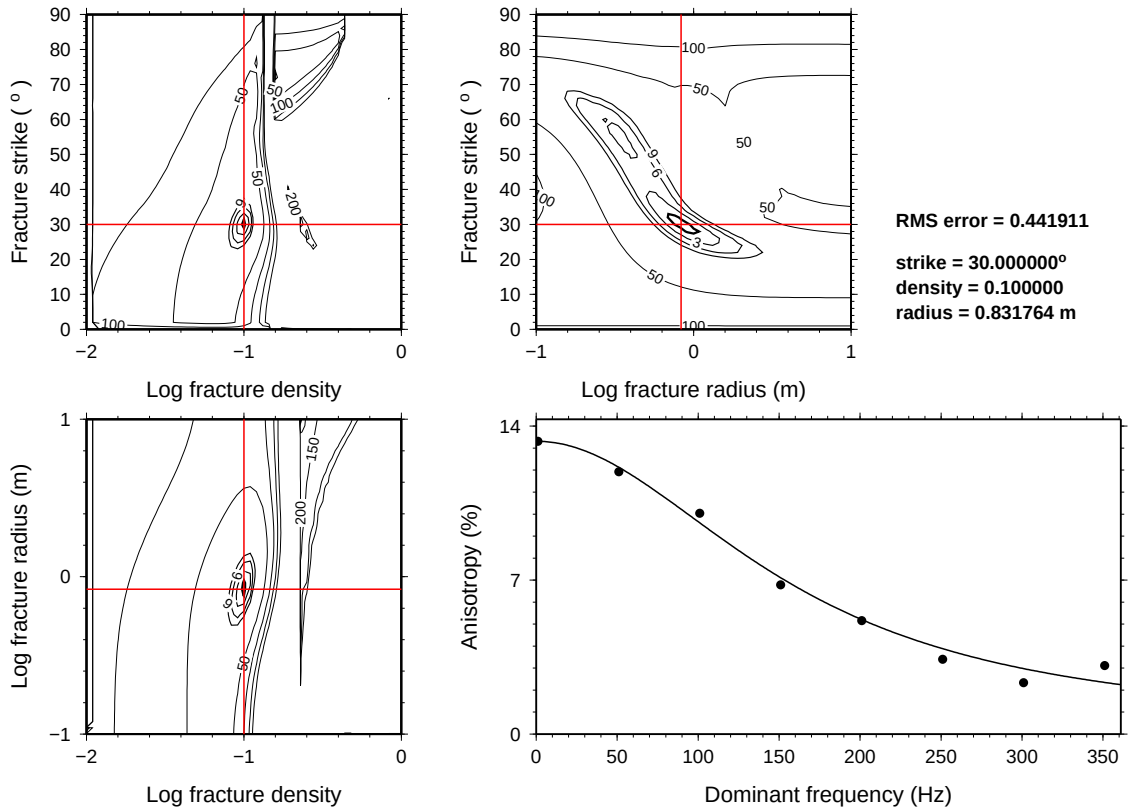

Figure 7.8: Inversion of frequency-dependent anisotropy synthetic data. Grid searches over fracture strike, density and radius. The thick black contour is the 90% confidence interval. The straight red lines in the misfit plots mark the inversion results. The right-bottom plot depicts the input synthetic data (dots) and the best-fit model (line). Random noise has been added to the synthetic data.

7.6 Results

I analyse events that have their raypaths entirely confined to the lithology units. Evidences of FDA effect have been observed in 11 events within the Fiqa, 46 events within the Natih A, 24 events within the Natih B-G1 and 6 events within the Natih B-G2. The number of FDA observations which passed the visual inspection of the misfit plots is 4 for the Fiqa, 11 for the Natih A, 9 for the Natih B-G1 and 2 for the Natih B-G2. The results from the inversion are summarised in Table 7.2. Examples of good inversions from each of the investigated lithology units are displayed in Figures 7.9-7.12.

Fracture radius (a_f)

The results from the inversion suggest that anisotropy is caused by micro-scale cracks in the Fiqa shale (1.3×10^{-6} m), metre-scale fractures in the Natih A reservoir (2.5 m) and centimetre-scale

Formation	Number of observations	Strike	Density	Radius (m)
Fiqa	4	variable	0.11-0.28 (0.18)	3×10^{-7}-2×10^{-6} (1.3×10^{-6})
Natih A	11	NE or NW	0.063-0.16 (0.11)	0.1-9.1 (2.5)
Natih B-G1	9	variable	0.036-0.21 (0.10)	0.005-0.04 (0.012)
Natih B-G2	2	variable	0.076-0.083 (0.08)	0.013-0.02 (0.017)

Table 7.2: Summary of fracture parameters obtained from frequency-dependent anisotropy inversion. Note that strike has 90° ambiguity. Numbers between brackets are average estimates.

fractures in the Natih B-G1 (0.012) and Natih B-G2 (0.017 m) units. There is no significant lateral variation in the fracture radius at the Natih A level (Figure 7.13a and Table 7.3). The variation becomes noticeable at the Natih B-G1 level (Figure 7.13b and Table 7.3) with the SE block having larger fractures (average 0.015 m) compared to the Graben block (average 0.0091 m) and the NW block (average 0.0082 m). Another interesting finding is that events recorded by monitoring well 5 (Horseshoe feature) show larger fracture sizes compare to those recorded by monitoring well 3 at both Natih A and Natih B-G1 levels (Table 7.3).

Dataset	SE block	Graben block	NW block	Well-3	Horseshoe
Natih A	2.6 (9)	-	2.7 (2)	1.7 (3)	5.0 (2)
Natih B-G1	0.015 (5)	0.0091 (1)	0.0082 (3)	0.0086 (4)	0.04 (1)

Table 7.3: Lateral variation of fracture radius. These are average estimates in unit of metre with the number between the brackets indicating the number of measurements.

Fracture density (ξ)

The Fiqa shale exhibits a high density (average 0.18) of micro-scale cracks. There is a general decline in fracture density with depth within the carbonate rocks. The average fracture density decreases from 0.11 within the Natih A to 0.10 within the Natih B-G1 to 0.08 within the Natih B-G2. Further investigation of fracture density, summarised in Table 7.4 and illustrated in Figure 7.14, reveals that fracture density is also varying laterally between the field blocks. There is a gradual decrease in fracture density in the NW direction, crossing the main graben faults. When considering the entire dataset, fracture density decreases from 0.13 in the SE block to 0.081 in the Graben block to 0.075 in the NW block.

Dataset	SE block	Graben block	NW block
All	0.13 (18)	0.081 (3)	0.075 (5)
Fiqa	0.18 (4)	-	-
Natih A	0.11 (9)	-	0.085 (2)
Natih B-G1	0.11 (5)	0.083 (1)	0.067 (3)
Natih B-G2	-	0.08 (2)	-

Table 7.4: Variation of fracture density between Field M blocks. These are average estimates with the number between the brackets indicating the number of measurements.

Fracture strike (α)

Fracture strike shows wide variability, except for the Natih A where it is predominant in the NE-SW direction (Figure 7.15). However, because of the 90° ambiguity, this strike can be in the NW-SE direction. Because of the wide variability and 90° ambiguity the inverted fracture strikes are not used in the subsequent interpretation.

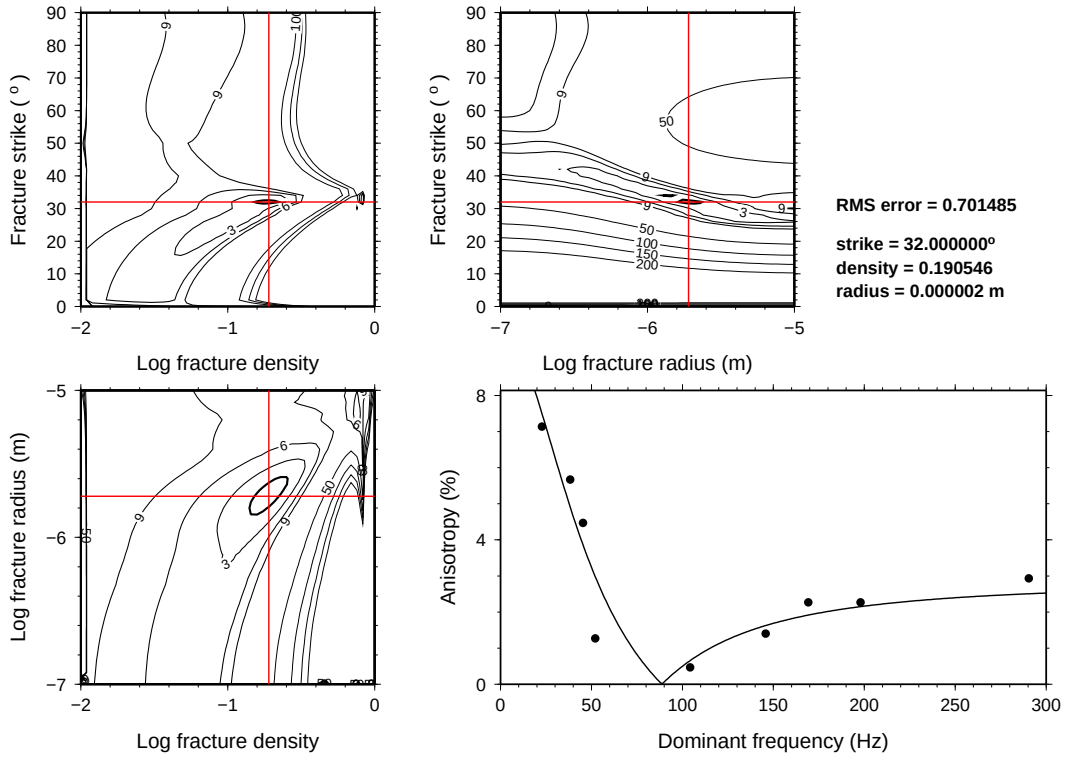

Figure 7.9: An example of frequency-dependent anisotropy inversion in the Fiqa shale (see Figure 7.8 caption). Note the singularity point (i.e., anisotropy=0%) at frequency ~90 Hz.

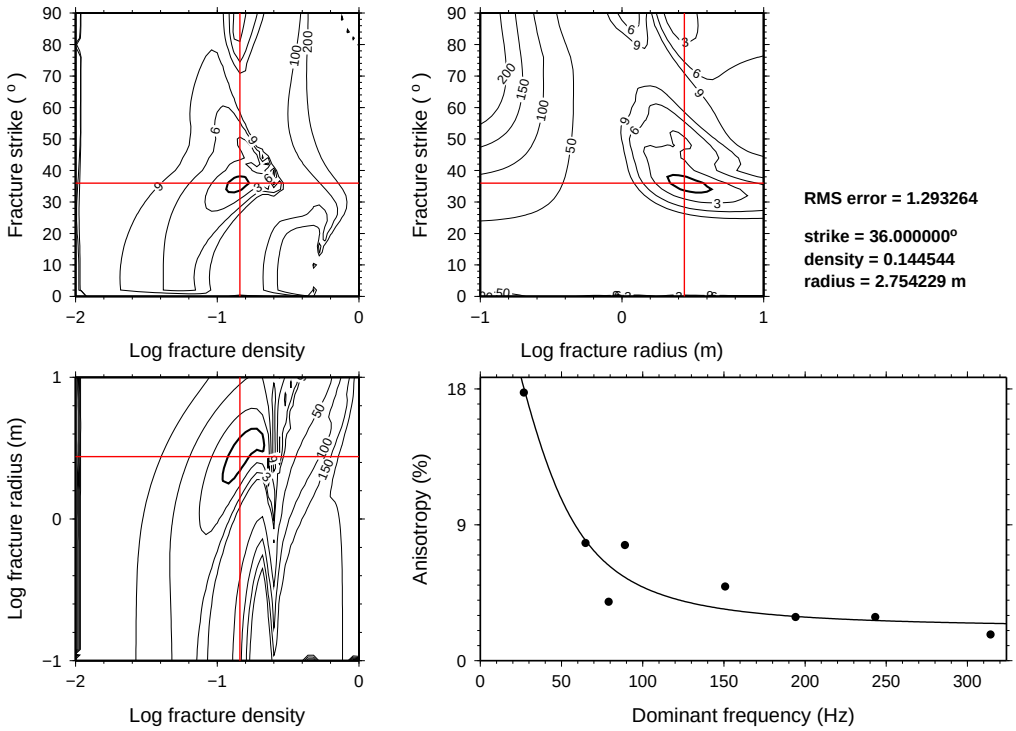

Figure 7.10: An example of frequency-dependent anisotropy inversion in the Natih A reservoir (see Figure 7.8 caption).

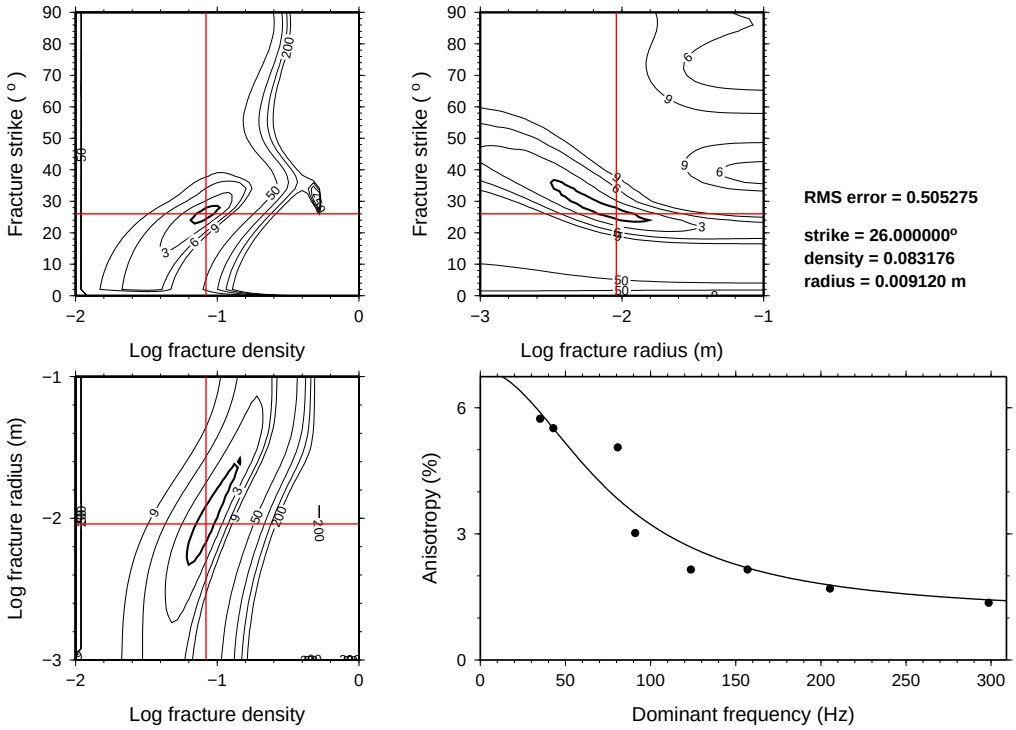

Figure 7.11: An example of frequency-dependent anisotropy inversion in the Natih B-G1 unit (see Figure 7.8 caption).

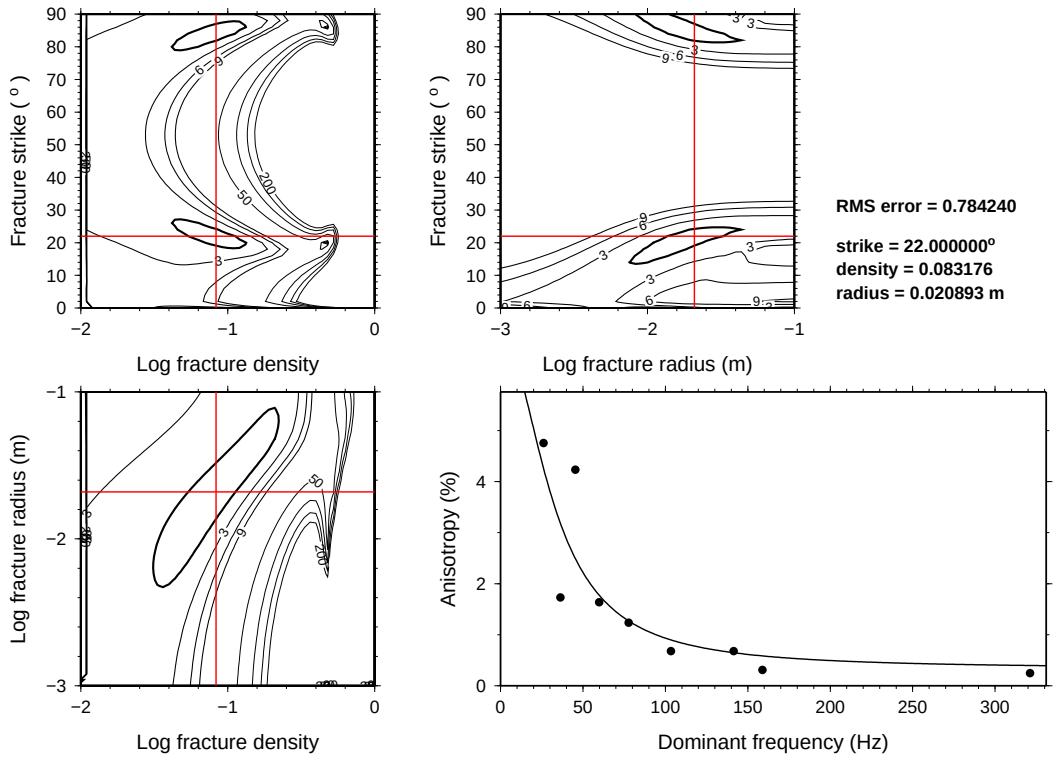

Figure 7.12: An example of frequency-dependent anisotropy inversion in the Natih B-G2 unit (see Figure 7.8 caption).

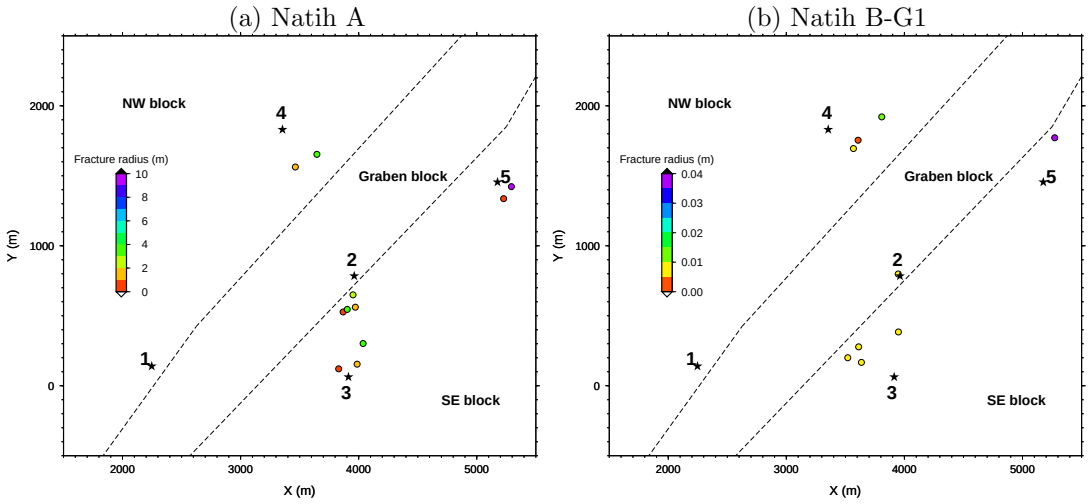

Figure 7.13: Lateral variation in fracture radius at (a) the Natih A level and (b) the Natih B-G1 level.

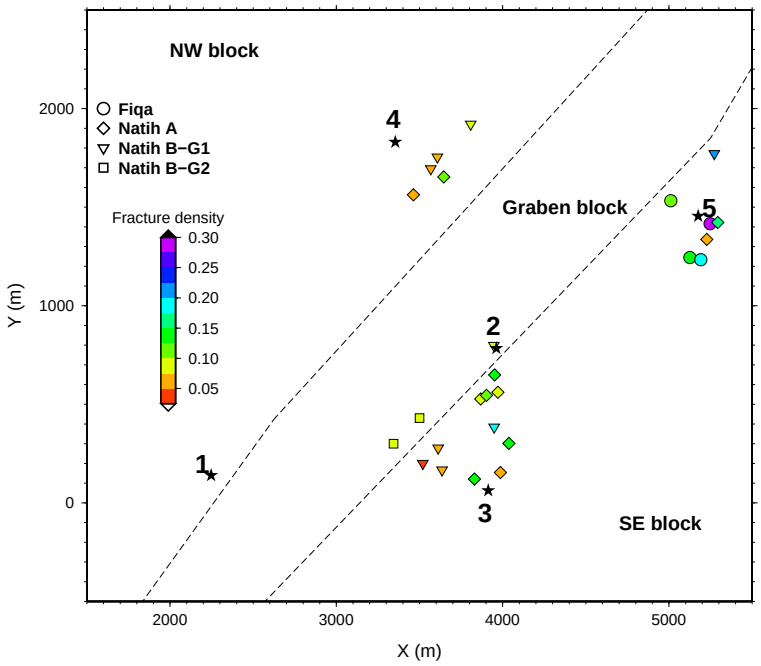

Figure 7.14: Lateral variation in fracture density. The average fracture density decreases from 0.13 in the SE block to 0.081 in the Graben block to 0.075 in the NW block.

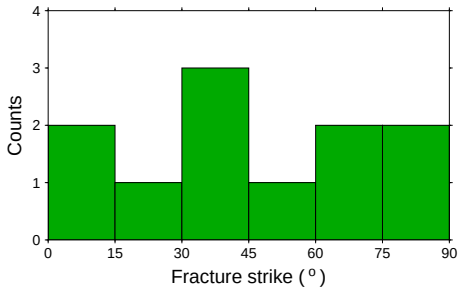

Figure 7.15: Histogram of fracture strike at the Natih A level.

7.7 Discussion

There is a good match between the real and modelled data, and the inversion for fracture parameters is robust. Furthermore, the consistency in the estimates of fracture density and size within each of the investigated lithology units (Table 7.2) indicates the reliability of the inversion. However, there is some uncertainty in the results due to a lack of knowledge of the relaxation time (τ_m). An estimate of fracture radius (a_f) is highly dependent on τ_m, as highlighted by Equation (5). Since we do not have measurements of τ_m for the field rocks, we estimate τ_m using published laboratory data. However, extrapolating from one rock type to another may result in significant and unquantifiable error which is then mapped into the fracture parameters obtained through inversion.

There is no independent estimate of fracture size within Field M to compare with. Al-Kindi (2006) analysed data from the Natih formation outcrops exposed in the Qusaibah anticline (part of the Salakh arch, see Chapter 2). He observed fractures with lengths in the range 4-22 m with fracture aperture between 3 and 14 mm. The Qusaibah anticline is mostly covered by the Natih A rocks. Fracture aperture is expected to be much smaller in the subsurface due to the burial effect. Note that the FDA inversion provides the fracture radius (length of major axis of spheroid) rather than the length. So there is a good agreement between the modelled fracture size at the Natih A level and that observed in the outcrops. Furthermore, borehole observations, summarised in Chapter 2, revealed that the Natih A is populated with fracture corridors and mega-fractures. No measure of their size is given, but they are most likely in the macro-scale.

The finding that fractures within the Horseshoe feature are much larger than those close to well 3 supports the argument that fractures close to well 3 were generated by fluid production. Fluid-generated fractures are expected to be smaller in size. The micro-scale fracture size shown by the Fiqa shale dataset indicates that macro-scale fractures are absent in the cap rock and the fluid communication, causing the FDA effect, occurs between pores and micro-scale cracks. This highlights the importance of the FDA analysis for assessing seal integrity.

The transition from micro-scale cracks in the Fiqa to meter-scale fractures in the Natih A justifies why dipole sonic logs give correctly estimated (4%) and underestimated (2%) δV_s magnitudes for the Fiqa and Natih A, respectively (see Chapter 2). Dipole sonic logs are short in seismic wavelength compared to microseismic data, and thus can not detect such meter-scale fractures in the Natih A reservoir.

There is a general decrease in fracture density with depth. The average fracture density decreases from 0.18 in the Fiqa cap rocks to 0.11 in the Natih A reservoir to 0.1 in the Natih B-G1 to 0.08 in the Natih B-G2. This decrease in fracture density is consistent with the variation in anisotropy with depth. The Fiqa and Natih A exhibit higher magnitudes of anisotropy compared to the underlying Natih B-G formation. Furthermore, the lateral decrease in average fracture density from 0.13 in the SE block to 0.081 in the Graben block to 0.075 in the NW block matches with the observations that the highest amounts of anisotropy lie to the SE part of the field and between the graben faults. We were not able to observe the lateral and depth variation in fracture density when we performed SWS inversion based on rock physics modelling in Chapter 6. This highlights the importance of analysing the frequency-dependent behaviour of anisotropy for fracture characterisation.

7.8 Conclusion

I have modelled observations of frequency-dependent shear-wave splitting anisotropy made on Field M microseismic data. An inversion code which incorporates the poroelastic model of Chapman (2003) is developed to invert for the fracture strike, density and size. The inversion code has the advantage that it can be used with any FDA dataset without prior knowledge of fracture parameters.

In terms of data processing, I have shown that using a filter with increasing width with higher frequencies is more applicable to microseismic data, compared to filter with a fixed width. The fluctuation in the estimates of Φ for the different frequency bands, caused by cycle skipping, is circumvented by fixing Φ to the value determined from SWS analysis on broadband data.

The estimated fracture sizes within the Natih A reservoir agrees with those observed in the formation outcrops. The variation in fracture density with lithology matches with the estimates of anisotropy magnitudes deduced from ordinary SWS analysis. Higher magnitudes of fracture density and anisotropy occur within the Fiqa and Natih A compared to the underlying Natih B-G.

Cumulatively, the results show that the modelling of the frequency-dependent behaviour of anisotropy serves as a tool to characterise reservoirs and assess seal integrity. The method is able to distinguish between the effect of micro-scale cracks and macro-scale fractures. Frequency-independent approaches to anisotropy analysis are not capable of discriminating between such fracture scales.

8
Shear-wave splitting tomography

8.1 Introduction

In the previous chapters, the interpretation of the shear-wave splitting (SWS) observations was based on the assumption that anisotropy is uniformly distributed along the raypath. However, this assumption is not generally true as the splitting we measure represents the bulk effect of all the encountered anisotropic structures along the raypath which their strength and orientation can vary significantly. Existing techniques are not able to deliver sufficient quantitative description of the distribution of anisotropy between source and receiver. The majority of researchers explain their SWS observations by comparing them with surface observations or existing models. Others attempt to explain their results using forward modelling (e.g., Hammond et al., 2010a,b). However, forward modelling does not fully explore the true extent of the parameter space and because of the non-uniqueness in SWS problems the error bounds on models may be misleading (Wookey, 2010). Recently, there have been some attempts to explain SWS observations in a tomographic inversion fashion (e.g., Zhang et al., 2007; Abt & Fischer, 2008; Long et al., 2008; Wookey, 2010). SWS tomography allows for a quantitative parameterisation of the spatial distribution of anisotropy and the determination of nonuniform anisotropic models. For example, such techniques can be used to explore the existence of two or more anisotropic layers (a common problem in the study of lithosphere anisotropy).

There are a few examples of SWS tomography documented in the literature. Zhang et al. (2007) developed a 3D SWS tomography which back project SWS delay times (δt) along raypaths derived from a 3D shear velocity model. They applied the technique to image the 3D anisotropy structure of the Parkfield region in California. Their results are biased partly due to the simplification in the technique by not including the fast-shear wave polarisation (Φ) in the inversion. Abt & Fischer (2008) presented a SWS tomography method to resolve anisotropy associated with subduction zones. They parameterised the mantle as 3D block model of crystallographic orientations with elastic properties of olivine and orthopyroxene. They tested their approach on data from the Nicaragua-Costa Rica subduction zone. Recently, Wookey (2010) proposed an extension to the method of Abt & Fischer (2008) that addresses the non-linearity behaviour of SWS inversion. In

the next section I describe in more details the approaches of Abt & Fischer (2008) and Wookey (2010), and I use the lattest to image anisotropy in Field M.

Previously, the interpretation of anisotropy in Field M was limited by the availability of rays confined to blocks/layers (see Table 5.3 in Chapter 5), rendering the fracture parameters unconstrained. This problem can be circumvented using tomographic imaging where rays crossing the boundaries separating layers and blocks can now be used in the analysis. Also, we have seen the failure of the SWS inversion using rock physics modelling in Chapter 6 in the presence of spatial anisotropy variation. Tomographic technique would rather confirm the existence of spatial variation in anisotropy. Hence, a better understanding of the anisotropy in Field M is expected.

I start this chapter by outlining the method of Abt & Fischer (2008) and its extension by Wookey (2010). Then, I explain my approach to formulate the case of Field M SWS tomography. Finally, I summarise the results and compare them with those from previous chapters.

8.2 Methodology

8.2.1 Description of the approach

The region of interest in the tomographic approach of Abt & Fischer (2008) is divided into domains (i.e., blocks). Each domain is represented by a uniform anisotropy, parameterised by a base elastic model (C_{ij}), three rotation angles defining the orientation of C_{ij} (β_1, β_2 and β_3 for rotation around x-, y- and z-axes, respectively) and a strength parameter (s). The later determines the dilution of C_{ij} which is performed using the Voigt-Reuss-Hill averaging method. The inversion works by adjusting the model parameters (β_1, β_2, β_3 and s) in each of the domains to match a collection of pre-existing splitting measurements in the following order:

1. For each domain, apply the rotations and dilution to C_{ij} to form a resultant anisotropic tensor.

2. Solve the Christoffel equation (see Chapter 6) to calculate Φ and, S_{fast} and S_{slow} velocities. Compute δt using S_{fast}, S_{slow} and the path length in each domain. Now, we have a SWS operator (Γ_i (Φ and δt)) for each domain.

3. Generate a synthetic wavelet and apply to it each Γ_i in propagation order.

4. Analyse the synthetic wavelet using the eigenvalue minimization method (EV, see Chapter 4) of Silver & Chan (1991). Then, compare the splitting measurements to those obtained from real data.

The misfit function in the Abt & Fischer (2008) approach combines the differences between observed and calculated splitting parameters. The inversion utilises a linearised, damped least-square algorithm. Moreover, the non-linear properties of SWS is accounted for, to some extent, by applying the inversion iteratively.

Wookey (2010) incorporated several modification to the approach of Abt & Fischer (2008). The primary one is the use of the waveform data themselves rather than inverting to minimise the misfit with a set of pre-determined splitting measurements. The method of Wookey (2010) works towards minimising the summed second eigenvalue of the covariance matrix of the two split shear-waves (λ_2) for all of the waveforms in the dataset. This means incorporating the analysis stage into the inversion and exempting from the need for a synthetic wavelet. In the new approach, Γ_i is applied directly to the data (in reverse propagation order) and then λ_2 is measured for the resulting waveform (similar to the way done in Silver & Chan (1991)). The total misfit is the sum of λ_2 for all n event-station pairs ($M{=}\sum \lambda_i$). In global seismology, if more than one phase is used (e.g., SKS and SKKS), then n is the number of all shear-wave arrivals included in the model.

The proposed scheme by Wookey (2010) has two main advantages over the method of Abt & Fischer (2008). First, it allows the inversion to restrict the search space for Φ and δt to that which is compatible with a prior knowledge of the anisotropy. Second, it can handle null measurements in the inversion. Anisotropic models with the correct orientation will yield a very small λ_2 in the null data, and will therefore be favoured by the inversion. However, the approach of Wookey (2010) has two main disadvantages over the one by Abt & Fischer (2008). First, the full waveform data must be used instead of using a pre-existing set of splitting measurements. This step requires intensive computation. Second, the inverse problem is not linearised which also requires long computation time. However, Wookey (2010) made the problem computationally feasible by incorporating a parallel algorithm to the inversion code.

Unlike Abt & Fischer (2008), Wookey (2010) treated the inverse problem as generally non-linear to remove the dependance on an initial model and allows the evaluation of a fuller ensemble of models. The Neighbourhood Algorithm (NA) method of Sambridge (1999a) is employed to treat the non-linearity of the inverse problem. The NA sampler uses a geometrical discretisation of the parameter space (Voronoi cells) and iteratively explores the cells which are most promising.

This gives a model ensemble that has fine coverage near minima in the misfit function and sparse coverage away from it. The NA method is controlled by: (1) the number of iteration (N_{iter}), (2) the number of test models per iteration (N_{mod}) and (3) the number of promising cells resampled per iteration (N_{res}).

The misfit function minimised is:

$$\chi^2 = \sum_{i=1}^{n} (\frac{\bar{\lambda}_{2,i}}{\sigma_i})^2 \tag{8.1}$$

where for n source-receiver pairs (if one phase is analysed as in microseismic data), $\bar{\lambda}_{2,i}$=$\lambda_{2,i}/\lambda_{1,i}$ is the normalised second eigenvalue of the ith pair. The normalisation of the eigenvalue is to remove scaling between different station sensitivities and event magnitudes. The error (σ_i) is derived from the signal-to-noise ratio following the definition of Restivo & Helffrich (1999) who define the signal level as the absolute maximum amplitude in the analysis window and the noise as the 2σ variation of the amplitude normal to initial polarisation of shear-wave after splitting is corrected. The devision by σ_i is to weight the inversion towards preferentially linearising the best data.

8.2.2 Preparation of data and domains

There are several inputs which must be supplied to the inversion. These are divided into two main categories: *parameter space* and *pathset*. The *parameter space* consists of a list of all domains in the model. The number of domains, their size and shape depend on the problem addressed. For each domain we need to specify the following:

- A base elastic model (C_{ij}).
- Rotation angles (β_1, β_2 and β_3) to orient C_{ij}. These angles can be fixed or varied within a range.
- A strength parameter (s). This is also can be fixed or varied within a range.

The *pathset* consists of descriptions of the source data and their associated raypaths. Description of the source data include defining:

- Filenames of the 3 orthogonal sets (a, b and c components in the case of microseismic data).
- The optimum shear-wave analysis window.

- The signal-to-noise ratio.
- The degrees of freedom of the data.

The optimum analysis window, signal-to-noise ratio and degrees of freedom can be determined using the cluster analysis method of Teanby et al. (2004b). The raypaths traversing the domains are described by specifying:

- The azimuth and inclination of the raypath through the domain.
- The distance travelled within the domain.

8.2.3 Workflow

Having prepared the data and domains for the inversion, the NA sampler then explore the parameter space according to the specified bounds of the free parameters. The model is evaluated in a similar way that I already described for the Abt & Fischer (2008) approach (see section 8.2.1 above), except that the SWS operator (Γ) is applied to the waveform data themselves instead of a synthetic wavelet. Γ is applied in a reverse order. Then, $\bar{\lambda}_{2,i}$ in the data is measured after all corrections are applied. The total misfit function is calculated following Equation (8.1).

After evaluating a set of test models (N_{mod}), the sampler uses the NA method to determine the number of promising regions (N_{res}) of the parameter space to resample. The global minima is a combination of rotation angles (β_1, β_2 and β_3) and strength parameter (s) that minimises the summed and weighted $\bar{\lambda}_{2,i}$, and consequently best linearise all the data. To measure the associated constraint in the best fitting model, Wookey (2010) used the method of Sambridge (1999b) which is a complement to the NA sampler. The method implements a Bayesian integration of the ensemble to generate probability density functions (PDFs). These are then used to investigate the confidence in the results and explore any trade-off between parameters. The tomographic inversion code incorporates a high degree of parallelisation, yielding a high level of computation efficiency. This makes the processing of large datasets (e.g., Field M microseismic data) feasible.

Since both methods work towards minimising the second eigenvalue (λ_2) of the covariance matrix, the tomographic inversion of Wookey (2010) is directly comparable to the EV method of Silver & Chan (1991). For example, for a simple hexagonal medium the Φ-δt space searched in the EV method is analogous to the search over β_3-s space in the tomographic inversion. This is highlighted in Figure 8.1 using synthetic good splitting, synthetic null splitting and a real

example. The three examples consider the case of a single ray travelling in one domain. In the case of multiple rays traversing the same domain the inversion becomes equivalent to error surface stacking techniques (see for example Restivo & Helffrich, 1999).

8.2.4 Formulating the Field M tomography

In the previous chapters we have concluded that the anisotropy in Field M is controlled by the proximity to the graben faults (lateral variation) and lithology (variation with depth). Thus, I formulate the tomographic problem to further explore this spatial variation in anisotropy. First, I assume the entire field as one domain. Then, I consider the case of three horizontal layers. These are the Fiqa shale, Natih A reservoir and Natih B-G unit. Finally, I investigate the case of having three domains separated by the graben fault planes. The faults are assumed to be vertical for simplicity as their dip is less than 10° from vertical.

The raypaths are assumed to be straight and the bending effect is ignored. This assumption might affect the final results but I use it to ease the preparation of the data and domains. The locations of events and recording stations, and the points at which rays cross the domain walls are used to determine the distance travelled within each domain.

For all inversions I use a uniform prior probability density function. The base elastic model (C_{ij}) is assumed to be represented by an elliptical anisotropy (i.e., the Thomsen's parameters (ε, δ and γ) are all set to be equal to s). The P- and S-wave velocities, and the rock density used to construct C_{ij} are summarised in Table 6.1 in Chapter 6. Then, C_{ij} is rotated in the vertical (β_1) and horizontal (β_3) planes, while varying the magnitude of s, to form tilted transverse isotropy (TTI) symmetry. To some extent, the TTI represents a medium embedded with a single set of fractures. Also, the magnitude of s should be proportional to the percentage difference between the fast and slow shear-wave velocities along the raypath (δV_s).

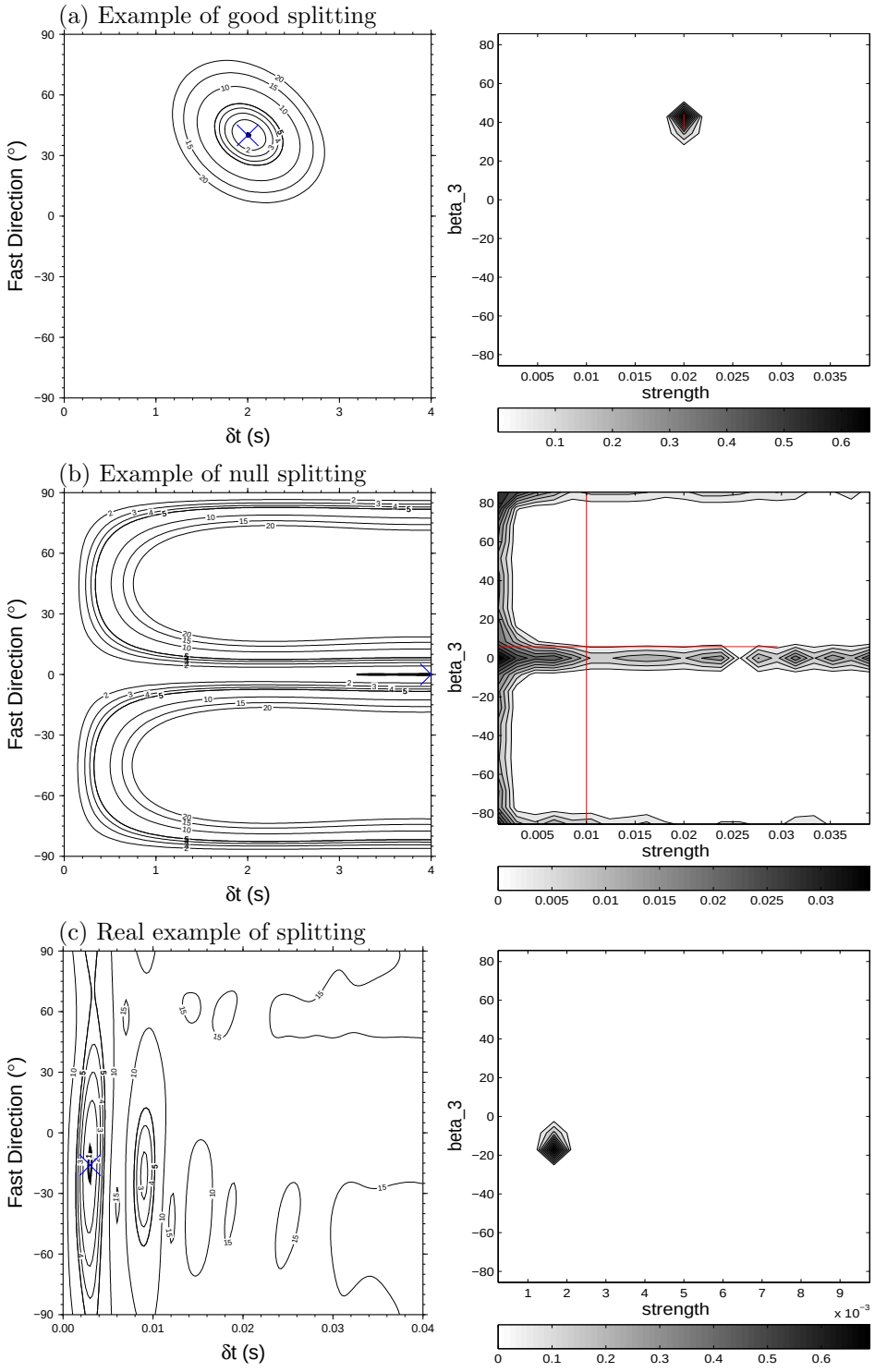

Figure 8.1: Comparison of using the eigenvalue minimisation method [Left panel, F-test error surface] and the tomographic inversion [Right panel, 2D probability density function] for the cases of: (a) synthetic splitting (Φ=40°, δt=2 s and initial polarisation=0°), (b) synthetic null splitting (Φ=0°, δt=2 s and initial polarisation=0°) and (c) real example of splitting (Φ=−16°, δt=3 ms and initial polarisation=115°). White noise has been added to the synthetic wavelets in (a) and (b).

8.3 Results

For the inversion I use the 325 reliable splitting measurements determined by the automated approach described in Chapter 4. The ray coverage is shown in Figure 8.2. It is clear that the ray coverage is more dense in the SE and Graben blocks compared to the NW block. Similarly, the ray coverage is better in the Natih A and Natih B-G compared to the Fiqa shale. The results are displayed in Figures 8.3-8.5, including summary table of the results at the end of each figure.

The inversion yields uniform probability density function (diamond shape) when inverting the entire dataset assuming single domain (Figure 8.3). The lowest misfit remains close to the average misfit which indicates that the inversion is not able to fit one model to the data. The inversion becomes more reliable when dividing the field into domains. Better constrained results are obtained when considering layered model (Fiqa, Natih A and Natih B-G, Figure 8.4) compared to the case when dividing the field into blocks separated by the graben faults (Figure 8.5). This may indicate that the lateral variation in anisotropy is more complicated compared to the variation with lithology. To get better resolution of the lateral variation in anisotropy, the field should be divided into smaller domains (e.g., 1x1 km blocks). However, this will require intensive computation and introduce more free parameters. Instead, I observe the lateral variation in anisotropy in a more localised scale by considering the rays transversing the Natih A (245 measurements) and the Natih B-G (249 measurements) separately. Rays transversing each of the two formations are then subdivided among three domains separated by the graben faults. The results are shown in Figures 8.6 and 8.7.

8.4 Discussion

The failure of the inversion to fit one model to the data when assuming single domain supports the existence of strong spatial variation in anisotropy in Field M as we have seen in the previous chapters. Better constrained results are obtained when dividing the field into domains and hence sensing the localised variation in anisotropy. The results are summarised in Figure 8.8. Assuming that the elastic tensor represents a medium with a single fracture set, overall, the inversion favours the NW-SE strike in most cases. This was also the case when inverting the entire dataset in Chapter 6 (see Table 6.3). When considering a layered model (Figure 8.4), the inversion shows subvertical fracture dip in the Fiqa (β_1=84°) and the Natih A (β_1=80°), and subhorizontal dip

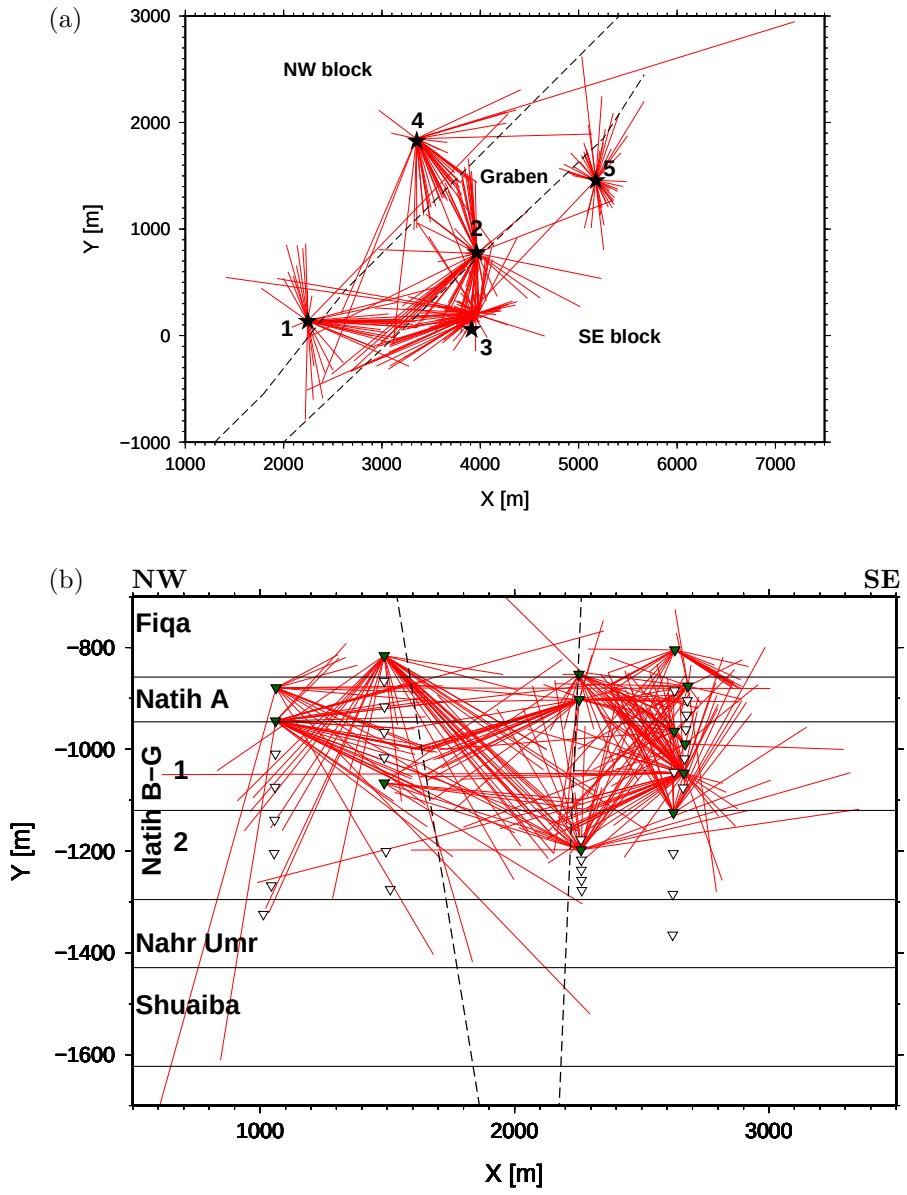

Figure 8.2: Spatial coverage of the rays used in the tomographic inversion shown in (a) map view and (b) NW-SE cross-section. Green triangles denote the stations with known tool orientation.

in the Natih B-G (β_1=41°). This generally agrees with the results obtained in Chapter 5 using ordinary SWS analysis (see Table 5.3). Furthermore, there is a general decrease in the magnitude of the dilution factor (s) from 0.03 in the Fiqa to 0.002 in the Natih A to 0.001 in the Natih B-G. This agrees with the variation in δV_s, although the magnitude of s at the Natih A is expected to be close to that found in the Fiqa or even higher.

The resultant probability density functions are highly scattered when assuming three domains separated by the graben faults (Figure 8.5), hence the results are not of use. However, better constrained solutions are obtained when considering the lateral variation across the faults within the Natih A and Natih B-G, especially in the latter one (Figures 8.6 and 8.7, see also the summary in Figure 8.8b). In both examples, the fracture dip is subvertical within the NW and Graben blocks. In the SE block, the fracture dip decreases to 58° within the Natih A and 46° within the Natih B-G. These dips agree with the 55° fracture dip obtained from the ordinary SWS analysis of measurements confined to the SE block (see Table 5.3 in Chapter 5). The fracture strike is oriented in the NW-SE direction for both the Graben and SE blocks. However, there is a switch from NW-SE to NE-SW fracture strike in the NW block when analysing rays traversing the Natih A and Natih B-G, respectively. The NW and Graben blocks at the Natih A level have higher magnitudes of s compared to the same blocks at the Natih B-G (Figure 8.8b). This agrees with the observations that the highly fractured Natih A reservoir is highly anisotropic compared to the non-producing Natih B-G formation. This variation, however, is not clear within the SE block. On the other hand, the later variation in s (i.e., between field blocks) within both the Natih A and Natih B-G contradicts with the variation in δV_s that the amount of splitting is higher in the SE and Graben blocks compared to the NW block.

The mismatching, in some cases, between the results from tomography and those obtained in the previous chapters might be due to the oversimplification by assuming a base elastic model of elliptical anisotropy. The other reason might be the problem of equivalencies (non-uniqueness) when dealing with multi-domain anisotropic models. For example, in the studies of multi-layer splitting it is possible to find a single layer solution which is of relatively similar likelihood to the two layer solution. Despite all this, the results look promising and open the door wide to improve our understanding of reservoir anisotropy in the future. I suggest that the inversion can be improved in the following ways:

- The elasticity tensor should be expressed in terms of HTI and VTI parameters as in Chapter 6. This will be more applicable to microseismic studies and will make the interpretation of the results much easier. The current design of the tomography code is more suitable for global seismology studies.

- More efficiency and better constrained solutions can be obtained by decreasing the number of free parameters or restricting their ranges. This requires additional information, probably, from other geophysical techniques or geological models.

- Incorporate a non-uniform prior probability density function in the ensemble evaluation. This will allow uncertainty in the imposed constraints to be included. Again, this requires supporting information about the nature of anisotropy.

- Include high quality SWS nulls in the inversion. This will add more constraints into the inversion.

Wookey (2010) applied the tomography approach to SKS data from the North Canadian shield region. The same data have been studied previously by Snyder & Bruneton (2007) who combined two layer splitting analysis with surface wave data to infer the existence of two distinct anisotropy layers within the lithosphere. Despite the high quality of the data, because of the problem of equivalencies, Wookey (2010) was not able to uniquely match the results by Snyder & Bruneton (2007) unless fixing the strike of the upper anisotropy layer (β_3) to that inferred by Snyder & Bruneton (2007). In addition, Wookey (2010) included null splitting measurements in the inversion. This example highlights the importance of incorporating external information into the inversion to minimise the risk of non-uniqueness even when dealing with high quality data.

8.5 Conclusion

SWS tomography is among the frontiers in the study of SWS. In this chapter I have illustrated its applicability to microseismic data using the Field M dataset. I follow the tomographic inversion approach of Wookey (2010). The inversion works by generating elastic tensor for each domain in the model and then orient the tensor according to a pre-specified rotation angles. The Christoffel equation is used to calculate SWS operator (Φ and δt) for each domain. Then, the splitting operator is applied to the real waveform data. The best model is the one with the minimum summed and weighted second eigenvalue of the covariance matrix (λ_2). The SWS inversion problem is treated as non-linear and handled using the Neighbourhood Algorithm of Sambridge (1999a). In this way the method is able to fully explore the complicated parameter space required to describe the anisotropy. Furthermore, the tomographic code incorporates a high degree of parallelisation that makes the processing of large data volumes feasible.

I applied the inversion to the reliable splitting measurements previously determined in Chapter 4. The inversion failed to converge to a solution when assuming one domain. Better constrained solutions are obtained when dividing the field into domains. This most likely indicates the existence of significant spatial variation in the anisotropy. In general, the orientations of the anisotropic symmetries (strike and dip) obtained from the inversion agree with those determined from ordinary SWS analysis in Chapter 5. However, there is some mismatching when comparing the strength factor (s) to the magnitudes of δV_s. This is attributed to the oversimplified assumption of elliptical anisotropy and to the problem of equivalencies when dealing with multi-domain anisotropic models.

Different ways of improving the inversion have been proposed. These include decreasing the number of free parameters or restricting their ranges with the aid of external information about the region of interest. The inclusion of null splitting measurements may also help improving the reliability of the results.

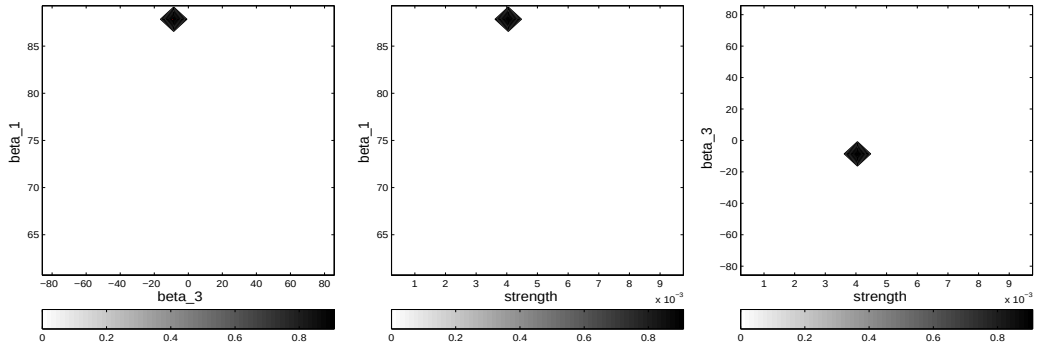

β_1 (°)	β_3 (°)	s	lowest misfit	average misfit
88±0.0	-9.2±0.01	0.004±0.0	6226	6232

Figure 8.3: Tomographic inversion results when inverting the entire dataset assuming one domain. 2D probability density functions for the orientation angles (β_1 and β_3) and strength (s).

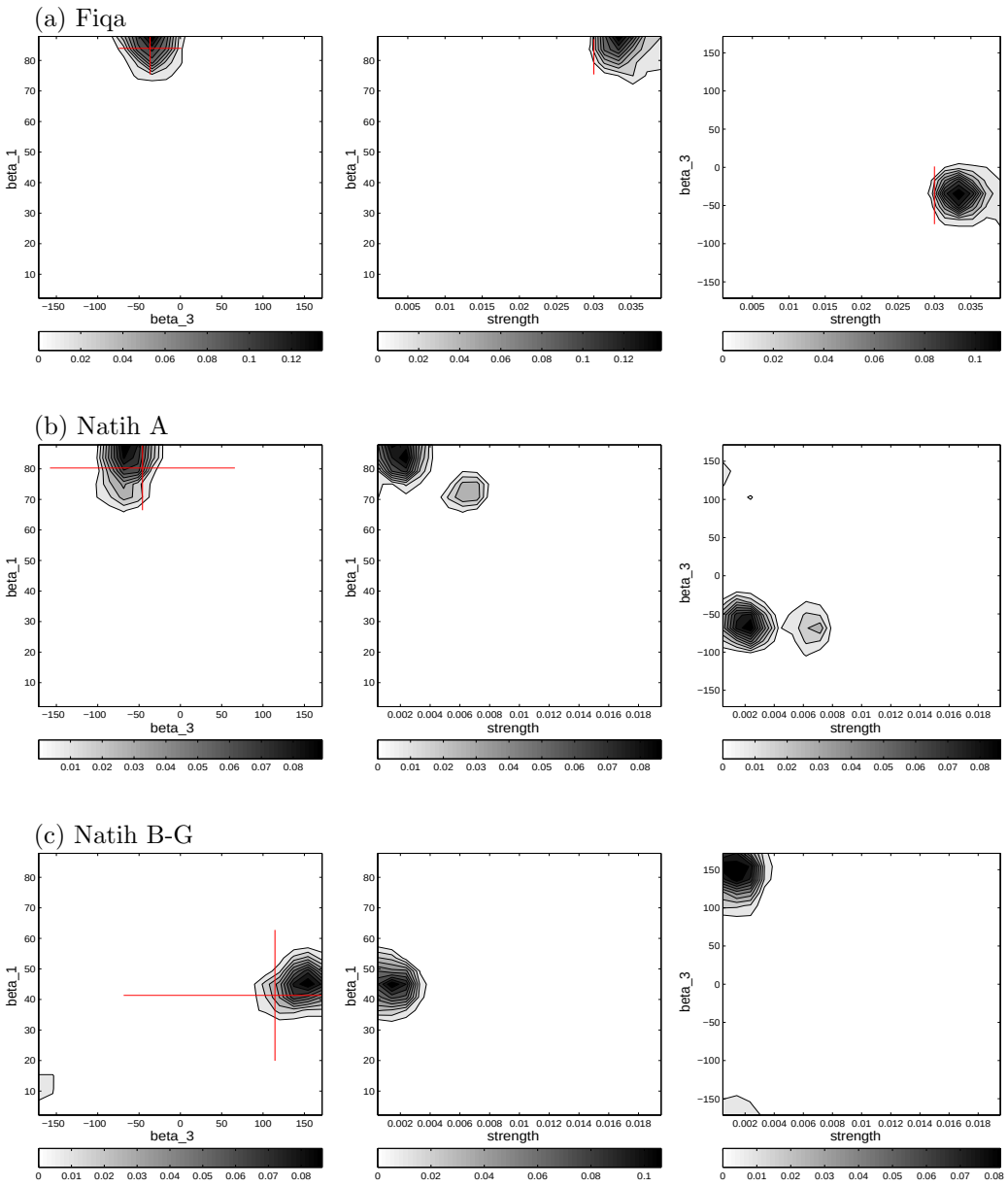

Fiqa			Natih A			Natih B-G		
β_1 (°)	β_3 (°)	s	β_1 (°)	β_3 (°)	s	β_1 (°)	β_3 (°)	s
84±4.4	-37±19.3	0.03±0.0	80±7.1	-46±57.1	0.002±0.0	41±10.9	114±93.4	0.001±0.0
lowest misfit		5448	average misfit		6618			

Figure 8.4: Tomographic inversion results when inverting the entire dataset assuming three domains separated by the boundaries between the Fiqa, Natih A and Natih B-G. 2D probability density functions for the orientation angles (β_1 and β_3) and strength (s). The red cross represents the 2σ errors.

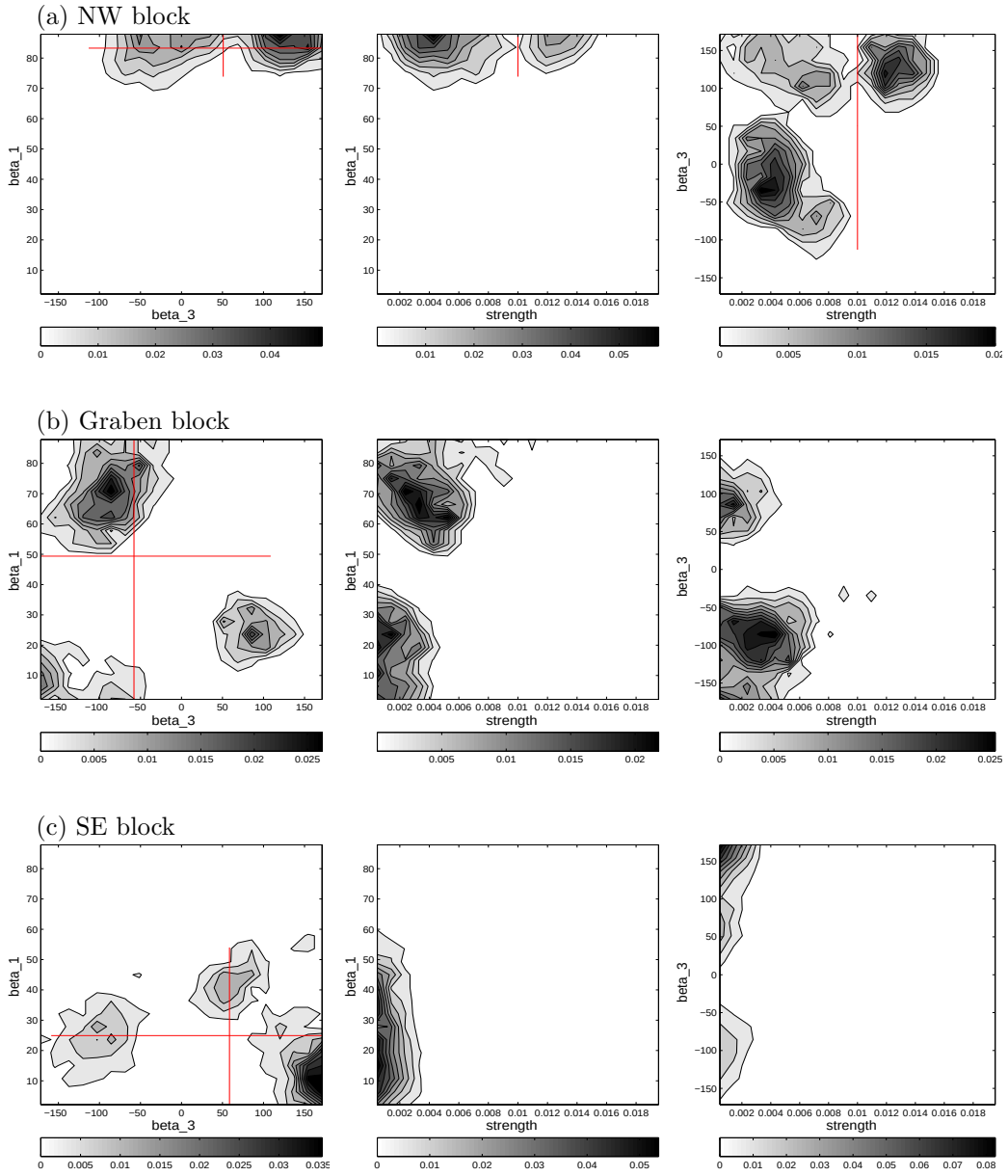

NW block			Graben block			SE block		
β_1 (°)	β_3 (°)	s	β_1 (°)	β_3 (°)	s	β_1 (°)	β_3 (°)	s
83±4.8	51±83.6	0.01±0.0	49±27.7	-58±85.0	0.002±0.0	25±14.8	59±110.7	∼0
lowest misfit		5595	average misfit		6851			

Figure 8.5: Tomographic inversion results when inverting the entire dataset assuming three domains separated by the planes of the graben faults. 2D probability density functions for the orientation angles (β_1 and β_3) and strength (s). The red cross represents the 2σ errors.

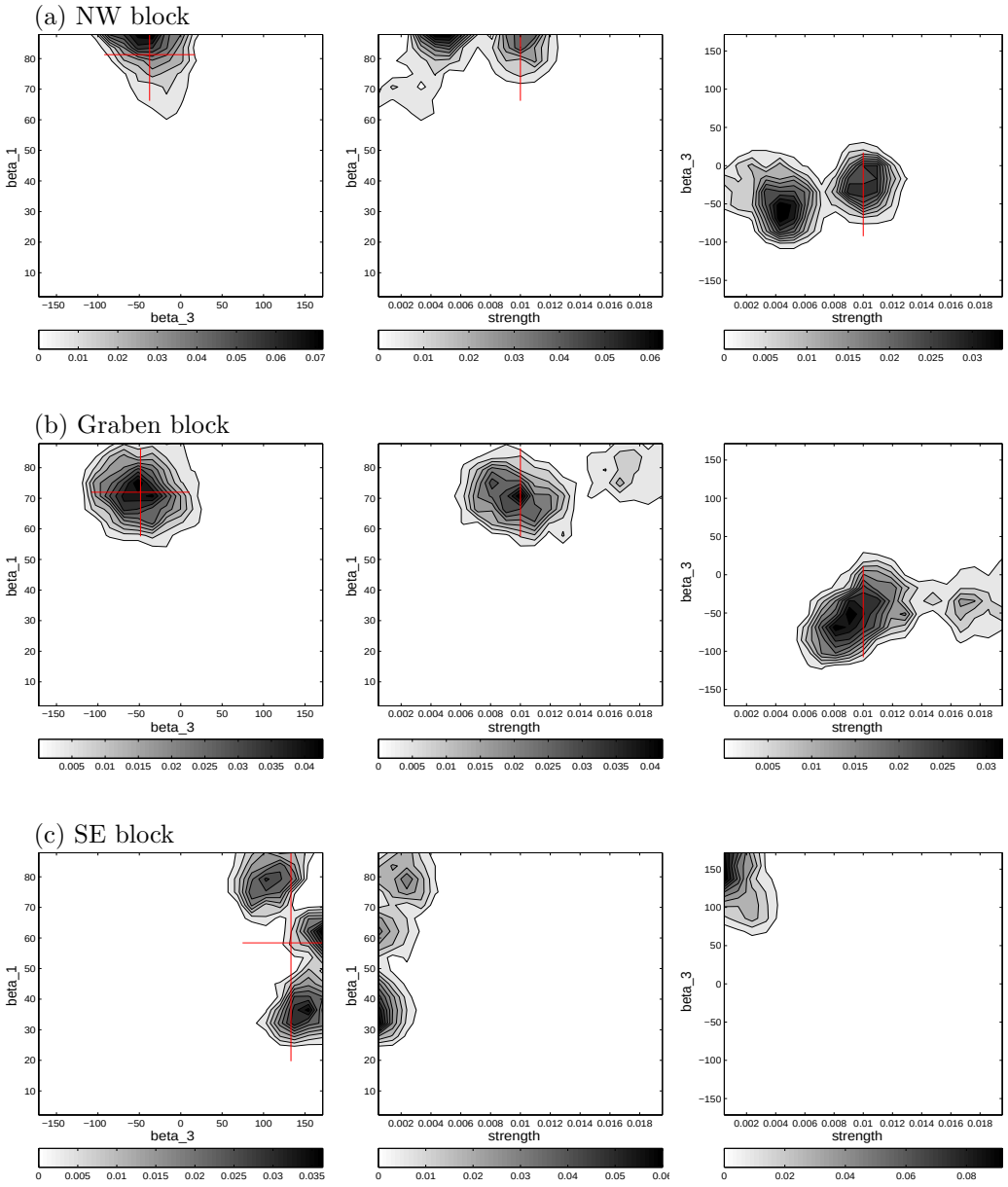

NW block			Graben block			SE block		
β_1 (°)	β_3 (°)	s	β_1 (°)	β_3 (°)	s	β_1 (°)	β_3 (°)	s
81±7.7	-38±27.9	0.01±0.0	72±7.4	-49±30.3	0.01±0.0	58±19.7	133±29.8	∼0
lowest misfit		4138	average misfit		4981			

Figure 8.6: Tomographic inversion results when inverting the rays traversing the Natih A reservoir assuming three domains separated by the planes of the graben faults. 2D probability density functions for the orientation angles (β_1 and β_3) and strength (s). The red cross represents the 2σ errors.

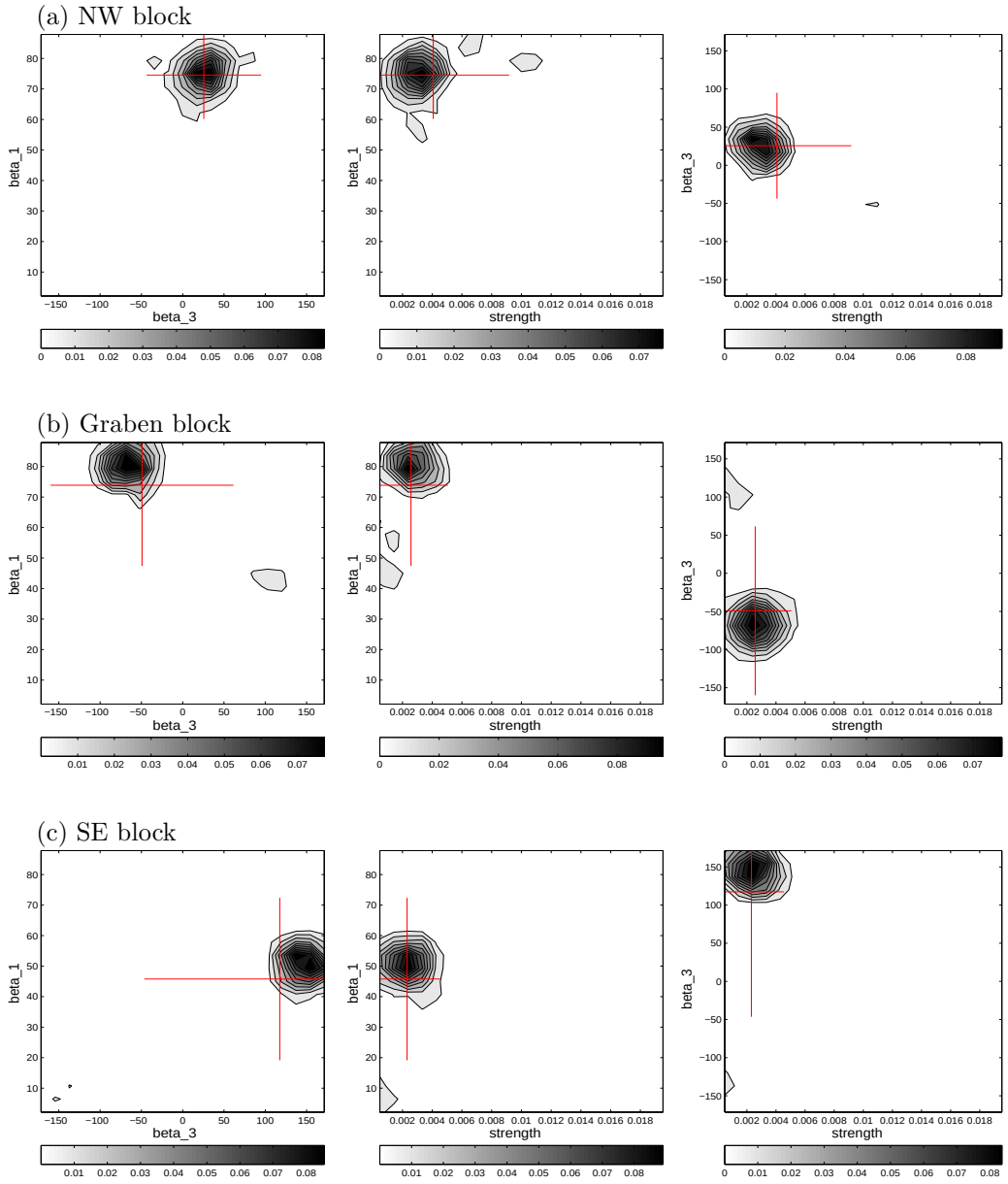

NW block			Graben block			SE block		
β_1 (°)	β_3 (°)	s	β_1 (°)	β_3 (°)	s	β_1 (°)	β_3 (°)	s
75±7.3	26±35.4	0.004±0.003	74±13.5	-49±56.5	0.003±0.001	46±13.6	117±83.6	0.002±0.001
lowest misfit		4263	average misfit		5352			

Figure 8.7: Tomographic inversion results when inverting the rays traversing the Natih B-G formation assuming three domains separated by the planes of the graben faults. 2D probability density functions for the orientation angles (β_1 and β_3) and strength (s). The red cross represents the 2σ errors.

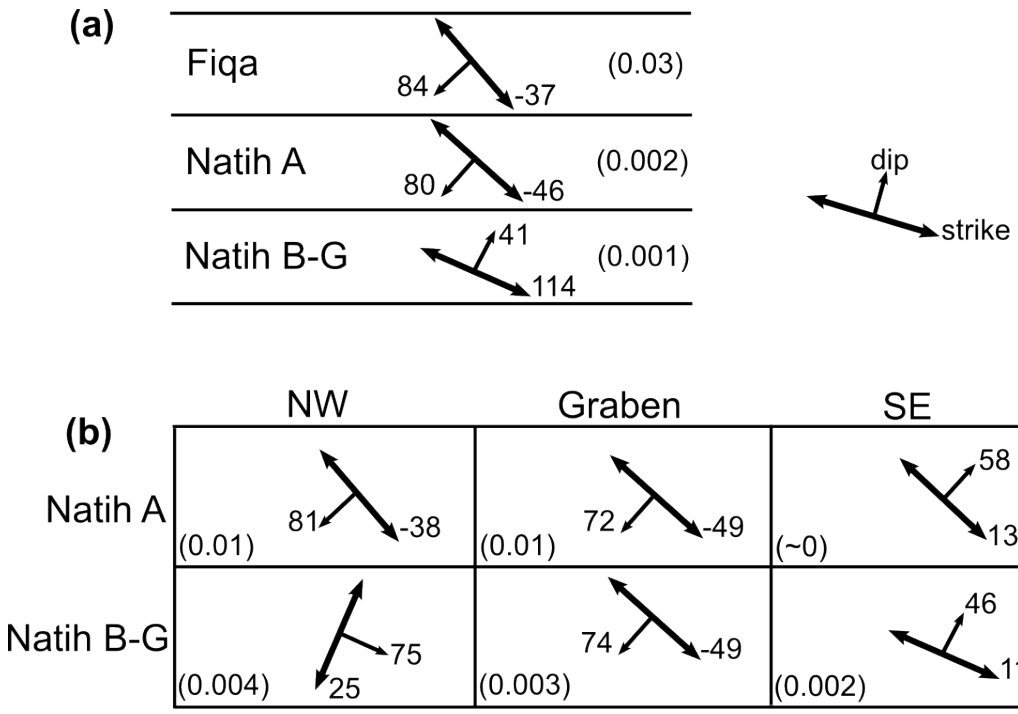

Figure 8.8: A summary cartoon of the results from shear-wave splitting tomography. (a) Results for the case of layered model. (b) Results for the cases when considering the rays traversing the Natih A and Natih B-G (separately). Numbers between brackets are the elastic tensor strength (s).

9
Conclusions

9.1 Introduction

"Microearthquakes are more than dots in a box"[1]. This thesis emphasises this statement by showing that a wealth of additional information can be extracted from the regularly observed clouds of events in reservoirs. The study explores the potential of using microseismic monitoring as a tool to characterise reservoir anisotropy and fractures. This was achieved by applying several shear-wave splitting (SWS) techniques to a microseismic dataset acquired from a petroleum field in Oman (referred to as Field M). These techniques include: (1) direct observation of the spatio-temporal variation in the splitting parameters (fast polarisation direction (Φ) and delay time (δt)), (2) SWS inversion for fracture and anisotropy parameters using rock physics modelling, (3) frequency-dependent anisotropy analysis and modelling and (4) SWS tomography. Throughout the study, the success of using SWS to characterise the Field M rocks was assessed by comparing the results to those previously obtained from other seismic and non-seismic techniques, and to the field geology.

When mentioning the phrase 'reservoir imaging', attention goes straight to active seismic surveying like 3D seismic and VSP. This project shows that there is promising potential in using microseismic monitoring as an imaging tool. Microseismic data, especially those acquired by borehole arrays, have the advantage of providing ~3D images of seismic anisotropy, allowing for the estimation of strike and dip of the anisotropic symmetry. Furthermore, microseismic data can provide an *in situ* measure of seismic anisotropy within and around a target, avoiding effects of the overburden, which is a problem in 3D and VSP seismic surveying. The other advantage of estimating anisotropy from microseismic data is that it is possible to observe changes in anisotropy over time. With knowledge of the field, the temporal change in anisotropy can be correlated with the geomechanical behaviour of the field.

In the following I summarise the conclusions from each stage of the research presented in this thesis. Then, based on these conclusions and the lessons learnt, I give some recommendations to the Field M operator. Finally, I provide some ideas for future research on the subject.

[1] Based on the article entitled "Beyond the dots in the box: Microseismicity-constrained fracture models for reservoir simulation" by Eisner et al. (2010).

9.2 Overview of conclusions

9.2.1 Statistics of the microseismic events

Prior to the SWS analysis, I presented a statistical analysis of the dataset. The aim was to gain insights into the dataset and how the seismicity and its associated parameters change with space and time. The following conclusions have been made.

- The majority of the events occurred within the highly compacting Natih A reservoir. These events have low magnitudes and are possibly caused by perturbations to the *in situ* stress conditions driven by gas production. This argument is supported by the correlation between seismicity levels and gas production rates from the Natih A reservoir.

- Events within the Natih B-G formation have higher magnitudes compared to those in the Natih A reservoir. The events are mostly clustered along the two graben faults that cross-cut the field formations, indicating that the seismicity is due to the reactivation of faults.

- The magnitudes of the source parameters (seismic moment, moment magnitude, source radius and stress drop) are dependent on lithology. The highest estimates are within the mechanically stable Natih B-G formation, whereas the lowest magnitudes are within the soft compacting Natih A reservoir. Moderate source parameter magnitudes are found within the Fiqa shale.

- The magnitude of the b parameter in the Gutenberg-Richter relation increases from 0.77 in the Fiqa shale to 0.85 in the Natih A and to 1.05 in the Natih B-G. This increase possibly reflects an increase in heterogeneity with depth and/or increase in pore pressure (decrease in effective stress).

9.2.2 Automation of shear-wave splitting

One of the aims of this thesis was to develop an automated SWS analysis method that can handle the growing size of microseismic data volumes. Obviously, it is too time consuming to process such large data volumes manually. Moreover, manual analysis and human interaction introduce subjectivity, which is an issue when it comes to ranking the reliability of splitting measurements. This study introduces an approach to automate the SWS analysis of microseismic data. The

approach combines the use of cross-correlation (XC) and eigenvalue minimisation (EV) methods, both optimised using a cluster analysis technique. Based on the misfit between the outputs from the XC and EV methods, an automated quality measure is given to each combination of splitting parameters (Φ and δt). The success of the approach is assessed by visually examining diagnostic plots of seismograms, particle motion and misfit surfaces.

The automated approach requires preset automation parameters that define a grid of S-wave analysis windows. I have shown the importance of considering the variation in the separation between the P- and S-wave arrivals and the size of the S-wave envelope, with variation in hypocentral distance. Such variation is attributed to the different amounts of attenuation the seismic waves experience, which is usually a function of distance travelled. The SWS approach yields more reliable measurements when using adaptive automation parameters (dependent on the hypocentral distance) compared to those obtained using fixed parameters. It should be noted that this may not be the case with all microseismic datasets, and more testing is required.

One of the benefits of the automated approach is that it allows testing many input parameters quickly. I took advantage of this to highlight the importance of choosing the right filter prior to the analysis to avoid biased results. I have tested using low pass filters of 100 Hz and 200 Hz prior to the analysis and found that the 200 Hz is the best filter. This choice of filter was guided by analysing the S-wave frequency content.

Owing to the low signal-to-noise ratio and the complexity of the waveforms in the Field M dataset, the automation approach was only successful in determining unreliable measurements (about 80% of the data). Visual examination of the diagnostic plots was necessarily to identify reliable measurements among the remaining one fifth of the dataset. However, the approach has been utilised in a fully automated way with other microseismic datasets (Wüstefeld et al., 2010; Jones, 2010).

The other advantage of the automated approach is the detection of SWS null measurements. Such measurements could be mistaken for reliable anisotropy measurements when relying on manual analysis. If interpreted carefully, null measurements can provide valuable information about the isotropic part of the medium the rays travel through. However, null measurements have been discarded in this study but guidance and recommendation on how to better exploit them is giving later in section 9.5.

9.2.3 Spatio-temporal variation of anisotropy

Using the automated SWS approach I was able to estimate SWS for 8545 source-receiver combinations. Stringent quality control reduced the number of acceptable measurements to 325. In order to understand limitations when interpreting these measurements, I modelled SWS in a range of synthetic rock models. I considered the cases of HTI (due to a set of vertical fractures), VTI (due to sedimentary fabric), orthorhombic (HTI plus VTI) and monoclinic (due to two non-orthogonal vertical fracture sets) anisotropic symmetries. For each model, the percentage difference between the fast and slow shear-wave velocities (δV_s) and, fast shear-wave strike and dip are computed using the Christoffel equation. The following guidelines were obtained:

- Good ray coverage is required to distinguish between different types of anisotropic symmetries.

- In HTI media, δV_s, fast strike and fast dip are dependent on ray azimuth and inclination, whereas in VTI media the three variables are only dependent on ray inclination.

- In HTI media, vertically travelling rays (up to 60° from vertical) are useful in estimating fracture strike. In contrast, subhorizontally travelling rays (±15° from horizontal) can be used to estimate fracture dip.

- For subhorizontal rays in HTI and monoclinic media caused by aligned fractures, the number of azimuthal peaks in δV_s indicates the number of fracture sets and the corresponding azimuths can be used to estimate their strikes.

- In VTI media, the dip of sedimentary fabrics can be recovered using subhorizontal arrivals.

Taken into account these guidelines, the accepted 325 measurements were used to investigate the nature of anisotropy in Field M and how it varies in space and time. The dataset was subdivided into groups by confining the source-receiver paths into blocks, clusters and lithological units. The overall conclusions can be summarised as follow:

- The amount of splitting ranges from 0 to 34 ms, mostly corresponding to variations in δV_s between 0% and 10%, but with a maximum of 18%.

- The anisotropy in the field is controlled by lithology and proximity to the main graben faults.

- High magnitudes of δV_s have been observed to the SE of the eastern-most graben fault (4.6%) and within the graben system (5.2%). The magnitude of δV_s decreases to 2.4% in the NW part of the field. This lateral variation in anisotropy is explained by the observation that the crest and the southern flank are faulted and fractured more extensively than the northern flank. The deformation and closure of fractures caused by high compaction rates in the NW part of the field provide another possible cause of the low anisotropy magnitudes.

- The highest magnitudes of δV_s are within the highly fractured Natih A reservoir (4.5%). The magnitude of δV_s decreases to 2.5% in the upper part of the Natih B-G formation (Natih B-G1) and 1.2% in the lower part of the same formation (Natih B-G2).

- The Fiqa shale exhibits moderate amounts of anisotropy (3.9%).

- In general, the detected fractures have strikes consistent with the patterns of the main faults. Measurements between and in the vicinity of the graben faults indicate NE-SW fracture strike parallel to the trend of the graben faults. In contrast, measurements outside the graben system show predominant NW-SE and NE-SW fracture strikes agreeing with the trend of the minor faults found in the SE and NW parts of the field.

- The majority of the measurements indicate subvertical fracture dip ($>70°$).

- Evidence of temporal variations in δV_s has been observed. In general, the magnitudes of δV_s are higher during summer months when gas production is at its maximum rate. However, such variations are not clear for measurements from the non-producing part of the carbonate formation (Natih B-G). The increase in δV_s during the summer is speculated to be controlled by the opening of fractures by fluid flow during production.

Overall, the results match those obtained from other techniques including shear-dipole logs, formation micro images (FMI) and core samples. They also agree with the geology and constraints from the tectonic setting of the field, including observations from the Natih formation outcrop.

The results show that anisotropy is controlled by lithology and proximity to faults. Such spatial variations have been previously recognised in studies of SWS in the vicinity of large active faults (for example the San Andreas fault in California (Boness & Zoback, 2006) and the North Anatolian fault (Peng & Ben-Zion, 2004)). This implies that interpretations derived from studies

on the reservoir scale can provide valuable insights into the interpretation of SWS on larger scales, and vice versa.

9.2.4 Shear-wave splitting inversion for anisotropy mechanisms

The splitting parameters were treated independently when analysing the spatio-temporal variation of anisotropy in Field M. To get a more quantitative description of the mechanisms behind the observed anisotropy, the splitting parameters were analysed simultaneously using a SWS inversion. The inversion is based on rock physics modelling and follows the approach of Verdon et al. (2009). Two inversions were performed with two different assumptions: (1) orthorhombic symmetry caused by a single fracture set embedded in a medium with a VTI sedimentary fabric, and (2) monoclinic media caused by two vertically aligned fracture sets. The inversion estimates fracture strike, density and strength of VTI anisotropy. The following conclusions can be made:

- The majority of the results show clear trade-offs in inversion parameters. This can be attributed to the spatial variation in anisotropy in Field M. The limited ray coverage shown by the real data also plays a role, rendering the inversion parameters poorly constrained, especially the fracture parameters.

- Generally, the estimated fracture strikes agree with those from ordinary SWS analysis (summarised in section 9.2.3). Rays travelling between the two graben faults reveal NE-SW fracture orientation, whereas rays travelling within the SE and NW parts of the field show predominant NW-SE and NE-SW fracture strikes.

- Fracture strike varies with lithology from 75° in the Fiqa shale to 35° in the Natih A reservoir to 55° in the Natih B-G1 unit. However, these estimates suffer from high levels of uncertainty due to limited ray coverage in subvertical directions.

- Estimates of fracture density are also poorly constrained due to the limited ray coverage in subvertical directions. The reliable estimates, generally, suggest little variation in fracture density which contradicts with the spatial variations in anisotropy observed from ordinary SWS analysis. However, better and more consistent estimates of fracture density were obtained from the analysis of frequency-dependent anisotropy (see next section).

- The strength of the VTI anisotropy is weak (γ=0.02), as expected for carbonate rocks. Weak VTI anisotropy is observed in the NW block and within the Fiqa shale and the Natih B-G formation. In contrast, the highly fractured parts of the field (i.e., SE and Graben blocks, and the Natih A reservoir) appear to lack any significant VTI anisotropy.

9.2.5 Fracture-induced frequency-dependent anisotropy

Evidence of frequency-dependent anisotropy has been observed in the Field M dataset. The observations were modelled using the Chapman (2003) poroelastic model. The model is based on the frequency-dependent squirt flow of fluids in porous fractured media.

The results show that fracture size varies from the micro-scale within the Fiqa shale cap rocks, to the meter-scale within the Natih A gas reservoir, to the centimetre-scale within the non-producing part of the carbonate formation (Natih B-G). Fracture density decreases with depth from 0.18 in the Fiqa, to 0.11 in the Natih A, to 0.10 in the Natih B-G1, to 0.08 in the Natih B-G2. There is also a lateral variation in fracture density from 0.13 in the SE block to 0.075 in the NW block. This variation agrees with the lateral variation in the magnitudes of δV_s from 4.6% in the SE block to 2.4% in the NW block, estimated using ordinary SWS analysis.

9.2.6 Shear-wave splitting tomography imaging

In the final stage of the research, I performed SWS tomography imaging following the recently developed approach of Wookey (2010). SWS tomography allows for a quantitative parameterisation of the spatial variation in anisotropy. This was not feasible using the previous techniques because they assume that the anisotropy is distributed uniformly along the raypath. The tomographic inversion was performed for four cases: (1) a single domain, (2) three domains separated by the boundaries between lithology units (Fiqa, Natih A and Natih B-G), (3) three domains separated by the graben faults and (4) three domains separated by the graben faults with inversions done separately for the Natih A and Natih B-G units (i.e., 6 domains). The following conclusions can be made:

- The inversion fails to converge to a solution when considering the entire field as one domain. This supports the existence of significant spatial variation in anisotropy in Field M as previously indicated using ordinary SWS analysis and SWS inversion based on rock physics modelling.

- Better constrained solutions are obtained when considering a layered model, compared to the case of dividing the field into blocks separated by the planes of the graben faults. This may indicate that the lateral variation in anisotropy is more complicated than the variation with lithology.

- In most cases, the inversion reveals a NW-SE fracture strike.

- When considering a layered model, the inversion shows subvertical fracture dip in the Fiqa and Natih A, and subhorizontal dip in the underlying Natih B-G formation. This agrees with the results obtained from ordinary SWS analysis (i.e., observing the dip of the fast shear-wave).

- When considering the lateral variation in anisotropy across the graben faults within the Natih A and Natih B-G, the results show that the elastic tensor strength is higher at the Natih A compared to the Natih B-G (only observed within the NW and Graben blocks). Assuming that the elastic tensor strength is proportional to δV_s, these observations support the conclusion that the fractured Natih A is highly anisotropic compared to the non-producing Natih B-G.

The study has shown the promising potential for using SWS tomography with microseismic data. I have suggested several ways to improve the inversion. These include decreasing the number of free parameters or restricting their ranges with the aid of supporting information from other geophysical techniques or geological models. The other way of improving the reliability of the results is to include null splitting measurements into the inversion. This will add more constraints to the inversion.

9.2.7 Workflow for shear-wave splitting in microseismic data

The stages of processing, analysing and modelling SWS throughout this project can be summarised in the workflow shown in Figure 9.1. This workflow can be used as a recipe for SWS analysis of microseismic data from hydrocarbon reservoirs, geothermal fields, mines and volcanoes. There is no obvious reason why this workflow can not be adopted to even deal with local and global earthquakes or, perhaps, laboratory measurements using ultrasonic signals.

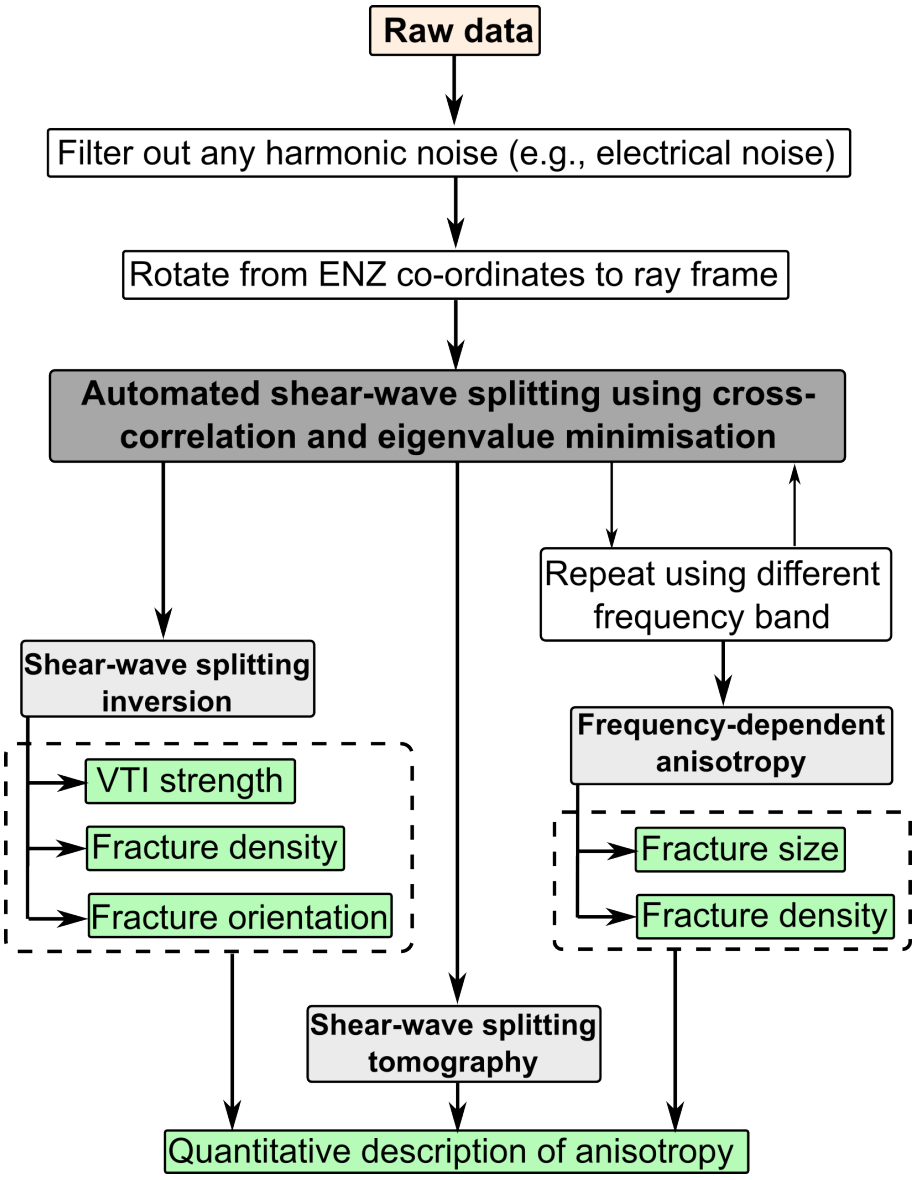

Figure 9.1: Workflow for shear-wave splitting analysis of microseismic data.

9.3 Achievements and significant contributions

In addition to the previously listed conclusions, this thesis has provided several original contributions to the scientific community. These include:

Tools for data reformatting and shear-wave splitting analysis and modelling

Throughout the project a collection of scripts and codes have been written or developed from existing ones. These include useful tools to:

- convert files from *stwf* to SAC format.
- extract information from XML files.
- automate SWS analysis.
- model SWS in synthetic rocks.
- invert SWS measurements.
- create synthetic frequency-dependent anisotropy curves.
- model frequency-dependent anisotropy observations.
- prepare data and domains for SWS tomography.

Detailed descriptions of these tools are given in Appendix A.

Automation of shear-wave splitting

Previous studies of SWS using microseismic data have relied on manual techniques. This thesis introduces a (semi-) automated approach to estimate splitting parameters. It benefits from an automated quality control based on the misfits in the outputs from the cross-correlation and eigenvalue minimisation methods. The approach has been successfully applied to the Field M dataset.

Shear-wave splitting inversion assuming two fracture sets

Code for the inversion for the parameters of two fracture sets have been developed during this study. The code is an extension to the original one by Verdon et al. (2009) which is limited to the case of a single fracture set embedded in a medium with a VTI symmetry.

The work on SWS inversion included using synthetic modelling to investigate the behaviour of the inversion in the cases of limited ray coverage and the presence of spatially varying anisotropy.

Establishment of frequency-dependent anisotropy analysis in microseismic data

This thesis marks the establishment of frequency-dependent anisotropy as an analysis tool that can be used with microseismic data, of course, after the original brief work by Al-Anboori et al. (2006). I wrote a code which implements the model of Chapman (2003) to predict and model frequency-dependent anisotropy. It has been successfully applied to the Field M dataset. The code has also been used to model frequency-dependent anisotropy observations in microseismic datasets from the Valhall and Cotton Valley fields (A. Wuestefeld, Uni. of Bristol, pers. comm., August 2010).

Shear-wave splitting tomography in microseismic data

I performed a feasibility study of using SWS tomography with microseismic data. This is the first time this technique has been applied to reservoir microseismic data. The outcomes look promising and open the door to improving our understanding of reservoir anisotropy in the future.

9.4 Recommendations to Field M operator

Having dealt with such a large dataset, several lessons have been learnt that the Field M operator may take into account for any future deployment of microseismic networks. The following recommendations are in order to get clearer picture of seismic anisotropy in the field, and hence better insights into its fracture system.

- The dense seismicity recorded at monitoring well 3 were caused by gas production from a nearby producer. The seismicity is very close to the monitoring well such that the separation between the P- and S-wave arrivals is very small and in some cases they contaminate each other. Future deployments should consider placing monitoring wells at a sufficient distance from producing wells. This will also help minimise noise levels.

- Due to limited ray coverage in the vertical plane, the estimates of fracture strike and density are not well constrained in most cases. To get better estimates of the two parameters, more geophones should be placed above and below the target (Natih A reservoir in this case or perhaps the seal) as to record events with raypaths at higher angles from horizontal.

- If some knowledge of fracture orientation in a specific part of the field is available, then the geophones should be placed such that the rays travel obliquely to the fracture planes. In this way the inversion is expected to yield better constrained fracture strike and density.

- Obviously, permanent or long time deployments are preferred for monitoring the behaviour of the field through the changes in the splitting parameters over time.

It should be noted that these recommendations are based on what I have learnt from SWS analysis. However, the final design of any microseismic network will be dependent on the availability of wells and will be guided by numerical modelling to test its detectability limit. Furthermore, these recommendations are not restricted to the Field M only, but should be considered in any similar cases.

Owing to confidentiality constraints, the available information about Field M is limited. Nevertheless, based on the available knowledge about the field and the microseismic experiment several conclusions have been made which might be of use to guide future management strategies. The key results are summarised in Tables 9.1 and 9.2 and translated into a summary cartoon in Figure 9.2. These results can be converted into the following suggestions:

- Future drilling programs should target places of high anisotropy (high fracture density), for example, the SE part of the field. At the moment, most of the producers are located in the NW flank.

- The majority of the measurements indicate subvertical fractures. No doubt these fractures enhance rock permeability. Thus, horizontal drilling is preferable over vertical drilling to maximise production.

- The SWS measurements surrounding the Horseshoe feature show that it is highly fractured and populated with large fractures (5 m). This means that the rocks of the Horseshoe compartment are of good quality. If the size of the compartment is large enough to accommodate an economic amount of natural gas, then this reservoir compartment should be considered in future field development strategies.

- The results show that the seal (Fiqa shale) is fractured. However, these fractures are very small (micro-scale), as revealed by the modelling of frequency-dependent anisotropy observations. These estimates come from a few SWS measurements. Therefore, further assessment

of the seal integrity should be conducted to confirm these results and avoid possibilities of fluid leakage.

- Existing geomechanical models of the field (Dudley et al., 2005; Qobi et al., 2009) lack the inclusion of fracture properties. Fractures play a role in controlling the overall mechanical properties of the formations. Thus, the outcomes from this study might be used to improve such models.

- The interpretation of the source parameters and the estimates of the b-value were restricted by the availability of information. Further analysis and interpretation of these parameters should be undertaken as they have the potential of delivering information for reservoir characterisation and hazard assessment.

- During Phase II of the experiment (i.e., after 9^{th} of July 2002), events were located every other day. A better picture of the correlation between seismicity and production/injection activities can be achieved by locating the remaining events. This would also increase the number of SWS measurements and hence provide better constrained fracture parameters.

Formation	Lithology	Mechanism	$M_\circ$ (GNm)	M	r (m)	$\Delta\sigma$ (MPa)	b-value
Fiqa	shale	seal arching	0.05	-0.9	2.9	1.1	0.77
Natih A	chalky limestone	compaction/gas production	0.02	-1.1	2.2	0.9	0.85
Natih B-G	chalky limestone	fault reactivation	0.09	-0.7	3.2	1.3	1.05

Table 9.1: Key characteristics of the Field M microseismic data. $M_\circ$ is seismic moment, M is moment magnitude, r is source radius and $\Delta\sigma$ is stress drop. These are median estimates except the magnitude of the b parameter which is determined from the best fit straight line to the frequency-magnitude plot (see Chapter 3).

Formation/ Block	Analysis of δV_s and Φ			Shear-wave splitting inversion							Frequency-dep. anisotropy		Tomography		
				orthorhombic			monoclinic								
	δV_s (%)	FS (°)	FD (°)	α (°)	ξ	γ	α_1 (°)	ξ_1	α_2 (°)	ξ_2	a_f (m)	ξ	β_1 (°)	β_3 (°)	s
Fiqa	3.9	-	72	75	[0.15]	0.02	[70]	[0.15]	[160]	[0.04]	1.3×10⁻6	0.18	84	-37	0.03
Natih A	4.5	[62] & [146]	73	[35]	0.01	-0.02	[110]	[0.07]	[170]	[0.02]	2.5	0.11	80	-46	0.002
Natih B-G	2.3	[14] & [120]	63	[135]	[0]	0.02	[110]	[0.03]	[20]	[0.03]	-	-	41	114	0.01
Natih B-G1	2.5	-	54 & 73	[55]	0.01	-0.02	40	0.04	120	0.02	0.012	0.10	-	-	-
Natih B-G2	[1.2]	-	[26]	[120]	[0.11]	[0.02]	[20]	[0.01]	[30]	[0.01]	0.017	0.08	-	-	-
SE block	4.6	39 & 132	55	[140]	0.02	-0.02	30	0.06	120	0.06	2.6	0.13	[83]	[51]	[0.01]
Graben block	5.2	27	[25]	[95]	[0.2]	[0.1]	[170]	[0.1]	[110]	[0.12]	-	0.081	[49]	[-58]	[0.002]
NW block	2.4	119	73	[90]	0.03	0	[40]	[0.03]	120	0.03	2.7	0.075	[25]	[59]	[∼0]
Horseshoe	3.9	-	83	130	0.09	0.06	110	0.05	20	0.05	5	-	-	-	-

Table 9.2: Key results from shear-wave splitting analysis. δV_s is percentage difference between the fast and slow shear-wave velocities along the raypath, Φ is the fast shear-wave polarisation direction, FS is fast strike, FD is fast dip, α is fracture strike, ξ is fracture density, γ is Thomsen's gamma, a_f is fracture radius, β_1 and β_3 are fracture dip and strike, respectively, from tomography and s is strength of the elastic tensor. Estimates of a_f for the SE and NW blocks come from the Natih A subset. Measurements shown in squared brackets are not well constrained because of a lack of available measurements or the interpreted existence of significant spatial variation in anisotropy.

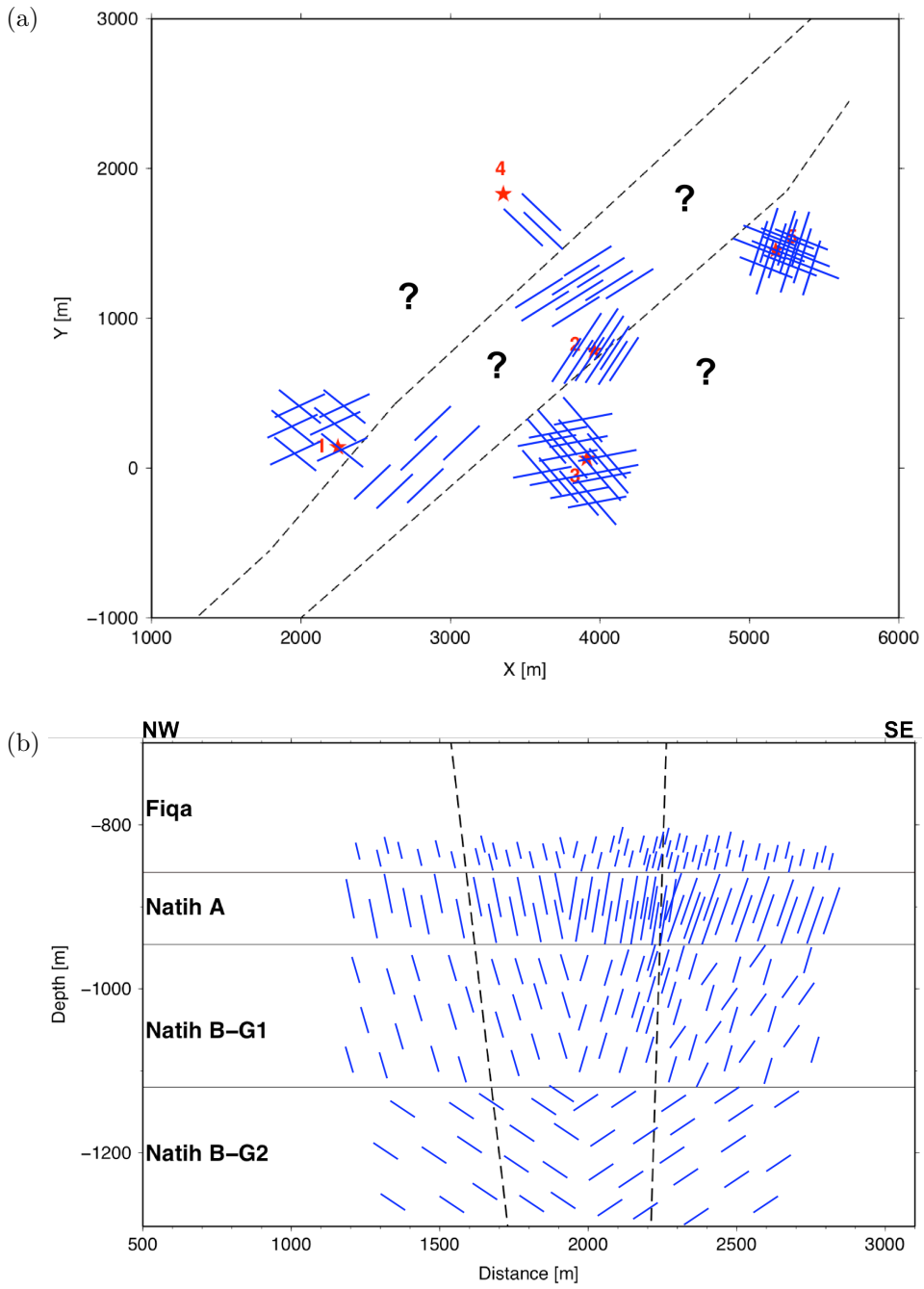

Figure 9.2: A schematic plot of the Field M fracture model based on results from shear-wave splitting analysis. (a) Map view showing fracture strike. (b) Cross-section showing fracture dip. In (a) and (b) the spacing between lines (i.e., fractures) is proportional to fracture density (or magnitude of δV_s). In (b) the length of lines is proportional to fracture size (but not to scale).

9.5 Scope for future work

Optimisation for real-time information

I believe that the proposed SWS workflow in Figure 9.1 can be further optimised to the point that it can deliver (near) real-time information about the monitored field's geomechanical behaviour. This will require an automatic triggering system, arrival auto-picker (e.g., Nippress et al., 2010) and event auto-locator (e.g., Oye & Roth, 2003). Then, the data can be clustered into time slides depending on the rate of seismicity. The SWS workflow illustrated in Figure 9.1 can be applied to each time slide. The outputs will provide, for example, information about the mechanics of fractures and the *in situ* stress regime. This approach seems feasible with frac jobs to understand the evolution of fractures in space and time, and hence the efficiency in stimulating the reservoir. More suggestions on optimising the SWS workflow can be found in Wüstefeld et al. (2010).

Such an 'optimised workflow' can be also applied to studies of seismic hazard in mining and the vicinity of volcanos and active faults. Real-time SWS measurements would offer information about changes in the stress field and rock stability, and thus potentially allow for early warning alerts.

Null shear-wave splitting measurements

Null SWS measurements have been discarded in this study. Such measurements can be used to gain information about the isotropic part of the imaged medium. However, this will require filtering out null measurements caused by high noise level. The useful null measurements can then be used in the SWS inversion and SWS tomography. This will likely give better constrained inversion parameters.

Advanced frequency-dependent anisotropy modelling

The existing code can be improved, for example, by incorporating boot-straping techniques with the inversion. This will help minimising the effect from outliers and will provide better estimates of errors in the inverted parameters.

There have been some developments recently to the Chapman (2003) model to handle more complicated fractured media such as the inclusion of conjugate and en-echelon fracture sets (Chapman, 2007, 2009). Generally, fractured reservoirs exhibit multiple fracture sets with different geometry and orientations. Such advancement in frequency-dependent anisotropy analysis and modelling would allow exploring more structurally complex reservoirs.

Focal mechanism

Earthquake focal mechanisms provide information about stress regime, and orientations of fault planes and their slip directions. Al-Anboori (2006) made an early attempt to estimate earthquake focal mechanisms with a subset of Field M dataset. This study was done manually and limited by the assumption of double-couple as the only mechanism. However, numerous studies have shown that non double-couple mechanisms (e.g., isotropic and compensated linear vector dipole (CLVD)) are common in induced seismicity (e.g., Julian et al., 1998; Miller et al., 1998; Sileny & Milev, 2008; Baig & Urbancic, 2010).

Integrating the results from focal mechanism and SWS analysis would offer a valuable information about the state of stress in the field. Such information can then be used to optimise reservoir models. I suggest estimating focal mechanisms of the Field M events as the next logical continuation of this study of SWS. Recently, there have been significant advancement in microearthquake focal mechanism analysis, which can be tested with the Field M dataset. Among these are the studies by Dahm et al. (1999), Vavryčuk (2007) and Baig & Urbancic (2010).

Attenuation anisotropy

Attenuation anisotropy in microseismic records can be estimated by comparing the relative frequency content of the fast and slow split shear-waves following the approach of Carter & Kendall (2006). In the presence of attenuation anisotropy the fast and slow shear-waves should experience different levels of frequency-dependent attenuation. This has the potential to distinguish between the different mechanisms of velocity anisotropy, which would be useful when interpreting SWS results. Additionally, attenuation anisotropy can offer information about pore fluid content and properties (Carter & Kendall, 2006).

Discrete fracture network and geomechanical modelling

Previous studies (e.g., Jones et al., 2004; Liu et al., 2009; Sausse et al., 2010) mainly focused on linking microseismic activity with dynamic reservoir processes via modelling, especially in frac jobs and seismic hazard assessment. It is time to push forward and incorporate the other attributes from microseismic data (e.g., fracture parameters and focal mechanisms) into reservoir models. Such attributes can be used to optimise discrete fracture network (DFN) and geomechanic models, which then can help in conditioning fluid flow simulations. A promising example is the work carried out by Eisner et al. (2010) using microseismic data from a treatment of shale gas reservoir in the USA. They translated information about fracture locations, orientations and failure

mechanism, determined from focal mechanisms, into a DFN model. In a similar way, fracture parameters obtained from SWS analysis can be used to populate DFN models. In general, fracture characterisation using SWS analysis provides valuable insights into the geomechanical behaviours of reservoirs.

References

Abt, D. L. & Fischer, K. M., 2008. Resolving three-dimensional anisotropic structure with shear wave splitting tomography, *Geophysical Journal International*, **173**(3), 859–886.

Aki, K., 1965. Maximum likelihood estimate of b in the formula log N= a-bM and its confidence limits, *Bulletin of the Earthquake Research Institute, Tokyo University*, **43**, 237–239.

Aki, K. & Richards, P., 2002. *Quantitative seismology*, University Science Books.

Al-Abri, S., 2003. *Fracture-induced anisotropy study using shear-wave splitting in the **** oil field, Oman*, Master's thesis, University of Leeds, United Kingdom.

Al-Anboori, A., 2006. *Anisotropy, focal mechanisms and state of stress in an oilfield: Passive seismic monitoring in Oman*, Ph.D. thesis, University of Leeds, United Kingdom.

Al-Anboori, A., Kendall, J.-M., & Chapman, M., 2006. Fracture-induced frequency-dependent anisotropy, **** Field, Oman, *68th EAGE Conference and Technical Exhibition, Vienna, Austria, Expanded Abstracts, A047*.

Al-Busaidi, R., 1997. The use of borehole imaging logs to optimize horizontal well completions in fractured water-flooded carbonate reservoirs, *GeoArabia*, **2**(1), 19–34.

Al-Harrasi, O. & Kendall, J.-M., 2010. Modelling frequency-dependent observations made on microseismic data, *72nd EAGE Conference and Exhibition incorporating SPE EUROPEC, Barcelona, Spain, Expanded Abstracts, F016*.

Al-Harrasi, O., Wüstefeld, A., & Kendall, J.-M., 2009. Towards a fully automated shear-wave splitting analysis of microseismic data, *71st EAGE Conference and Exhibition, Amsterdam, The Netherlands, Expanded Abstracts, X013*.

Al-Harrasi, O., Al-Anboori, A., Wüstefeld, A., & Kendall, J.-M., 2010a. Seismic anisotropy in a hydrocarbon field estimated from microseismic data, *Geophysical Prospecting, DOI: 10.1111/j.1365-2478.2010.0915.x*.

Al-Harrasi, O., Kendall, J.-M., & Chapman, M., 2010b. Fracture characterisation using frequency-dependent shear-wave anisotropy analysis of microseismic data, *Geophysical Journal International, in review*.

Al-Kindi, M., 2006. *Structural evolution and fracture pattern of Salakh arch*, Ph.D. thesis, University of Leeds, United Kingdom.

Ameen, M., 2003. Fracture and in-situ stress characterization of hydrocarbon reservoirs: definitions and introduction, in *Fracture and in-situ stress characterisation for hydrocarbon reservoirs*, vol. 209, pp. 1–6, ed. Ameen, M., Geological Society, London, Special Publications.

Amitrano, D., 2003. Brittle-ductile transition and associated seismicity: Experimental and numerical studies and relationship with the b-value, *Journal of Geophysical Research*, **108**(B1), DOI:10.1029/2001JB000680.

Angerer, E., Crampin, S., Li, X. Y., & Davis, T. L., 2002. Processing, modelling and predicting time-lapse effects of overpressured fluid-injection in a fractured reservoir, *Geophysical Journal International*, **149**(2), 267–280.

Ata, E. & Michelena, R. J., 1995. Mapping distribution of fractures in a reservoir with P-S converted waves, *The Leading Edge*, **14**(6), 664–676.

Audigane, P., Royer, J. J., & Kaieda, H., 2002. Permeability characterization of the Soultz and Ogachi large-scale reservoir using induced microseismicity, *Geophysics*, **67**(1), 204–211.

Backus, G. E., 1962. Long-wave elastic anisotropy produced by horizontal layering, *Journal of Geophysical Research*, **67**(11), 4427–4440.

Baig, A. & Urbancic, T., 2010. Microseismic moment tensors: A path to understanding frac growth, *The Leading Edge*, **29**(3), 320–324.

Baker Atlas GEOScience, 1999. In-situ stress analysis, *Unpublished Petroleum Development Oman report prepared by Baker Atlas GEOScience*.

Baria, R., Baumgärtner, J., Gérard, A., Jung, R., & Garnish, J., 1999. European HDR research programme at Soultz-sous-Forts (France) 1987-1996, *Geothermics*, **28**(4-5), 655–669.

Barnes, A. E., 1993. Instantaneous spectral bandwidth and dominant frequency with applications to seismic reflection data, *Geophysics*, **58**(3), 419–428.

Bell, J. S., 1990. Investigating stress regimes in sedimentary basins using information from oil industry wireline logs and drilling records, in *Geological applications of wireline logs*, vol. 48, pp. 305–325, eds Hurst, A., Lovell, M. A., & Morton, A. C., Geological Society, London, Special Publications.

Bokelmann, G. H. R. & Harjes, H. P., 2000. Evidence for temporal variation of seismic velocity within the upper continental crust, *Journal of Geophysical Research*, **105**(B10), 23879–23894.

Boness, N. L. & Zoback, M. D., 2004. Stress-induced seismic velocity anisotropy and physical properties in the SAFOD Pilot Hole in Parkfield, CA, *Geophysical Research Letters*, **31**(15), DOI:10.1029/2003GL019020.

Boness, N. L. & Zoback, M. D., 2006. Mapping stress and structurally controlled crustal shear velocity anisotropy in California, *Geology*, **34**(10), 825–828.

Bourne, S. J., Maron, K., Oates, S. J., & Mueller, G., 2006. Monitoring reservoir deformation on land - Evidence for fault re-activation from microseismic, InSAR, and GPS data, *68th EAGE Conference and Exhibition, Vienna, Austria, Expanded Abstracts, E026*.

Bowman, J. R. & Ando, M., 1987. Shear-wave splitting in the upper-mantle wedge above the Tonga subduction zone, *Geophysical Journal of the Royal Astronomical Society*, **88**(1), 25–41.

Bridges, D. L. & Gao, S. S., 2006. Spatial variation of seismic b-values beneath Makushin Volcano, Unalaska Island, Alaska, *Earth and Planetary Science Letters*, **245**(1-2), 408–415.

Brune, J. N., 1970. Tectonic stress and the spectra of seismic shear waves from earthquakes, *Journal of Geophysical Research*, **75**(26), 4997–5009.

Buland, R., 1976. The mechanics of locating earthquakes, *Bulletin of the Seismological Society of America*, **66**(1), 173–187.

Carter, A. J. & Kendall, J.-M., 2006. Attenuation anisotropy and the relative frequency content of split shear waves, *Geophysical Journal International*, **165**(3), 865–874.

Chambers, K., Kendall, J.-M., Brandsberg-Dahl, S., & Rueda, J., 2010. Testing the ability of surface arrays to monitor microseismic activity, *Geophysical Prospecting*, **58**(5), 821–830.

Chapman, M., 2001. *Modelling the wide-band laboratory response of rock samples to fluid pressure changes*, Ph.D. thesis, University of Edinburgh, United Kingdom.

Chapman, M., 2003. Frequency-dependent anisotropy due to meso-scale fractures in the presence of equant porosity, *Geophysical Prospecting*, **51**(5), 369–379.

Chapman, M., 2007. Frequency-dependent anisotropy of rocks with complex fracture networks, *EAGE/SEG Research Workshop, Perugia, Italy, Expanded Abstracts, A21*.

Chapman, M., 2009. Modeling the effect of multiple sets of mesoscale fractures in porous rock on frequency-dependent anisotropy, *Geophysics*, **74**(6), D97–D103.

Chapman, M., Zatsepin, S., & Crampin, S., 2002. Derivation of a microstructural poroelastic model, *Geophysical Journal International*, **151**(2), 427–451.

Chapman, M., Maultzsch, S., & Liu, E., 2003a. Some estimates of the squirt-flow frequency, *SEG Annual Meeting, Dallas, Texas, 26-29 October*.

Chapman, M., Maultzsch, S., Liu, E., & Li, X., 2003b. The effect of fluid saturation in an anisotropic multi-scale equant porosity model, *Journal of Applied Geophysics*, **54**(3-4), 191–202.

Chesnokov, E., Queen, J., Vichorev, A., Lynn, H., Hooper, J., Bayuk, I., Castagna, J., & Roy, B., 2001. Frequency dependent anisotropy, *SEG Expanded Abstracts*, **20**(1), 2120–2123.

Chichinina, T., Sabinin, V., & Ronquillo-Jarillo, G., 2006. QVOA analysis: P-wave attenuation anisotropy for fracture characterization, *Geophysics*, **71**(3), C37–C48.

Chun-lai, W., Ai-xiang, W., Xiao-hui, L., & Rui, L., 2009. Study on fractal characteristics of b value with microseismic activity in deep mining, *Procedia Earth and Planetary Science*, **1**(1), 592–597.

Coy, G., 2003. Sedimentological and diagenetic controls on rock strenght and compaction withing the Natih A in **** 448 and through integration with additional cored and uncored wells in the wider **** Field, North Oman, *Unpublished Petroleum Development Oman report prepared by Badley Ashton*.

Crampin, S., 1978. Seismic wave propagation through a cracked solid: polarization as a possible dilatancy diagnostic, *Geophysical Journal of The Royal Astronomical Society*, **53**(3), 467–496.

Crampin, S., 1981. A review of wave motion in anisotropic and cracked elastic-media, *Wave Motion*, **3**(4), 343–391.

Crampin, S., 1984. Effective anisotropic elastic constants for wave propagation through cracked solids, *Geophysical Journal of the Royal Astronomical Society*, **76**(1), 135–145.

Crampin, S., 1994. The fracture criticality of crustal rocks, *Geophysical Journal International*, **118**(2), 428–438.

Crampin, S. & Chastin, S., 2003. A review of shear wave splitting in the crack-critical crust, *Geophysical Journal International*, **155**(1), 221–240.

Crampin, S. & Gao, Y., 2006. A review of techniques for measuring shear-wave splitting above small earthquakes, *Physics of the Earth and Planetary Interiors*, **159**(1-2), 1–14.

Crampin, S. & Peacock, S., 2008. A review of the current understanding of seismic shear-wave splitting in the Earths crust and common fallacies in interpretation, *Wave Motion*, **45**(6), 675–722.

Crampin, S. & Zatsepin, S. V., 1997. Modelling the compliance of crustal rock-II. Response to temporal changes before earthquakes, *Geophysical Journal International*, **129**(3), 495–506.

Crampin, S., Bush, I., Naville, C., & Taylor, D., 1986. Estimating the internal structure of reservoirs with shear-wave VSPs, *The Leading Edge*, **5**, 35–39.

Crampin, S., Volti, T., & Stefansson, R., 1999. A successfully stress-forecast earthquake, *Geophysical Journal International*, **138**(1), F1–F5.

Dahm, T., Manthei, G., & Eisenblatter, J., 1999. Automated moment tensor inversion to estimate source mechanisms of hydraulically induced micro-seismicity in salt rock, *Tectonophysics*, **306**(1), 1–17.

De Keijzer, M., Hillgartner, H., Al Dhahab, S., & Rawnsley, K., 2007. A surface-subsurface study of reservoir-scale fracture heterogeneities in Cretaceous carbonates, North Oman, in *Fractured reservoirs*, vol. 270, pp. 227–244, eds Lonergan, L., Jolly, R. J. H., Rawnsley, K., & Sanderson, D. J., Geological Society, London, Special Publications.

Del Pezzo, E., Bianco, F., Petrosino, S., & Saccorotti, G., 2004. Changes in the coda decay rate and shear-wave splitting parameters associated with seismic swarms at Mt. Vesuvius, Italy, *Bulletin of The Seismological Society of America*, **94**(2), 439–452.

Droste, H. & Steenwinkel, M. V., 2004. Stratal geometries and patterns of platform carbonates: The Cretaceous of Oman, in *Seismic imaging of carbonate reservoirs and systems*, vol. 81, pp. 185–206, eds Eberli, G., Masaferro, J. L., & Sarg, J. F. R., AAPG Memoir.

Droste, H. J., 1998. **** Shuaiba fault and fracture modeling, *Unpublished Petroleum Development Oman internal report No: OYP/003/07/98*.

Dudley, J., van der Linden, A., & Mueller, G., 2005. Geomechanical modelling of a pore collapsing carbonate: Compaction and subsidence of a field in Oman, *International Petroleum Technology Conference, 21-23 November, Doha, Qatar, Paper 10680-MS*.

Dunne, W. & North, C., 1990. Orthogonal fracture systems at the limits of thrusting: an example from southwestern Wales, *Journal of Structural Geology*, **12**(2), 207–215.

Dyer, B. C., Jones, R. H., Cowles, J. F., Barkved, O., & Folstad, P. G., 1999. Microseismic survey of a North Sea reservoir, *World Oil*, **220**(3), 74–78.

Eisner, L., Williams-Stroud, S., Hill, A., Duncan, P., & Thornton, M., 2010. Beyond the dots in the box: Microseismicity-constrained fracture models for reservoir simulation, *The Leading Edge*, **29**(3), 326–333.

Evans, M. S., Kendall, J.-M., & Willemann, R. J., 2006. Automated SKS splitting and upper-mantle anisotropy beneath Canadian seismic stations, *Geophysical Journal International*, **165**(3), 931–942.

Farrell, J., Husen, S., & Smith, R. B., 2009. Earthquake swarm and b-value characterization of the Yellowstone volcano-tectonic system, *Journal of Volcanology and Geothermal Research*, **188**(1-3), 260–276.

Feignier, B. & Grasso, J., 1991. Relation between seismic source parameters and mechanical properties of rocks: a case study, *Pure and Applied Geophysics*, **137**(3), 175–199.

Filbrandt, J. B., Al-Dhahab, S., Al-Habsy, A., Harris, K., Keating, J., Al-Mahruqi, S., Ozkaya, S. I., Richard, P. D., & Robertson, T., 2006. Kinematic interpretation and structural evolution of North Oman, Block 6, since the Late Cretaceous and implications for timing of hydrocarbon migration into Cretaceous reservoirs, *GeoArabia*, **11**(1), 97–140.

Fischer, P. A., 2004. Valhall life of field seismic: Permanent, on-demand 4D, *World Oil*, **225**(3), 38–40.

Frohlich, C. & Davis, S. D., 1993. Teleseismic b values; or, much ado about 1.0, *Journal of Geophysical Research*, **98**(B1), 631–644.

Fukao, Y., 1984. Evidence from core-reflected shear waves for anisotropy in the Earth's mantle, *Nature*, **309**(5970), 695–698.

Gerstenberger, M., Wiemer, S., & Giardini, D., 2001. A systematic test of the hypothesis that the b value varies with depth in California, *Geophysical Research Letters*, **28**(1), 57–60.

Gibowicz, S. J. & Kijko, A., 1994. *An introduction to mining seismology*, Academic Press.

Granger, P. Y., Rollet, A., & Bonnot, J. M., 2000. Preliminary evaluation of azimuthal anisotropy over the Valhall Field using C-wave data, in *Anisotropy 2000: Fractures, Converted Waves and Case Studies*, pp. 49–67, eds Ikelle, L. & Gangi, A., Society of Exploration Geophysicists.

Grasso, J. R., 1992. Mechanics of seismic instabilities induced by the recovery of hydrocarbons, *Pure and Applied Geophysics*, **139**(3-4), 507–534.

Grechka, V. & Tsvankin, I., 2000. Inversion of azimuthally dependent NMO velocity in transversely isotropic media with a tilted axis of symmetry, *Geophysics*, **65**(1), 232–246.

Guest, W. S. & Kendall, J.-M., 1993. Modelling seismic waveforms in anisotropic inhomogeneous media using ray and Maslov asymptotic theory: applications to exploration seismology, *Canadian Journal of Exploration Geophysics*, **29**(1), 78–92.

Gutenberg, B. & Richter, C. F., 1944. Frequency of earthquakes in California, *Bulletin of the Seismological Society of America*, **34**(4), 185–188.

Hall, S. A. & Kendall, J.-M., 2000. Constraining the interpretation of AVOA for fracture characterisation, in *Anisotropy 2000: Fractures, Converted Waves and Case Studies*, pp. 107–144, eds Ikelle, L. & Gangi, A., Society of Exploration Geophysicists.

Hall, S. A. & Kendall, J.-M., 2003. Fracture characterization at Valhall: Application of P-wave amplitude variation with offset and azimuth (AVOA) analysis to a 3D ocean-bottom data set, *Geophysics*, **68**(4), 1150–1160.

Hammond, J., Kendall, J.-M., Angus, D., & Wookey, J., 2010a. Interpreting spatial variations in anisotropy: insights into the Main Ethiopian Rift from SKS waveform modelling, *Geophysical Journal International*, **181**(3), 1701–1712.

Hammond, J. O. S., Wookey, J., Kaneshima, S., Inoue, H., Yamashina, T., & Harjadi, P., 2010b. Systematic variation in anisotropy beneath the mantle wedge in the Java-Sumatra subduction system from shear-wave splitting, *Physics of the Earth and Planetary Interiors*, **178**(3-4), 1–13.

Hanks, T. C. & Wyss, M., 1972. The use of body-wave spectra in the determination of seismic-source parameters, *Bulletin of the Seismological Society of America*, **62**(2), 561–589.

Helbig, K. & Thomsen, L., 2005. 75th Anniversary Paper - 75-plus years of anisotropy in exploration and reservoir seismics: A historical review of concepts and methods, *Geophysics*, **70**(6), 9ND–23ND.

Herman, G. C., 2009. Steeply-dipping extension fractures in the Newark basin, New Jersey, *Journal of Structural Geology*, **31**(9), 996–1011.

Herz, U., 2004. Geomechanical analysis, **** field, Natih formation, *Unpublished report submitted to Petroleum Development Oman by Baker Atlas GEOScience*.

Hodder, M., 2004. **** field: structural analysis, rock typing and permeability prediction of integrated core and FMI borehole image data, *Unpublished Petroleum Development Oman report prepared by Baker Atlas GEOScience Bahrain*.

Hornby, B., Schwartz, L., & Hudson, J., 1994. Anisotropic effective-medium modeling of the elastic properties of shales, *Geophysics*, **59**(10), 1570–1583.

Horne, S. & MacBeth, C., 1994. Inversion for seismic anisotropy using genetic algorithms, *Geophysical Prospecting*, **42**(8), 953–974.

House, N., Fuller, B., Shemeta, J., & Sterling, M., 2004. Integration of surface seismic, 3D VSP, and microseismic hydraulic fracture mapping to improve gas production in a tight complex reservoir, *SEG Expanded Abstracts*, **23**, 414–416.

Hudson, J. A., 1980. Overall properties of a cracked solid, *Mathematical Proceedings of the Cambridge Philosophical Society*, **88**, 371–384.

Hudson, J. A., 1981. Wave speeds and attenuation of elastic waves in material containing cracks, *Geophysical Journal of the Royal Astronomical Society*, **64**(1), 133–150.

Hudson, J. A., Liu, E., & Crampin, S., 1996. The mechanical properties of materials with interconnected cracks and pores, *Geophysical Journal International*, **124**(1), 105–112.

Jervis, M. & Dasgupta, S. N., 2009. Recent microseismic monitoring results from VSP and permanent sensor deployment in Saudi Arabia, *EAGE Workshop on Passive Seismic, Limassol, Cyprus, Expanded Abstracts, A10*.

Johnston, J. & Christensen, N., 1995. Seismic anisotropy of shales, *Journal of Geophysical Research*, **100**(B4), 5991–6003.

Jones, G., 2010. *Microseismicity in the Ekofisk Field: faulting and fracturing in a compacting chalk reservoir*, Ph.D. thesis, University of Bristol.

Jones, R. H. & Asanuma, H., 2004. Optimal four geophone configuration, vector fidelity and long-term monitoring, *66th EAGE Conference and Exhibition, Paris, France, Expanded Abstracts, Z99*.

Jones, R. H., Raymer, D., Mueller, G., Rynja, H., & Maron, K., 2004. Microseismic monitoring of the **** Oilfield, *66th EAGE Conference and Exhibition, Paris, France, Expanded Abstracts, A007*.

Julian, B., Miller, A., & Foulger, G., 1998. Non-double-couple earthquakes 1. Theory, *Review of Geophysics*, **36**(4), 525–549.

Jupe, A. J., Jones, R. H., Wilson, S. A., & Cowles, J. F., 2003. Microseismic monitoring of geomechanical reservoir processes and fracture-dominated fluid flow, in *Fracture and in-situ stress characterisation for hydrocarbon reservoirs*, vol. 209, pp. 77–86, ed. Ameen, M., Geological Society, London, Special Publications.

Kaarsberg, E. A., 1959. Introductory studies of natural and artificial argillaceous aggregates by sound-propagation and X-ray diffraction methods, *Journal of Geology*, **67**(4), 447–472.

Kay, I., Sol, S., Kendall, J.-M., Thomson, C., White, D., Asudeh, I., Roberts, B., & Francis, D., 1999. Shear wave splitting observations in the Archean craton of Western Superior, *Geophysical Research Letters*, **26**(17), 2669–2672.

Kendall, J.-M., 2000. Seismic anisotropy in the boundary layers of the mantle, in *Earth's Deep Interior: Mineral Physics and Tomography from the Atomic to the Global Scale*, vol. 117, pp. 149–175, eds Karato, S., Stixrude, L., Liebermann, R. C., & Masters, T. G., Geophysical Monograph Series, American Geophysical Union.

Kendall, J.-M., Fisher, Q. J., Crump, S. C., Maddock, J., Carter, A., Hall, S. A., Wookey, J., Valcke, S. L. A., Casey, M., Lloyd, G., & Ismail, W. B., 2007. Seismic anisotropy as an indicator of reservoir quality in siliciclastic rocks, in *Structurally complex reservoirs*, vol. 292, pp. 123–136, ed. Jolley, S., Geological Society, London, Special Publications.

Kendall, J.-M., Al-Harrasi, O., Verdon, J. P., Wuestefeld, A., & Al-Anboori, A., 2009. Fracture characterisation using estimates of shear-wave splitting from microseismic data, *EAGE Workshop on Passive Seismic, Limassol, Cyprus, Expanded Abstracts, A07*.

Kendall, R. R. & Kendall, J.-M., 1996. Shear-wave amplitude anomalies in south-central Wyoming, *The Leading Edge*, **15**(8), 913–920.

Klemm, H., Quseimi, I., Novali, F., Ferretti, A., & Tamburini, A., 2010. Monitoring horizontal and vertical surface deformation over a hydrocarbon reservoir by PSInSAR, *First Break*, **28**(5), 29–37.

Kristiansen, T., Barkved, O., & Patillo, P., 2000. Use of passive seismic monitoring in well and casing design in the compacting and subsiding Valhall Field, North Sea, *SPE European Petroleum Conference, Paris, France, SPE (65134-MS)*.

Kwiatek, G., Plenkers, K., Nakatani, M., Yabe, Y., & Dresen, G., 2010. Frequency-magnitude characteristics down to magnitude -4.4 for induced seismicity recorded at Mponeng gold mine, South Africa, *Bulletin of the Seismological Society of America*, **100**(3), 1165–1173.

Lahaie, F. & Grasso, J. R., 1999. Loading rate impact on fracturing pattern: lessons from hydrocarbon recovery, Lacq gas field, France, *Journal of Geophysical Research*, **104**(B8), 941–954.

Laubach, S., Marrett, R., & Olson, J., 2000. New directions in fracture characterization, *The Leading Edge*, **19**, 704–711.

Leonard, T. & Hsu, J. S. J., 1999. *Bayesian methods*, Cambridge University Press, New York.

Levin, V., Droznin, D., Park, J., & Gordeev, E., 2004. Detailed mapping of seismic anisotropy with local shear waves in southeastern Kamchatka, *Geophysical Journal International*, **158**(3), 1009–1023.

Li, Y. G., Teng, T. L., & Henyey, T. L., 1994. Shear-wave splitting observations in the Northern Los Angeles Basin, Southern California, *Bulletin of the Seismological Society of America*, **84**(2), 307–323.

Li, Y. P., Cheng, C. H., & Toksoz, M. N., 1998. Seismic monitoring of the growth of a hydraulic fracture zone at Fenton Hill, New Mexico, *Geophysics*, **63**(1), 120–131.

Litsey, L. R., MacBride, W. L., Al-Hinai, K. M., & Dismukes, N. B., 1986. Shuaiba reservoir geological study, **** Field, Oman, *Journal of Petroleum Technology*, **38**(7), 651–661.

Liu, E., Crampin, S., Queen, J., & Rizer, W., 1993. Behaviour of shear waves in rocks with two sets of parallel cracks, *Geophysical Journal International*, **113**(2), 509–517.

Liu, E., Queen, J. H., Li, X. Y., Chapman, M., Maultzsch, S., Lynn, H. B., & Chesnokov, E. M., 2003. Observation and analysis of frequency-dependent anisotropy from a multicomponent VSP at Bluebell-Altamont field, Utah, *Journal of Applied Geophysics*, **54**(3-4), 319–333.

Liu, E., Chapman, M., Hudson, J. A., Tod, S. R., Maultzsch, S., & Li, X. Y., 2005. Quantitative determination of hydraulic properties of fractured rock using seismic techniques, in *Understanding the Micro to Macro Behaviour of Rock-Fluid Systems*, vol. 249, pp. 29–42, ed. Shaw, R. P., Geological Society, London, Special Publications.

Liu, E., Crampin, S., & Queen, J. H., 2007. Fracture detection using crosshole surveys and reverse vertical seismic profiles at the Conoco Borehole Test Facility, Oklahoma, *Geophysical Journal International*, **107**(3), 449–463.

Liu, X., Lolon, E., Li, X., Chen, B., Cipolla, C., & Wang, C., 2009. Integrating microseismic mapping, fracture modeling and reservoir modeling optimizes well performance in the Changqing Field, *Asia Pacific Oil and Gas Conference & Exhibition, 4-6 August, Jakarta, Indonesia, Paper 121528-MS*.

Liu, Y., Zhang, H., Thurber, C., & Roecker, S., 2008. Shear wave anisotropy in the crust around the San Andreas fault near Parkfield: spatial and temporal analysis, *Geophysical Journal International*, **172**(3), 957–970.

Liu, Y. F., Teng, T. L., & Yehuda, B. Z., 2004. Systematic analysis of shear-wave splitting in the aftershock zone of the 1999 Chi-Chi, Taiwan, earthquake: Shallow crustal anisotropy and lack of precursory variations, *Bulletin of the Seismological Society of America*, **94**(6), 2330–2347.

Long, M. D., de Hoop, M. V., & van der Hilst, R. D., 2008. Wave-equation shear wave splitting tomography, *Geophysical Journal International*, **172**(3), 311–330.

Lynn, H., Simon, K., Bates, C., Layman, M., Schneider, R., & Jones, M., 1995. Use of anisotropy in P-wave and S-wave data for fracture characterization in a naturally fractured gas reservoir, *The Leading Edge*, **14**, 887–893.

Lynn, H. B. & Thomsen, L. A., 1990. Reflection shear-wave data collected near the principal axes of azimuthal anisotropy, *Geophysics*, **55**(2), 147–156.

Lynn, H. B., Beckham, W. E., Simon, K. M., Bates, C. R., Layman, M., & Jones, M., 1999. P-wave and S-wave azimuthal anisotropy at a naturally fractured gas reservoir, Bluebell-Altamont Field, Utah, *Geophysics*, **64**(4), 1312–1328.

MacBeth, C., 1996. Interpreting qS1 polarizations due to intersecting fractures, *SEG Expanded Abstracts*, **15**, 758–761.

Mallick, S., Craft, K. L., Meister, L. J., & Chambers, R. E., 1998. Determination of the principal directions of azimuthal anisotropy from P-wave seismic data, *Geophysics*, **63**(2), 692–706.

Marson-Pidgeon, K. & Savage, M. K., 1997. Frequency-dependent anisotropy in Wellington, New Zealand, *Geophysical Research Letters*, **24**(24), 3297–3300.

Maultzsch, S., 2005. *Analysis of frequency-dependent anisotropy in VSP data*, Ph.D. thesis, University of Edinburgh, United Kingdom.

Maultzsch, S., Chapman, M., Liu, E., & Li, X., 2003. Modelling frequency-dependent seismic anisotropy in fluid-saturated rock with aligned fractures: implication of fracture size estimation from anisotropic measurements, *Geophysical Prospecting*, **51**(5), 381–392.

Maultzsch, S., Chapman, M., Liu, E., & Li, X., 2007. Modelling and analysis of attenuation anisotropy in multi-azimuth VSP data from the Clair field, *Geophysical Prospecting*, **55**(5), 627–642.

Maxwell, S. & Urbancic, T., 2001. The role of passive microseismic monitoring in the instrumented oil field, *The Leading Edge*, **20**, 636–639.

Maxwell, S. C., Young, R. P., Bossu, R., Jupe, A., & Dangerfield, J., 1998. Microseismic Logging of the Ekofisk Reservoir, *SPE/ISRM Rock Mechanics in Petroleum Engineering, Trondheim, Norway, SPE/ISRM (47276-MS)*.

McClusky, S., Reilinger, R., Mahmoud, S., Ben Sari, D., & Tealeb, A., 2003. GPS constraints on Africa (Nubia) and Arabia plate motions, *Geophysical Journal International*, **155**(1), 126–138.

Mercadier, C. G. & Mäkel, G. H., 1991. Fracture patterns of Natih formation outcrops and their application for reservoir modelling of the Natih field, North Oman, *SPE Middle East Oil Show, 16-19 November, Bahrain, Paper 21377-MS*.

Miller, A. D., Foulger, G. R., & Julian, B. R., 1998. Non-double-couple earthquakes. 2. Observations, *Review of Geophysics*, **36**(4), 551–568.

Miller, V. & Savage, M., 2001. Changes in seismic anisotropy after volcanic eruptions: Evidence from Mount Ruapehu, *Science*, **293**(5538), 2231–2233.

Mogi, K., 1962. Magnitude-frequency relation for elastic shocks accompanying fractures of various materials and some related problems in earthquakes, *Bulletin of Earthquake Research Institute*, **40**, 831–853.

Mori, J. & Abercrombie, R. E., 1997. Depth dependence of earthquake frequency-magnitude distributions in California: Implications for rupture initiation, *Journal of Geophysical Research*, **102**(B2), 15081–15090.

Mueller, M. C., 1991. Prediction of lateral variability in fracture intensity using multicomponent shear-wave surface seismic as a precursor to horizontal drilling in the Austin Chalk, *Geophysical Journal International*, **107**(3), 409–415.

Munson, C. G., Thurber, C. H., Li, Y., & Okubo, P. G., 1995. Crustal shear wave anisotropy in southern Hawaii: spatial and temporal analysis, *Journal of Geophysical Research*, **100**(B10), 20367–20377.

Nippress, S. J., Rietbrock, A., & Heath, A. E., 2010. Optimized automatic pickers: application to the ANCORP data set, *Geophysical Journal International*, **181**(2), 911–925.

Oye, V. & Roth, M., 2003. Automated seismic event location for hydrocarbon reservoirs, *Computers and Geosciences*, **29**(7), 851–863.

Ozkaya, I., Hodder, M., Herz, U., & Swindells, E., 2004. Integrated reservoir evaluation from borehole images, openhole logs and cores, Natih-A reservoir, **** Gas Field, Northern Oman, Phase I, *Unpublished Petroleum Development Oman report prepared by Baker Atlas GEOScience Bahrain*.

Peng, Z. & Ben-Zion, Y., 2004. Systematic analysis of crustal anisotropy along the Karadere–Duzce branch of the North Anatolian fault, *Geophysical Journal International*, **159**(1), 253–274.

Pérez, M., Gibson, R., & Toksöz, M., 1999a. Detection of fracture orientation using azimuthal variation of P-wave AVO responses, *Geophysics*, **64**(4), 1253–1265.

Pérez, M., Grechka, V., & Michelena, R., 1999b. Fracture detection in a carbonate reservoir using a variety of seismic methods, *Geophysics*, **64**(4), 1266–1276.

Pointer, T., Liu, E., & Hudson, J. A., 2000. Seismic wave propagation in cracked porous media, *Geophysical Journal International*, **142**(1), 199–231.

Potters, J. H., Groenendaal, H. J., Oates, S. J., Hake, J. H., & Kalden, A. B., 1999. The 3D shear experiment over the Natih field in Oman. Reservoir geology, data acquisition and anisotropy analysis, *Geophysical Prospecting*, **47**(5), 637–662.

Press, W. H., Flannery, B., Teukolsky, S. A., & Vetterling, W. T., 1989. *Numerical recipes*, Cambridge University Press New York, 2nd edn.

Prioul, R., Plona, T., Kane, M., Sinha, B., Kaufman, P., & Signer, C., 2004. Azimuthal anisotropy using shear dipole sonic: insights from the AIG 10 well, Corinth Rift Laboratory, *Comptes Rendus Geosciences*, **336**(4-5), 477–485.

Qobi, L., Ita, J., von Winterfeld, C., Shukaili, J., & Qusseimi, I., 2009. Depletion effects on a currently active fault and existing subsidence bowl: Geomechanics assessment - giant field Northern Oman, *International Petroleum Technology Conference, 7-9 December, Doha, Qatar, Paper 13339-MS*.

Rathore, J., Fjaer, E., Holt, R., & Renlie, L., 1995. P-wave and S-wave anisotropy of a synthetic sandstone with controlled crack geometry, *Geophysical Prospecting*, **43**(6), 711–728.

Raymer, D. & Jones, R. H., 2004. Final report on microseismic monitoring of production operations in the **** Field, Oman - Phase 2, *Unpublished report submitted to Shell International Exploration and Production by VetcoGray Controls Limited*.

Raymer, D., Jones, R. H., & Fisher, A., 2003. Final report on the PDO/ABB collaborative microseismic monitoring trial in the **** Field, Oman, *Unpublished report submitted to Petroleum Development Oman by ABB Offshore Systems Limited*.

Restivo, A. & Helffrich, G., 1999. Teleseismic shear wave splitting measurements in noisy environments, *Geophysical Journal International*, **137**(3), 821–830.

Rumpker, G., Tommasi, A., & Kendall, J.-M., 1999. Numerical simulations of depth-dependent anisotropy and frequency-dependent wave propagation effects, *Journal of Geophysical Research*, **104**(B10), 23141–23153.

Rutledge, J. & Phillips, W., 2003. Hydraulic stimulation of natural fractures as revealed by induced microearthquakes, Carthage Cotton Valley gas field, east Texas, *Geophysics*, **68**(2), 441–452.

Rutledge, J. T., Phillips, W. S., & Schuessler, B. K., 1998. Reservoir characterization using oil-production-induced microseismicity, Clinton County, Kentucky, *Tectonophysics*, **289**(1-3), 129–152.

Saito, T., Sato, H., & Ohtake, M., 2002. Envelope broadening of spherically outgoing waves in three-dimensional random media having power-law spectra, *Journal of Geophysical Research, DOI:10.1029/2001JB000264*.

Sambridge, M., 1999a. Geophysical inversion with a neighbourhood algorithm-I: Searching a parameter space, *Geophysical Journal International*, **138**(2), 479–494.

Sambridge, M., 1999b. Geophysical inversion with a neighbourhood algorithm-II. Appraising the ensemble, *Geophysical Journal International*, **138**(3), 727–746.

Sausse, J., Dezayes, C., Dorbath, L., & Genter, A., 2010. 3D model of fracture zones at Soultz-sous-Forets based on geological data, image logs, induced microseismicity and vertical seismic profiles, *Comptes Rendus Geoscience*, **342**(7-8), 531–545.

Sayers, C. & Rickett, J., 1997. Azimuthal variation in AVO response for fractured gas sands, *Geophysical Prospecting*, **45**(1), 165–182.

Sayers, C. M. & van Munster, J. G., 1991. Microcrack-induced seismic anisotropy of sedimentary rocks, *Journal of Geophysical Research*, **96**(B10), 16529–16533.

Schoenberg, M. & Sayers, C. M., 1995. Seismic anisotropy of fractured rock, *Geophysics*, **60**(1), 204–211.

Scholz, C. H., 1968. The frequency-magnitude relation of microfracturing in rock and its relation to earthquakes, *Bulletin of the Seismological Society of America*, **58**(1), 399–415.

Segall, P., 1989. Earthquakes triggered by fluid extraction, *Geology*, **17**(10), 942–946.

Seher, T. & Main, I. G., 2004. A statistical evaluation of a 'stress-forecast' earthquake, *Geophysical Journal International*, **157**(1), 187–193.

Shapiro, S., Rothert, E., Rath, V., & Rindschwentner, J., 2002. Characterization of fluid transport properties of reservoirs using induced microseismicity, *Geophysics*, **67**(1), 212–220.

Shapiro, S. A., Zien, H., & Hubral, P., 1994. A generalized ODoherty-Anstey formula for waves in finely layered media, *Geophysics*, **59**(11), 1750–1762.

Shemeta, J. E., Davis, T. L., Roth, M., & Riley, R. B., 2007. Seeing Beyond the Frac: Integration of hydraulic fracture mapping with multicomponent 3D seismic data, *SPE Rocky Mountain Oil and Gas Technology Symposium, Denover, Colorado, USA, Paper 108160-MS*.

Shih, X. R. & Meyer, R. P., 1990. Observation of shear wave splitting from natural events: South Moat of Long Valley Caldera, California, June 29 to August 12, 1982, *Journal of Geophysical Research*, **95**(B7), 11179–11195.

Sileny, J. & Milev, A., 2008. Source mechanism of mining induced seismic events–Resolution of double couple and non double couple models, *Tectonophysics*, **456**(1-2), 3–15.

Sileny, J. & Plomerova, J., 1996. Inversion of shear-wave splitting parameters to retrieve three-dimensional orientation of anisotropy in continental lithosphere, *Physics of the Earth and Planetary Interiors*, **95**(3-4), 277–292.

Silver, P. G. & Chan, W. W., 1988. Implications for continental structure and evolution from seismic anisotropy, *Nature*, **335**(6185), 34–39.

Silver, P. G. & Chan, W. W., 1991. Shear wave splitting and subcontinental mantle deformation, *Journal of Geophysical Research*, **96**(B10), 16429–16454.

Snyder, D. & Bruneton, M., 2007. Seismic anisotropy of the Slave craton, NW Canada, from joint interpretation of SKS and Rayleigh waves, *Geophysical Journal International*, **169**(1), 170–188.

Stein, S. & Wysession, M., 2003. *An introduction to seismology, earthquakes, and earth structure*, Wiley-Blackwell.

Sze, E., 2005. *Induced seismicity analysis for reservoir characterization at a petroleum field in Oman*, Ph.D. thesis, Massachusetts Institute of Technology (MIT), USA.

Tatham, D., Lloyd, G., Butler, R., & Casey, M., 2008. Amphibole and lower crustal seismic properties, *Earth and Planetary Science Letters*, **267**(1-2), 118–128.

Teanby, N., Kendall, J.-M., Jones, R. H., & Barkved, O., 2004a. Stress-induced temporal variations in seismic anisotropy observed in microseismic data, *Geophysical Journal International*, **156**(3), 459–466.

Teanby, N., Kendall, J.-M., & van der Baan, M., 2004b. Automation of shear-wave splitting measurements using cluster analysis, *Bulletin of the Seismological Society of America*, **94**(2), 453–463.

Terken, J. M. J., 1999. The Natih petroleum system of North Oman, *GeoArabia*, **4**(2), 157–180.

Thomsen, L., 1986. Weak elastic anisotropy, *Geophysics*, **51**(10), 1954–1966.

Thomsen, L., 1995. Elastic anisotropy due to aligned cracks in porous rock, *Geophysical Prospecting*, **43**(3), 805–829.

Thomsen, L., 1999. Converted-wave reflection seismology over inhomogeneous, anisotropic media, *Geophysics*, **64**(3), 678–690.

Thomsen, L., 2002. *Understanding seismic anisotropy in exploration and exploitation*, SEG/EAGE Distinguished Instructor Short Course (No. 5).

Tichelaar, B. W. & Hatchell, P. J., 1997. Inversion of 4-C borehole flexural waves to determine anisotropy in a fractured carbonate reservoir, *Geophysics*, **62**(5), 1432–1441.

Tod, S. & Liu, E., 2002. Frequency-dependent anisotropy due to fluid flow in bed limited cracks, *Geophysical Research Letters*, **29**(15), 39–1.

Tsvankin, I., 1997. Reflection moveout and parameter estimation for horizontal transverse isotropy, *Geophysics*, **62**(2), 614–629.

Urbancic, T., Baig, A., & Bowman, S., 2010. Complexity of hydraulic fractures - The b-value, *72nd EAGE Conference and Exhibition incorporating SPE EUROPEC, Barcelona, Spain, Expanded Abstracts, P561*.

Utsu, T., 1965. A method for determining the value of b in a formula log n= a-bM showing the magnitude-frequency relation for earthquakes, *Geophysical Bulletin of Hokkaido University*, **13**, 99–103.

Valcke, S. L. A., Casey, M., Lloyd, G. E., Kendall, J.-M., & Fisher, Q. J., 2006. Lattice preferred orientation and seismic anisotropy in sedimentary rocks, *Geophysical Journal International*, **166**(2), 652–666.

van der Kolk, C. M., Guest, W. S., & Potters, J. H. H. M., 2001. The 3D shear experiment over the Natih field in Oman: the effect of fracture-filling fluids on shear propagation, *Geophysical Prospecting*, **49**(2), 179–197.

Vavryčuk, V., 2007. On the retrieval of moment tensors from borehole data, *Geophysical Prospecting*, **55**(3), 381–391.

Vecsey, L., Plomerová, J., & Babuška, V., 2008. Shear-wave splitting measurements - Problems and solutions, *Tectonophysics*, **462**(1-4), 178–196.

Verdon, J. P., Angus, D. A., Kendall, J.-M., & Hall, S. A., 2008. The effect of microstructure and nonlinear stress on anisotropic seismic velocities, *Geophysics*, **73**(4), D41–D51.

Verdon, J. P., Kendall, J.-M., & Wüstefeld, A., 2009. Imaging fractures and sedimentary fabrics using shear wave splitting measurements made on passive seismic data, *Geophysical Journal International*, **179**(2), 1245–1254.

Verdon, J. P., Kendall, J.-M., & Maxwell, S. C., 2010. A comparison of passive seismic monitoring of fracture stimulation from water and CO2 injection, *Geophysics*, **75**(3), MA1–MA7.

Volti, T. & Crampin, S., 2003. A four-year study of shear-wave splitting in Iceland: 1. Background and preliminary analysis, in *New Insights into structural interpretation and modelling*, vol. 212, pp. 117–133, ed. Nieuwland, D. A., The Geological Society, London, Special Publications.

Wang, Z., 2002. Seismic anisotropy in sedimentary rocks, part 2: Laboratory data, *Geophysics*, **67**(5), 1423–1440.

Warren, N. W. & Latham, G. V., 1970. An experimental study of thermally induced microfracturing and its relation to volcanic seismicity, *Journal of Geophysical Research*, **75**(23), 4455–4464.

Werner, U. & Shapiro, S., 1999. Frequency-dependent shear-wave splitting in thinly layered media with intrinsic anisotropy, *Geophysics*, **64**(2), 604–608.

Wiemer, S., 2001. A software package to analyze seismicity: ZMAP, *Seismological Research Letters*, **72**(2), 374–383.

Wiemer, S. & Katsumata, K., 1999. Spatial variability of seismicity parameters in aftershock zones, *Journal of Geophysical Research*, **104**(B6), 13135–13151.

Wiemer, S. & Wyss, M., 2002. Mapping spatial variability of the frequency-magnitude distribution of earthquakes, *Advances in Geophysics*, **45**, 259–302.

Wiemer, S., McNutt, S. R., & Wyss, M., 1998. Temporal and three-dimensional spatial analyses of the frequency–magnitude distribution near Long Valley Caldera, California, *Geophysical Journal International*, **134**(2), 409–421.

Willis, M., Burns, D., Rao, R., Minsley, B., Toksöz, M., & Vetri, L., 2006. Spatial orientation and distribution of reservoir fractures from scattered seismic energy, *Geophysics*, **71**(5), O43–O51.

Wilson, S., Jones, R., Wason, W., Raymer, D., & Jaques, P., 2004. Passive seismic makes sense for 4D reservoir monitoring, *First Break*, **23**, 59–65.

Winterstein, D. F., De, G. S., & Meadows, M. A., 2001. Twelve years of vertical birefringence in nine-component VSP data, *Geophysics*, **66**(2), 582–597.

Woessner, J. & Wiemer, S., 2005. Assessing the quality of earthquake catalogues: estimating the magnitude of completeness and its uncertainty, *Bulletin of the Seismological Society of America*, **95**(2), 684.

Wookey, J., 2010. Direct probabilistic inversion of shear-wave data for anistropy, *Bulletin of the Seismological Society of America, In review*.

Wüstefeld, A., 2007. *Methods and application of shear-wave splitting: The East European Craton*, Ph.D. thesis, Universite Montpellier II, France.

Wüstefeld, A. & Bokelmann, G., 2007. Null detection in shear-wave splitting measurements, *Bulletin of the Seismological Society of America*, **97**(4), 1204–1211.

Wüstefeld, A., Al-Harrasi, O. H., Verdon, J. P., Wookey, J., & Kendall, J.-M., 2010. A strategy for automated analysis of passive microseismic data to study seismic anisotropy and fracture characteristics, *Geophysical Prospecting*, **58**(5), 755–773.

Wyss, M., Klein, F., Nagamine, K., & Wiemer, S., 2001. Anomalously high b-values in the South Flank of Kilauea volcano, Hawaii: evidence for the distribution of magma below Kilauea's East rift zone, *Journal of Volcanology and Geothermal Research*, **106**(1-2), 23–37.

Yang, M., Elkibbi, M., & Rial, J., 2005. An inversion scheme to model subsurface fracture systems using shear wave splitting polarization and delay time observations simultaneously, *Geophysical Journal International*, **160**(3), 939–947.

Young, R. P., Maxwell, S. C., Urbancic, T. I., & Feignier, B., 1992. Mining-induced microseismicity: monitoring and applications of imaging and source mechanism techniques, *Pure and Applied Geophysics*, **139**(3-4), 697–719.

Zatsepin, S. V. & Crampin, S., 1997. Modelling the compliance of crustal rock-I. Response of shear-wave splitting to differential stress, *Geophysical Journal International*, **129**(3), 477–494.

Zhang, H., Liu, Y., Thurber, C., & Roecker, S., 2007. Three-dimensional shear-wave splitting tomography in the Parkfield, California, region, *Geophysical Research Letters*, **34**(24), L24308.

Zhang, Z. & Schwartz, S. Y., 1994. Seismic anisotropy in the shallow crust of the Loma Prieta segment of the San Andreas fault system, *Journal of Geophysical Research*, **99**(B5), 9651–9661.

Zinke, J. & Zoback, M., 2000. Structure-related and stress-induced shear-wave velocity anisotropy: observations from microearthquakes near the Calaveras fault in central California, *Bulletin of the Seismological Society of America*, **90**(5), 1305–1312.

Zoback, M. & Zinke, J., 2002. Production-induced normal faulting in the Valhall and Ekofisk oil fields, *Pure and Applied Geophysics*, **159**(1-3), 403–420.

A
List of programs used in the study

In this appendix I list the programs, codes and scripts used in this project. These softwares were written/developed by myself unless otherwise stated. Sufficient credit and acknowledgement have been given when using libraries and subroutines created by other researchers (inside the program source files when appropriate). The software packages are listed in different tables according to in which chapter they have been used, starting from Chapter 3. A copy of these packages is included in the CD attached to this thesis, with further details on how to compile and use each program.

Package name	**Programming language(s)**	**Description and use**
XMETAL	-	The X-windows version of the Microseismic Event Timing And Location is a microseismic processing package by Schlumberger. It is used to: (1) convert seismograms from tetrahedral configuration to three orthogonal set, (2) align seismograms with the geographic co-ordinates and (3) remove electrical noise using a predictive filter.
asc_to_stwf	F & C	Convert the 120 ascii files exported from XMETAL to one stwf binary file.
data_preparation	C	Collection of C-shell scripts to: rename files, create directory for each event and finally, move files to their associated directory.
time_picks	A, F, C & S	Extract absolute P- and S-wave time picks from XML files (developed from the original version by Steve Oates (Shell)). Then, form ascii tables of relative time picks.
event_location	F & C	Create file for each event containing information like location, origin time and magnitude .... etc.
stwf_to_sac	F & C	Convert files from stwf format to SAC format.
source_parameters	A	Extract the magnitudes of the event source parameters from XML files.
ZMAP	M	Seismicity analysis package used mainly to estimate *b*-value and analyse its spatio-temporal change (Written by S. Wiemer).

Table A.1: List of software packages used in Chapter 3. (ascii = American Standard Code for Information Interchange, stwf = Simple Triggered Waveform interchange Format, XML = eXtensible Markup Language, SAC = Seismic Analysis Code, F = FORTRAN, C = C-shell, A = awk and S = SAC macro.)

Package name	**Programming language(s)**	**Description and use**
ENZ_to_abc	F & S	Rotate seismograms from east-north-vertical co-ordinates to ray frame. It gives the option of rotating seismograms based on P-wave particle motion or source-receiver straight line (developed from the original versions by N. Teanby and A. Al-Anboori).
P_S_separation	F, C & S	Read SAC files and compute the time difference between the P- and S-wave time picks.
SHEBA_XC	F, C, S & G	Automated shear-wave splitting analysis package. Developed, with the help of A. Wuestefeld, from the original code (SHEBA) by J. Wookey.
SWS_plot_inspection	F & S	Helps in inspecting the diagnostic plots in a fast way.
Quality_plots	M	Useful visualisation of the measurement qualities from SHEBA_XC (written by A. Wuestefeld).
2D_histogram	M	MatLab script to plot 2D histograms (written by M. O'Brien).

Table A.2: List of software packages used in Chapter 4. (F = FORTRAN, C = C-shell, S = SAC macro, G = GMT (Generic Mapping Tools) and M = MatLab.)

Package name	**Programming language(s)**	**Description and use**
synthetic_SWS	F & M	Create synthetic examples of shear-wave splitting in a range of anisotropic symmetries. Contains 'ematrix6' package by D. Mainprice and J. Wookey.
ani_calc	F	It reads Field M 1D velocity model and calculate the percentage difference between the fast and slow shear-wave velocities along the raypath (δV_s) (developed from the original version by A. Al-Anboori).
abc_to_ENZ	F	Rotate the estimates of the fast polarisation direction from the ray frame to the geographic co-ordinates to yield fast polarisation strike and dip (developed from the original version by N. Teanby and A. Al-Anboori).
sphani	F & G	Draw lower-hemisphere projection plots (written by A. Al-Anboori).
azimuthal	F	Analyse the azimuthal variation of δV_s, fast strike and fast dip. It includes the moving average code by N. Teanby.
temporal	F	Analyse the temporal variation of δV_s, fast strike and fast dip. It includes the moving average code by N. Teanby.

Table A.3: List of software packages used in Chapter 5. (F = FORTRAN, G = GMT (Generic Mapping Tools) and M = MatLab.)

Package name	Programming language(s)	Description and use
MISHED	F & G	Modelling and Inverting SHEar wave Differences. Shear-wave splitting inversion code written by J. Verdon. It models the case of a single fracture set embedded in a VTI anisotropic medium.
2Frac	F, G & C	Shear-wave splitting inversion assuming two fracture sets. Developed from the MISHED code.

Table A.4: List of software packages used in Chapter 6. (F = FORTRAN, C = C-shell, G = GMT (Generic Mapping Tools))

Package name	Programming language(s)	Description and use
microFDA	F, C & G	Model frequency-dependent anisotropy observations and invert for fracture size and density. It incorporates the Chapman 2003 code.
microFDA_full	F, C & G	Similar to microFDA, but this version invert for fracture size, density and strike.
microFDA_synthetic	F, C & G	Generates frequency-dependent anisotropy synthetic curves. It incorporates the Chapman 2003 code.

Table A.5: List of software packages used in Chapter 7. (F = FORTRAN, C = C-shell, S = SAC macro, G = GMT (Generic Mapping Tools))

Package name	Programming language(s)	Description and use
Tomography	F & C	Collection of codes to perform shear-wave splitting tomography (written by J. Wookey). It incorporates the Neighbourhood Algorithm.
XML_generator	F	Collection of FORTRAN scripts to read the outputs from shear-wave splitting analysis and generates XML files that will be used in the tomography inversion..

Table A.6: List of software packages used in Chapter 8. (F = FORTRAN, C = C-shell)